MECHANISMS & RECOGNITION

OF

HYPER-EXTENSION AT MAGMA-POOR RIFTED MARGINS

by

Kenneth Gerard McDermott

A thesis submitted to the University of Birmingham for the degree of

DOCTOR OF PHILOSOPHY

School of Geography, Earth, and Environmental Sciences
University of Birmingham
September 2012

Abstract

Magma-poor rifted margins (MPRMs) are characterised by extreme crustal attenuation that increases ocean ward, serpentinised mantle, detachment fault systems and low volumes of syn-rift magmatism. An apparent "extension discrepancy" exists at MPRMs, whereby the amount of stretching accommodated by *seismically observable* faults is far less than that required to thin the entire crust to the extent observed on wide-angle seismic and gravity models. *Unrecognised* polyphase faulting can accommodate the required extension. High degrees of stretching require polyphase faulting (PPF), so that the extension discrepancy may simply be a failure to recognise multiple generations of faulting at MPRMs. The polyphase faulting hypothesis is tested through the consideration of the structural geometries likely to result, generation of synthetic seismic images from those geometries and comparison of synthetic images with reflection seismic data from the hyper-extended Porcupine Basin. From this comparison, I have identified at least two cross-cutting fault generations on the margins of the Porcupine Basin. The models demonstrate PPF can accommodate extremely high strain but is practically un-interpretable when $\beta \geq$ c.2.5, remaining hidden on hyper-extended crust. Crustal embrittlement is achievable over two fault generations (minimum) leading to hyper-extension and mantle serpentinisation, with the remaining extension likely accommodated by serpentinite detachment systems.

For my parents

Acknowledgments

Table of Contents

Table of Figures

Table of Tables

CHAPTER 1

Introduction

1.1 Crustal extension: Pure and Simple

Continental rifting and break-up is a first order tectonic process leading ultimately to the formation of oceanic crust and the generation of new tectonic plate margins. Classical models of how extension progresses in the continental crust invoking either pure-shear mechanisms (e.g. McKenzie, 1978) or simple-shear mechanisms (e.g. Wernicke, 1985) are commonly used to explain the development of many rift basins and have been applied to rifted margins also (Le Pichon & Sibuet, 1981), with limited success.

For the pure-shear (McKenzie, 1978) model the magnitude of post-rift subsidence is directly related to the magnitude of lithospheric stretching (β_L) and whole crustal stretching (β_c). The original McKenzie, (1978) model proposes that stretching is uniform with depth, i.e. the lithosphere and the crust should be stretched to the same degree (see Fig. 1.1). The implication with uniform stretching is that the all crustal layers would also stretch to the same degree, so that the stretching associated with faulting (β_f) should be diagnostic of the extensional strain suffered by the whole crust (β_c). One of the predictions made by uniform stretching is that the maximum post-rift subsidence should be spatially coincident with the maximum syn-rift subsidence, so in effect the maximum thickness of post-rift sediments should directly overlie the thinnest crust. A “steers-head” geometry is commonly observed in many rift basins, where post-rift sediments onlap the rift flanks (White & McKenzie, 1988).

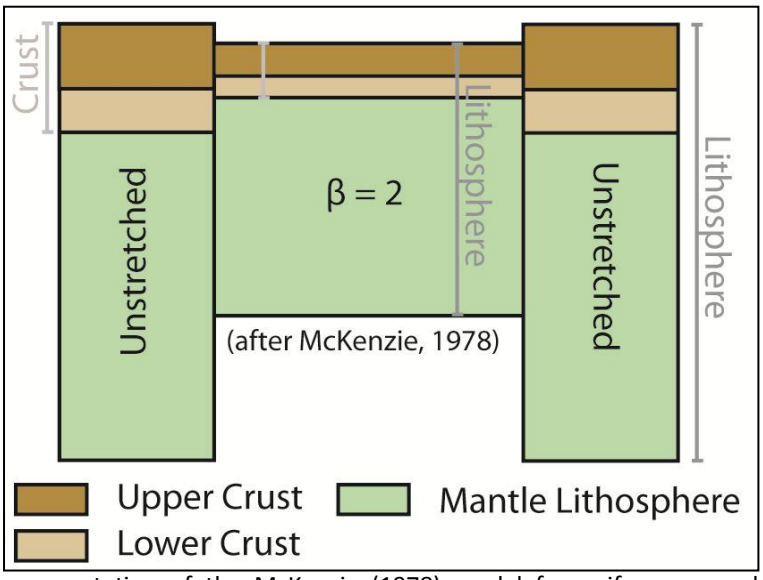

Fig. 1.1: Simple representation of the McKenzie (1978) model for uniform pure shear stretching. 100% extension of unthinned lithosphere yields β = 2. The strain is distributed uniformly throughout the lithospheric layers. Lithosphere (βL = 2), Whole crust (βwc = 2), and Upper Crust (βuc = 2).

This geometry is not predicted by be accounted for by the simple uniform stretching model (McKenzie, 1978). However, if the lithospheric mantle is stretched to the same degree as the crust but over a slightly wider region, leading to different distributions of crustal and mantle thinning, then the observed sedimentation pattern can be accounted for (White & McKenzie, 1988). Stretching the mantle lithosphere over a wider region also avoids potential space problems that may result if the amount of stretching were differential between upper and lower portions of the crust/lithosphere (White & McKenzie, 1988).

In contrast to the pure-shear model, there is the simple shear (Wernicke, 1985) model (Fig. 1.2), where stretching in the crust is non-coaxial. Extension is accommodated by a shallowly dipping lithospheric scale shear-zone in this model (Wernicke, 1985). One of the predictions of crustal extension over a lithospheric scale shear zone is that the post-rift thermal subsidence will be dislocated from the area of maximum fault controlled subsidence and deposited on relatively unfaulted crust (Wernicke, 1985; Allen & Allen, 2005).

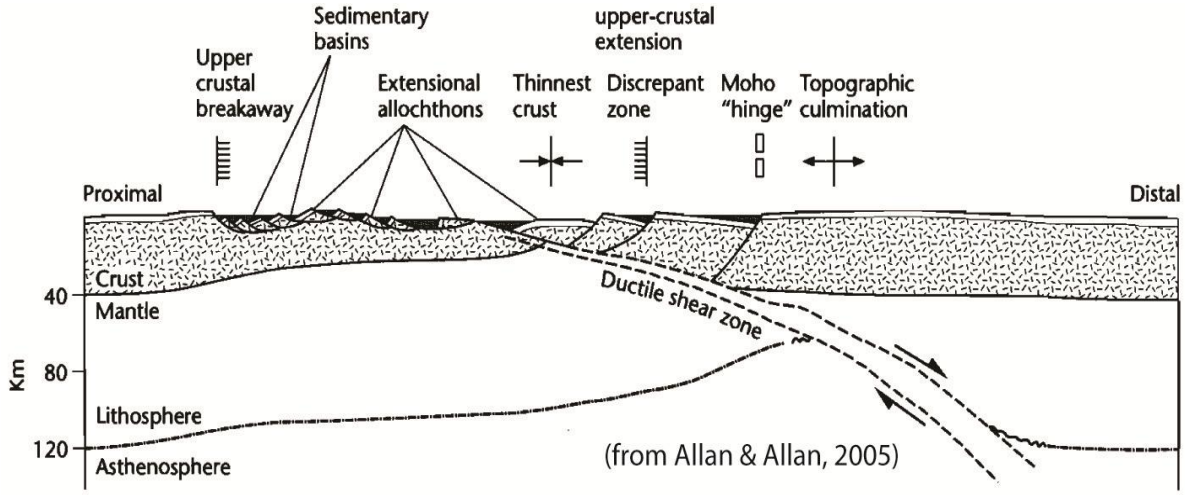

Fig. 1.2: Wernicke, (1985) simple-shear model for lithospheric stretching (taken from Allan & Allan, 2005). The model requires a through-going lithospheric shear zone, and is derived from observations made in the Basin & Range Province (W. USA). Deformation style is different within the hangingwall and foot wall of the shear zone, with low-angle faults/detachment systems with highly faulted upper crust present in the footwall (lower-plate) of the shear zone, relatively little upper crustal faulting, but significant crustal thinning (via exhumation of lower crustal material in the footwall of the shear zone), without being expressed as upper crustal faulting.

Pure-shear models have been very useful for predicting the structural and sedimentary geometries of rift basins (White & McKenzie, 1988; Allen & Allen, 2005) having success in industry also by enabling many petroleum plays to be identified. This dissertation focuses on regions where the crust has been hyper-extended as at rifted continental margins (here defined as, $\beta \geq 4$, or where mantle serpentinisation has occurred), where the classical models do not work as well as they do for relatively low-strain continental rift basins. Within this thesis I consider a specific style of rifted margin, known as a Magma-Poor Rifted Margin, and investigate their structural evolution.

1.2 Magma-Poor Rifted Margins

A Magma-Poor Rifted Margin (MPRM) (Fig. 1.3) is characterised by very low volumes of syn-rift volcanism, stretching factors which tend towards infinity oceanward, extremely deep water parallel to the margin, partially serpentinised subcontinental lithospheric mantle

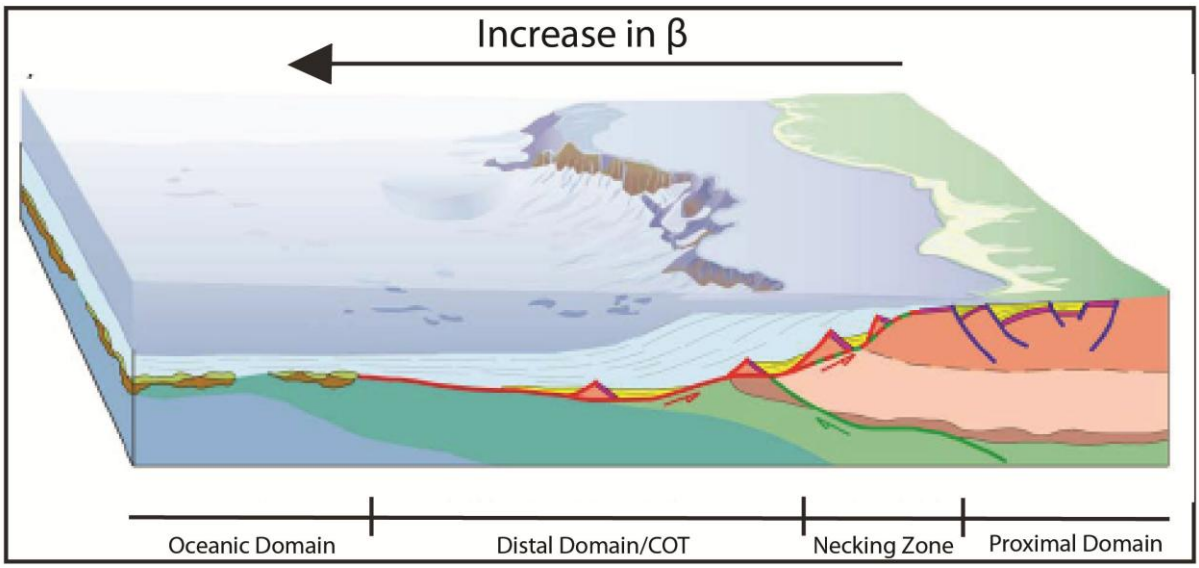

Fig. 1.3: Structural architecture of a typical Magma-Poor Rifted Margin. Note the extremely stretched crust in the necking zone, and hyper-extended crust in the COT overlying a zone of exhumed continental mantle. There is no continent-ocean boundary.

underlying hyper-extended crust in the continent-ocean transition (COT), and a Zone of Exhumed Continental Lithospheric Mantle (ZECM) (Whitmarsh et al., 2001; Péron-Pinvidic & Manatschal, 2009). The observation of a ZECM brought to the surface along low-angle detachment faults at MPRMs called the applicability of the McKenzie (1978) pure-shear stretching model into question (Péron-Pinvidic & Manatschal, 2009) as it had no means of accounting for mantle exhumation and the formation of a COT. MPRMs comprise about 30% of all passive margins: about 50% are magma-rich and 20% transform margins (Reston, 2009a). However, the processes occurring at magma-poor margins may also apply to the

early stages of rifting at many magma-rich margins and associated basins, such as the Rockall Trough, the Faroe-Shetland Basin and the Vøring and Møre Basins. Furthermore, several margins, such as parts of the South Atlantic margins, are covered by such thick sequences of sediment and salt that it is not always clear if they are magma-rich or magma-poor. As a result, an understanding of the processes occurring at magma-poor margins has more general implications for the process of continental breakup.

Fig. 1.4: Palinspastic restorations from the W. Iberian Margin COT, along serpentinite detachment systems. (a) Tagus Abyssal Plain, (b) W. Galicia Margin. Note that when the faults are restored the crust is ≤10km thick.

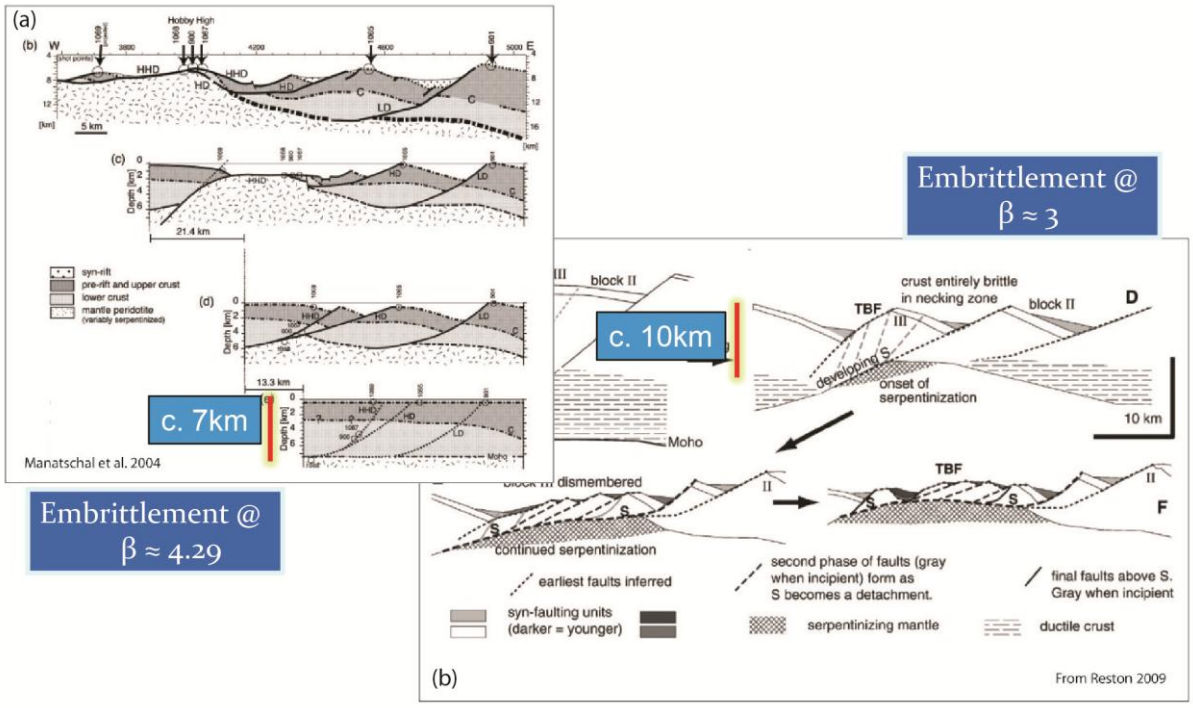

Significant crustal thinning, prior to serpentinite detachment initiation must have occurred.

The recognition of detachment faults at MPRMs (Krawczyk et al., 1996; Pickup et al., 1996; Reston et al., 1996) may suggest that a simple-shear model akin to Wernicke (1985) may be at play. Lister et al. (1986) elaborated on this idea, discussing the idea of a detachment fault penetrating the entire lithosphere and leading to continental breakup. One of the predictions of a through-going detachment fault is that conjugate margins would be

fundamentally asymmetric in both their overall geometries but also in terms of extensional style. Hence, Lister et al. (1986) defined "upper plate" (hangingwall) margins (margins that have been thinned by removal of lower crustal material along a detachment system, while leaving upper crustal lithologies with relatively low amounts of stretching when compared to the total crustal thinning) and "lower plate" (footwall) margins (margins with intense ductile deformation, and often accompanied by intense faulting, similar to metamorphic core complexes).

A fundamental weakness of the Wernicke or simple shear model is the requirement that a single shear zone or detachment pass from the surface through to the base of the lithosphere. Rheological modelling by, among others, Huismanns & Beaumont (2003) suggests that the likelihood of propagating a detachment through the entire thickness of the crust and lithosphere is quite low. Coupled with this, the detachment faults recognised at MPRMs are predominantly late-stage structures, only becoming active after the crust had already undergone significant thinning (to ≤ 10km) (Manatschal, 2004; Reston, 2007) and so are only responsible for a maximum c. 33% of the total crustal thinning (Fig. 1.4).

Moreover, it has been recognised that almost all rifted margins would appear to be "upper plate" margins (Driscoll & Karner, 1998) since on both conjugate margins the whole crust is thinned to a greater degree than the upper crust. However as this is at odds with the concept of asymmetric simple shear extension along a single detachment fault, it appears that the upper plate-lower plate concept is flawed. This apparent paradox leads to an infamous tectonic problem at MPRMs known as the "extension discrepancy".

1.3 The Extension Discrepancy

The extension discrepancy is simply that the amount of extension that can be attributed to the observed faults (β_f) is far less than that required to explain either the subsidence or the observed crustal thinning. It was originally noted not for rifted margins but for the North Sea. Ziegler (1983) noted an apparent discrepancy between the thermal subsidence phase relative to the syn-rift phase in the northern North Sea. Here, thicker sediments in the post-rift sequence of the Viking Graben are observed than might be expected given the extension accomodated by the seismically imaged faults, defining an extension discrepancy. Ziegler (1983) appealed to the effects of an earlier Triassic rifting event, generally considered to be of limited regional importance (White 1990), to supplement the main rifting episode in the Mid-Late Jurassic. Wood & Barton (1983) also noted an apparent inverse discrepancy where the crustal thinning (derived seismically) was in excess of that predicted by the subsidence analysis. Wood & Barton, (1983) appeal to an earlier stretching event that thinned the crust prior to the main rift event, although the thermal anomaly from the early rifting event would have decayed by the time of the main rifting in the basin. When the earlier rifting event is considered the crustal stretching (β_{wc}) compares well with the subsidence derived stretching (β_L), but stretching derived from faulting was consistently less than that observed from crustal scale seismic models and thermal subsidence analysis (Wood & Barton, 1983). Later work (White 1990) shows that errors incurred in the derivation of subsidence curves, in particular estimates of palaeowater depth, can lead to over estimating β_{WL} and deep seismic profiles over the Viking Graben have shown that β_{uc} (upper crustal stretching) and β_{wc} are within error of one another. The maximum post-rift thickness is also coincident with the maximum crustal thinning (White, 1990) which suggests that there has been no LC (lower

crust) flow or decoupling (Hopper and Buck, 1998). Any remaining discrepancy is explainable by sub-seismic scale faulting (Marrett & Almendinger, 1992, Walsh & Watterson, 1992). See **Section 1.3.1** for more details.

The extension discrepancy has also been noted for rifted margins, and has been the focus of much debate in recent times, particularly at MPRMs. The observation that all margins appear to be "upper plate" margins (Driscoll & Karner, 1998) led to the suggestion that crustal stretching at rifted margins is highly depth-dependent (see **Section 1.3.2**). Sibuet (1992) noted that stretching estimated from observable faults marginward of the S-reflector on the Galicia margin are in agreement with stretching estimates from whole crustal thinning, but as one moves oceanward, above the S-reflector, stretching from observable faults is grossly insufficient to account for the whole crustal thinning. Observations from a number of rifted margins (including the Goban Spur Margin and the W. Galicia Margin) made by Davis & Kusznir (2004) have shown that stretching derived from faults (β_f) is apparently far less than is observed for β_{wc} (as derived from wide-angle refraction seismic data, and gravity modelling) with the discrepancy increasing as one moves toward the continent-ocean transition (Fig. 1.5), agreeing with the observations of Sibuet (1992). The apparent discrepancy has been noted for both MPRMs as well as VRMs with β_f averaging about 1.3 (Davis & Kusznir, 2004).

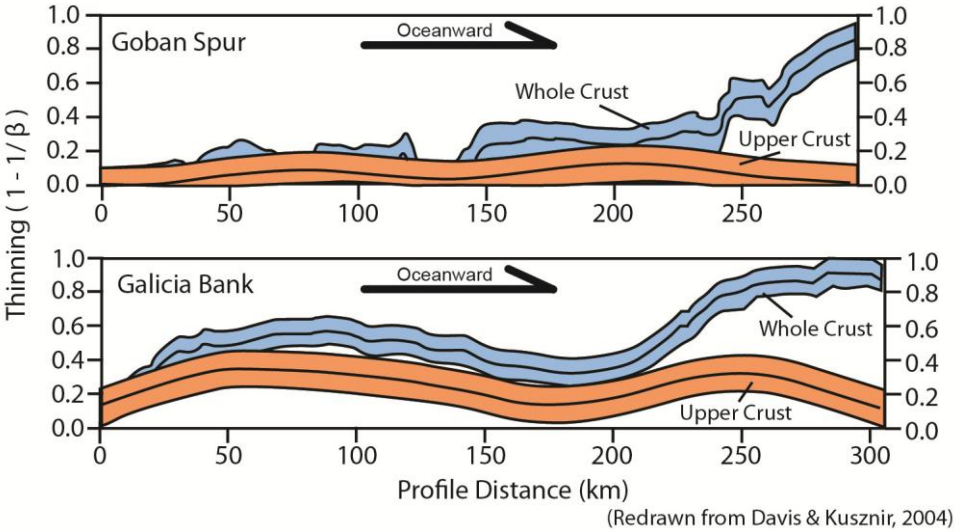

Fig. 1.5: Thinning profiles generated from analysis of stretching derived from faults (upper crust), and that derived for the whole crust from wide-angle seismic and gravity models, across the Goban Spur Margin, and Galica Margin. Not hoe upper crustal stretching (from seismically observable faults) remains low across the entire margin, but whole crustal thinning increases dramatically oceanward. This is the "extension discrepancy".

The observation that the crust and lithosphere are consistently stretched and thinned by a far greater amount than is suggested from the observable upper crustal faults, defines the extension discrepancy. It appears as though the classical extensional models (both pure and simple shear) cannot account for the stretching observations made from highly ($\beta \leq 3$) to hyper-extended crust. Below, I discuss some of the potential mechanisms that have been suggested to be capable of thinning the crust and lithosphere without requiring much extension from faults (or at least much observable extension), and attempt to reduce, remove or explain the extension discrepancy.

1.3.1 Partially Solved by Shear Direction or Small-Scale Faulting?

The method by which most studies have estimated fault related extension has basically been by summation of fault heaves only of the biggest faults, and internal deformation of fault blocks is not considered (Le Pichon & Sibuet, 1981; Davis & Kusznir, 2004). However, it has

been noted that hangingwall deformation is very rarely accommodated by vertical shear (White et al., 1986), and that disregarding, or not accounting for, inclined shear within the fault blocks can result in underestimating β_f by as much as a factor of two (Jackson & White, 1989). Therefore simple measurement of a faults heave may not give an accurate measurement of the extension accommodated by a given fault. Davis & Kusznir (2004) implicitly state that they considered any hangingwall deformation to be achieved via vertical shear, and so have potentially significantly underestimated the amount of extension that has actually occurred over the margin.

Further to this, studies of the amount of stretching that is accommodated by cumulative extension of fractally distributed, small-scale faults and "dead fault" populations - which have all contributed to overall extension in a rift system (Walsh et al., 1991) - have shown that up to 40% stretching can remain unaccounted for when estimations of stretching are made from seismically observable faults. Marrett & Allmendinger (1992) demonstrate that by using fractal scaling relationships that small-scale faults can account for 25 – 60% of "missing" extension. These studies suggest that when only the large, seismically observable faults are considered (as is common practice), β_f will be in some cases severely underestimated.

It appears as though the extension discrepancy at intra-continental rift basins can easily be accounted for by considering the effect of small-scale faults. However, Davis & Kusznir (2004) note that even when sub-seismic or small-scale faults are factored in, the extension discrepancy at hyper-extended MPRMs remains.

So, although the cumulative effect of small-scale faulting and the inclusion of inclined shear into fault derived stretching estimations for the upper crust can account for some of the "missing" extension, it is still not sufficient to remove it entirely. Therefore, in order to account for the extension discrepancy there must be additional processes at work.

1.3.2 Explained by Depth-Dependent Stretching/ Thinning?

In an effort to explain how observed upper crustal faults (on which all upper crustal stretching is taken to have occurred) are apparently incapable of accommodating the stretching/thinning observed for the whole crust as seen on wide-angle seismic profiles and gravity models, and to explain the observation that all margins are apparently "upper plate" margins (Driscoll & Karner, 1998), depth-dependent stretching/thinning (DDS/T) models of lithospheric and crustal stretching have been developed. In general the DDS/T requires that the thinning in the lower crust is decoupled from the upper crust (Driscoll & Karner, 1998; Davis & Kusznir, 2004; Healy & Kusznir, 2007; Kusznir & Karner, 2007). In these models the lower crust is removed via flow, either continentward or oceanward and driven by an upwelling divergent flow field akin to that thought to drive sea-floor spreading (Fig. 1.6), resulting in significant thinning of the lower crust relative to the upper crust (Davis & Kusznir, 2004; Kusznir & Karner, 2007). For the DDS/T models to work, the upper crust must be decoupled from the lower crust during rifting and the lower crust must be capable of flow. However, significant lower crustal flow is only possible if the temperature at the base of the crust is sufficient to lower the viscosity of the lower crust enough, approximately 700 - 800° C for an initially 30km thick crust (Pérez-Gussinyé et al., 2003). The temperature required for this to occur is most strongly controlled by the dominant mineralogy for the

lower crust and to a lesser extent the initial thickness of the crust (Hopper and Buck, 1998). If the lower crust was capable of flow at rifted margins, gravitationally driven lateral flow gradients might be expected to cause LC flow towards the rift axis (Buck, 1991). Instead, the divergent flow field associated with active asthenospheric upwelling is purported to drive lower crustal flow away from the rift axis, continentward (Kusznir & Karner, 2007).

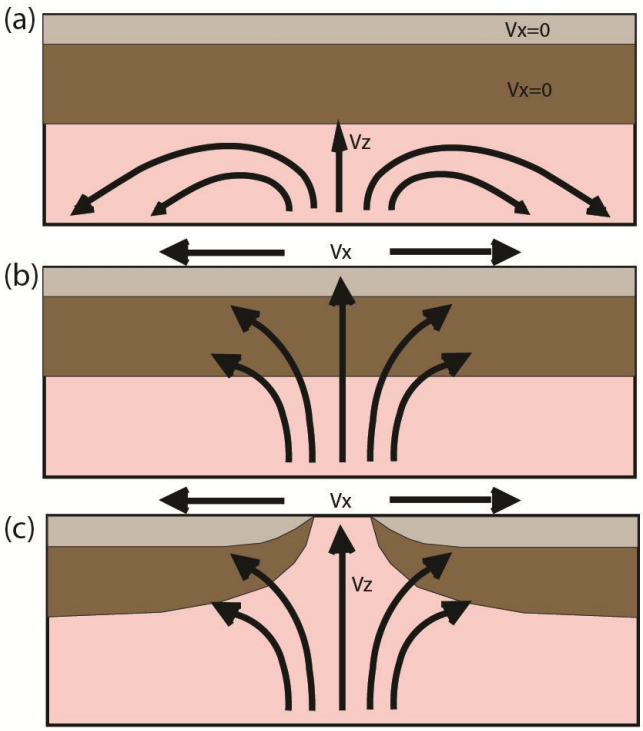

Fig. 1.6: The basic depth-dependent stretching/thinning mechanism - Upwelling divergent flow (redrawn from Davis & Kusznir, 2004). (a – c) Flow field impinges at the base of the lower crust initiating extension, via lower crustal flow, while only facilitating very minor upper crustal extension. Once crustal rupture is achieved the lower crust has been dramatically thinned oceanward, while the upper crust is relatively unthinned. The flow field may continue and initiate sea-floor spreading.

The models are attractive as upwelling divergent flow field within the lithosphere might not just explain the extension discrepancy through DDS/T, but might also explain other observations at rifted margins, such as mantle exhumation at the COT (Whitmarsh et al 2001, Pickup et al. 1996), the bathymetric profile, and post-rift subsidence (Kusznir & Karner, 2007). The divergent flow field would also provide a mechanism for the smooth and simple

transition from lithospheric stretching and thinning to sea-floor spreading (Kusznir & Karner, 2007). A problem with this is that in order to have both displacement of lower crust away from the rift axis (displaced landward) and development of a ZECM, where the subcontinental lithospheric mantle is displaced oceanward, two opposite displacement senses are required, and this is not predicted by the proposed mechanism for DDS/T. An upwelling divergent flow field should only be capable of displacing material landward, not oceanward.

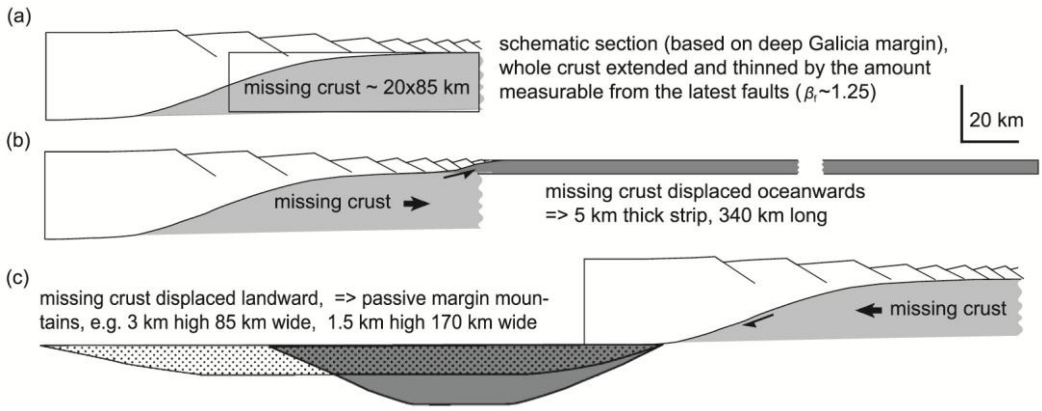

Fig. 1.7: Area balance considerations for the DDS mechanism (after Reston 2009b). (a) shows that in order for the amount of thinning observed at MPRMs, 1700kmsq of lower crustal material must be removed. (b) If the crust is displaced oceanward then a thin (5km) strip of lower crustal material would need to be spread out for over 340km. (c), if the lower crust were to be displaced landward, isostatic uplift would result in rifted margin mountains. These mountains would be 3km high if the displaced crust was put into a zone c. 85km wide, or 1.5km high, if displaced into a zone 170km wide. Neither of these end-members are observed at real MPRMs.

There are, however, some significant problems with this mechanism. First is the question of where the displaced lower crustal material has actually gone; simple area balance considerations (Reston, 2009b) highlight the problem (Fig.1.7). A second problem is the requirement that the lower crust be capable of flow. IODP drilling legs (103, 149, 173, 210) have sampled the lower crustal rocks and basement from the COT on the South Iberian Abyssal Plain, W. Iberian Margin (Manatschal et al., 2001; Péron-Pinvidic et al., 2007) and found that it is dominantly of mafic composition rather than acidic as is often assumed in

DDS/T calculations (Manatschal et al., 2001; Péron-Pinvidic and Manatschal, 2008). At sites 900 and 1068 from ODP legs 149 and 173, samples of meta-gabbro, amphibolite, and meta-anorthosite were sampled (Manatschal et al., 2001). The dominant mineralogies of these lithologies consist of feldspars, pyroxenes and amphiboles. These typically mafic compositions would require very high crust-mantle temperatures (c. 700 - 800°), which they are unlikely to attain in an initially 30km thick crust, to allow the lower crust to flow and cause diffuse decoupling (Hopper and Buck 1998). Similarly, elsewhere many exhumed lower crustal rocks are granulite facies anhydrous mafic lithologies (Quinlan et al., 1993; Van Den Berg et al., 2005), suggesting the lower crust is very often depleted in silica. Furthermore, the presence of both lower crustal rocks and also upper crustal rocks and early syn-rift sediments where the crust has thinned to just a few km indicates that the lower crust has not been significantly displaced away from the upper crust: both are present in adjacent fault blocks within the continent-ocean transition (Reston, 2009). This suggestion has also been made for the Goban Spur – Flemish Cap margins (Keen et al., 1989) where reflective lower crust (thought to represent lower crustal lithologies) can be identified within tilted fault blocks right up to the interpreted COB.

The lower crust is even more likely to resist flow at MPRMs, as lower crustal temperatures are probably relatively low during the formation of MPRMs due to cooling and suppression of melt generation which takes place as the crust thins (Reston 2007). The cooling is more pronounced on sediment starved margins and margin basins as the insulating effect of the

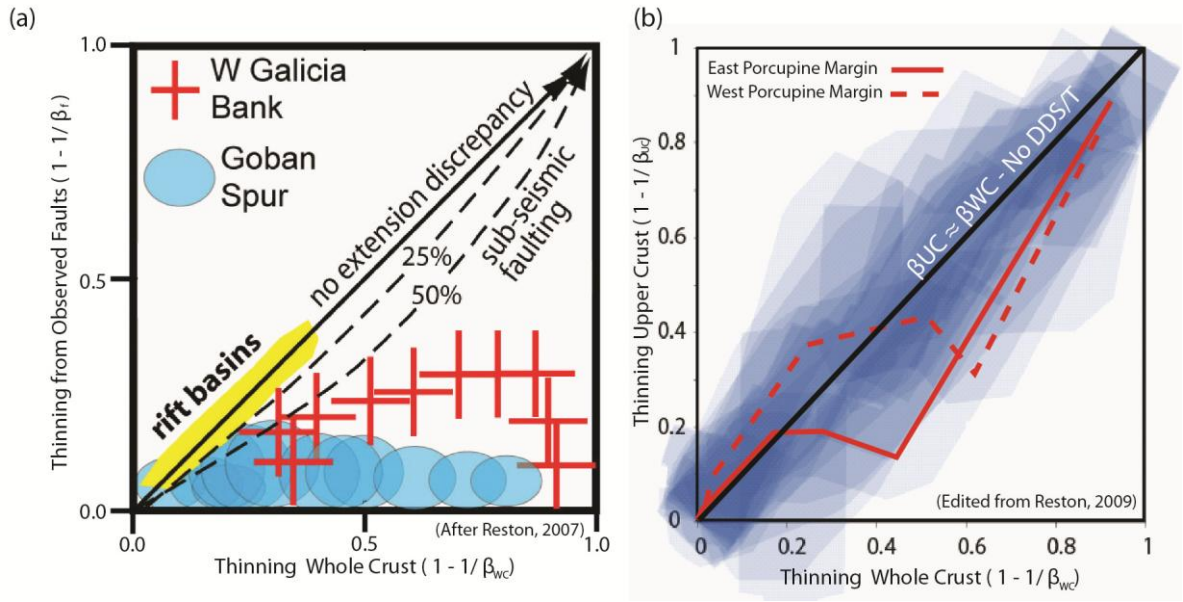

Fig. 1.8: (a) Taking the thinning calculated from faulting and for the whole crust from the Goban Spur and Galicia Margin (Fig. 1.2), and plotting thinning from observed faults against whole crustal thinning, it can be seen that the margins plot towards the bottom and right, well away from the diagonal (where they would plot if uniform stretching applied). Whole crustal thinning >> thinning from observed faulting – even when sub-seismic scale faulting is considered. (b) Plot of upper crustal thinning vs. whole crustal thinning. Generated from analysis of refraction seismic velocity models for the margins of the north and central Atlantic. Not that the relationship plots generally along the diagonal, suggesting that the upper and lower crust are thinning by the same amount. There is no evidence for DDS/T (see text for details).

sediment is not present (Hopper and Buck 1998). Pérez-Gussinyé & Reston (2001) have also demonstrated that, given the likely rheological structure of the crust prior to rifting (and the time scales involved) as rifting progresses creeping layers within the crust will become progressively thinner, resulting in coupling of crustal layers. Rheological coupling within the crust increases to the point where the entire crust will become fully embrittled, so that faults may cut through the crust and introduce sea-water to the mantle, beginning the process of mantle serpentinisation. Complete rheological coupling of the crust for LC with strength that might be approximated by a mixture of quartzitic and anorthitic minerals is predicted to occur at $3 \leq \beta \leq 5$.

Furthermore, through analysis of velocity models derived from refraction seismic profiles from the North and Central Atlantic MPRMs (including their conjugates and magma-poor margin basins) it can be demonstrated that upper crustal thinning is apparently proportional to whole crustal thinning (Fig. 1.8) (Reston, 2007 & 2009b). This observation suggests that sufficient thinning occurred in the upper crust to account for the observed crustal thinning at these margins, and so there is no requirement to thin the crust via depth-dependent mechanisms.

1.3.3 Solved by Unrecognised (Polyphase) Faulting?

It is clear that the seismically observable faults at many MPRMs are not capable of accommodating the observed crustal thinning (Fig. 1.5). Models of the evolution of crustal rheology over rift durations have shown that it is unlikely that DDS/T will occur in a lot of cases (**Section 1.3.2**), so another mechanism to hyper-extend the crust is necessary.

If the extension calculated from seismically observable faults is equal to the upper crustal thinning, then the lower crust must be stretched more than to the upper crust, the extension discrepancy becomes real and large scale DDS/T may be important in explaining the observed stretching. However, as demonstrated by Reston (2007 & 2009b), upper crustal thinning is proportional to that of the whole crust, and so if all upper crustal stretching is considered to be accommodated via brittle mechanisms (i.e. faulting) then there would be no extension discrepancy.

Therefore, by implication the observed faults, even when distributed deformation is considered (Davis & Kusznir, 2004), are not sufficient to account for the stretching in the upper crust. One fault generation is capable of accommodating $\beta \approx 1.7 – 2.0$ (Jackson &

White, 1989), so it is probable (if the bulk of upper crustal deformation occurs via faulting mechanisms) that there are multiple phases of faulting occurring when the crust reaches high β values (Fig. 1.8). Polyphase faulting models have been proposed, and shown to facilitate high-strain extension in a number of high-extensional regions: the western USA (Proffett, 1977), Eastern Betic Cordillera, SE Spain (Booth-Rea et al., 2002; Booth-Rea et al., 2004), and the W. Iberian Margin (Reston, 2005), (Fig. 1.9). However, if the complete set of faults is not recognised, then the amount of extension will be underestimated, providing an explanation of the extension discrepancy fully in keeping with the expected evolution of a hyper-extended MPRM.

When the seismic observations are coupled with the rheological evolution models (Pérez-Gussinyé & Reston, 2001), and the observation of lower crustal lithologies at the COT (Manatschal et al., 2001), the case against the application of large scale DDS/T mechanisms in the formation of MPRMs is strengthened as it is unlikely that the lower crust would be able to flow (as discussed in **Section 1.3.2**).

A number of major structural, and not necessarily mutually exclusive, models have been suggested to hyper-extend the continental crust. These involve polyphase faulting (cross-cutting fault generations) followed by extension along low-angle detachment faults (Reston 2005; Reston 2007; Reston 2009b), large offset detachment faults (Manatschal et al., 2001; Manatschal., 2004; Lavier & Manatschal, 2006; Manatschal et al., 2007; Péron-Pinvidic & Manatschal, 2009), and extension over multiple generations of sequentially active faults (Ranero & Pérez-Gussinyé, 2010).

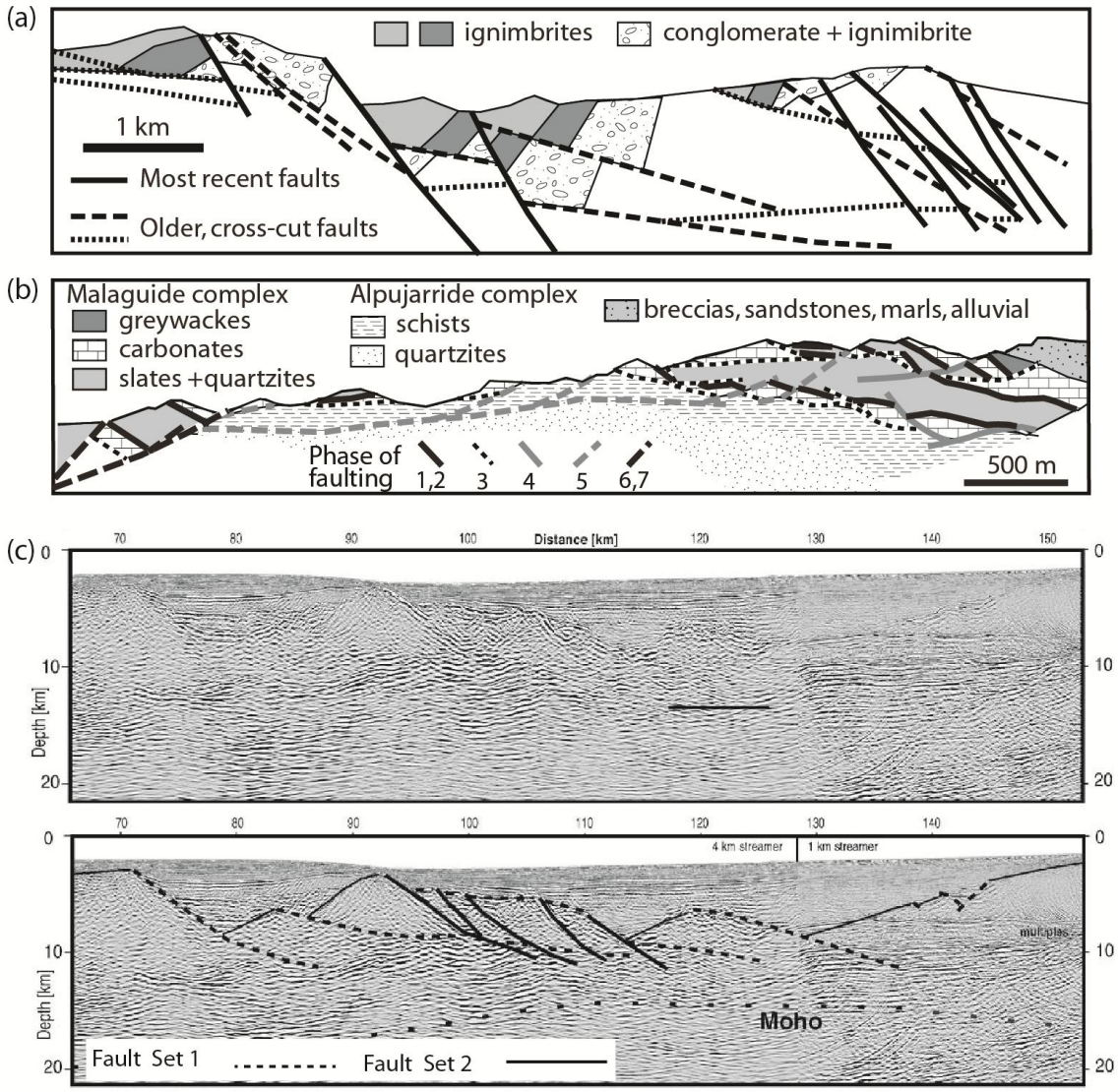

Fig. 1.9: Examples of high-strain polyphase faulting extensional systems. (a) Yerrington district, W. USA (Proffett, 1977 – redrawn by Reston, 2007) highlights cross-cutting relationships between latest faults and passively rotated earlier faults. (b) Cross-section through Sierra de la Tercia, SE Spain (Booth-Rea et al., 2004 – redrawn by Reston 2007), showing multiple generations of extensional detachment faults that have thinned a crustal section originally c.20km thick to only 1km. Seven phases of faulting are interpreted. (c) Uninterpreted and interpreted seismic section from the Galicia Interior Basin (Reston, 2005). Two successive generations of faults are interpreted accommodating $\beta \approx 3$.

While the polyphase faulting (PPF) model is capable of accommodating the strain observed in hyper-extended regions independently (something which I will attempt to demonstrate throughout the main body of this thesis), the mechanism can also be shown to play an

important role in some of the alternative structural mechanisms for hyper-extension that have been proposed (discussed more fully in **Chapter 5**).

In this thesis, I will investigate the polyphase faulting (PPF) mechanism, studying its mechanical feasibility, likely seismic expression, and demonstrating where the mechanism can actually be observed on seismic data (examples from the Porcupine Basin, and some examples from the North Sea and W. Iberian Margin). I will show that the PPF mechanism is capable of accommodating the degree of stretching that is observed at MPRMs and other hyper-extended regions, without the requirement of large scale depth-dependent mechanisms. I will also show (in **Chapter 5**) how the PPF mechanism compares with the other structural mechanisms (Manatschal-style, and the Ranero & Pérez-Gussinyé (2010) model) having presented the evidence supporting the PPF mechanism in the preceding chapters.

1.4 Thesis Structure

This thesis explores the possibility that the polyphase faulting (PPF) mechanism for extension might be capable of accounting for the apparent extension discrepancy observed at MPRMs. It explores the diagnostic structures likely to be produced by PPF and which of these structures are likely to be reproduced and identifiable on seismic data. The conceptual and mechanical models presented, together with published geological sections where PPF is considered to have extended the crust, are shown to be capable of extending the crust by the amounts that are observed at MPRMs. If the rheological conditions are favourable, these levels of extensional strain can be achieved by only three fault generations. Finally the

models developed are applied to, and shown to exist at the hyper-extended Porcupine Basin, west of Ireland.

The general layout of the thesis is as follows:

In **Chapter 2** regional pre-Stack Depth Migration (PSDM) reflection seismic data from the Porcupine Basin is analysed and stretching profiles across the basin are constructed. On the basis of these data, together with gravity and refraction seismic models, the basin is reclassified as a Magma-Poor Aulacogen (MPA). As the highly-extended crust has not been ruptured (although it does appear to have been on the cusp) it is an excellent place to study the structures that are present on both sides of a rift that eventually would lead to continental break-up.

Chapter 3 deals with the PPF mechanism in detail, highlighting different end-members and the associated structural geometries that are likely to be associated with the mechanism. The mechanics of the PPF mechanism are also considered in detail, and highlight the importance of evolving stress fields and rheological conditions during the rifting process. Onshore examples of where the PPF mechanism from the western USA are palinspastically restored in order to demonstrate how much extension the PPF mechanism is capable of accommodating. The onshore examples are then compared with the conceptual and mechanical models of PPF and are found to fit reasonably well with mechanical PPF model. Many of the structural features predicted by the conceptual PPF model can also be seen to varying degrees in the onshore sections.

Synthetic seismic models of some of the conceptual structural models (including a conceptual MPRM extended via the PPF mechanism), as well as the published geological cross-sections from **Chapter 3** are investigated in **Chapter 4**. The resulting synthetic seismograms demonstrate how the PPF mechanism is extremely unlikely to be recognised or interpreted correctly on seismic data, even when (simulated) perfect time migrations are generated, and when all structures generate seismic reflections. I show the PPF identifiers that are predicted from the models in **Chapter 3** and show how these are expressed on each of the synthetic seismograms.

In **Chapter 5** the synthetic seismograms are compared to the seismic data from the Porcupine Basin, and one section from the Goban Spur Margin (another example of an MPRM) in order to identify PPF structures in the newly classified Porcupine MPA. I show how there is evidence for the development of PPF structures in the basin and discuss the implications.

Finally, **Chapter 6** gives a brief overview and concludes the work**.**

CHAPTER 2

The Porcupine Basin: An Example of a Highly Strained, Magma-Poor Aulacogen

2.1 Introduction

The Porcupine Basin shares many similar characteristics to Magma-Poor Rifted Margins (MPRMs) such as the W. Iberian Margin. Here, I will demonstrate the presence of characteristics common to both MPRMs and the Porcupine Basin: margin parallel deep water zones, highly thinned continental crust dissected by extensional detachment faults, an undercrust of partially serpentinised subcontinental lithospheric mantle, and very low volumes of syn-rift magmatism (Whitmarsh et al. 2001). The resulting comparison warrants a reclassification of the basin as a High-Strain, Magma-Poor Aulacogen. As such, the Porcupine Basin provides a natural laboratory in which to study the evolution of MPRMs as the individual rift margins are not separated by thousands of kilometres of oceanic crust.

2.1.1 Basin Overview & Previous Work

The Porcupine Basin is a large, deep, V-shaped basin (opening towards the south), which trends N-S, west of Ireland (Fig. 2.1). The basin has been subdivided into two sub-basins, the Main Porcupine Basin (MPB), and the Porcupine Seabight Basin (PSB) (Tate, 1993; Naylor et al., 2002). The basin is known to have undergone multiple rifting episodes between the Late Carboniferous and the Late Jurassic (Tate & Dobson, 1992; Shannon et al., 1993; Tate, 1993), with the main rifting event considered to have occurred during the Mid-Late Jurassic to the earliest Cretaceous, lasting c. 35 - 40Ma (White et al., 1992; Tate, 1993). Based on the 2012 geological timescale (Gradstein et al., 2012) the rift duration is shortened to c. 27 – 32 Ma.

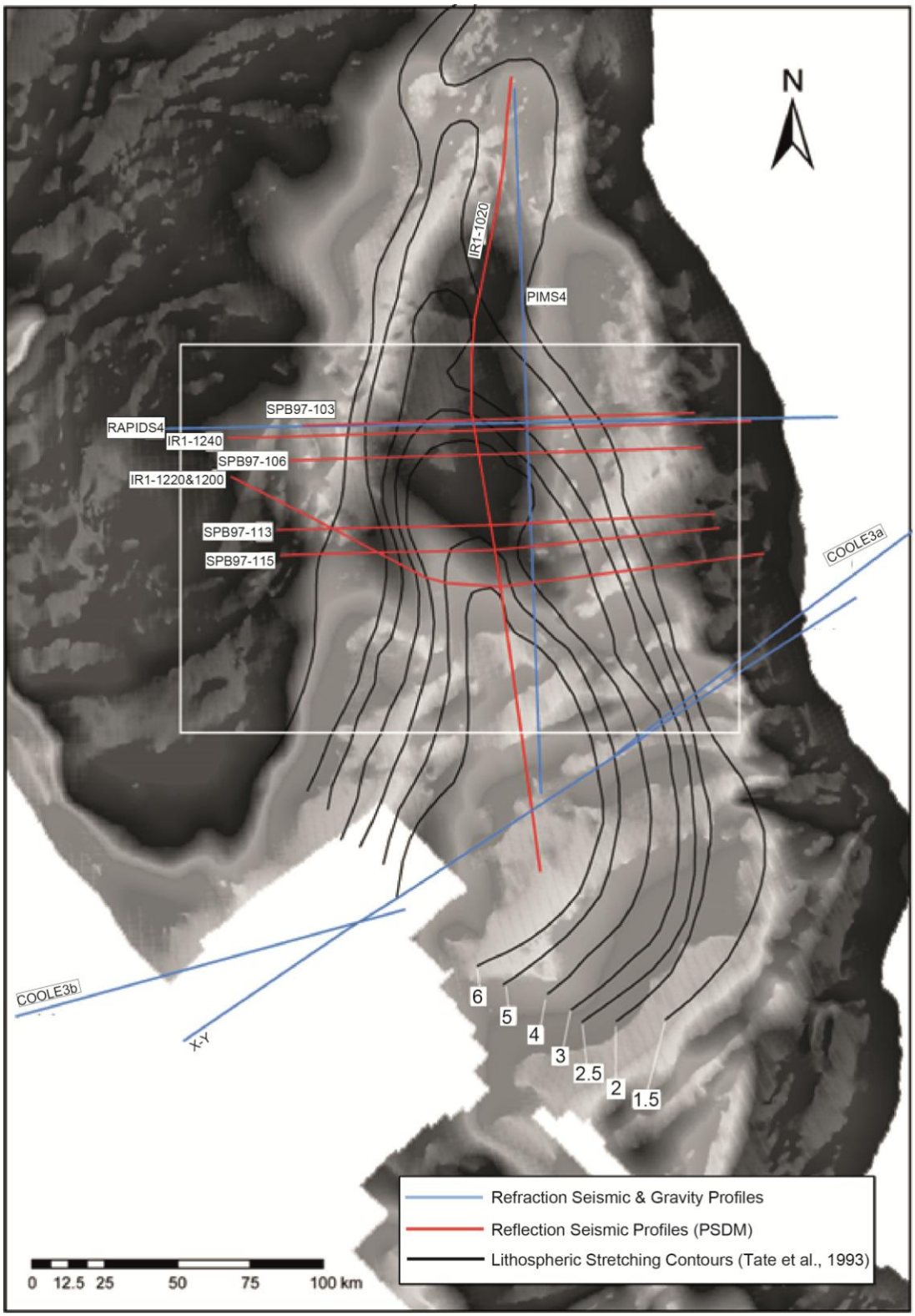

Fig. 2.1: Free-Air Gravity map of the Porcupine Basin. Positive gravity anomalies (dark gray) define the basin margins. Negative anomalies (light gray) define the basin. The intra-basin gravity high defines a feature called the Porcupine Arch. A subset of the refraction and potential field models are plotted along with the reflections seismic data described in this chapter. The reflection data are concentrated over the Porcupine Arch region. Lithospheric stretching contours (Tate et al.,1993) are also shown. White box indicates the location of Fig. 2.10.

Shannon et al. (1991) place the major phase of rifting between the base Bajocian and earliest Cretaceous, lasting c. 27Ma (based on the 2012 geological timescale Gradstein et al., 2012).

Very high levels of extensional strain have been accumulated by the basin as a result of these rifting episodes, in particular the Late Jurassic – earliest Cretaceous rifting phase. Crustal/lithospheric extension was considered to increase both southwards along, and across the axis of the basin, concomitant with aerial widening and deepening of the basin (White et al, 1992; Tate et al, 1993; Fig. 2.1).

Estimates for the magnitude of lithospheric stretching (β_L) calculated from subsidence data taken from wells in the northern part of the basin show that $\beta_L \geq 6$ toward the centre of the basin (Fig. 2.1), (White et al., 1992; Tate et al, 1993). Since the only wells available were in the north of the basin (Fig. 2.2) the contours that cover the entire basin were generated by extrapolating the subsidence data along seismic sections. Jones et al. (2001) re-evaluated some of the wells that were used for the original Tate et al. (1993) analysis, changing slightly some of the stretching estimates (see Fig. 2.2). All of the re-evaluated wells fit within the original contours presented by Tate et al. (1993) except for one (35/19-1, Fig. 2.2). On the whole the stretching estimates of Jones et al. (2001) should not change the original stretching contours very much. This is discussed (with a possible augmentation to the stretching contours presented by Tate et al., 1993) in **Section 2.4**. Assuming coaxial extension of the lithosphere, and an initial crustal thickness of 30km (Lowe & Jacob, 1989), the implication is that the crust at its most highly stretched point will be c. 5km thick (Based on the original Tate et al., 1993 contours). However, earlier work investigating the crustal

thickness beneath the Porcupine Basin using geophysical methods (wide-angle refraction seismic, potential field and magnetic surveys) have suggested that the continental crust thins from c. 30km on the Irish mainland to c. 10 km in the PSB (Makris et al, 1988; Conroy & Brock, 1989) (Fig. 2.1). This level of thinning yields a crustal stretching factor (β_C) of $\beta \approx 3$ for the PSB.

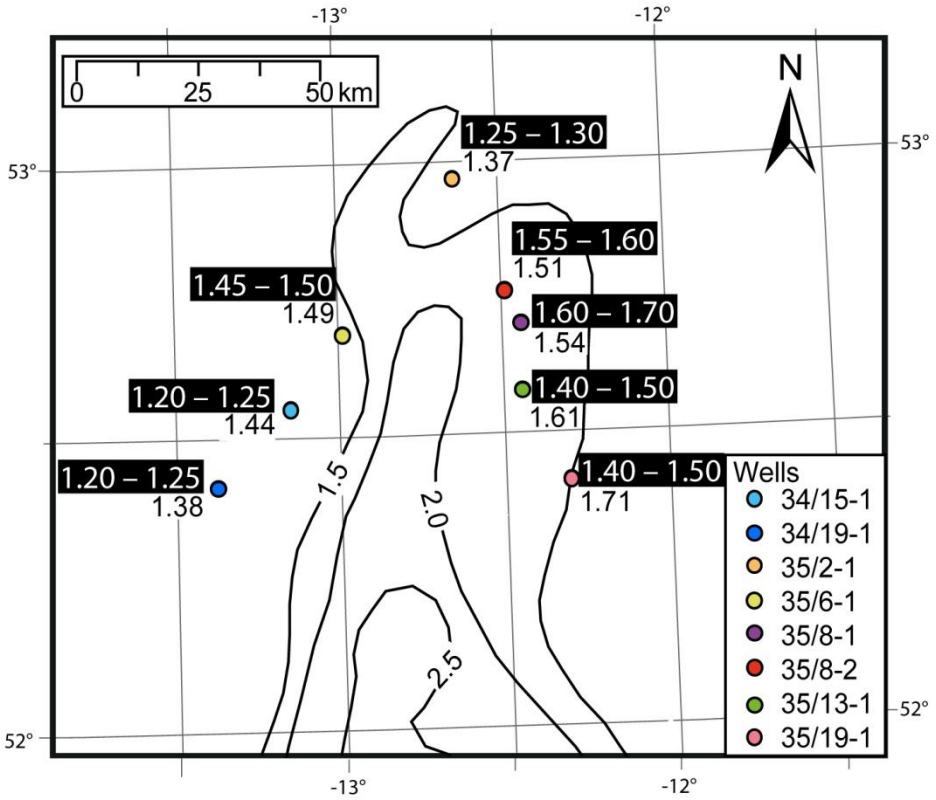

Fig. 2.2: Zoom in on northern portion of the Tate et al. (1993) stretching contours ($\beta = 1.5 – 2.5$) where they are constrained by well data. The re-evaluated stretching factors for each well (Jones et al., 2001) are also plotted. The Tate et al. (1993) estimates are shown as white on black text and the estimates of Jones et al. (2001) are shown as black on white text. Note that all the re-evaluated wells remain within the appropriate contour except for 35/19-1. This suggests that there would not be a major change in the overall stretching calculated from subsidence across the basin. An augmented $\beta = 2$ contour is shown in **Section 2.4**.

A series of very good quality wide-angle refraction experiments have been performed across the Irish Atlantic margin since the 1980's, the RAPIDS experiments (RAPIDS1 – 4), and have shown that the continental crust beneath both the Rockall and Porcupine Basins is extremely

thin (Makris et al., 1991; Hauser et al., 1995; O'Reilly et al., 1995; O'Reilly et al., 1996; Morewood et al., 2002; O'Reilly et al., 2006). The RAPIDS4 experiment is a transverse profile that runs east – west across the Main Porcupine Basin and crosses a feature known as the Porcupine Arch (Fig. 2.1). Results from this experiment show that the crust is locally 2 – 3 km thick (O'Reilly et al., 2006), corresponding to $\beta_C \approx 10 - 15$. Extreme stretching in the region of the Porcupine Arch was also noted on the most recent refraction experiment in the basin, PIMS4 (Hauser et al., 2010) that runs N – S along the axis of the basin (Fig. 2.1). The PIMS4 velocity profile suggests that the crust increases in thickness away from the Porcupine Arch towards the north (to c. 30km), and the south (to 8-10 km, $\beta_C \approx 3$ - 3.75). In the south the PIMS4 data is very similar to the thicknesses that were observed on the COOLE3a&b refraction lines (Makris et al., 1988). The refraction profiles from the Porcupine Basin discussed above are shown in Fig. 2.3a. From these data, Fig. 2.3b demonstrates that the crust in the Porcupine Basin appears to thin across the basin, but that it thickens northward and southward of the Porcupine Arch.

The estimates of extreme crustal thinning derived from the refraction experiments are in good agreement with recent gravity models of the region (Kimbell et al., 2010; Welford et al., 2010; Welford et al., 2012). However, a major point of note and potential problem is that the crustal thicknesses estimated from these experiments (and the reflection seismic interpretations presented in this chapter) do not agree with the estimate made by Tate et al. (1993), or the more recent estimates (made for individual wells) of Jones et al. (2001). This is discussed further in the following section.

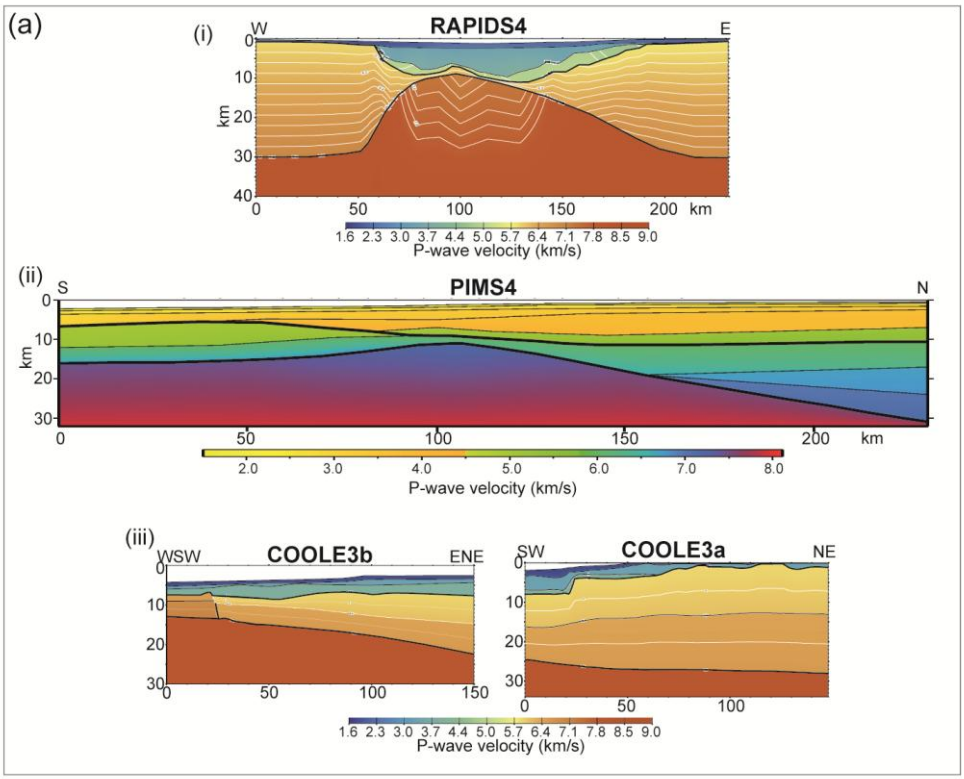

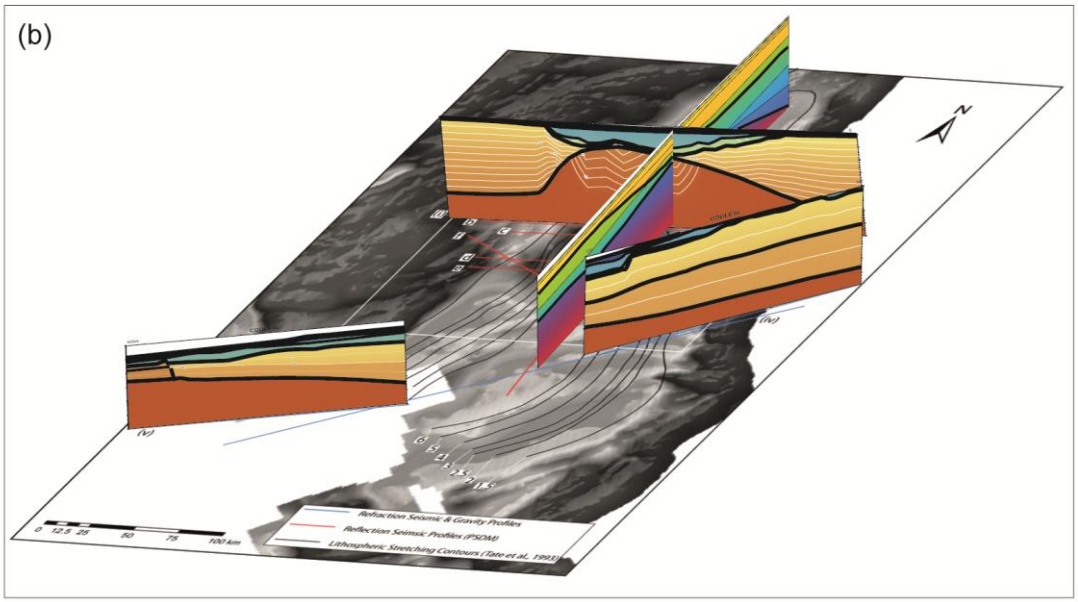

Fig. 2.3: (a) Refraction seismic lines from the Porcupine Basin. (i) RAPIDS4 (regridded from O'Reilly et al., 2006), (ii) PIMS4 (Hauser et al., 2010), (iii) COOLE3a&b (regridded from Makris et al., 1988). (b) Fence diagram showing of the Porcupine Basin refraction seismic dataset overlaid on Fig. 2.1. The velocity profiles demonstrate that (contrary to what the Tate et al. (1993) subsidence analysis suggests) the crust thins dramatically to c. 3 km at the Porcupine Arch and thickens northwards to c. 30km, and southwards to c. 8 – 10 km.

2.1.2 The Role of Magmatism & Mantle Serpentinisation

There appears to be disparity between estimates of crustal thinning obtained from the different techniques discussed in **Section 2.1.1** above. At the Porcupine Arch, where Tate et al. (1993) have suggested $\beta \leq 4$ from thermal subsidence analysis, the seismic refraction experiments (and reflection seismic describe in **Section 2.2**) suggest more extreme values, $\beta \leq 10 - 12$. In the PSB there is an inverse of the situation at the Porcupine Arch. There, estimates of stretching from subsidence analysis ($\beta \geq 6$) are higher than estimates from refraction seismic and potential field investigations ($\beta \approx 3$) (Makris et al, 1988; Conroy & Brock, 1989; Tate et al., 1993).

To account for this, Tate et al. (1993) invoke significant magmatic underplating beneath the basin (c. 4 – 10 km thick). However, the postulated melt thickness is based on calculations involving instantaneous rifting that are inappropriate to use where the basin has undergone finite rift durations (Bown & White, 1995). For rift duration of c. 27 - 32Ma, very little, if any syn-rift magmatism is expected to develop in the basin (Fig. 2.4(a(i)), and Reston et al., 2004). This assumes an asthenospheric temperature of 1300° C (relatively cool, but appropriate given the observation of partially serpentinised mantle beneath the basin – discussed further below).

It is possible that a relatively small amount of latest syn-rift magmatism could have been generated if the initial asthenospheric temperature were higher than c. 1300° C (initial temperature assumed in Fig. 2.4a(i)), or if the duration of rifting was at or slightly below the range shown in Fig. 2.4a(i). Furthermore, based for a rift duration of c. 27 - 32Ma, where asthenospheric temperatures are elevated to 1400° C, the maximum melt thickness that will

be generated for $\beta = 6$ is c. 3 km when finite duration rifting is considered (Fig. 2.4(iii)). This amount is far short of the 10 km thick melt that Tate et al. (1993) invoke for similar temperatures. However, the none of none of the seismic refraction data in the PSB (Fig. 2.3) appear to support the case for mafic underplating. Lower crustal seismic velocities are typical of continental crust at ≤ 6.6 km/s (Makris et al., 1988, Fig. 2.3). Seismic velocities of ≥ 7.1 km/s appear to be typical of mafic underplating along much of the eastern Atlantic margin (Barton & White, 1995; Barton & White, 1997; Vogt et al., 1998).

Three-dimensional gravity modelling conducted by Welford et al. (2010) suggests that densities similar to mid-lower crustal lithologies dominate the Porcupine Seabight Basin. This may potentially suggest a region of mantle serpentinisation and exhumation within the PSB. The PIMS4 profile (Hauser et al., 2010) does not intersect with the COOLE3 profiles (Makris et al., 1988) meaning that in the PSB the data is not capable of distinguishing between serpentinised mantle and mid/lower crustal lithologies due to technological limitations at the time it was shot (Boillot et al., 1989). Since serpentinised mantle is geophysically and isostatically similar to crustal material (Reston et al., 2004) an overestimation of crustal thickness and underestimation of β_C could have occurred in the PSB region . The stretching in the PSB is discussed more fully below and in **Section 2.4**).

The RAPIDS3&4 and PIMS4 wide-angle experiments have identified the presence of partially serpentinised mantle peridotites beneath the highly thinned crust of both the Porcupine and Rockall Basins (Hauser et al., 1995; O'Reilly et al., 1996; O'Reilly et al., 2006; Hauser et al., 2010). The presence of the serpentinite has been identified due to the recognition of anomalously high V_P/V_S values and low P_n velocities for the Rockall and Porcupine Basins

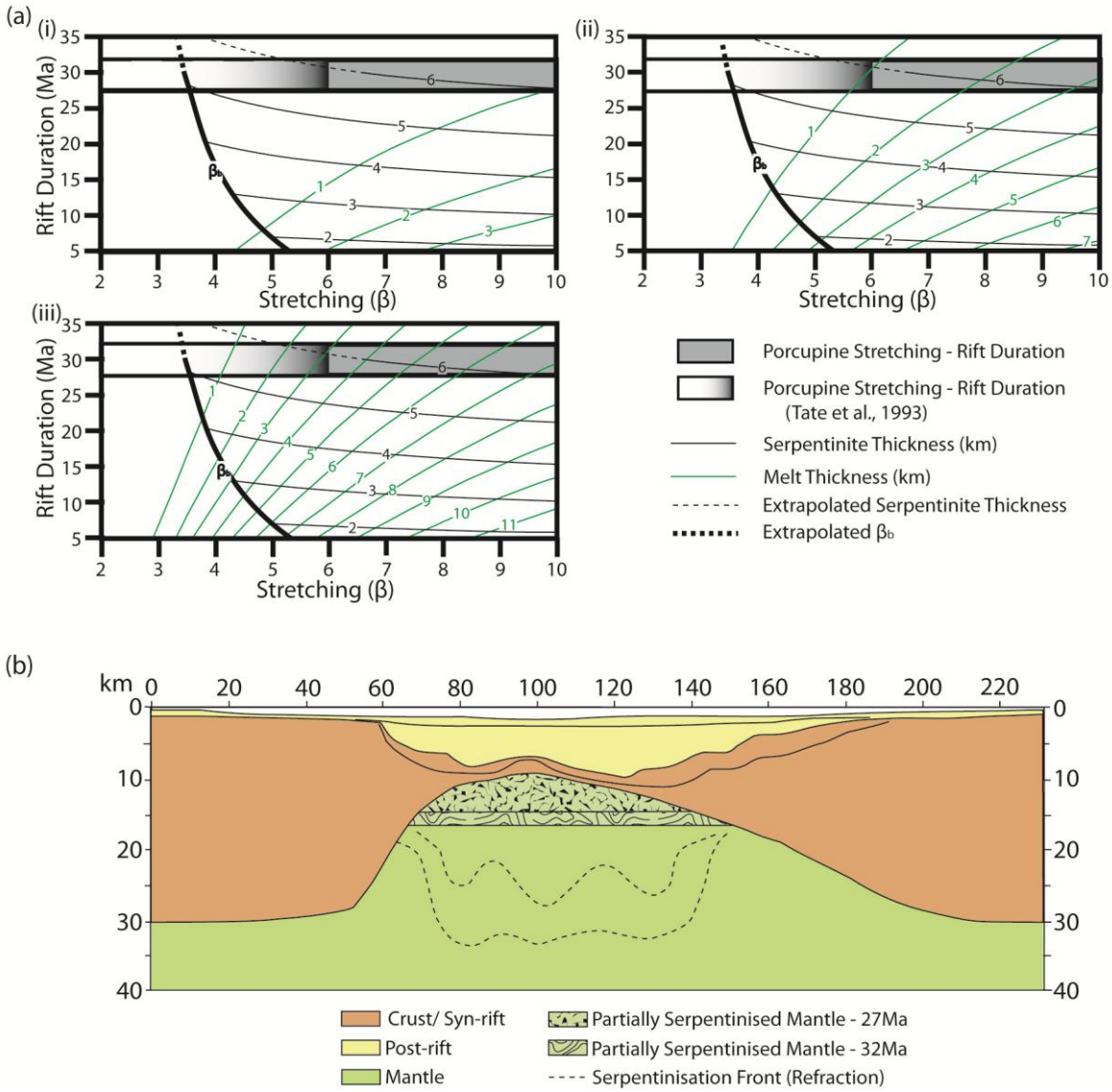

Fig. 2.4: (a) Melt thickness (based on Bown & White, 1995), serpentinite undercrust thickness and predicted crustal embrittlement based on Pérez-Gussinyé & Reston, (2001), with respect to rift duration and stretching factor. (i)Mantle T = 1300° C; very little melt is expected to be generated (requires shortest potential rifting duration and extremely high-strain). (ii) Mantle T = 1350° C; Low volumes of melt are expected for Tate et al., (1993)'s stretching estimates with greater volumes predicted for observed crustal thinning (see (b), and 2.3). (iii) Mantle T = 1400° C; Large volumes of melt are expected to be generated for a wide range of stretching factors and the whole range of potential rift durations. (i - iii) A serpentinite undercrust > 6km is expected for stretching estimated (for the upper region of the serpentinite stability field - 500° C. Rift duration taken from amended dates (Shannon et al., 1991; Tate et al., 1993 - see text for details). (b) Crustal cross section (O'Reilly et al., 2006) showing a minimum thickness of serpentinite which may have developed beneath the Porcupine Arch, based on (a) during pure-shear rifting. 5.5 – 6.0km is the minimum thickness likely to be present as the refraction data suggests the serpentinising zone may have been thicker (dashed lines). Thickness based on the Pérez-Gussinyé & Reston, (2001) models are less than that which is potentially observed on the RAPIDS4 profile (O'Reilly et al., 2006). It may be that a simple shear model may be more applicable.

respectively (O'Reilly et al, 1996; O'Reilly et al, 2006; Hauser et al., 2010). In the case of the Porcupine Basin, the identified region of mantle serpentinisation is spatially coincident with a major, positive free-air gravitational anomaly (Fig. 2.1; Reston et al., 2001; Readman et al., 2005) and does not appear to continue southwards into the PSB. Boillot et al. (1989), term a body of serpentinised mantle beneath highly-thinned crust, undercrusting in order to distinguish the process of mantle serpentinisation from the process of magmatic underplating. The observation of serpentinised mantle beneath the Porcupine Arch supports previous suggestions as to its presence from reflection seismic data, and gravity modelling over the Porcupine Arch (Reston et al., 2001; Reston et al., 2004, Readman et al., 2005).

Not surprisingly, the identification of serpentinite beneath the Porcupine Basin has significant implications for the basin's evolution, and its classification as a whole. Rift-related serpentinisation of continental mantle material is commonly observed where the continental crust has been hyper-extended, for example at magma-poor rifted margins (MPRMs) such as the adjacent Goban Spur margin (GSM) (Loudian & Chian, 1999; Bullock & Minshull, 2005), the W. Iberian Margin (WIM) and its conjugate the Newfoundland Margin (NFM) (Manatschal et al., 2001; Whitmarsh et al., 2001; Reston et al., 2005; Tucholke et al., 2007, Welford et al., 2010).

In fact, partial serpentinisation of subcontinental mantle and even exhumation of the serpentinised mantle is characteristic of the continent-ocean transition (COT) at magma-poor rifted margins (Loudian & Chian, 1999; Whitmarsh et al., 2001; Péron-Pinvidic et al., 2008). Given the duration of rifting and the crustal stretching factors observed from the RAPIDS4 and PIMS4 refraction profiles a serpentinite undercrust of up to a maximum of 10

km might be expected beneath the Porcupine Arch (based on theoretical models by Pérez-Gussinyé & Reston (2001), and is supported by results from the RAPIDS4 profile (O' Reilly et al., 2006; Fig. 2.4b).

The presence of serpentinite beneath the Porcupine Basin may explain some of the disparity between the geophysically derived and thermal subsidence-derived crustal thicknesses. The serpentinisation reaction leads to volume increase and density reduction (Coleman, 1971); thus, potential field data may overestimate crustal thickness and the depth at which the crust-mantle boundary (CMB) is estimated will reflect the position of the seismic Moho - "normal" density mantle peridotites - rather than the true CMB - the interface between serpentinised peridotites and crustal material.

Baxter et al. (2001) noted that the region of the Porcupine Arch is not isostatically equilibrated and invoke anomalously strong crust beneath the feature (compared with the South Porcupine Basin) to account for the subsidence deficit. However, O'Reilly et al. (1996) state that serpentinised mantle material can, as a result of density inversion, dynamically support and uplift basement material, and invoke mantle serpentinisation as the cause of a subsidence deficit observed from the Rockall Basin. Uplift of relatively low density serpentinised peridotites can offset post-rift subsidence and so calculations of lithospheric and crustal stretching will underestimate the actual amount of crustal stretching that has occurred. This situation is very likely the cause of the disparity between stretching estimates from the RAPIDS4 & PIMS4 refraction profiles, and the subsidence derived estimates at the Porcupine Arch.

It follows that crustal stretching values obtained using thermal subsidence data can only be considered a minimum value for the true extent of crustal stretching as mantle serpentinisation, or even other additions to the crust such as magmatic underplates can cause the crust to appear thicker on seismic images and gravity models (Reston et al., 2004). The degree of serpentinisation beneath the Porcupine Arch is far greater than observed beneath the Rockall Basin (O'Reilly et al., 2006), where a c. 4 – 5 km , or c. 7 – 13 km thick undercrust, depending on the initial temperature serpentinisation occurs (see Fig. 2.4(b)). Therefore, it is probable that the β_L values calculated by Tate et al. (1993) serve only as a minimum estimate for the true amount of extension which has taken place at the Porcupine Arch.

In the Porcupine Seabight region, all of the geophysical surveys are in agreement that the crust is 8 – 10 km thick. It should be noted, however, that these geophysical methods are non-unique and in some cases other factors can explain the evidence (see **Section 2.4)**. The discrepancy between the geophysically derived crustal thickness and that implied from subsidence estimates is discussed further in **Section 2.4**.

2.2 Seismic Analysis

In this chapter I present new data from ION-GXT's "IR1" long offset, deep penetration, 2D reflection seismic survey, which they acquired in 2007 as part of their NE AtlanticSPANS^{TM} project (Fig. 2.1), as well as some lines from Geoteam's SPB97 survey. The data is pre-Stack Depth Migrated (PSDM), to a depth of 30km for the IR1 survey, and a depth of 18km for the SPB97-survey. Presented here are two lines from the IR1 survey, and three PSDM lines from the SPB97 survey. The lines presented are dip-sections (with a general east-west orientation)

crossing the Porcupine Arch, a conspicuous gravity high in the central part of the basin, running approximately north-south, and are quite closely spaced along its length (See Fig. 2.1 for locations). The data clearly show extreme extension and thinning both across and along the axis of the Porcupine Arch. The PSDM reflection seismic data lends itself well to analysis of crustal thinning, and results can be compared to other methods such as refraction seismic and gravity modelling.

Basin-scale line drawing interpretations were constructed for each seismic line and from these interpretations picks were made for the base of the post-rift sediment pile and also for the crust-mantle boundary (CMB). In some cases multiple picks were made due to slightly ambiguous CMB positions (gradational, rather than sharp boundaries being one example). For the purposes of this analysis, syn-rift sediment is included in estimates for overall crustal thickness. This is because the syn-rift sediment thickness would have affected the depth to the brittle-ductile transition, due to both insulating effects keeping the temperature higher and due to the added overburden increasing pressure (O'Reilly et al., 1996; Pérez-Gussinyé and Reston, 2001), and, therefore, would have exerted some control on the point at which the entire crust undergoes brittle deformation, which in turn predicates the point at which mantle serpentinisation initiates (O'Reilly et al., 1996; Pérez-Gussinyé & Reston, 2001) (see **Section 1.1.3.2**).

β_C, the crustal stretching factor was calculated for each line based on the relationship: $\beta_C = Z_0 / Z_1$ where, Z_0 is the undeformed crustal thickness, here taken as 30km (Lowe & Jacob, 1989). Z_1 is the observed/ measured crustal thickness, taken at 5km intervals along each seismic section (See **Appendix A**).

$\beta_C = Z_0 / Z_1$ where, Z_0 is the undeformed crustal thickness, here taken as 30km (Lowe & Jacob, 1989). Z_1 is the observed/ measured crustal thickness, taken at 5km intervals along each seismic section (See **Appendix A**).

Following the calculation of β_C it was possible to compute the thinning factor across the basin using the relationship:

Thinning = $1 – (1 / \beta)$.

The thinning factor is a neater way of illustrating the amount of extension which has occurred in the basin than using β-values alone. Using the stretching and thinning information, it is possible to generate contours for β_C and $1-(1/\beta)$ for the basin, based on the interpretations of the reflection seismic data (Fig. 3). These contours can then be compared with published estimates for crustal stretching.

2.2.1 Crustal Scale Descriptions of Seismic Data

For these crustal-scale interpretations the following criteria were adopted in interpreting the base of the post-rift sediment pile and the base of the crust.

The base of the post-rift sediment pile for each profile was chosen by identifying the deepest expression of reflectors onlapping structural or topographic features. In many but not all cases the base of the post-rift sequence is marked by relatively high amplitude reflections. Angular unconformities, formed between the syn-rift tilted fault blocks and the later post-rift, were also used to identify the base of the post-rift succession. In some cases it is extremely difficult to distinguish between true post-rift sediment packages and latest (or multiphase) syn-rift sediments, since the later syn-rift packages are not strongly tilted.

The crust-mantle boundary (CMB) is identified in a number of ways. Where the reflection profiles (Fig. 2.3) are coincident with or adjacent to refraction seismic profiles (e.g. RAPIDS4 (O'Reilly et al., (2006); PIMS4 (Hauser et al., (2010), or where gravity modelling has been conducted along the reflection seismic lines (e.g. SPB97-103 (Reston et al., 2001; Readman et al., 2005)), it is possible to infer where the seismic/petrologic Moho lies on the reflection seismic data. This additional information is especially useful beneath the margins of the basins where deep imaging becomes difficult and where the seismic record does not continue deep enough. The BIRPS deep crustal reflection seismic profiles (Reston, 1987) covering much of NW European Margin, image a striped seismic texture at the base of the lower crust. The base of the reflective lower crust, where imaged on the data presented here, is taken as the CMB. Unfortunately, the reflective lower crust is seldom observed on the data presented here, but does appear sporadically. Thirdly, in some cases the CMB/Moho is expressed on the data as a moderately to strongly reflecting feature, sometimes forming quite continuous, unbroken reflections, while at other times expressed as discontinuous but traceable reflections along the base of the crust. In the latter two cases it is important to refer to the refraction/gravity data, where available, as a guide as to where the best CMB/Moho pick is located.

Once the depth to base post-rift and the CMB have been elucidated, the crustal thickness (here taken as crystalline basement and syn-rift sediments combined). This is due to the insulating effect the overlying sediment has on where the brittle-ductile transition lies and so they must be included when estimates of crustal embrittlement are being calculated. The following are very brief descriptions of the seismic lines presented, including some notes on post-rift thickness and CMB/Moho geometry.

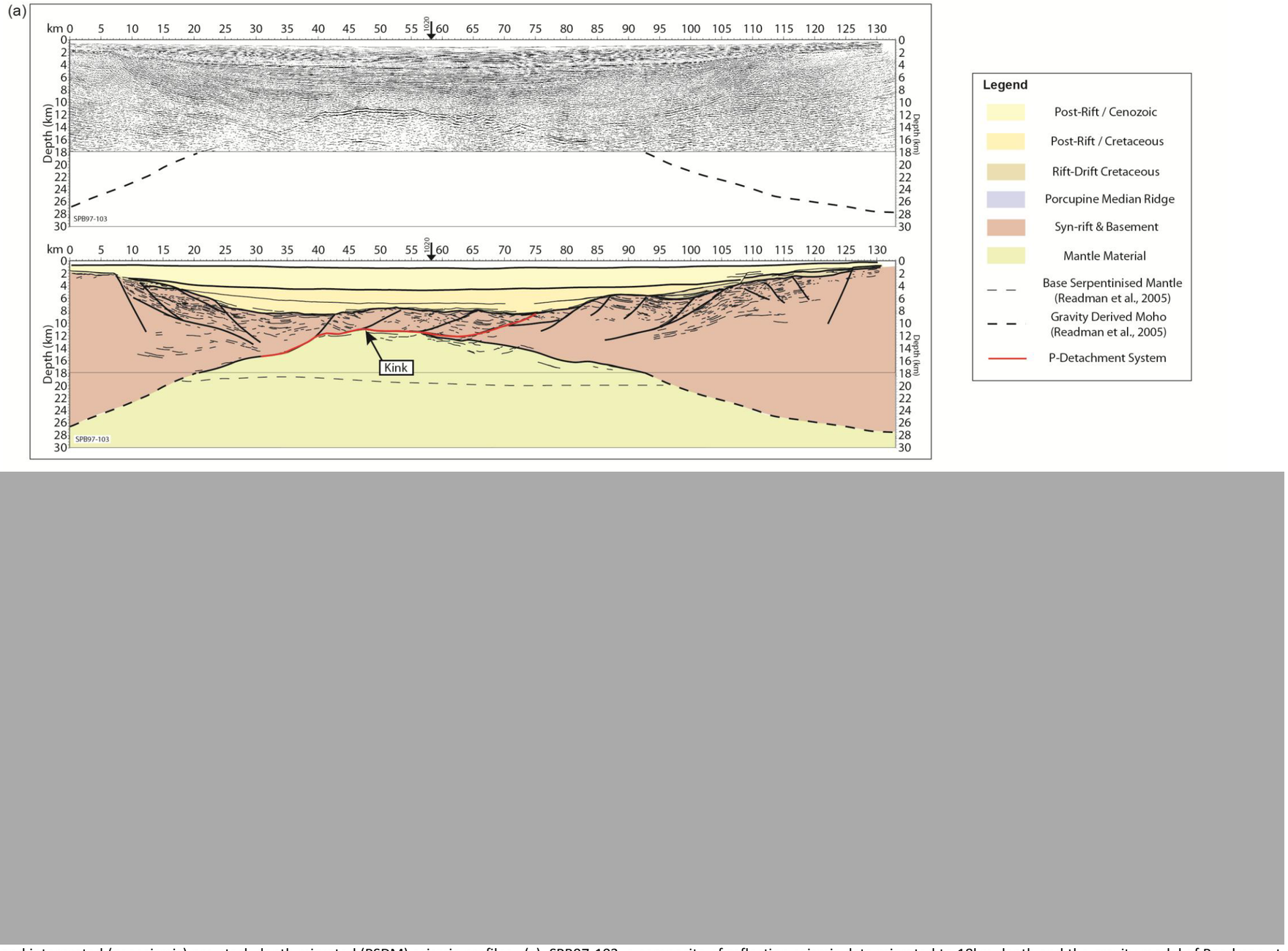

Fig. 2.5: Uninterpreted and interpreted (geoseismic) pre-stack depth migrated (PSDM) seismic profiles. (a) SPB97-103; a composite of reflection seismic data migrated to 18km depth and the gravity model of Readman et al., (2005). Line covers the entire crustal thickness. Faults soling onto the P-detachment are clearly observable. Western Margin is complicated by multiple fault generations. Well imaged fault blocks on the eastern margin. (b) IR1-10240. Migrated to a depth of 30km, images the entire crustal thickness. Western Margin is complicated by multiple fault generations, and faults soling onto the P-detachment can be seen in the central part of the basin. A potential exhumation fault is present at km 75. Well imaged fault blocks on the eastern margin

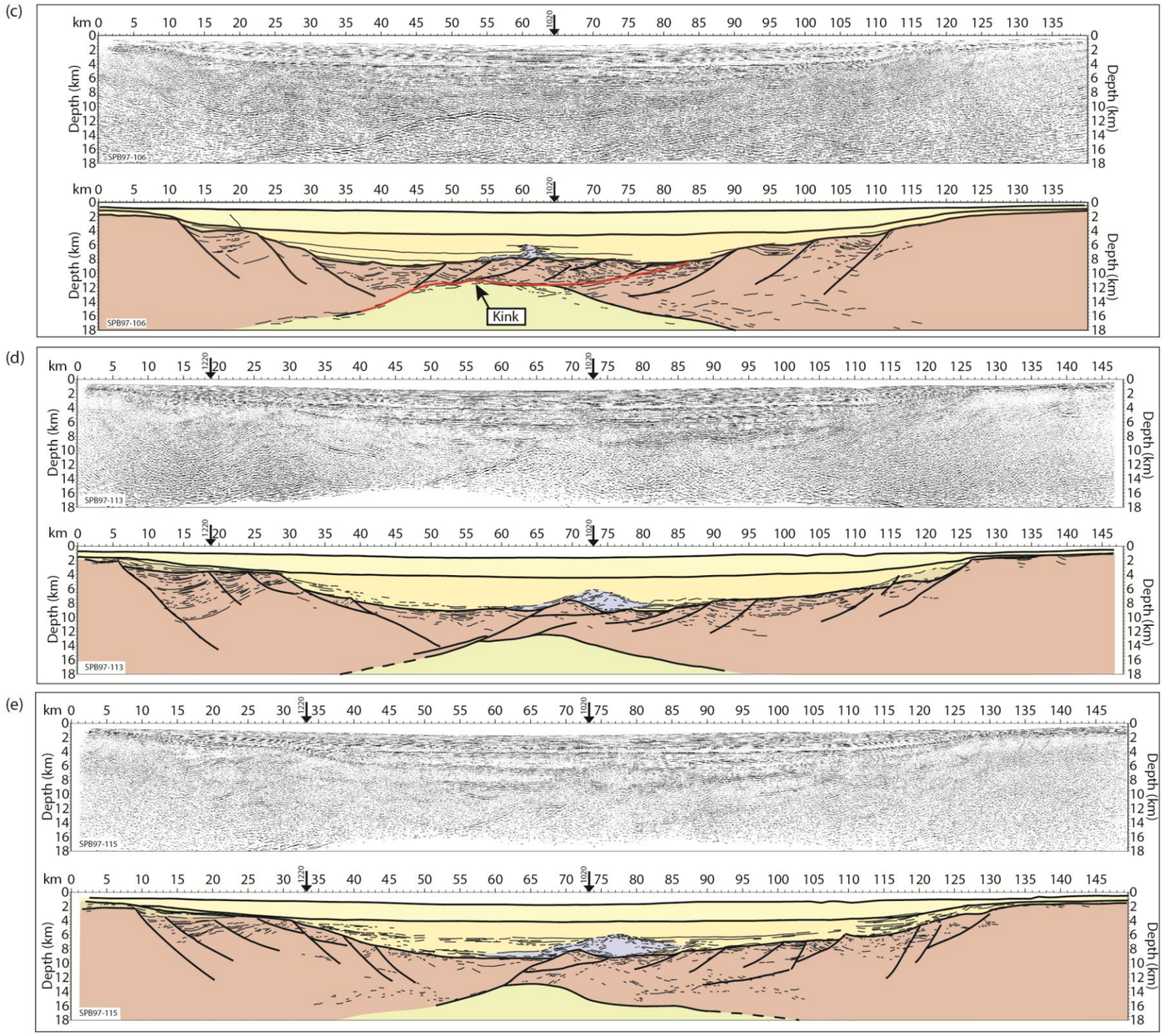

Fig. 2.5 (c): SPB97-106, depth migrated to 18km. Western fault blocks more clearly imaged (potential for multiple fault generations). Northernmost expression of the Porcupine Median Ridge, atop the P-detachment system. Well imaged fault blocks on the eastern margin. (d) SPB97-113; data is migrated to a depth of 18km. Western Margin is complicated by multiple fault generations. P-Detachment not present, but possible precursor (through-going crustal fault) is. PMR appears as a mounded structure within the eastern sub-basin. Eastern Margin fault blocks are not well developed. (e) SPB97-115; data is migrated o a depth of 18km. Good example of multiple fault generations on the western margin. No P-detachment system, but possible precursor (through-going crustal fault) is present. Fault blocks are not particularly well imaged on the eastern margin.

Fig. 2.5 (f): - IR1-1220 & 1200; composite of two dip sections, migrated to a depth of 30 km. Images entire crustal thickness. The PMR appears as a well-developed mounded structure in the centre of the basin. Multiple fault generations are developed on the western margin. The CMB is offset by a possible precursor to the P-detachment system west of the PMR. Fault blocks are not well imaged on the eastern margin. (g) IR1-1020; segment of axial seismic profile, migrated to a depth of 30km. The profile demonstrates thinning of the crust southwards toward the Porcupine Arch, and thickening southwards away from the Porcupine Arch. The PMR appears as a very large elongate mounded structure. The P-detachment appears to be scooped_shaped.

2.2.1.1 Line SPB97 – 103 (PSDM)

Line 103, presented in Fig. 2.5a, is the northern-most PSDM dip section. Fig. 2.1 shows that 103 is located adjacent to the RAPIDS4 profile. Independent gravity models (Reston et al., 2001; Readman et al., 2005) have been conducted along the profile. As a result there is good control on where the CMB is interpreted on the reflection data.

From the data it appears that the Porcupine Arch, manifested here as a structural high, separates the basin into two sub-basins, one west and one east. The western sub-basin contains a post-rift sediment thickness of c. 7.0 km, while the eastern sub-basin also contains a post-rift sediment thickness of c. 7.0 km. Over the central high, the post-rift thickness reduces to c. 5.5 km. This is counter to the unusual situation where it might be expected that the thickest post-rift succession would be at the centre of the basin.

The data also shows the Moho (in this case, more correctly referred to as the CMB) where it is shallower than 18 km, and is manifested as a very bright, quite continuous reflection package rising from the east and west margins towards the centre of basin. The CMB has been termed the P-reflector west of km 56.5, by Reston et al. (2001) and by Reston & McDermott (2011). They interpret this reflector package as a detachment fault system (discussed in greater detail in **Section 3.1**), similar to the S-detachment from the W. Galicia Margin (Reston et al., 2007). The adjacent refraction seismic profiles (RAPIDS4 & PIMS4), as well as gravity models (Reston et al., 2001; Readman et al., 2005), suggest that a body of partially serpentinised mantle exists beneath the Porcupine Arch, and as such the P-detachment system represents a structural Moho. Below 18 km depth the CMB is taken from Readman et al.'s (2005) coincident gravity model. The CMB rises at c. 22° at km 0 –

20.5, and becomes more steeply dipping (c. 30°) marginward, between km 33.5 – 39.5, forming the root zone of the convex-up P-detachment system, similar in geometry to the S-detachment (Manatschal et al., 2001; Reston et al., 2007; Reston & McDermott, 2011). Here the CMB is be recognised as a high-amplitude albeit discontinuous series of reflections. In the central part of the basin the structural Moho is a striking feature, appearing as high amplitude, continuous, and relatively level reflection at between km 39.5 – 56.5 and reaching a minimum depth of c. 11.2 km. The P detachment system becomes an intra-crustal detachment system – reflections are considerably weaker than where it forms the CMB, possibly due to fracture healing (Hölker et al., 2002) – at km 56.5 – 74.5, rising to a depth of c. 8.5km. The CMB dips beneath the eastern margin of the basin at a relatively shallow angle (c. 12°) at km 56.5 – 133. The eastern expression of the CMB is not as clear as in the central and western parts of the basin, appearing instead as highly discontinuous, high amplitude reflections. East of km 56.6 the CMB may represent the Moho proper, with some potential reflective lower crust imaged at km 95 – 107 at c. 15 km depth (Fig. 2.3a).

The geoseismic section (Fig. 2.5a) highlights the dramatic crustal thinning toward the basin centre. Locally the crust of the Porcupine Arch has been thinned to 2-3 km, agreeing well with estimates of crustal thickness from the nearby RAPIDS 4 (O' Reilly et al., 2006) and PIMS4 (Hauser et al., 2010) refraction seismic profiles.

2.2.1.2 Line IR1-1240

Line 1240 (Fig. 2.5b) is roughly coincident with the RAPIDS 4 wide-angle profile, and 6 – 7 km south of SPB97-103 (Fig. 2.1), and showcases the extreme crustal attenuation over the structural Porcupine Arch.

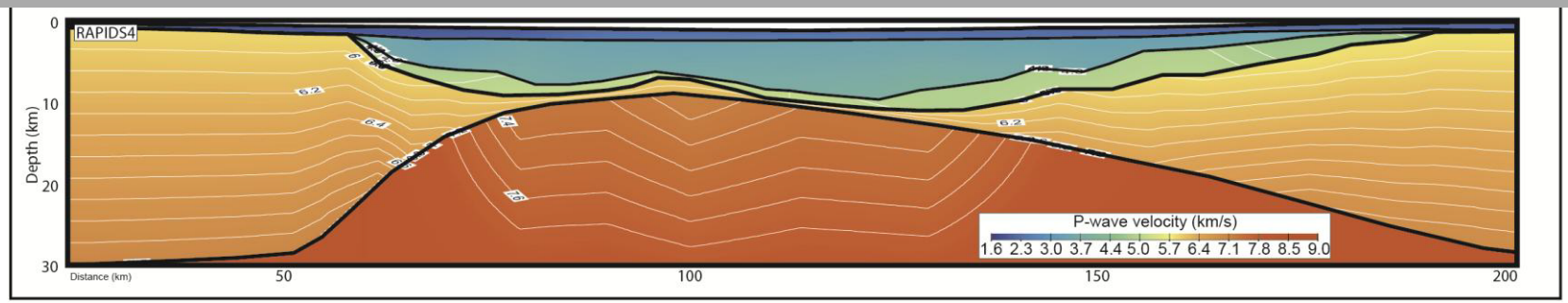

Fig. 2.6: The coincident seismic reflections and refraction profiles (IR1-1240 and RAPIDS4 (regridded from O'Reilly et al., 2006) respectively) that cross the Porcupine Arch (see Fig. 2.1. Note the extreme crustal thinning at the centre of the basin evident on both profiles. Although the interpretation of the IR1-1240 is not exactly the same as that of RAPIDS4 the Moho is seen to rise to similar depth on both profiles. The RAPIDS4 profile also shows a region of low velocity mantle beneath the centre of the basin that has been interpreted as a serpentinite undercrust (O'Reilly et al., 2006). Note the width of the low-velocity mantle extends from km 45 – 120 on the RAPIDS4 profile (relative to IR1-1240).

The interpreted data (Fig. 2.5b) also show two sub-basins separated by the high of the Porcupine Arch. Maximum post-rift sediment thicknesses range from c. 7.1 km in the western sub-basin, c. 5.5 km above the Porcupine Arch, and c. 6.7km for the eastern sub-basin.

The CMB/Moho characteristics present on line 1240 are similar to those observed on line 103, with the key difference being that the entire thickness of the crust is imaged due to the migration of the data down to a depth of 30 km. The CMB/Moho rises from a depth of c. 30 km at km 15 to c. 10.8 km at km 66, beneath the western margin, dipping at c. 24° marginward. The CMB/Moho here is recognised mainly by a series of high amplitude reflections that are very discontinuous. In some cases it is possible to pick the CMB/Moho by identifying the base of the sporadically imaged reflective lower crust (e.g. km 27 – 42, from c. 26.5 – 19 km depth). The reflective lower crust does not appear to be present everywhere in the data, and is not present at all in the central part of the basin. The P-detachment/CMB dips westward at c. 27° at km 56 – 66. The detachment system levels out at km 66 – 77, beneath the Porcupine Arch at a depth of c. 11km, and becomes an intra-crustal detachment east of km 77. The detachment breakaway is present at the base-post-rift at km 101 (Fig. 2.3b). As with Line 103, the CMB beneath the Porcupine Arch is characterised by a very bright and continuous reflection that generally dips very gently to the west. East of km 77 the Moho proper descends gently, dipping on average at c. 10° to a depth of c. 27.7 km at km 178. The CMB beneath the eastern margin is more complex than its conjugate. Reflections reminiscent of mantle shear zones (Reston, 1990) are present and dip more steeply (c. 24°) to the east than the Moho reflections (e.g. km 115 – 125, and

possibly km 130 – 145). The Moho beneath the eastern margin appears to be more diffuse than its western counterpart. Here it is mainly recognised by picking the base of the reflective lower crust packages, as well as the occasional bright, high amplitude reflections. The overall crustal geometry is very similar to the results presented by O'Reilly et al. (2006) (see Fig. 2.6), and the basin can be seen to be asymmetric. This asymmetry may be caused by the P detachment system.

The P-detachment appears to be offset by c. 1 km at km 70 – 74. This offset is caused by a possible exhumation fault (Fig. 2.5b), similar to mantle unroofing detachments described by Reston & McDermott (2011), that would likely have caused total crustal rupture and mantle exhumation had extension continued. The exhumation fault effectively separates the crust into two discrete, conjugate margins. It can be seen that both margins have differing geometries, both in terms of CMB/Moho depth and the distribution of the post-rift sediments, and as a result, there is are distinct differences between the crustal geometries of each margin. From the crustal scale interpretations (Fig. 2.3b) it is apparent that the crust of the western margin markedly thins over a relatively short distance when compared to the eastern margin, which thins over a much greater distance and displays a gentler CMB. This asymmetry is likely caused by late stage attenuation accommodated by the P-detachment system.

2.2.1.3 Line SPB97-106(PSDM)

Line 106 is located approximately 8 km further south along the Porcupine Arch than IR1-1240 (Fig. 2.1). The data are migrated to a depth of 18 km, and demonstrate the nature of crustal thinning across the Porcupine Arch.

As with the previously described lines, line 106 shows a significant accumulation of post-rift sediments. These sediments have collected within two sub-basins separated by the structural high of the Porcupine Arch. Both the western and eastern sub-basins have accumulated c. 7.6 km of post-rift sediments, while the central high is covered by c. 6.8 km of post-rift sediments (Fig. 2.5c).

The data here image the most northerly expression of a topographic high, which is referred to in the literature as the Porcupine Median Volcanic Ridge (PMVR) (Tate, 1993; Tate et al., 1993; White et al., 1992; Shannon et al., 1999) but here is renamed the Porcupine Median Ridge (PMR). A multitude of interpretations which appear to explain many of the characteristics of the ridge have been put forward: volcanic edifice (Tate 1993; Tate et al., 1993; Shannon et al., 1999; and many others); a hyaloclastic mound (Calves et al., 2012); a serpentinite mud volcano (Reston et al., 2001; Reston et al., 2004); and a fault block (O' Sullivan et al., 2010). ExxonMobile are planning to drill the feature in the spring of 2013, where final proof is likely to be obtained for what the structure is. Most workers are in agreement that there may be a carbonate build-up on top of the structure (e.g. Reston et al., 2004; O'Sullivan et al., 2010; Calves et al., 2012). While I have not made an attempt to solve this controversy, the data appear to support an interpretation of the PMR as some sort of mounded feature that is on top of the syn-rift/basement (Fig. 2.5 c – f), that in some cases appears to be sitting atop clinoforms prograding from the east at the base of the post-rift (Fig. 2.5c – f). The PMR is interpreted as interfingering with the post-rift sediments, probably of Early Cretaceous age (Fig. 2.5c). The PMR is not investigated in great detail here and is

included as part of the post-rift succession as it is clearly sitting on top of the syn-rift/basement level, as can be seen on the axial seismic section (Fig. 2.5f).

As was the case with the previous lines, the CMB rises from where it is first imaged at c 18 km depth at km 18, to c. 16 km depth at km 37. The CMB here produces high-amplitude, relatively unbroken reflectors. A structural CMB is formed by the P-detachment system beneath Porcupine Arch, its root dipping west at c. 25° between km 37 and 47, rising from c. 16 – 11.6 km depth. The CMB over this distance is a very high amplitude and unbroken, continuous reflection. From km 47 – 64 the CMB flattens to form a slightly convex up geometry (due to offset on the P-detachment by a late exhumation fault (Reston & McDermott, 2011) beneath the Porcupine Arch, reaching a minimum depth of 10.6km at km 54.5 (Fig. 2.5c). East of km 64, the P-detachment becomes an intra-crustal feature and its breakaway is present at the base of the post-rift succession at km 83.5. The CMB dips gently eastwards at c. 15° but is complicated by possible mantle/ lower crustal shear zones which may have displaced an allochthonous block of lower crust toward the basin centre (km 60.5 – 65, 11.6 – 13 km depth (Fig. 2.5c). The CMB character over the interval km 60.5 – 91 is varied, the reflections are high amplitude but are generally discontinuous, with some potential reflective lower crust present on the data between km 73 – 97.5 (Fig. 2.5c) directly above the interpreted CMB.

2.2.1.4 Line SPB97-113 (PSDM)

Located approximately 25 km south of line 106 (Fig. 2.1), line 113 is migrated to a depth of 18 km and highlights a change in the basin-scale structure of the crust. The main difference between line 113 and the previously discussed lines is that the crust begins to thicken

southwards, as suggested by the PIMS 4 refraction profile (Hauser et al., 2010) and is seen on the axial reflection profile IR1-1020 (Fig. 2.5g). The PMR also is a more prominent feature and forms a large topographic high within the post-rift succession. A fault-bounded, structural high beneath the PMR separates the two post-rift sub-basins (Fig. 2.5d).

As with the previously described lines, line 113 displays significant accumulations of post-rift sediments within sub-basins. The western basin has accumulated up to 7.5 km of post-rift sediment, and the eastern sub-basin contains up to 7.5 km. Over the central structural high the post-rift section, including the PMR is c. 6 km thick.

The PMR is very well developed in this section of the basin and forms a prominent topographic high within the post-rift succession, and as with line 106 it is not included in the syn-rift/basement.

The CMB on line 113 appears to be relatively symmetrical beneath the basin. On the depth migration the CMB/Moho is not imaged on the western margin until km 49, where it appears at a depth of c. 15.5 km, although an extrapolated CMB pick is shown for the western margin in Fig. 2.5d. The CMB rises moderately over the interval km 49 – 56, at an angle of c. 20°, as a high amplitude generally continuous reflection. This reflector appears to be the root of a low-angle fault cutting down into the mantle (a possible precursor to the P-detachment system), suggesting that the crust is embrittled at this point. Between km 56 – 65 the CMB rises to c. 12.5 km, and appears to form the root of a low angle fault that propagates up into the basement above, again a possible precursor to the P-detachment system. Here, the CMB produces a bright but discontinuous reflection. East of km 65 the CMB levels out and

dips eastwards at c. 13° toward km 92.5, where the CMB descends below 18km depth. At this interval, the CMB is likely the true crustal base and is interpreted by picking the base of areas where stripy lower crust appears to be present, as well as picking sporadic high-amplitude reflections. The CMB beneath the eastern margin is not as well defined as on the western margin since it is probably not a structural boundary.

2.2.1.5 Line SPB97-115

Line 115 (Fig. 2.5e) is located approx. 8.5 km south of line 113 (Fig. 2.1) and is migrated to a depth of 18 km. The extension across the basin, as with line 113, is not accommodated by a detachment system. The PMR, again, is a prominent feature on the data and forms a large topographic high within the post-rift succession and is grouped with the post-rift sediments with regard to crustal thickness calculations. The PMR sits atop a fault-bounded block that forms a structural high, separating two sub-basins.

Line 115 displays significant accumulations of post-rift sediments within the western and eastern sub-basins. The western basin has accumulated up to 7.6 km, and the eastern sub-basin contains up to 7.3 km. Over the central structural high the post-rift section, including the PMR, is c. 6.2 km thick.

The CMB on line 115 appears to be relatively symmetrical beneath the basin. On the depth migration the CMB/Moho is not imaged on the western margin until km 51.5, where it appears at a depth of c. 16 km, although an extrapolated CMB pick is shown for the western margin in Fig. 3e. The CMB rises gently over the interval km 51.5 – 61.5, at an angle of c. 18°, as a discontinuous but high-amplitude reflector. Imaging beneath western post-rift sub-

basin is not as good as in previously described lines. A fault (or potentially two faults) cuts up through the crust at km 61.5 at c. 30° (a possible precursor to the P-detachment system), beneath the PMR, suggesting that the crust is fully embrittled at this point. At a depth of c. 13 km, the CMB levels out between km 61.5 and km 70, and may be a structural feature, similar to the central region of line 113. Where there are reflections within the crust that may be suggestive of fault structures cutting up towards the post-rift (Fig. 2.5e), dipping eastward at an average angle of c. 10 from km 70 – 103. and dips below the data coverage. The CMB on the eastern margin and beneath the PMR is not very well imaged but can be picked out by intermittent high-amplitude reflectors that generally dip towards the east. The CMB over this region is probably the true base of the crust and there are hints of reflective lower crust sporadically imaged. CMB observations from the intersection of line 115 with IR1-1020 (Fig. 2.5g) aid in identification of the CMB pick, but the CMB beneath the eastern margin is generally poorly defined since it is likely not a structural boundary, as the CMB beneath the western margin potentially is.

2.2.1.6 Line IR1-1200&1220

IR1-1200 & 1220 (Fig. 2.5f) is a composite of two seismic lines which intersect at the centre of the basin (Fig. 2.1) over the PMR approximately 12.5 km south of 115, but the 1220 segment intersects the western margin of line 113 and line 115. The line 1200 segment of the profile is orientated roughly east-west, whereas line 1220 segment is orientated in a more WNW-ESE direction. The data is migrated to a depth of 30 km, and images the entire thickness of the crust at the margins.

As on the previously described lines, in this part of the basin a considerable thickness of post-rift sediments has been accumulated. Again, there are two sub-basins separated by a central structural high. The post-rift sediment pile reaches a maximum thickness of c. 7km in the western sub-basin, c. 7km (including the PMR) in the eastern sub-basin, and c. 5.5km over the central structural high.

The CMB rises from c. 27 km depth beneath the western margin km 10, to c. 15km at km 63, at an angle of c. 7°, steepening to c. 17° at km 40. The CMB manifests as a series of high-amplitude, discontinuous reflections beneath the majority of the margin. There are also some examples of reflective lower crust that can be picked out in the uninterpreted data (Fig. 2.5f). At km 63 the CMB levels out at c. 15 km depth, where begins to dip slightly east and is offset by a westerly, moderately dipping fault propagating up towards the PMR at an angle of c. 27°, at km 74. As on lines 113 and 115, this fault is likely a precursor to the P-detachment system present on the three most northerly lines. The CMB is offset by c. 1 km and can be traced east at an average depth of between 14.5 and 17 km, dipping at ≤ 5°. At km 125 the CMB dips more steeply (c. 20°) beneath the eastern margin to a depth of c. 26km at km 151, and remains at this depth to the eastern edge of the profile. The CMB under the central part of the basin is recognised by comparison with the intersecting IR1-1020 profile (Fig. 2.5g) as well as intermittent high-amplitude reflectors. Beneath the eastern margin, between km 143 and 190, the CMB is recognised by well-developed reflective lower crust at km 143 – 190, and where the CMB climbs to c. 17km, basinward, reflective lower crust is variably imaged.

It can be seen in the geoseismic interpretation (Fig. 2.5f) that the crustal structure appears to be roughly symmetrical in this part of the basin, with a slightly more pronounced CMB topography beneath the eastern margin.

2.2.1.7 Line IR1-1020

Due to mis-ties in the data, line 1020 (Fig. 2.5g) is not included in the construction of stretching contours presented in **Section2.3**. One of the most notable examples of a seismic mis-tie is present at the intersection between IR1-1020 and IR1-1200&1220 in the region of the PMR (see Fig. 2.7). The seismic profile is however, very useful for matching and identifying the base post-rift and CMB reflections along the axis of the basin.

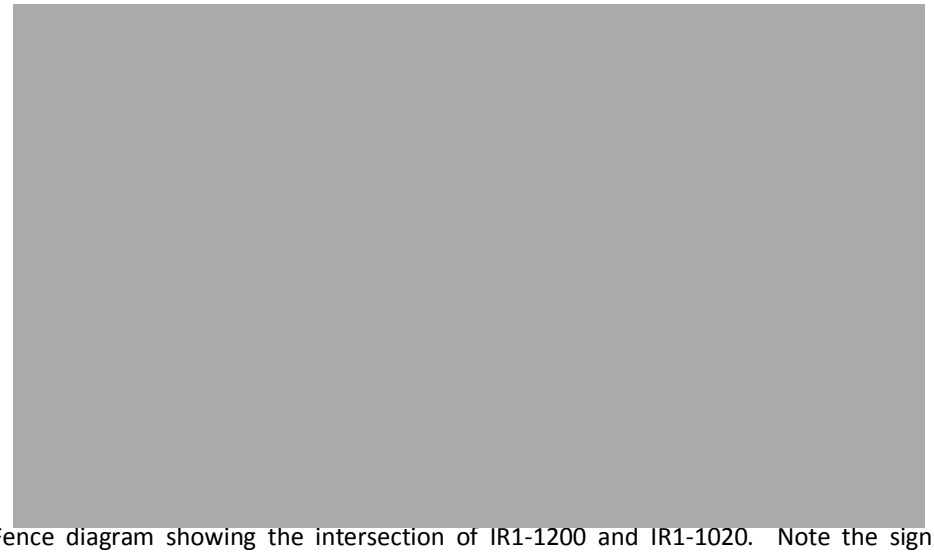

Fig. 2.7: Fence diagram showing the intersection of IR1-1200 and IR1-1020. Note the significant mis-tie between the lines. This is most noticeable for the top PMR reflections. The offset of reflections that should tie is c. 1200m. For this reason IR1-1020 is not used to generate the contours in Fig. 2.10a.

The data is migrated to a depth of 30 km and as such images the entire thickness of the crust and the top few kilometres of lithospheric mantle beneath the basin. The data and interpretation (Fig. 2.5g) mirror the results of the PIMS4 refraction experiment (Hauser et al., 2010) and show how the crust thins from the north towards the Porcupine Arch (from c. 10 km to 2 – 3 km on the data), and that the crust again thickens to a maximum of c. 9 km southwards beneath the PMR (which manifests as a very large, apparently mounded structure on the data). At the Porcupine Arch, the P-detachment system is interpreted from km 127 – 160 and is observed to have a concave up geometry, cutting down through the entire crustal thickness and forming a structural CMB between km 141 and 147. The CMB is identified on the data by comparison with the adjacent PIMS 4 refraction profile and the identification of sporadic high-amplitude reflections and occasional packages of reflective lower crust. Unfortunately, imaging of structure beneath the PMR is not ideal and it is difficult to observe continuous reflectivity.

2.3 Results

Based on interpretations of the seismic data presented in **Section 2.2**, crustal attenuation plots have been generated for each profile (Fig. 2.8). The attenuation plots highlight the extreme stretching and thinning that the crust has undergone in the region of the Porcupine Arch.

In general, β values approach or exceed 10 towards the centre of the basin (the Porcupine Arch region). The seismic dip-sections described in **Section 2.2** clearly demonstrate the degree of crustal attenuation across the axis of the basin. Plots of crustal attenuation have been drafted based on the seismic analysis (see **Appendix A**), and are presented in Fig. 2.8.

The geometry of the stretching curves for the dip sections clearly show the stretching and thinning gradient is greater for the western margin than the east over the Porcupine Arch region (Fig. 2.8i – iii) suggesting that crustal attenuation is asymmetrical in this part of the basin. This is not too surprising, considering that extension in this region is accommodated by the generally west dipping, "P" serpentinite detachment system. This structure has been interpreted by some authors as the top of the crystalline crust (e.g. Johnston et al., 2001). However, Reston et al. (2001), and Reston et al. (2004) have compared the reflector geometries associated with the P-reflection beneath the Porcupine Arch to those of the S-detachment system on the W. Iberian Margin and based on this comparison interpreted the P-reflector as serpentinite detachment system forming a structural CMB. The S-detachment has been shown to be detachment system from seismic observations (structural relationships (Reston et al., 2007), and waveform analysis (Leythaeuser et al., 2005)). A similar structure was drilled during leg 173 of the ODP further south on the South Iberia Abyssal Plain and found to represent a low-angle detachment system (Manatschal et al., 2004). Further support for the detachment interpretation for the P-detachment comes from the recent recognition of partially serpentinised mantle beneath the Porcupine Arch (O'Reilly et al., 2006; Hauser et al., 2010). This asymmetry across the Porcupine Arch between the eastern and western margins has been alluded to previously by several authors (Baxter et al., 2001; Reston et al, 2001; Reston et al, 2004; O'Reilly et al, 2006) but is clearly demonstrated here on the basin scale in these reflection data.

The presence of serpentinite beneath the Porcupine Arch (Reston et al., 2001; O'Reilly et al., 2006; Hauser et al., 2010) requires that the crust must have deformed via brittle

mechanisms in order for serpentinisation of mantle peridotite to initiate. Pérez-Gussinyé & Reston (2001) have calculated that for an aggregate crust (roughly 50:50 mix of anorthitic and quartzitic crust), crustal embrittlement should be achieved once crustal stretching reaches $3 \leq \beta \leq 5$. Petrophysical investigation of a suite of lower crustal xenoliths combined with refraction seismic investigations of the lower crust from SW Ireland have shown that the lower crust in the region is increasingly depleted in silica with depth and that the lower crust is c. 60% silica (O' Reilly et al., 2009).

The observed magnitude of crustal attenuation (Fig. 2.8 i – iii) at the Porcupine Arch is far in excess of $3 \leq \beta \leq 5$. As the crust has undergone this degree of stretching it can be assumed here that the crust deformed entirely via brittle mechanisms (Pérez-Gussinyé & Reston, 2001), and so allows for partial serpentinisation of the underlying mantle to initiate.

In Fig. 2.8 the zone where the crust has achieved $3 \leq \beta \leq 5$ is plotted, indicating where the crust may deforms entirely by brittle mechanisms (basinward of this zone) and where it does not (marginward of the zone). The geoseismic sections in Fig. 2.9 show where the crust is predicted to become embrittled and suggest the point at where it has become embrittled from observation of faults offsetting or soling onto the CMB. In general it seems that the crust does become embrittled over the predicted range for the Porcupine Arch region.

South of the Porcupine Arch, where the Porcupine Median Ridge is best developed, crustal attenuation appears to be roughly symmetrical (Figs 2.5d – f & 2.9d – f, and Fig. 2.8iv – vi). The axial section, IR1-1020 (Fig. 2.5g & 2.9g, Fig. 2.8(vii)) runs down the axis of the Porcupine Arch and recording high stretching and thinning factors.

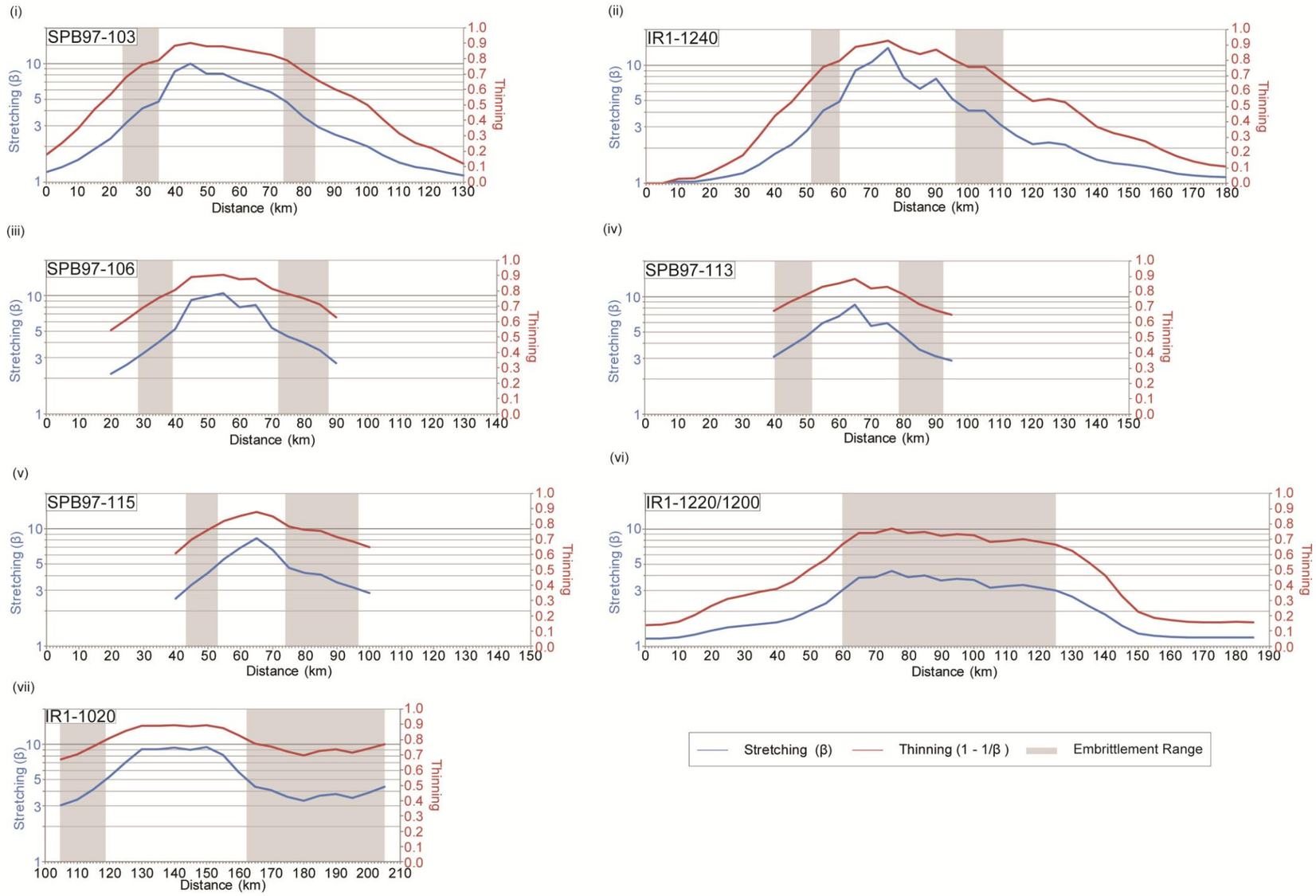

Fig. 2.8: Plots of crustal attenuation for each of the seismic profiles in Fig. 2.3. Crustal stretching (on the left axis) and crustal thinning (on the right axis) are plotted against distance along the seismic profiles. Area where the crust is predicted to become embrittled, $3 \leq \beta \geq 5$, is highlighted on each plot. Note asymmetry of attenuation profiles i – iii, and relative symmetry of profiles iv – vii. See Fig. 2.1 for locations of profiles.

It shows that although the magnitude of stretching and thinning is extremely high along the axis of the Porcupine Arch, the degree of crustal attenuation does not simply increase southwards, as is suggested by subsidence derived stretching estimates (Tate et al., 1993), but rather increases towards the Porcupine Arch and decreases away from it, as is suggested by the PIMS4 refraction profile (Hauser et al., 2010). The lower degree of crustal attenuation south of the Porcupine Arch may suggest that strain is partitioned within the basin, potentially across some structure (possibly the Clare lineament, discussed in **Section 2.4**).

In general, the entire crust undergoes brittle deformation at some point within the predicted range (generally towards the higher end of the scale) along each of the seismic profiles. A possible exception may exist for IR1-1020, where faults imaged beneath the PMR do not appear to cut down to the CMB and instead sole out some kms above it. There may be a terrane boundary somewhere along the profile which may have a different lower crustal make up than in the vicinity of the Porcupine Arch (discussed further in **Section 2.4**).

A more accurate method of determining at which point the crust becomes embrittled, or one that may be used collaboratively with direct observation of through going faulting, would be to use high resolution refraction seismic data to identify where the margins of the serpentinisation front lie. Comparing the RAPIDS4 wide-angle crustal model with the coincident SPB97-103 and IR1-1240 lines shows that the point at which the crust has become embrittled is actually more marginward than can be determined from the

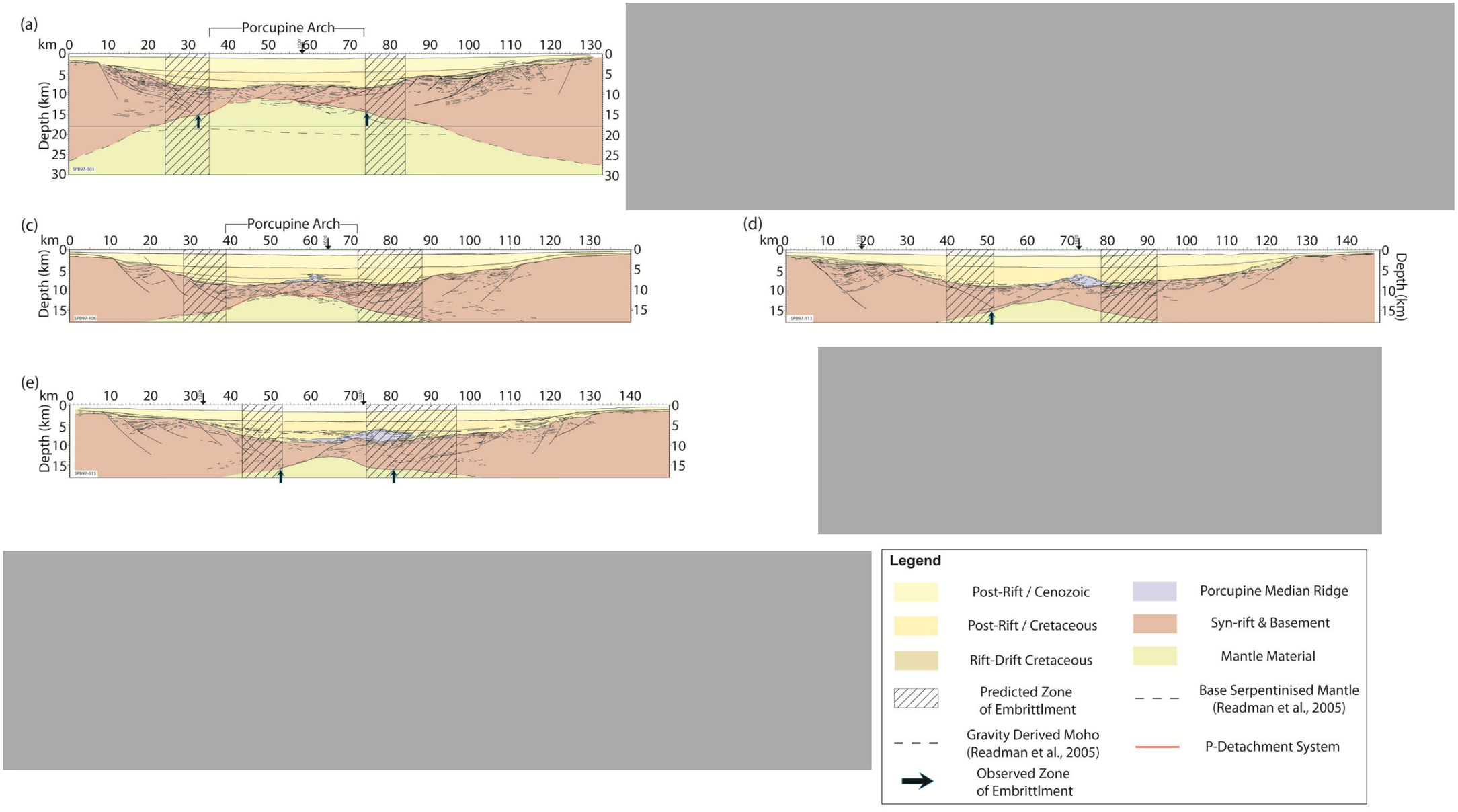

Fig. 2.9: Geoseismic sections based on uninterpreted data from Fig. 2.3. The distance over which total crustal embrittlement is predicted to occur based on the models of Pérez-Gussinyé & Reston, (2001) is shown on each section, as are the points where faults are seen to cut the CMB, sole onto it, or where groups of reflectors trend towards it. In some cases it is not clear where the crust becomes brittle from the seismic data alone. (a) Geoseismic interpretation of SPB97-103, (b) Geoseismic interpretation of IR1-1240, (c) Geoseismic interpretation of SPB97-106, (d) Geoseismic interpretation of SPB97-113, (e) Geoseismic interpretation of SPB97-115, (f) Geoseismic interpretation of IR1-1220 & 1200, (g) Geoseismic interpretation of IR1-1020. It can be seen for these sections that structures that intersect (and offset) the CMB only ever occur basinward of the predicted zone of crustal embrittlement.

reflection data alone (compare Figs 2.6 & 2 9b). From RAPIDS4 it appears that serpentinite occurs over the range km 45 – 120. The limit of the serpentinised mantle coincident with where the combined crustal plus syn-rift sediment thickness is c. 10 km thick (β ≈ 3) in the west, and c. 13 km thick (β ≈ 2.3) in the east. The refraction data (Fig. 2.6) suggest that embrittlement of the crust occurred earlier than what can be seen on the reflection seismic. The point at which the crust becomes embrittled may coincide with changes in deformation style in the crust (faults active at relatively high-angles give way to faults active at progressively lower angles). This can be seen on the reflection data in Fig. 2.6. The serpentinisation from being more marginward in the refraction data than on the reflection data (Fig.2 6 &Fig. 2.9b) makes sense in that the serpentinisation process must have initiated before the displacement on serpentinite detachments (cf. P-detachment) can occur.

Lubrication of fault zones with serpentine may allow low-angle faulting (see **Section 3.2.7**; Reston et al., 2007) to occur in the Porcupine Basin (Reston et al., 2001; Reston et al., 2001). For the Porcupine Arch region the initiation of low-angle faulting (P-detachment) appears to be the cause for the sharp increase in the stretching gradient seen in (Figs 2.8(i, ii, iii) & 2.10a).

The P-detachment is consistently within or slightly basinward of the range of embrittlement shown in Fig. 2.9, and structures are only seen to intersect or offset the CMB basinward of the embrittlement zone (see Figs 2.6 & 2.9). Contours of crustal stretching factors have been generated (Fig. 2.10a) by drawing lines of equal stretching between each of the seismic profiles presented in Figs. 2.5 & 2.9, and can be easily compared to those presented by Tate

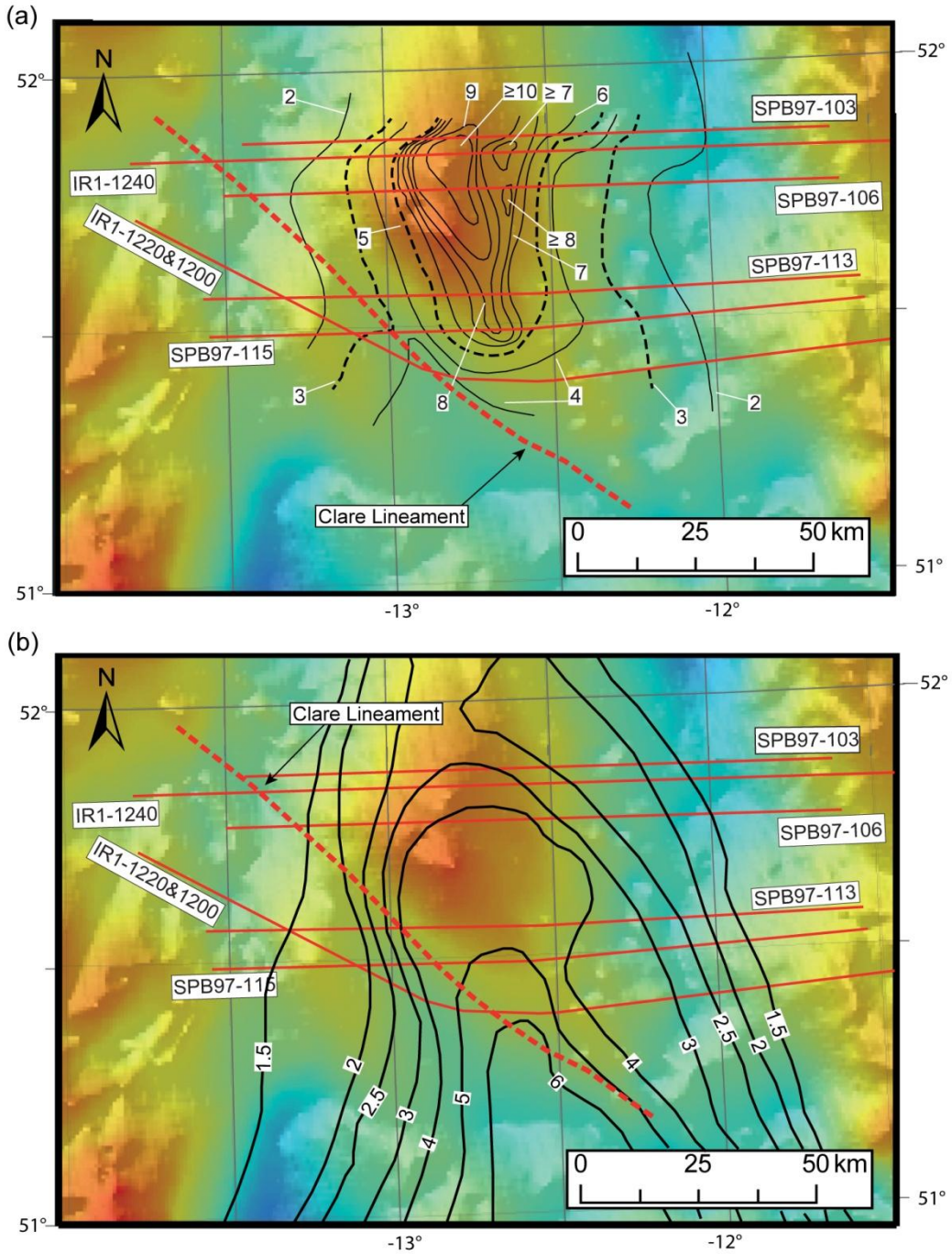

Fig. 2.10: (a) Contours of crustal stretching, interpreted from results of seismic analysis (Fig. 2.5), for the Porcupine Arch region of the Porcupine Basin. Each contour is numbered according to its β-value. Dashed lines are β = 3 and β = 5 contours and bound where total crustal embrittlement is predicted to occur. Note that the stretching values greater than 4 appear to be confined to the Porcupine Arch region (gravity high), north of the approximate location of the Clare Lineament (red dashed line), interpreted to run parallel to an apparent lineament in the gravity data on the SW side of the Porcupine Arch. (b) Lithospheric stretching contours derived from subsidence analysis (Tate et al., 1993), numbered according to their β-value. Dashed contours bound the region where the crust is predicted to become embrittled Note that the geometries of the contours appear not to be affected by the Clare Lineament, and suggest that stretching increases southwards (if coaxial strain is assumed). See text for suggestions as to why the observed crustal stretching appears to be at odds with the stretching derived from subsidence analysis

et al., 1993 (Fig. 2.10b). The contours shown in Fig. 2.10a illustrate the general partitioning of strain within the basin.

Since the seismic data used for the generation of the stretching contours are relatively sparse the contours have quite a course resolution away from the seismic profiles where the stretching data are known. The contours between the seismic profiles are guided in part by the shape of the basin and trends that are observable in the gravity data, and so a tighter grid of PSDM seismic data would be useful to generate more accurate, high resolution contours.

2.4 Discussion

The contours of crustal stretching for the Porcupine Arch region (Fig. 2.10a) tend to cluster around the large gravity high, taken here to relate to the partially serpentinised mantle undercrusting the Porcupine Arch (Reston et al., 2001, and O'Reilly et al., 2006). The tightly clustered contours on the western side of the gravity high are roughly coincident with the probable trace of the root zone for the P-detachment system (Fig. 2.10a). The presented estimate of crustal attenuation in the Porcupine Arch region (Figs 2.5 & 2.9, Fig. 2.8, Fig. 2.10a) is consistent with both gravity and refraction studies (Readman et al., 2005; O'Reilly et al., 2006; Hauser et al., 2010) but not with stretching estimates derived from subsidence analysis at, or south of the Arch (Tate et al., 1993; compare Fig. 2.10a & b).

As suggested in **Section 2.1.2**, the serpentinite undercrust beneath the Porcupine Arch supports the overlying crust (effectively acting as if it were continental material in terms of

isostasy), reducing subsidence in the region of the extreme crustal thinning. The subsidence derived stretching values of β = 3 – 4 (Fig. 2.1, Fig. 2.10b, Tate et al., 1993) at the Porcupine Arch could be reconciled with the observed crustal thickness there if the thickness of the serpentinite is c. 8 km thick. Fig. 2.4 suggests that a serpentinite body up to 6 km could have been generated beneath the Porcupine Arch given rift duration and degree of stretching. Decreasing the CMB temperature to less than 500° C during serpentinisation would increase this thickness. The seismic velocity models (Fig. 2.3) suggest that the serpentinised region beneath the Porcupine Arch is at least 10 km thick, agreeing well with the estimate for the serpentinite thickness estimated by Readman et al. (2005) (Fig. 2.5b). It appears as though an 8 km thick serpentinite undercrust (giving an effective crustal thickness of c. 10 – 11 km, or β ≈ 3) is reasonable, possibly reconciling the discrepancy between the observed crustal thickness and the subsidence derived stretching in the region of the Porcupine Arch. Fig. 2.11 appears to support the hypothesis that mantle serpentinisation may be the reason for the subsidence discrepancy at the Porcupine Arch. The redrawn β = 2 subsidence derived contour (based on the re-evaluated subsidence analysis of Jones et al., 2001) appears to match reasonably well with the β = 2 contour extracted from the reflection seismic analysis described in **Section 2.3**. If mantle serpentinisation initiates at β = 3 (Pérez-Gussinyé & Reston, 2001), or slightly below this (as potentially could have been the case for the eastern margin of IR1-1240 (see Fig. 2.6), then it might be expected that the subsidence derived and observed crustal stretching will not match. There are insufficient well data in the basin to test the idea fully. It would be very useful to generate new subsidence derived contours based on the estimates of Jones et al. (2001) combined with more recent seismic data. The

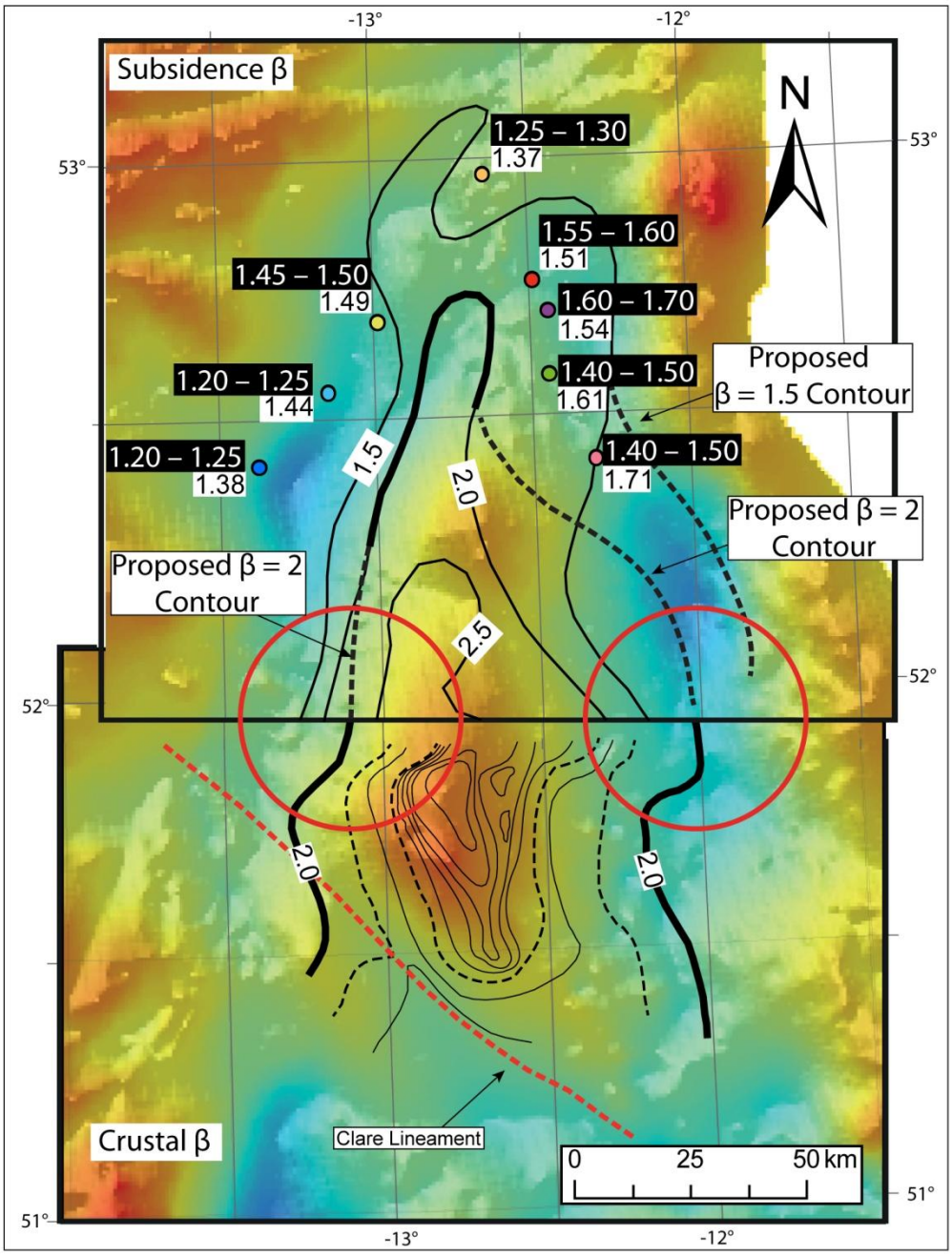

Fig. 2.11: This figure shows the subsidence derived stretching estimates (top panel) where they are best constrained by well data. The original Tate et al. (1993) estimates are shown as white on black, and the revised estimates of Jones et al. (2001) are shown as black on white. The bottom panel is the crustal β map based on seismic observations presented in this chapter.. Note that the original subsidence contours (solid black lines) do not match at all with the crustal stretching contours. However, the "proposed β = 2" contour, based on the stretching estimates presented by Jones et al. (2001) appears to match quite well (shown in red circles) with the β =2 contour observed for the seismically derived estimates.

seismic data that was used by Tate et al. (1993) to extrapolate their stretching contours across the entire basin dates from the 1970's, and could definitely be improved upon now.

Based on the apparent agreement between the β = 2 contours for the subsidence derived and observed crustal stretching it might be expected that there would be close agreement up until the point at which crust was embrittled and mantle serpentinisation began.

Further south crustal stretching does not appear to be as great as that suggested from subsidence analysis (compare Fig. 2.10a & b), forming an inverse subsidence discrepancy. The crustal stretching values obtained from analysis of the reflection data south of the Porcupine Arch, presented in **Sections 2.2 & 2.3**, are in relative agreement with the refraction and gravity studies of Hauser et al., 2010, Makris et al., 1988, and Conroy & Brock, 1989 which yield a $\beta_{max} \approx 4$, whereas the subsidence data suggest β = 6. As previously mentioned in **Section 2.1.2**, Tate et al. (1993) suggested that 4 – 10 km of underplating may have occurred in the PSB as a result of decompression melting in the PSB. However, as was discussed, this probably did not occur and so this discrepancy must have been caused by some other mechanism.

Tate et al., (1993) appeal to an Eocene stretching event and an associated phase of thermal subsidence to account for the anomalous post-rift sediment thickness in the south of the basin and include this in their stretching estimations. They concede however, that there does not appear to be any faulting related to this postulated Eocene subsidence and suggest that evidence for this late rifting event was yet to be found.

More recently, Jones et al. (2001) suggested that the renewed subsidence in the Eocene may have been caused by a loss of dynamic support from the Iceland plume. They suggest that the plume (or anomalously hot sublithospheric mantle) may have caused transient uplift beneath the basin from Cretaceous times. Praeg et al., (2005) advanced an alternative that also invoked a loss of dynamic support from the mantle to account for the anomalous subsidence in the Eocene and suggested that this may have been driven by a reorganisation of convection cells in the upper mantle beneath the region as seafloor spreading initiated in the newly formed North Atlantic Ocean. Taking these hypotheses (Jones et al., 2001, and Preag et al., 2005) into consideration it may be possible to reconcile the geophysical crustal thickness estimates from the PSB (Makris et al., 1988; Conroy & Brock, 1989; Hauser et al., 2010) with those derived from subsidence analysis (Tate et al., 1993). Since Tate et al. (1993) included the considered the Eocene subsidence to be a result of renewed rifting, rather than a loss of mantle support, when constructing their stretching contours it is possible that they may have overestimated the amount of stretching in the PSB.

Another, possibly more reasonable, explanation for the inverse subsidence discrepancy in the PSB may be due to rheological contrast between the Main Porcupine basin (Porcupine Arch region) and the PSB. The crust in the region of the Porcupine Arch, north of a feature known as the Clare Lineament (Tate, 1992) (see Fig. 2.10a for location), has been fully embrittled and serpentinite detachment tectonics initiated. Here the basin is c. 125 km wide. South of the Clare Lineament the basin is significantly wider, at c. 160 km, but widespread crustal embrittlement, detachment tectonics, and mantle serpentinisation do not appear to have occurred. The Clare Lineament may act as a terrane boundary separating regions of

contrasting rheology. This has also been suggested by Readman et al. (2005) based on structural style and grain across the lineament.

Huismans & Beaumont (2011) modelled two contrasting rift modes that may be applicable to the situation in the Porcupine Basin. They present a "Type 1" rift mode where stretching a strong lithosphere leads to the crust rupturing before the mantle lithosphere resulting in mantle exhumation, and a "Type 2" rift mode where the mantle lithosphere ruptures before a relatively weak crust and no exhumation occurs. The Porcupine Arch region may represent a precursor to a "Type 1" mode, and the PSB may represent a precursor to a "Type 2" situation in the terminology of Huismans & Beaumont (2011). Classifying the PSB as a Type 2 rift requires that deformation between the crust and mantle lithosphere is decoupled with less thinning in the relatively weak crust compared to that in the mantle lithosphere (Huismans & Beaumont, 2011). It might be expected that there would be greater subsidence produced than observations of crustal thickness might suggest for the PSB. The relatively weak crust in the PSB can be further argued for by comparing it to the East Orphan Basin (Fig. 2.12). The East Orphan Basin was conjugate to the Porcupine Basin prior to the initiation of seafloor spreading in the North Atlantic.

Subsidence analysis (Keen & Dehler, 1993) from the East Orphan Basin suggests factors of $\beta = 2.5 – 5.0$ for the most highly stretched portion (conjugate to the mouth of the Porcupine Basin), agreeing reasonably well with the stretching factors ($\beta \geq 6$) reported by Tate et al. (1993) for the PSB. Although the stretching observed within the East Orphan Basin is within the range where crustal embrittlement is predicted to occur ($3 \leq \beta \leq 5$, Pérez-Gussinyé & Reston, 2001) refraction seismic studies in the region (Chian et al., 2001) suggest that the

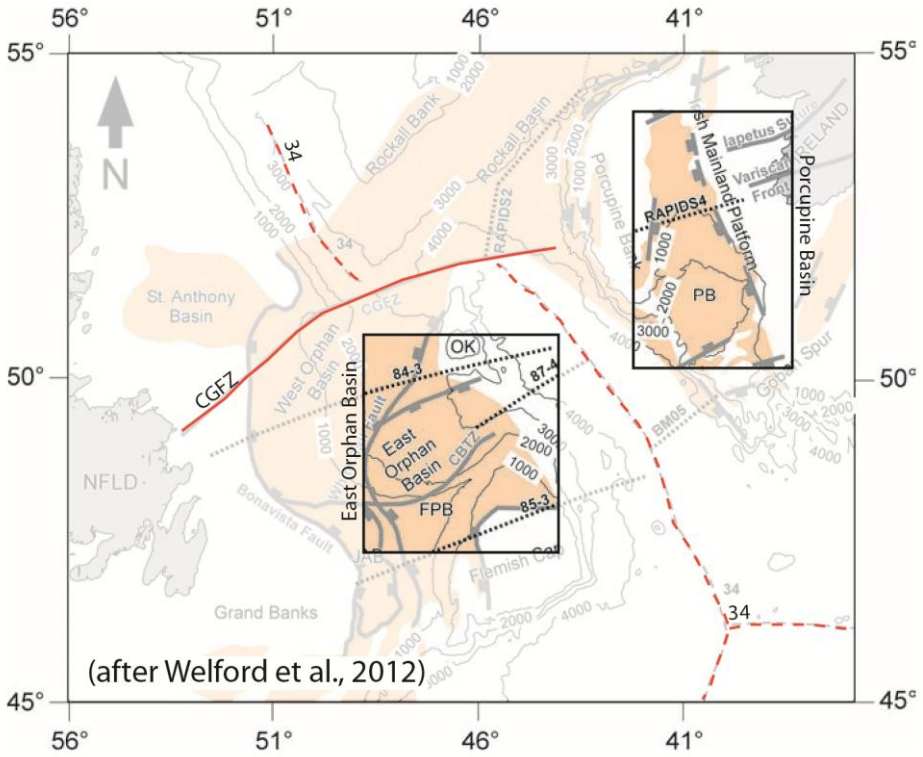

Fig. 2.12: Pre-break up restoration (to anomaly 34) showing the conjugate nature of the Porcupine Basin with the East Orphan Basin. Note that both basins open towards one another. CGFZ – Charlie-Gibbs Fracture Zone.

crust is underlain by unaltered mantle, suggesting that crustal embrittlement did not occur. This appears to be similar to what is observed for the PSB (as discussed above) where there is no strong evidence that serpentinisation of the mantle had initiated south of the Clare Lineament. Welford et al.. (2012) have suggested that the highly stretched crust of the Orphan Basin is relatively weak and was not embrittled and may represent a "Type 2" rift in the terminology of Huismans & Beaumont (2011), and reached a similar conclusion from their comparison with the PSB.

It is reasonable to treat the Porcupine Basin as a magma-poor aulocogen, where breakup was not achieved, that can be readily compared to magma-poor rifted margins such as the Iberia-Newfoundland rift system. Many of the characteristics of MPRMs have been

identified within the basin; extreme crustal stretching, partial serpentinisation of subcontinental lithospheric mantle, low-volumes of syn-rift magmatism and deep water. It may be that there is a narrow zone of incipient mantle exhumation in the vicinity of the Porcupine Arch as seen on seismic reflection profiles SPB97-106 and IR1-1240 (discussed in **Section 2.2**). As such the Porcupine Basin is an ideal place to study the pre-breakup structure of the crust in a magma-poor setting.

2.5 Conclusions

The Porcupine Basin, specifically the Porcupine Arch region of the basin, has been shown to share many characteristics with MPRMS such as extreme crustal attenuation, partial serpentinisation of subcontinental lithospheric mantle, and low-volumes of syn-rift magmatism, and may be reclassified as a magma-poor aulacogen. Analysis of crustal attenuation (considering the effects of rheological evolution driven by prolonged crustal extension) has shown that as the crust reaches the point at which its entire thickness becomes brittle stretching gradients increase dramatically basinward. This increase in stretching gradient appears to be focused on a serpentinite detachment system. The profile of crustal attenuation that has been constructed for the basin does not support a simple southwards increase in extension, as has been suggested from subsidence analysis. Instead the PSB appears to be a large region of highly to hyper-extended ($\beta \approx 3 - 4$) that is likely only fully embrittled locally. There does not appear to be any seismic evidence for mantle serpentinisation. Extensional strain also appears to have been partitioned and strongly focused north of the Clare Lineament (a probable rheological terrane boundary) onto a serpentinite detachment fault known as the P-detachment system.

The discrepancy between the subsidence derived stretching values for the basin and the crustal stretching values (from observations presented in this chapter and published refraction seismic data) may be explained by different rift modes across the Clare Lineament. North of the lineament the anomalously low subsidence derived stretching may be explained by partial serpentinisation of the subcontinental mantle beneath the Porcupine Arch which yields an effective crustal thickness consistent with the subsidence data. South of the Clare Lineament it appears as though crustal embrittlement and mantle serpentinisation was not achieved. The crust may have been weaker than that to the north and the mantle lithosphere thinned to a greater degree, which may have led to an apparent subsidence excess relative to the observed crustal thickness in the south.

The basin provides the perfect hunting grounds for structural mechanisms capable of accommodating such large amounts of extensional strain. The following chapters describe the potential mechanisms; progressive polyphase faulting and detachment tectonics (**Chapter 3**). In **Chapter 4** synthetic seismograms are generated of the extensional structures presented in **Chapter 3**, for comparison with data from the Porcupine Basin in **Chapter 5**.

CHAPTER 3

Mechanics & Evolution of High Strain Extensional Systems

3.1 Introduction

The mechanisms by which the continental crust is thinned to the point of separation, as at Magma-poor rifted margins (MPRMs), and in some cases margin basins (those associated with the eventual break-up), remain the subject of much debate,

One of the main issues that is under debate is how does the crust thin to the extremes that commonly observed at MPRMs. In this chapter potential structural mechanisms are described and demonstrated to be capable of accommodating sufficient stretching to allow the degree of thinning that is observed at MPRMs. The problem stems from the observation that stretching factors, β_f, calculated from seismically observable faults in these regions cannot account for the extensional strain - even when sub-seismic scale faulting (Walsh et al., 2001) is considered (when compared to whole crustal stretching, β_{WC}, derived from gravity and wide-angle seismic studies (Wood & Barton, 1983; Zeigler, 1983; Davis & Kusznir, 2004; Kusznir & Karner, 2007; Reston, 2007). This problem has been termed “the extension discrepancy” by Reston (2007). Many models have been suggested to account for the apparent discrepancy observed in these hyper-extended regions; convective removal, or margin-ward displacement of the lower crust away from the extending region (Davis & Kusznir, 2004; Kusznir & Karner, 2007; Huismanns & Beaumont, 2007), large-offset “top-basement” normal faulting (Manatschal et al., 2004; Lavier & Manatchal, 2006; Reston, 2007), and polyphase faulting (Reston, 2005; Reston 2007; Reston 2009).

The brittle (upper) crust is extended and thinned by normal faulting. Normal faults are ubiquitous features in extensional regions, and are the most common and most efficient way of stretching and thinning the brittle (upper) crust. Commonly normal faults are observed to be active at dips ≥ 35° (Jackson & White, 1989). There are however, examples from regions of continental extension, both onshore and on marine seismic profiles, where more shallowly inclined normal faults, termed low-angle normal faults, have been described (Buck, 1988; Axen, 2007; Chamberlin, 1982; Proffett, 1977; Miller et al., 1983; Gans et al., 1985; Manatschal et al., 2001; Reston et al., 2007; and many others). Controversy exists as to whether these low-angle normal faults (LANFs) initiated at low angles, were simply active at low-angles having formed at higher angles, or were passively rotated to low angles after they had ceased to be active. However, it has been noted that larger amounts of displacement can be accommodated by a single LANF than is possible to accumulate on a single high-angle normal fault (HANF), due to the higher gravitational restoring forces that would act upon a HANF (Forsyth, 1992). Although definitive seismogenic LANFs (dip ≤ 30°) are so far, unknown from teleseismic data (Jackson & White, 1989; Collettini & Sibson, 2001), potentially suggesting that the LANFs have been rotated into position, more local seismicity (Abers, 2001; Rietbrock et al., 1997) does appear to show that some slip may occur at angles less than about 35°. However, Johnson & Loy (1992) suggested that a large magnitude (M≈7) earthquake may have occurred on a LANF (dipping at c. 20° as imaged on reflection seismic data) in SE Arizona. The fault in question crops out at a Quaternary fault scarp significantly steeper than 20° (Johnson & Loy, 1992), and they concede that it is possible that an active (blind) HANF not imaged on the data may have caused the measured

seismicity. The aforementioned earthquake notwithstanding, seismogenic LANFs (if they exist) appear to be extremely rare. Furthermore, the geometry of syn-rift wedges has been used to argue that the low-angle S detachment slipped at less than 20° west of Spain (Reston et al., 2007). Low-angle slip is also inferred from the geometry of many now inactive detachment faults found in the western US (e.g. see the review by Axen and Bartley, 1997).

Notwithstanding the controversy about whether low-angle normal faults do really slip at low-angles, it is clear that the present day orientation of many LANFs can be attributed to passive rotation of abandoned early structures by later active structures (Proffett, 1977; Chamberlin, 1982; Proffett & Dilles, 1984; Reston, 2005; and Reston 2009), as is discussed in greater detail in **Section 3.2**. Other LANFs may have formed as part of a rolling-hinge system (Buck, 1988; Buck, 1991), in which a fault roots at a relatively high-angle, and as it accumulates displacement the footwall is flexurally rotated to very low angles, becoming inactive (see Fig. 3.1). Depending on whether or not that fault had rotated sufficiently to become inactive while in the subsurface, the resulting inactive fault may be covered by small fault blocks transferred from the hangingwall to the footwall by the propagation of new faults up from the still active steep root zone (Reston and Ranero, 2011). However a feature of the rolling-hinge model is that it requires the brittle upper crust to be weak and hence probably thin, allowing sharp flexure, and also a mechanism to minimise gravitational resistance to footwall uplift: either lower crustal flow (Buck, 1988; Buck 1991) or mantle serpentinisation (Reston and Ranero, 2011). The rolling-hinge mechanism seems particularly applicable for the formation of oceanic-core complexes (OCCs) adjacent to slow and very slow spreading ridges (Ranero & Reston, 1999; Smith et al., 2006; Tucholke et al., 2008;

Reston & Ranero, 2011), where seismic and seismicity data hint at convex-up structures that steepen towards the root zone (Reston et al., 2004; de Martin et al., 2007).

Numerical modelling shows that rifting, accommodated by either HANFs or LANFs may be controlled by the thickness of the brittle crust (Lavier & Buck, 1999; Buck & Lavier, 2001). Extension over multiple HANFs (each accommodating relatively small amounts of displacement before being abandoned) is favoured where there is a relatively thick brittle crust, whereas when the brittle layer is ≤ 10km thick it is possible for a fault to accumulate very large amounts of displacement by flexurally rotating its footwall while maintaining a relatively steep root zone (Lavier & Buck, 1999; Buck & Lavier, 2001).

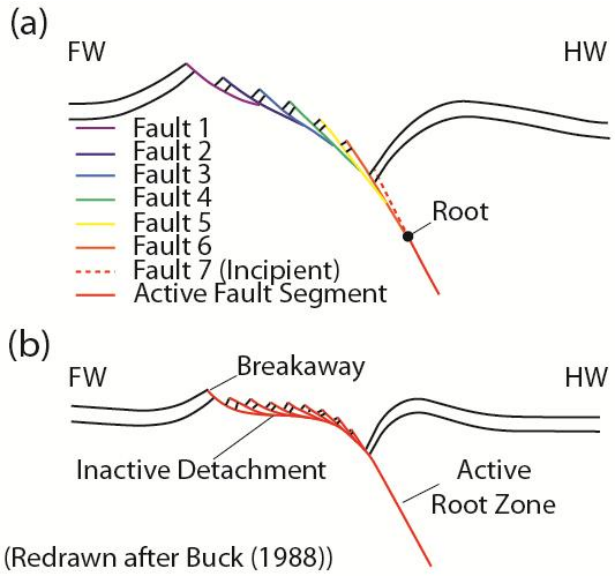

Fig. 3.1: Rolling hinge model for the development of low-angle normal faults (Buck, 1988). (a) Master fault roots beneath the hangingwall (HW) initiating with steep dip. The uplifted footwall (FW) is flexurally rotated out of favourable orientation for continued slip and the upper section is abandoned. Meanwhile a new fault segment propagates upwards into the HW from the root zone, and the process continues. (b) Continued extension cause to the inactive portion of the fault to be flexurally rotated to a sub-horizontal orientation, with abandoned fault segments apparently detaching onto the surface. As in (a) the active portion, the "root" of the fault remains at a relatively steep angle throughout extension .

There is some evidence that detachment fault systems at MPRMs may also have formed, in part, by a modified rolling-hinge system (Reston et al., 2007), in that some faults appear to be convex-up, steepening downdip from sub-horizontal to root at steeper angles (Reston & McDermott, 2011). For instance, Fig 3.2 demonstrates how the S detachment (currently sub-horizontal beneath the Galicia margin) may originally have rooted at c. 30° beneath the Newfoundland margin; the P detachment beneath the Porcupine Basin roots at a slightly lower angle of c. 20° beneath the Porcupine Bank (Reston et al., 2007; Reston & McDermott, 2011) (see Fig. 3.2). As will be discussed in **Section 3.2.7,** the root zones of both the S and P detachment systems are mechanically feasible due to the effects of serpentine, and would have been capable of accumulating active displacement. Similar detachment geometries appear to be quite common at OCCs (Ranero & Reston, 1999; Smith et al., 2006; Reston & Ranero, 2011).

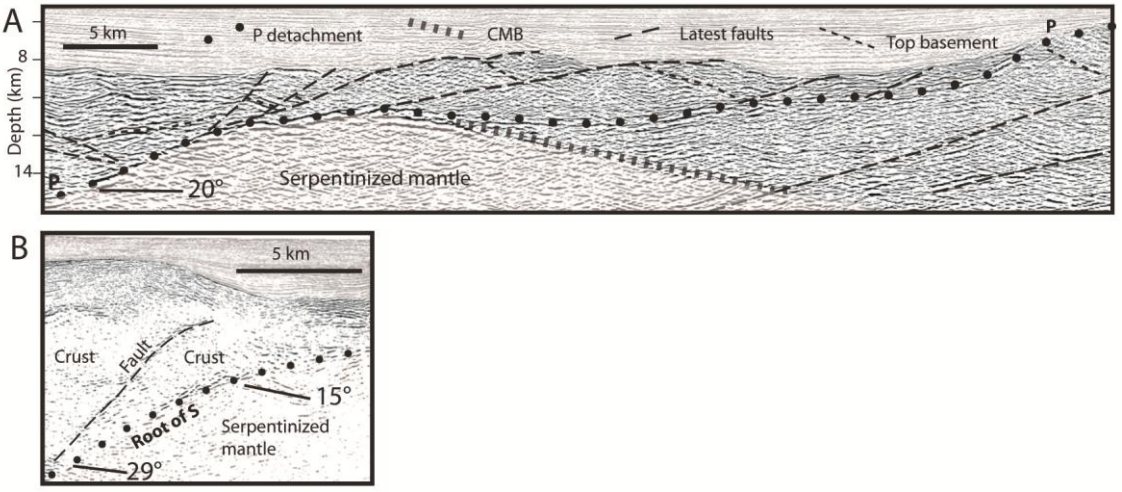

Fig. 3.2: Seismic sections which demonstrate the convex-up nature of serpentinite detachment systems (after Reston & McDermott, 2011). (a) P-detachment from the Porcupine Basin, west of Ireland rooting at c. 20° to the west and shallowing eastward to sub-horizontal. (b) Root zone for the S-detachment (known from W. Iberia Margin) on the Newfoundland Margin, dips at c. 30° west, at depth and at c. 15° shallower in the section.

It should also be noted that when seismically observable displacement accommodated by detachment systems at MPRMs has been restored (Manatschal et al., 2004; Reston et al., 2007), the crust is c. 7 – 10 km thick (β ≈ 4.3 – 3). For this degree of crustal stretching, rheological coupling of crustal layers may be expected (Fig. 3.3) and the entire crust embrittled (Pérez-Gussinyé & Reston, 2001), allowing faults and fluids to penetrate down to the mantle and initiate the process of serpentinisation. The low frictional coefficient of serpentine (Reston et al., 2007) and extremely thin crust (Lavier & Buck, 1999; Buck & Lavier, 2001) may allow for the formation of low-angle normal faulting in this setting.

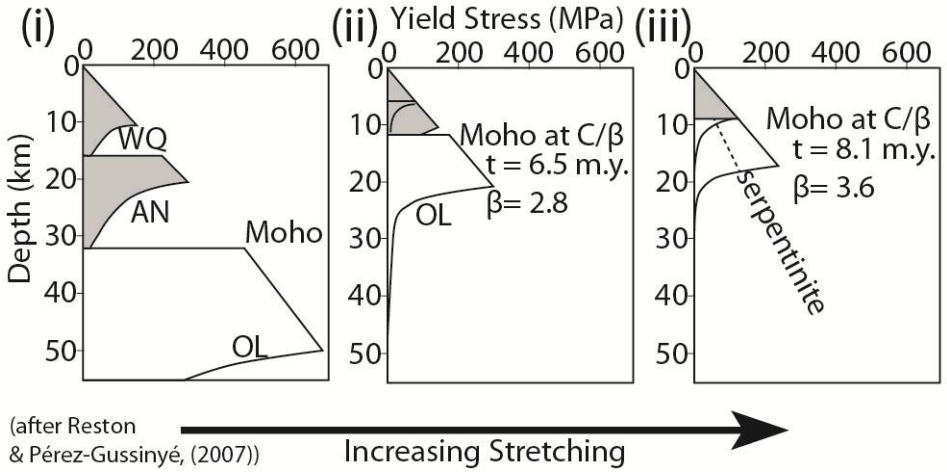

Fig. 3.3: Figure taken from Reston & Pérez-Gussinyé, (2007) demonstrating rheological coupling of the crust leading to total crustal embrittlement with increasing extensional strain. WQ = wet quartz, AN = anorthosite, OL = Olivine. (i) Initial crustal set up. There are two regions of plastic deformation at the base of the upper and lower crust. (ii) Rheological coupling of the upper and lower crust. The crust deforms mostly by brittle processes but a relatively thin region of plastic deformation remains. (iii) Entire crust deforms by brittle process and is coupled to the upper portion of the mantle. Serpentinisation occurs and as a result mantle yield strength is reduced.

So, for the case of MPRMs, there is a probable transition in active faulting style from dominantly high-angle normal faulting (in the initial rifting stages) to low-angle normal faulting (in the latest rifting stages) as the crust is thinned. As such, we might expect rotating HANFs to thin the crust and passively rotate any earlier fault generations present to

lower angles, and finally, in the latest stages of rifting, to be succeeded by flexurally rotating low-angle normal fault (serpentinite detachment) systems that focus extension in the rift zone (Pérez-Gussinyé & Reston, 2001). Essentially a pure shear extensional regime is succeeded by simple-shear/asymmetric extension (Reston & Pérez-Gussinyé, 2007) but overall it is likely that this transition is only present within the crust and that on the whole the lithosphere extends mostly via pure-shear. Reston & McDermott (2011) have shown that roughly symmetrical expanses of exhumed mantle on the Newfoundland-Iberia Rifted Margins have been exhumed by successive generations of detachment faulting (see Fig. 3.4).

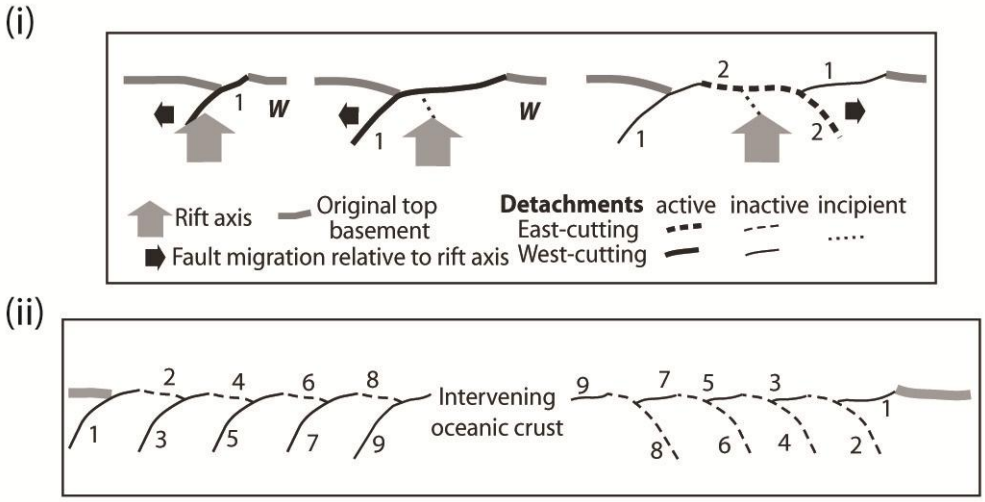

Fig. 3.4: Development of roughly symmetrical expanses mantle exhumed along multiple detachment faults (edited after Reston & McDermott, 2011). (i) Progressive development of sequentially active detachment systems. Detachment initiates (left), root zone migrates away from rift axis with the hangingwall (middle). Detachment becomes inactive and its footwall is dissected by a new detachment with opposite polarity, nearer the rift axis leaving the break away and root zone of the original detachment fault stranded on either side of the succeeding detachment. (ii) Continuing this process of exhuming mantle over detachment faults which are sequentially active with opposite polarities under magma-poor conditions produces potentially wide zones of exhumed mantle on either side of the oceanic crust with landward dipping reflectors representing fossil detachment root zones.

In this chapter, I demonstrate how successive generations of extensional faulting (polyphase faulting, PPF) can contribute to extremely high levels of extensional strain, ultimately leading to whole crustal embrittlement (Pérez-Gussinyé & Reston, 2001) and mantle exhumation. I

also suggest why the mechanism may remain inconspicuous on seismic data. Previously published onshore sections from the western US are presented and palinspastic restorations are completed and are compared with the PPF model.

3.2 Identification of Polyphase Faulting structures

Polyphase faulting (PPF), although a relatively simple concept and capable of accommodating very large amounts of extensional strain is largely unrecognised on seismic data, although potential PPF structures have been interpreted on the W. Iberian Margin (Reston 2005; Reston et al., 2007; Reston 2007; Reston et al., 2009). Onshore examples of PPF have also been noted from the western USA (some of which are discussed in **Section 3.3**) where cross-cutting faults characteristic of the PPF mechanism can be demonstrated clearly from outcrop. PPF was first described onshore by Proffett (1977) from the Yerrington district, Nevada, where at least three successive phases of faulting can be observed. PPF has also been recognised onshore in a number of other localities in the USA including the Lemitar Mountains, New Mexico (Chamberlin, 1982), and the North Snake Range Detachment (NSRD) in Nevada, where multiple generations of faulting have been recognised in the hanging wall of the detachment system (Miller et al., 1983; Gans et al., 1985).

3.2.1 Polyphase Faulting: Model Description

The model presented here (Fig. 3.5) is the simplest case for both monopole and dipole polyphase faulting end-member variants. The basic concept of the complex structural geometries that might be expected to result from the PPF mechanism is clearly demonstrated, and are comparable to the models of Reston (2005). The simplified model

assumes the following: rigid fault blocks (no internal distributed deformation, c.f. Walsh & Watterson's (1991) soft-domino faulting model); planar faults; fault parallel shear, effectively reducing the predicted extension of the model (Jackson & White, 1989); faults/blocks are allowed to rotate through 30°; constant sediment supply (reduces gravitational restoring forces (Forsythe, 1992) and prevents mass-wastage); and no sediment compaction. The model also demonstrates increasing structural complexity with greater extensional strain.

3.2.2 Monopole Polyphase Faulting

For the monopole variant (Fig. 3.5a) the first generation faults are allowed to rotate by 30°, and as they do so sediments accumulate within the half-graben, thickening towards the footwall block. Following this rotation, the first generation faults will have accumulated an extensional strain of $\beta \approx 1.7$ and are abandoned (Fig. 3.5a(ii)).

If regional stresses remain favourable to extension, then stretching the crust to $\beta \approx 3$ requires a second generation of faults to propagate that are in turn allowed to rotate by 30°. At this stage the degree of crustal stretching brings the crust into the lower end of the predicted range for total crustal embrittlement of $\beta \approx 3 – 5$, as predicted by Pérez-Gussinyé & Reston (2001) for a mix of anorthitic – quartzitic lower crust (50:50 mix). The structures resulting from the propagation and rotation of the second fault generation are seen to be quite complicated at this stage, with early syn-rift sediments tilted to high-angles (especially relative to the second generation faults) and first generation faults rotated to sub-horizontal orientations (Fig. 3.5a(iii)). If the crust has been embrittled, mantle serpentinisation may

initiate and further extension will likely be accommodated by a precursor structure to a serpentinite detachment fault (see **Section 2.2.1.4**).

If the crust has not become embrittled and extensional stresses continue to act, a third fault generation may be propagated to accommodate the strain. The third fault generation, if allowed to rotate by c. 30°, could potentially stretch the crust to $\beta \approx 5$ (Fig. 3.5(iv)), bringing it to the upper range of where the crust is expected to become embrittled for an aggregate lower crustal rheology (Pérez-Gussinyé & Reston, 2001). The structures resulting from three cross-cutting fault generations are very complicated (Fig. 3.5a(iv)). The forerunners to the third fault set and their associated sediments are passively rotated. This passive rotation causes the earliest syn-rift sediments (and top-basement) to be tilted to sub-vertical orientations. The first generation fault sets themselves are now overturned and dipping in the opposite direction to how they initiated (Fig. 3.5a(iv)).

3.2.3 Dipole (See-Saw) Polyphase Faulting

If the second fault generation propagates with opposite polarity to the first, the dipole PPF variant develops. Fig. 3.5b demonstrates conceptually how di-pole (see-saw) PPF system might develop. The See-Saw variant of PPF produces relatively simple (large scale) geometries compared with mono-pole PPF. Strongly tilted stratigraphy and LANFs are not expected to develop.

Extension begins with faults dipping in one direction and then rotate to a minimum dip of 30° (Fig. 3.5b(i – ii)) same as Fig. 3.5a(i – ii). Following lock-up and abandonment of the first fault generation, a second fault set is propagated and allowed to rotate to a minimum angle of 30° (Fig. 3.5b(iii)), this time with opposite polarity to the first fault generation.

Continued extension facilitated by the second fault generation will cause rotation of fault blocks counter to that of the earliest fault sets, and as such the sediment that accumulates in the associated half-grabens will thicken in the opposite direction to the early syn-rift sediments. As the rotation of fault set two is counter to that of the first fault, set early faults may be passively re-orientated to steeper angles, potentially bringing them within the range reactivation (see **Section 3.2.8**).

If the second fault generation were able to accommodate c. 30° of rotation, then the first fault set would regain its original dip of c. 60°, at which point the system will have accommodated $\beta \approx 3$ over two fault generations, potentially embrittling the crust (c.f. Pérez-Gussinyé & Reston, 2001). In this model the faults are allowed to rotate fully to illustrate the concept (see **Section 3.2.5**).

Fig. 3.5b(iv) demonstrates the geometries that might be expected if the earliest, re-orientated, set of faults were reactivated and proceeded to accumulate displacement. Tilting of all previous structures and associated sediments resumes in the same direction as the original fault set and another syn-rift sediment package is deposited, thickening toward the active fault, oppositely to the second generation syn-rift package, but in the same direction as the first, effectively stacking alternating wedges of opposing thickening direction in a See-Saw motion. Strain hardening (Agnon & Reches, 1995) however, could potentially cause the focus of extension to relocate or a new fault generation to cut through what would appear to be a conjugate fault system. It is likely that faults would never get the chance to rotate through a full 30° for reasons discussed in **Section 3.2.6.**

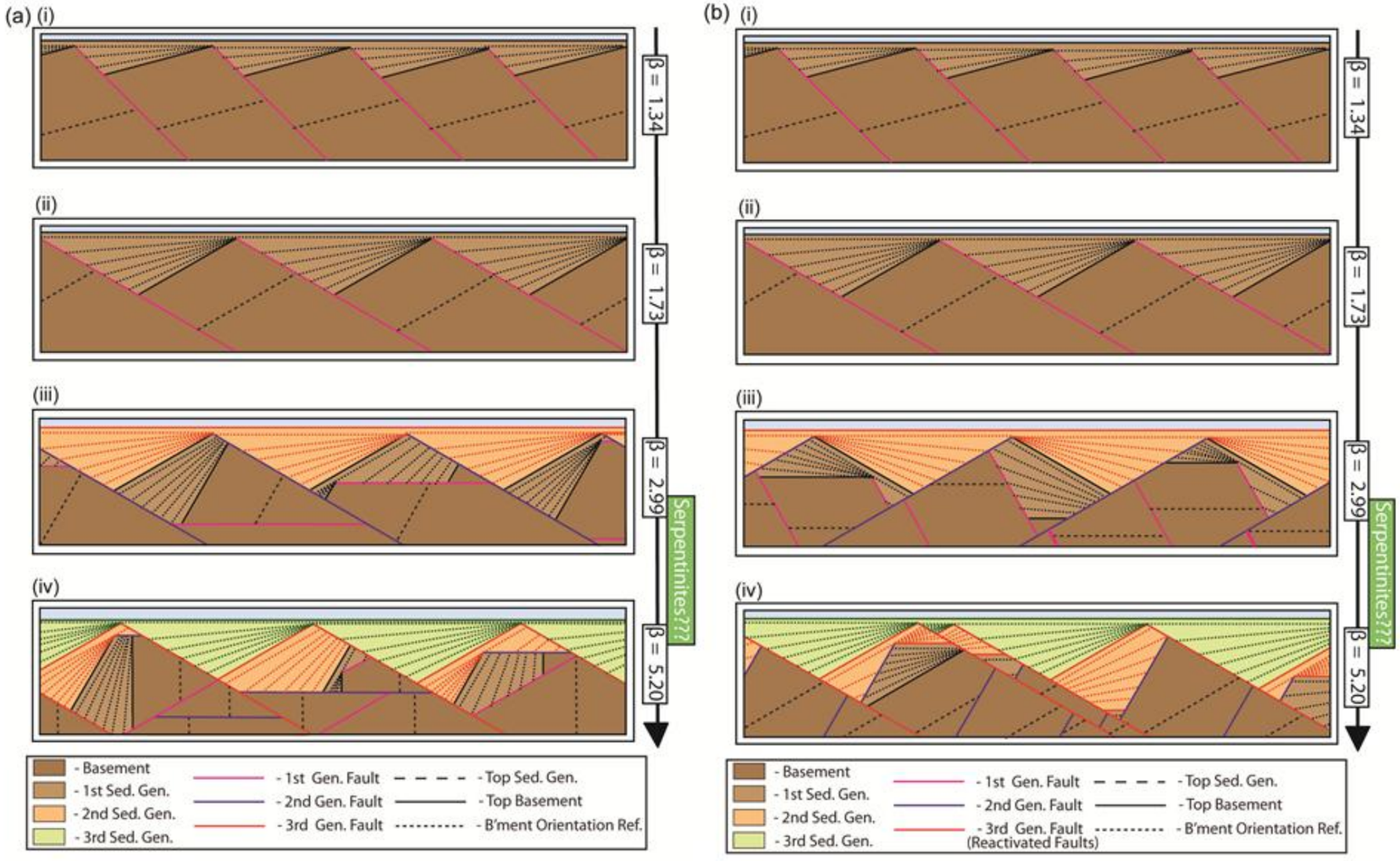

Fig. 3.5: Conceptual Polyphase Faulting (PPF) models demonstrating progressively more complex structural geometries as crustal stretching increases, with total crustal embrittlement and mantle serpentinisation assumed to take place at $3 \leq \beta \leq 5$ (c.f. Pérez-Gussinyé & Reston, 2001). (a) Mono-pole PPF variant. Faulting initiates and blocks begin to rotate (i) until they reach a dip of c. 30° and lock-up (ii) (see Section **3.3.6** & Fig. 3.7). (iii) A new set of faults is propagated synthetically to the first fault generation, rotated towards 30° and abandoned. Note passively rotated first generation structures and sediments. (iv) A third fault generation propagates rotates towards 30° and reorientates all preceding fault sets and associated sediments resulting in highly complex structural geometries. (b) Dipole PPF variant. (i – ii) same as in (a). Second generation fault propagates with opposite polarity, rotates to 30°, reorientating all preceding structures (see Section 2.2.2). Note geometry of syn-rift wedge. (iv) The first generation faults are reactivated, and begin to rotate tilt the whole system in a "see-saw" fashion. Note direction of the syn-rift sediment wedge. It is likely that in a real situation it would take more fault generations than are shown in (b) to achieve embrittlement (see **Section 3.2.8**)

3.2.4 Identifiers of Polyphase Faulting

The seismic response to PPF structures is discussed in **Chapter 4** but, generally speaking, the latest (monopole) fault sets will be most conspicuous on seismic data, with earlier fault generations likely to be interpreted as noise or perhaps basement fabrics where the structure is not known initially. High-angle structures are not well resolved by seismic methods, likely rendering the top basement and early syn-faulting sediments invisible at high β values. As such, direct seismic evidence for the earliest fault sets will be unclear and difficult to interpret. Fig. 3.6, which has accumulated β ≈ 3, demonstrates some of the key features or identifiers that may be expected from both the monopole, and dipole variants of the PPF mechanism.

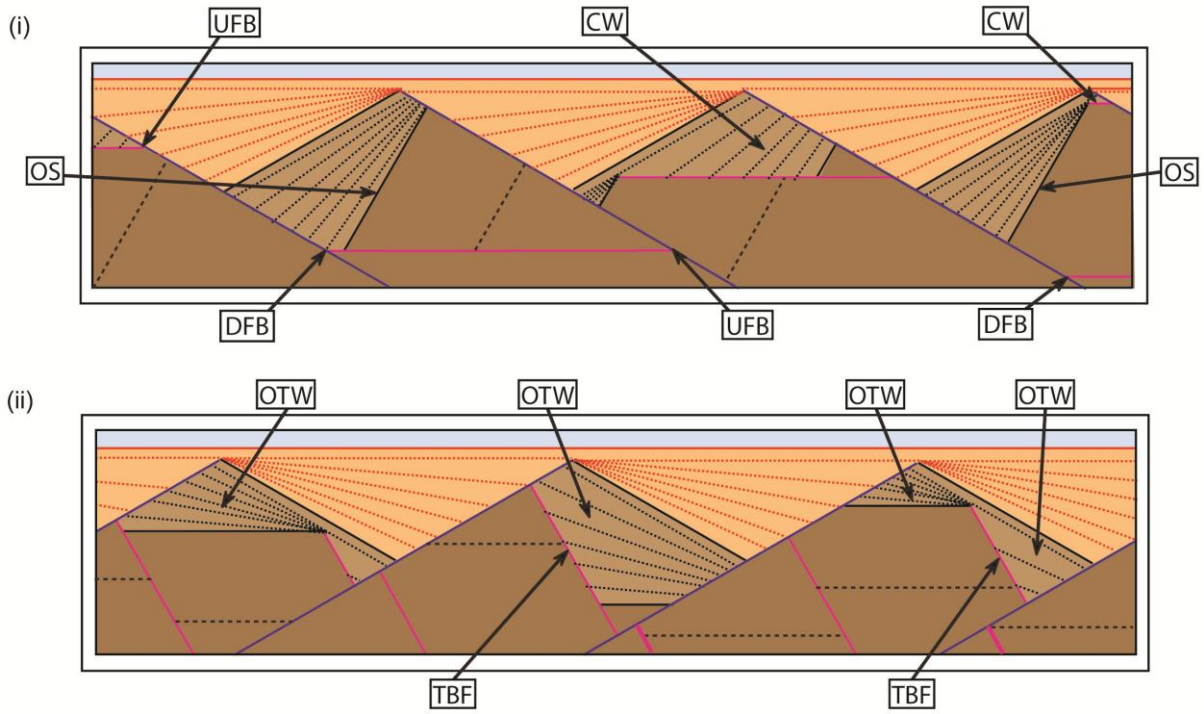

Fig. 3.6: Identifiers of polyphase faulting, based on Fig. 3.5a(iii) & 3.5b(iii). Colour coding is as in Fig. 3.5. (i) Mono-pole PPF variant. CW – Crestal Wedge; UFB – Up-dip Fault Bifurcation; DFB – Down-dip Fault Bifurcation; OS – Oversteepened Stratigraphy. (ii) Dipole PPF variant. TBF – Top Basement Fault; OTW – Oppositely Thickening Wedge.

A Crestal Wedge (Fig. 3.6(i)) is an excellent identifier of the PPF mechanism. If enough strain is accommodated by two or more generations of cross-cutting fault then it is possible that a fault bounded wedge can be stranded on the footwall crest of the latest fault generation. However, their preservation potential is entirely dependent on the sediment supply to the margin/basin. If this PPF identifier is to survive, the footwall crest must be buried relatively quickly in order to limit the amount of mass-wastage and erosion that would otherwise destroy any evidence of its existence.

Fault plane bifurcations (cross-cutting fault relationships) are essential in recognising the PPF mechanism. Bifurcations come in two varieties: down-dip fault bifurcations (DFBs), and up-dip fault bifurcations (UFBs). UFBs, if preserved, are the simplest to recognise and may have an inter-fault angle of 5 – 30°, depending on the amount of rotation the initial fault generation accommodated and the angle at which the superseding fault initiated. Depending on the level of strain accommodated by the bifurcating (cross-cutting) faults, UFBs actually form the basal and edge bounding faults of crestal wedges.

DFBs (if imaged on seismic data) are very useful identifiers of the PPF mechanism, and are normally found in the hangingwall of the latest fault generations (Fig. 3.6(i)). As such they have a much higher preservation potential than crestal wedges and UFBs. A major hindrance of using DFBs to identify PPF is that the cross-cutting faults need to generate reflections (requiring that they produce a velocity contrast). The seismic record time also needs to be sufficient to image any reflections that may be produced within the hanging wall of the latest fault generation.

Oversteepened stratigraphy (OS) is the final, and possibly the most easily recognised, identifier of the PPF mechanism (Fig. 3.6(i)). Being present above top-basement level significantly increases the chances that it is imaged on seismic data, unless the stratigraphy has been tilted to very high angles. OS also has a greater chance of being preserved than a CW for example. It might be expected that fault-bedding intersections would occur at c. 60° downdip and c. 120° updip along a given fault (assuming that the bedding was horizontal at the initiation of fault displacement). Considering that in general only relatively high-angle (late-stage) faults appear to be identifiable from seismic data at MPRMs and high-strain basins, any deviations from this (i.e. where the downdip intersection angle is greater than 60 - 70°, approaching 90° or greater) would suggest that pre-tilting of the stratigraphy must have occurred before the more easily recognised (generally high-angled) fault begins to accumulate displacement. If it were assumed that there was no pre-tilting of stratigraphy, then restoring the stratigraphy to horizontal (assuming that it was originally deposited horizontally) requires that the fault initiated with sub-vertical to overturned dips, which is not mechanically feasible. Thus, oversteepened stratigraphy relative to the latest generation faults is an extremely useful identifier of the PPF mechanism where CWs, UFBs, or DFBs are not present on seismic data, and many examples are described in **Section 3.3**. Examples of where OS has been used to infer the possibility of the PPF mechanism being present in the Porcupine Basin are described in **Chapter 5**. Using OS may be problematical, however, where there is significant internal deformation of the fault blocks, as has been postulated for MPRMs by Le Pichon & Sibuet (1981). Here layer-parallel stretching as described by Ferrill et al. (1998) can have the effect of reducing the dip of the stratigraphy. If this were to occur,

the result would be that the crust is effectively thinned as the fault blocks flatten. One of the potential problems that this would create is that the layering within the fault blocks could potentially reorientate and flatten to such a degree that they actually appear as though they may be related to the latest generation faults as the fault bedding angles would be reduced. However a potential way to tell if this flattening has occurred would be to identify faults within the hangingwall of the latest generation fault blocks (for example) and note where layering forms acute angles downdip (which would imply that a fault had initiated at very low angles of any observable early fault generations). This complication notwithstanding, OS is a very powerful identifier of the PPF mechanism and has one of the greatest preservation potentials of all of the above PPF identifiers.

The dipole PPF mechanism produces relatively simple structural geometries when compared with the monopole mechanism, potentially making it more difficult to identify on seismic data (Fig. 3.6(ii)). Neither LANFs (passively rotated faults), nor OS are predicted to occur as a result of the dipole PPF mechanism. The key to identifying the mechanism is to identify different syn-rift packages. Generally the syn-rift sediments associated with one fault generation will thicken in the opposite direction to the preceding or succeeding fault generations (Fig. 3.6(ii)). However, it should be noted that sediment compaction may reduce the prominence of this identifier and make it more subtle. Another feature of the dipole PPF mechanism is that the top basement can quite often be formed by a preceding fault generation (Fig. 3.6(ii)).

3.2.5 Progressive Crustal Extension: Fault Block Rotation

According to classical fault mechanics (Anderson, 1951), faults form when the yield stress of a rock mass is exceeded by the imposed differential stresses within the crust. Once this occurs, the rock will fail and a fault forms at some angle θ to the maximum principal stress, σ_1 – generally between 20 – 30° (depending on the frictional coefficient of the rock mass). For extensional systems, σ_1 is vertical and equal to lithostatic stress. If a newly formed fault is to accumulate large amounts of displacement, it must begin to rotate and increase its angle to σ_1, in order to reduce gravitational restoring forces acting on the uplifting footwall and subsiding hangingwall that would otherwise act to prevent extension (Forsythe, 1992). This rotation is especially important in sediment-starved rifts where gravitational instability of the footwall and hangingwall blocks can be significant, potentially resulting in degradation of the footwall via mass-wastage processes (Berger & Roberts, 1999; McLeod & Underhill, 1999).

Rotation of extensional faults forms the fundamental attribute associated with domino-style faulting (and by extension, the polyphase faulting model), and as fault dip shallows it is possible to accumulate significant extension quite rapidly (Forsythe, 1992; Buck & Lavier, 2001; Abers, 2001). The degree to which an active fault may rotate is controlled by the cohesive strength of the rock mass and the Coulomb and Byerlee failure criteria, as well as the evolving stress state of the system during progressive extension (see **Section 3.2.6**).

3.2.6 Evolving Stress Fields: Fault Mechanics and Polyphase Faulting

Reduction in fault dip through block rotation may continue up to the point where the differential stresses required for continued displacement along the fault equal those that are required to propagate a new fault. This process of “strain hardening” forces a fault to lock

and be abandoned (Agnon & Reches, 1995). The maximum rotation an active fault can achieve depends on the cohesive strength of the intact rock mass (greater cohesive strengths theoretically allow larger rotations), as well as the value of maximum confining pressure σ_1 (reducing σ_1 increases the potential rotation range, by increasing the potential reactivation range (Fig. 3.7)).

In order to properly describe the rotation of extensional faults mechanically, it is necessary to consider how the stress state evolves as extension progresses. Once a fault is formed and begins to accumulate displacement, so stretching and thinning the crust, the value of σ_1 (lithostatic stress in extensional systems) is reduced. This reduction in lithostatic stress as it turns out is quite important for facilitating the rotation of a fault to lower angles. Fig. 3.7 demonstrates the incremental evolution of two-dimensional stress field as a fault accumulates displacement. The Byerlee (1978) failure criterion (where the frictional coefficient, μ, equals 0.85 from empirical rock measurements) is key to mechanically predicting how much rotation may occur on a given fault, at a given lithostatic stress.

The key thing to note is that in each stage of Fig. 3.7 σ_1 is incrementally reduced which has the effect of increasing the possible reactivation range for fractures. This in turn allows for a fault to remain active to the lower end of permissible reactivation angles for the given stress state. For the case of Fig. 3.7(i), a fault initiating at an angle of 60° with σ_1 equal to 200 MPa may rotate and remain active to 45°. By rotating to 45° the fault stretches and thins the crust reducing σ_1 to 160 MPa, so increasing the reactivation window (Fig. 3.7(ii)).

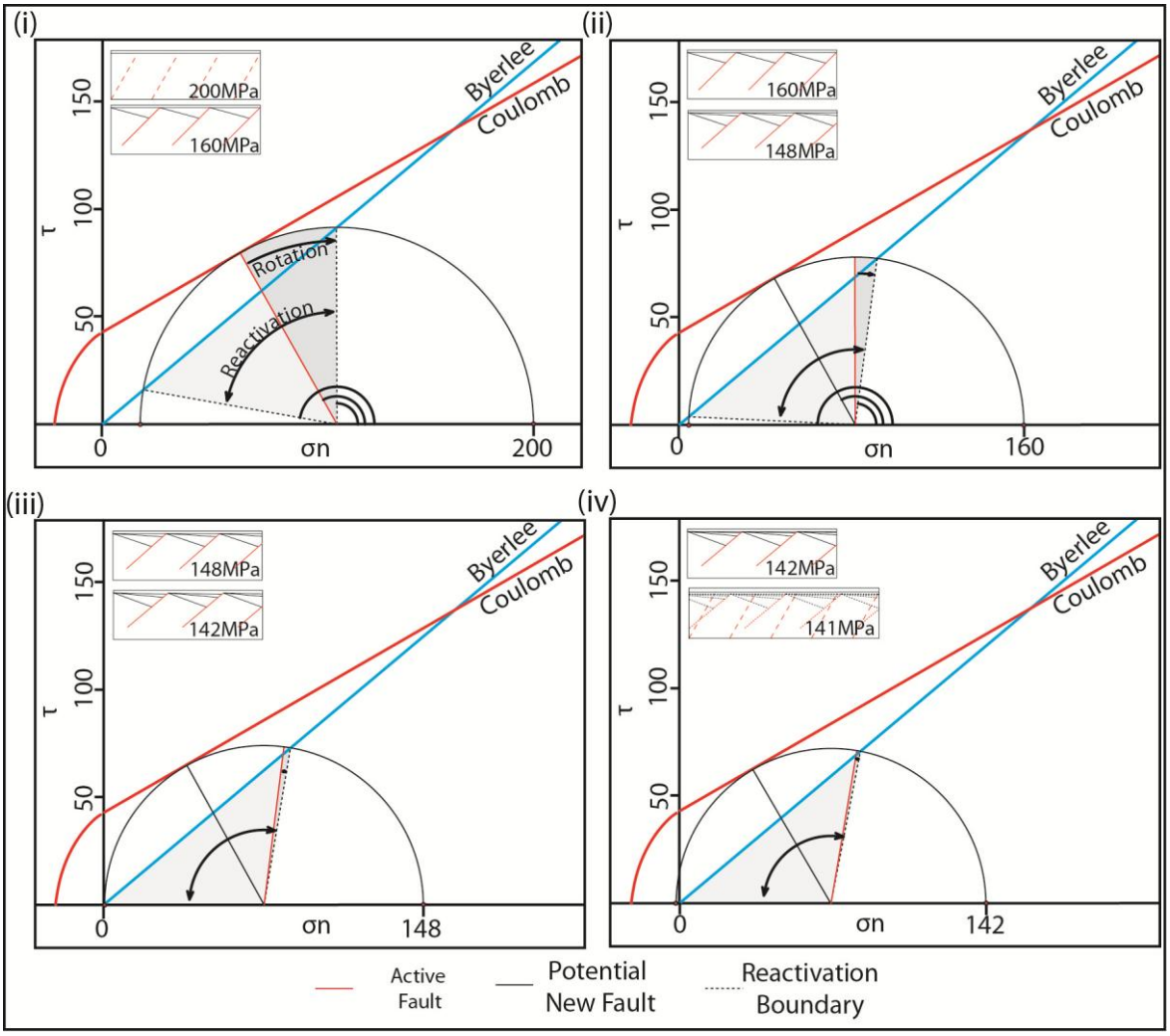

Fig. 3.7: Mohr circle diagram highlighting the criteria for normal fault rotation and reduction in lithostatic stress (σ1) as the layer is incrementally thinned (i – iv) by displacement along this fault. Rotation of fault and associated stress changes are shown incrementally and describe the full rotation range for an unfractured rock mass of cohesive equal to 45MPa. The orientation of the fault for the value of σ1 at the beginning and end of each increment is shown in the individual panels, and rotates to progressively lower angles until the differential stresses required for further displacement equal those requited to propagate a new fault, and it is abandoned, having accommodated extension of β ≈ 1.4 (see Table 1) – assuming rigid block rotation.

As there is already an extant fault present within the reactivation window of Fig. 3.7(ii) it is possible to "reactivate" this fault and continue its rotation to lower angles while simultaneously reducing σ_1. This process continues, but with every reduction in lithostatic stress increasingly smaller rotations are possible and the active fault nears its lowest

permissible active angle of 39.5° at 142MPa (Fig. 3.7(iv)). As long as regional stresses favour extensional faulting this process is capable of continuing to remain active to the point where the extant fault is equal in dip to the lowest permissible dip as determined by the reactivation range. Once this stress state occurs, the fault is abandoned (it locks up) and extension must either move to an adjacent location, or a new fault will propagate, cross-cutting the initial fault set. **Table 3.1** summarises the increments of fault rotation as the stress state evolves through progressive extension.

σ_1 (MPa)	Fault Generation	Reactivation Range (Byerlee)	Fault Rotation		Stretching β
200	1	N/A	60.0° → 45.0°	R = 15°	1.23
160	$1_{react.}$	88.0° → 41.5°	45.0° → 41.5°	R = 3.5°	1.08
148	$1_{react.}$	90.0° → 40.0°	41.5° → 40.0°	R = 1.5°	1.04
142	$1_{react.}$	90.0° → 39.5°	40.0° → 39.5°	R = 0.5°	1.01
Fault 1 locked	60.0° → 39.5°	R_{Tot} = 20.5°	β_{tot} = 1.40		$\beta_{(Distrib.\ Def)} \approx 1.96$

Table 3.1: Data extracted from Fig. 3.7 are tabulated here. Table documents the incremental rotation of the second fault generation and how with increasing rotation (and so extension) the lithostatic stress (σ_1) is reduced. Reactivation range widens and the degree of fault rotation decreases until it is abandoned. Total rotation and stretching from the first fault generations (both for the case of rigid blocks and distributed deformation) is summarised at the base of the table.

In most circumstances, a fault may rotate 15° – 30°, before it locks due to strain hardening (Agnon & Reches, 1995). A maximum of c. 20.5° of rotation, given the starting conditions, is achievable by Fault 1 before lock-up in this example (Fig. 3.7; Table 3.1). This suggests that a fault may remain active under normal circumstance to angles ≥ 30°, although it is possible to decrease the minimum active dip angle by introducing fluid overpressures (Axen, 1992), by precipitating minerals with low frictional coefficients to the fault zone, or by rotating the stress field in the locality of the fault (e.g. Parsons & Thompson, 1993).

The mechanics of faulting suggest that a fault may remain active under normal circumstances only to angles ≥ 30°, is supported by the lack of seismogenic normal faults with angles lower than c. 30° (Jackson & White, 1989; Colletini & Sibson, 2001) although slip has been observed on faults at 30° (Abers, 2001). This observation adds weight to the hypothesis that many low-angle normal faults observed onshore and on marine seismic data may have been passively rotated into position (Proffett, 1977; Reston, 2005; Axen, 2007).

3.2.7 Progressive Crustal Extension via Polyphase Faulting

Following from the example given in the previous section (Fig. 3.7), if crustal extension is to continue and remain focused in one area, it is necessary to propagate a new fault generation to accommodate the strain. As strain is localised in the extending region, the crust is thinned and lithostatic stress is reduced further.

As described in the previous section, once a fault rotates to its maximum permissible dip it will lock up and a new fault must be propagated, and in the case of Fig. 3.7 the single fault generation stretched the crust by c. $\beta = 1.40$ (assuming rigid fault block rotation) or c. $\beta = 1.96$ if distributed deformation (an additional 40% extension accommodated by small scale (fractal) structures (Walsh et al., 1991), where depending on the scale of observation the deformation could be considered to be plastic/ductile). Such distributed deformation may also flatten the faults and contribute to their rotation to low angles and eventual lock-up. Calculations (Reston, unpublished) show that distributed deformation may actually slightly reduce the total amount of extension that can be accommodated on a generation of faulting before it locks up, and that the amount of extension that can be accommodated by a single generation of faults is potentially less than that accommodated by a fully rigid system.

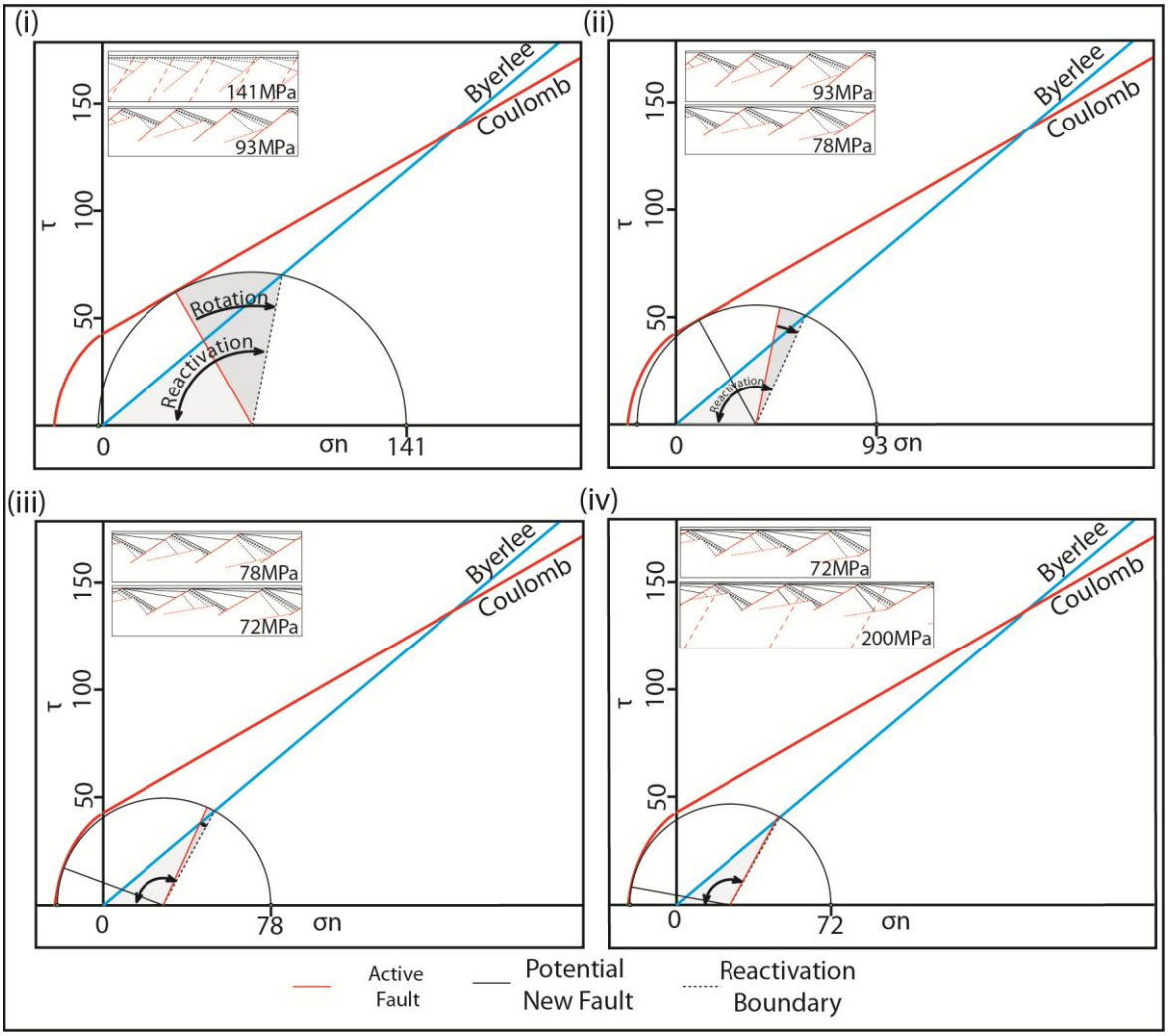

Fig. 3.8: Mohr circle diagram demonstrating the criteria for a second (succeeding) phase of normal fault rotation in a pre-stretched brittle layer (c.f. Fig. 3.7). Note further how lithostatic stress (σ_1) is further reduced as the layer is progressively (incrementally (i – iv)) thinned by extension along the second generation fault. As with Fig. 3.7 the orientation of the fault for each increment of rotation in the individual panels, and rotates, passively tilting the earlier structures that are now outside of the reactivation window, to progressively lower angles until the differential stresses required for further displacement equal those requited to propagate a new fault, and it too, is abandoned, having accommodated a total extension of $\beta \approx 2.8$ (see Table 3.2) – assuming rigid block rotation.

If a second fault is considered to propagate cross-cutting Fig. 3.7, a larger rotation range is possible in Fig. 3.8, than was possible for Fig. 3.7, due to the reduction in the confining stresses and an enlarged reactivation range (Fig. 3.8; Table 3.2).

Fault rotation occurs in the same manner as in **Section 3.2.6** before the second generation fault is abandoned. Following lock-up of Fault 2 at c. β = 2.00 (rigid block rotation), or at c. β = 2.80 (including 40% distributed deformation) (Table 3.2).

σ_1 (MPa)	Fault Generation	Reactivation Range (Byerlee)	Fault Rotation		Stretching β
141	2	90.0° → 39.5°	60.0° → 39.5°	R = 20.5°	1.52
93	$2_{react.}$	90.0° → 33.0°	39.5° → 33.0°	R = 6.5°	1.20
78	$2_{react.}$	90.0° → 30.5°	33.0° → 30.5°	R = 2.5°	1.08
72	$2_{react.}$	90.0° → 30.0°	30.5° → 30.0°	R = 0.5°	1.02
Fault 2 locked	60.0° → 30.0°	R_{Tot} = 30°	β_{tot} = 2.00		$\beta_{(Distrib.\ Def)}$ ≈ 2.8
β_{F1+F2} = 2.80	$\beta_{(Distrib.\ Def)}$ ≈ 5.5	Crustal Embrittlement & Mantle Serpentinisation at β = 3			

Table 3.2: Data extracted from Fig. 3.8 are tabulated here. Table documents the incremental rotation of the second fault generation and how with increasing rotation (and so extension) the lithostatic stress (σ_1) is reduced, the reactivation range widens and the amount of incremental fault rotation decreases to the point at which it is abandoned. The total rotation and stretching of the second fault generation, as well as the product of the stretching from both the first and second fault generations (both for the case of rigid blocks and distributed deformation) is summarised at the base.

The total stretching of the system at this point is the product of stretching for each separate fault generation, i.e. β ≈ 2.80 for rigid rotation and β ≈ 5.50 including 40% distributed deformation (Table 3.2). It is important to note that 40% is a maximum amount and in reality, this is likely to be far lower.

Assuming an initial crustal thickness of 30 km prior to the initiation of stretching then, by the time the second fault set has been abandoned (in the rigid fault block scenario), the crust will have thinned to c. 10.7 km (β = 2.80), increasing the thickness of the brittle layer, and so the lithostatic stress. Total crustal embrittlement may initiate at c. β = 3 (the lower end of the range over which embrittlement is predicted to occur for an aggregate lower crust (Pérez-Gussinyé & Reston, 2001)). So, if the crust is taken to deform entirely via brittle mechanisms, allowing fluids to penetrate down to the mantle and begin the process of serpentinisation by β = 3, then the third generation fault set need only rotate c. 4° before

embrittlement occurs (Fig. 3.9; **Table 3.3**). Once crustal embrittlement is achieved, the fault rotation criteria changes. The lowest angle to which a fault can rotate is no longer controlled by the frictional coefficient of fractured rock (c.f. Byerlee (1978) failure criterion), but instead by the frictional coefficient of serpentine (Fig. 3.9(ii)), which may now be available to lubricate the fault system due to the initiation of partial mantle serpentinisation.

In Fig. 3.9 the third fault generation effectively forms the precursor to a serpentinite detachment fault system, and is capable of rotating to as low as c. 22° (assuming no fluid overpressure, and rigid block rotation) (Fig. 3.9(v); **Table 3.3**). $\beta \approx 5.6$ may be achievable with only three phases of faulting, thinning the crust to only c. 5.4km. By introducing a transient fluid overpressure (along sealed faults, which prevent hydro-fracturing of the hangingwall), it is possible to reduce the active fault dip to c. 13° (Reston et al., 2007). Fluid overpressure is likely to be transient in a normal fault zone over geologically short timescales (Townend & Zoback, 2000; Zoback and Townend, 2001) but observations from exhumed normal fault zones show that fault valve action and lateral migration of fluid overpressure along strike of a fault zone may be important for regulating the fluid pressure (Sibson, 2000). Reston et al. (2007) have calculated that if sealing of hangingwall fractures can maintain a cohesive strength of 20MPa a Pf of 15MPa may develop and allow very low angle slip on a serpentinite detachment fault.

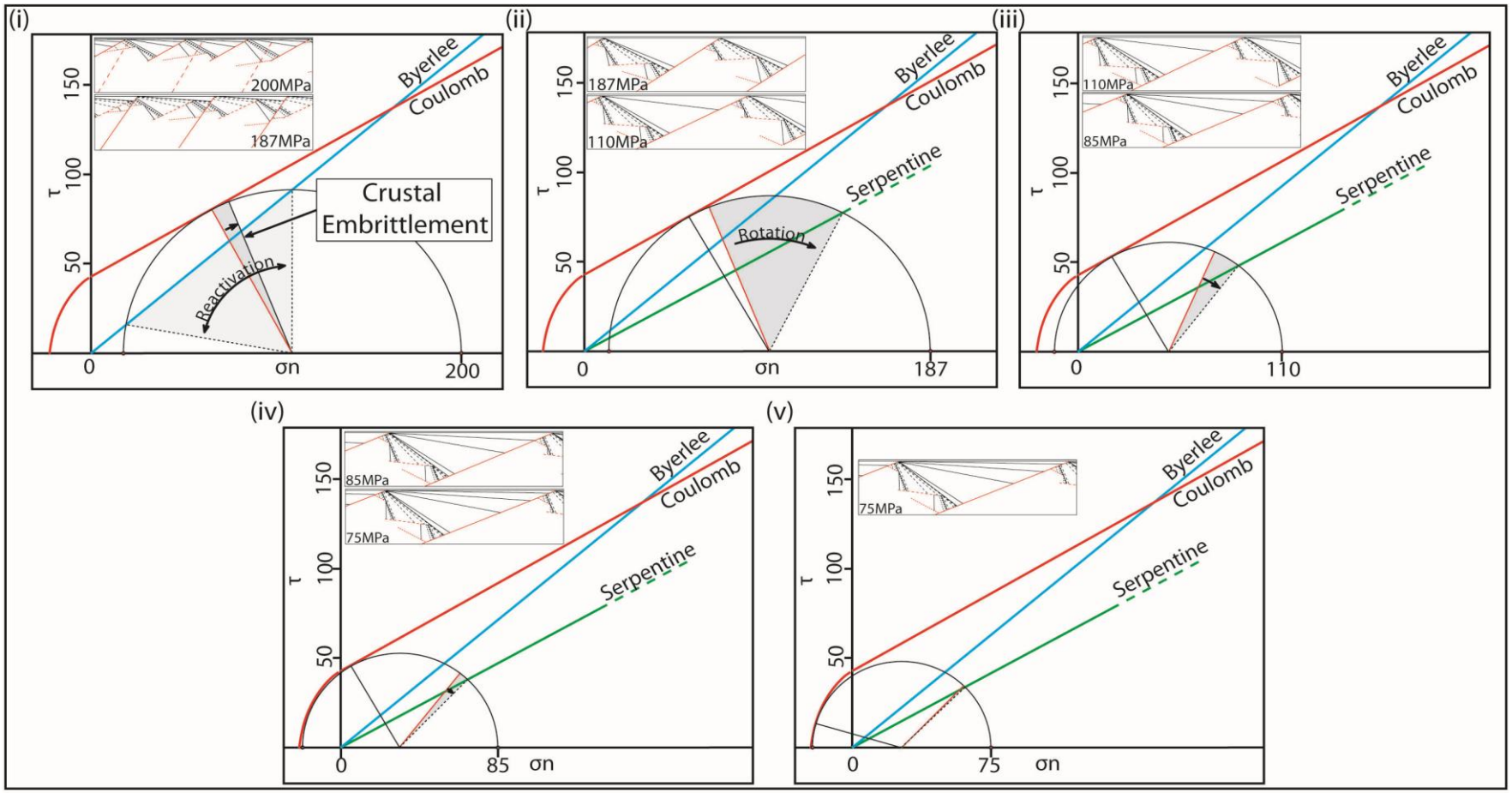

Fig. 3.9: Following from Fig. 3.8, a third fault generation is propagated, but in this case crustal embrittlement and mantle serpentinisation is assumed to occur at β ≈ 3. (i) 4° of fault rotation (see Table 3) is necessary to achieve crustal embrittlement and create fluid conduits to the mantle to begin serpentinisation process allowing serpentine to be precipitated along the fault. (ii – iv) Minimum angle of fault activity is now controlled by frictional coefficient of serpentine (μ = 0.3). The fault is now effectively, a serpentinite detachments, and as it rotates it passively rotates structures from Fig. 3.8, overturning the first generation faults. (v) The third fault generation is abandoned at a minimum dip of 22° (where with no elevated fluid pressures are present). The three fault generations having accommodated β ≈ 5.6 (see Table 3.3).

σ_1 (MPa)	Fault Generation	Reactivation Range (Byerlee)	Fault Rotation		Stretching β
200	3	N/A	60.0° → 56.0°	R = 4°	1.07
187	$3_{react.}$	85.0° → 44.5°	56.0° → 33.0°	R = 23°	1.70
110	$3_{react.}$	85.5° → 44.0°	33.0° → 26.0°	R = 7°	1.30
85	$3_{react.}$	90.0° → 35.5°	26.0° → 23.0°	R = 3°	1.13
75	$3_{react.}$	90.0° → 31.0°	23.0° → 22.0°	R = 1°	1.05
Fault 3 locked	60.0° → 30.0°	R_{Tot} = 30°	β_{tot} = 2.00		$\beta_{(Distrib.\ Def)} \approx 2.8$
		$\beta_{F1+F2+F3}$ = 5.6	$\beta_{(Distrib.\ Def)} \approx 15.4$		

Table 3.3: Data extracted from Fig. 3.9 are tabulated here. Table documents the incremental rotation of the third fault generation (crustal embrittlement is assumed to have occurred at 187MPa) and how with increasing rotation (and so extension) the lithostatic stress (σ_1) is reduced, the reactivation range widens and the amount of incremental fault rotation decreases to the point at which it is abandoned. The total rotation and stretching accommodated by the third fault generation, as well as the product of the stretching from all three fault generations (both for the case of rigid blocks and distributed deformation) is summarised at the base.

From the model presented above, it could be suggested that if the lower crust is relatively strong and cold, it is possible to focus extension along a low-angle serpentinite detachment system without needing to initially thin the crust over more than 2 fault generations (e.g. Figs 3.7 & 3.8). The remaining crustal strain will likely be strongly focused along this serpentinite detachment system (Fig. 3.9). Alternatively, if the lower crust is composed of hotter, relatively weak material, total crustal embrittlement and partial mantle serpentinisation will require crustal thinning over more fault generations before total embrittlement is achieved (e.g. the Woodlark Basin (Pérez-Gussinyé & Reston, 2001)).

3.2.8 Mechanical feasibility of Dipole Polyphase Faulting

When a succeeding fault initiates it can propagate either synthetically or antithetically to the first fault set (Fig. 3.5b), provided there are no regional stress rotations. Synthetically propagating, or mono-pole polyphase faulting is the simplest case, its mechanics are discussed above. Following abandonment of the original fault set, a new fault with opposite polarity to the first (if propagated) would rotate the original in the opposite direction to the

first fault generation, and re-orientate and steepen the original fault sets, potentially returning them to the zone of reactivation, and possibly allowing displacement to resume on the original fault set. It is also possible that both fault sets will oppose the motion of the other at a certain point, leading to strain hardening, and further faulting may either propagate through this system or migrate away from it.

Fig. 3.10 demonstrates the mechanical feasibility of the dipole (see-saw) mechanism for the situation immediately following lock-up of the first fault generation at c. 38° (Fig. 3.7). In Fig. 3.10(i), faults are considered to have no cohesive strength (Byerlee, 1978). In this example the second fault generation can be active at c. 60°; however, due to the assumed lack of cohesion on the first generation fault (now at low-angle) rotation of the second generation fault would passively rotate the first generation fault back into the reactivation window, causing both faults to be active simultaneously. The opposing rotation that would result from the active faults causes the whole system to lock due to strain hardening, forcing either new faults to be propagated through the locked system or the focus of extension to be relocated. The suggestion from Fig. 10(i) is that the see-saw model as described in **Section 3.2.3** is not mechanically feasible. However, Tommasso et al. (2008) reported a form of the dipole PPF model from the northern North Sea (Fig. 3.11) demonstrating that the mechanism must be feasible in nature. The first fault phase (Fig. 3.11) is abandoned at 35°, and the latest fault phase was active at high-angle, with some degree of rotation (although there is a significant portion of the displacement that is vertical). The identification of a dipole fault system by Tommasso et al. (2008) demonstrates that the mechanism is feasible.

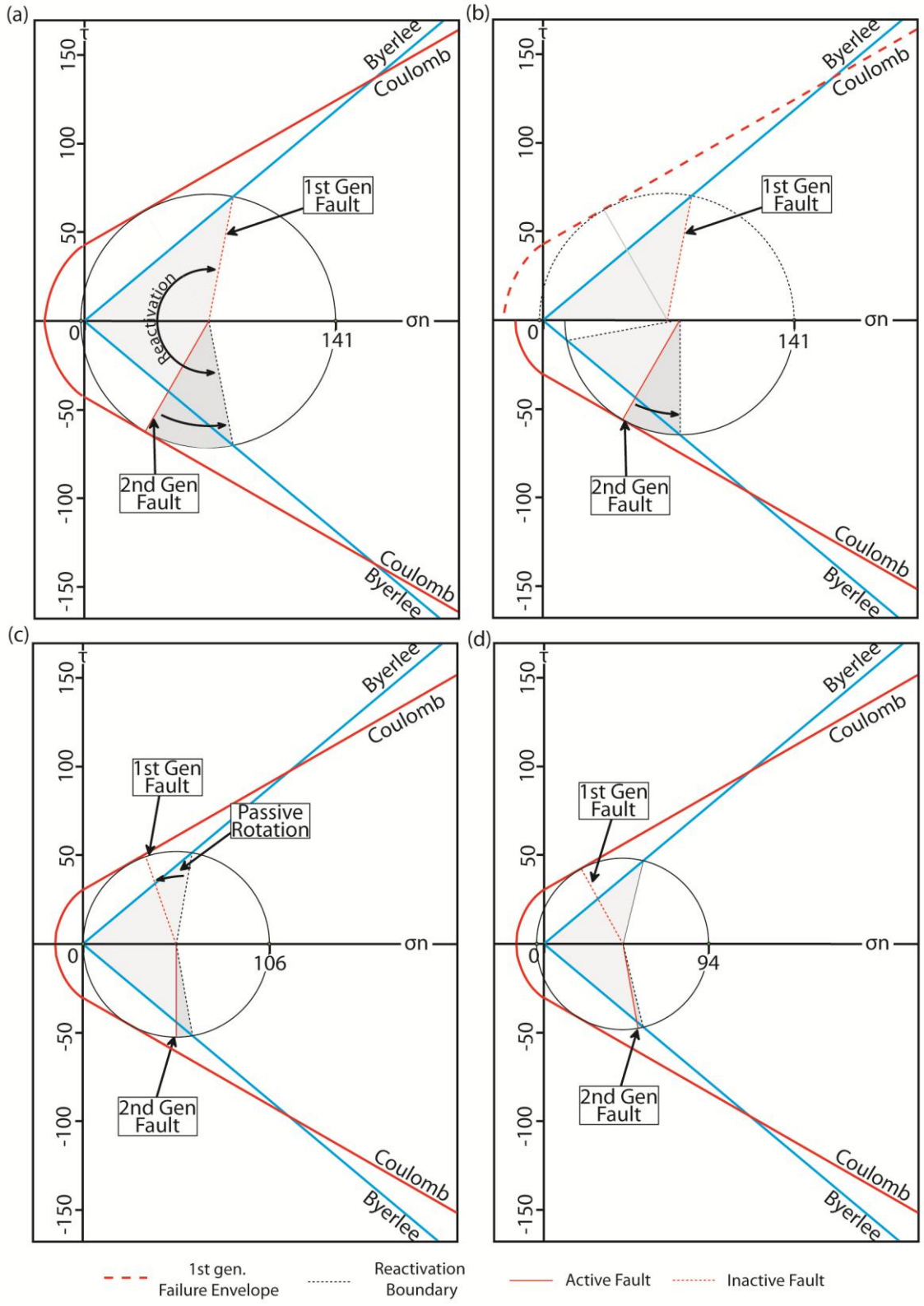

Fig. 3.10: Mohr circle demonstrating criteria for normal faulting in a Dipole PPF system. (i) In this example faults, regardless of age, are assumed to have no cohesive strength. First generation fault has reached lowest permissible rotation and has been abandoned (c.f. Fig. 3.7). A second fault generation propagates with opposite polarity. Any rotation of the second generation fault re-orientates the first, putting into the

reactivation window causing both faults to be active simultaneously with opposing motions leading to lock up of whole system. (ii) First generation fault has undergone fracture healing, and strengthening, resulting in reduction of the rock mass's overall strength to that of the fault. The second generation fault is propagated and begins to steepen the original fault, but it is not reactivated. (iii) Reduction in σ1 due to stretching allows further rotation of fault. (iv) Second generation fault locks following completion of final rotation increment. First generation fault is not perfectly orientated to become reactivated, initiating a see-saw system (provided the second generation fault regains some strength from crack healing

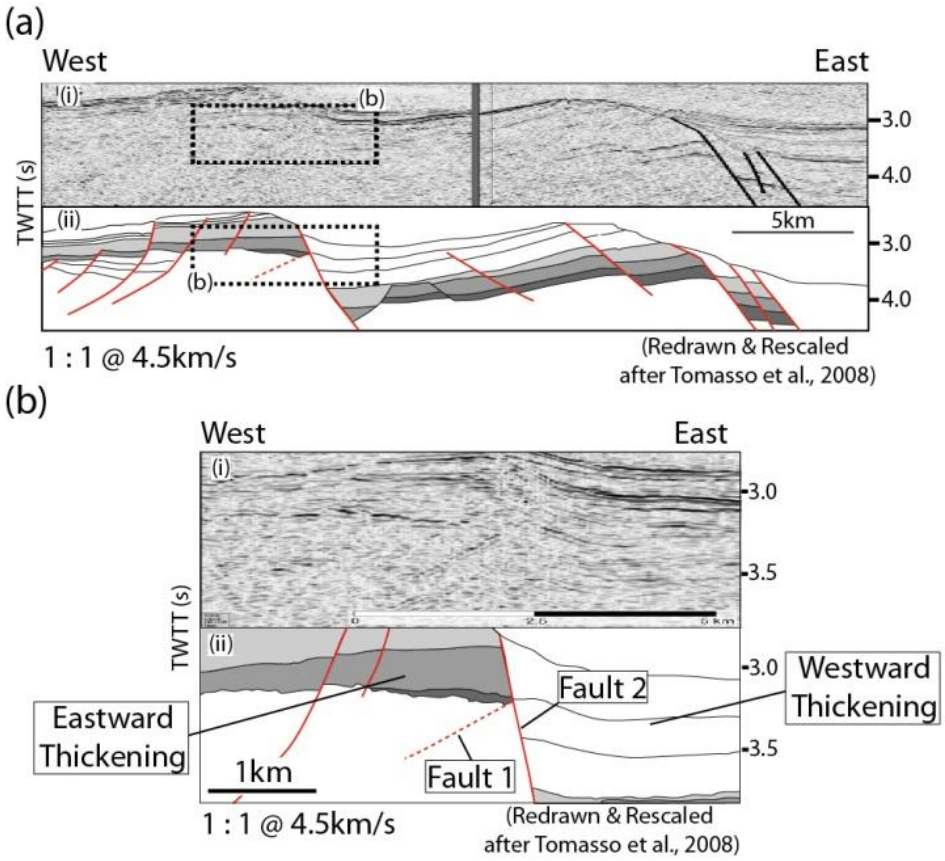

Fig. 3.11: taken and redrawn from Tommasso et al., 2008 showing a seismic example of the dipole PPF mechanism from the North Sea. Seismic data and interpretation are redrawn, and rescaled in order to pseudo-depth migrate the structures. (a) It can be seen clearly that fault 1, is orientated at a low-angle and is cut by the much higher angle late stage, oppositely dipping fault. (b) note opposite directions of thickening for the fault's associated sediments. A small degree of fault rotation has occurred on the later fault generation (labelled fault 2), potentially supporting the predictions made in Fig. 3.8(ii – iv). The majority of displacement appears to be vertical. It is possible that sediment deposition kept pace with space generation and may have mitigated the gravitational restoring forces (Forsythe, 1992) that otherwise would require the fault to rotate to a greater degree.

In order for the mechanics of a dipole fault system to work the original fault must regain strength so it will not fail the instant displacement occurs on the latest fault generation. It

has been noted by a number of authors that fracture healing, or crack sealing of faults can occur during the interseismic period along faults, through mineral precipitation and gouge/damage zone compaction (Reynard et al., 2000; Tenthorey et al., 2003; Tenthorey & Cox, 2006), allowing a fault to regain cohesive strength to perhaps 30 MPa (Tenthorey et al., 2003). To account for the renewed cohesive strength of the first generation fault, the failure envelope in Fig. 3.10(ii – iv) intersects the shear stress axis at 30 MPa. The original unfractured rock mass had a cohesive strength of 45 MPa, and defined the original Coulomb failure envelope (Figs. 3.7 – 3.9). As discussed previously, reducing the cohesive strength of the rock mass also has the effect of reducing the maximum rotation attainable by a given fault within it. Although the second fault generation is orientated within the reactivation window for the duration of second generation fault rotation, reactivation of the first generation fault will not occur until the second generation has locked. This is because while the second fault generation is active it has zero cohesive strength, so displacement will naturally occur along this structure rather than through reactivation of the older structure. Once frictional lock-up of the second generation fault occurs, and provided it has sufficient time to regain strength, continued extension in the system will be accommodated by the reactivated first generation fault, which will begin to rotate the system in the original direction. This will only occur provided extensional forces remain active on the system and the stress orientations remain the same. Fig. 3.10(ii – iv) and Table 3.4 only consider the motion of the second generation fault as it re-orientates the first generation fault. It can be envisaged that this process can occur at infinitum, or until the point at which the crust becomes embrittled and serpentinite detachments initiate.

σ1 (MPa)	Fault Gen.	Reactivation Range (Byerlee)	Fault Rotation	Stretching (β)
141	2	85.0° → 45.0°	60.0° → 45.0° R = 15°	1.33
106	2react.	90.0° → 40.0°	450° → 40.0° R = 5°	1.13
94	2react.	90.0° → 38.0°	40.0° → 38.0° R = 2°	1.05
Fault 2 Locked		60.0° → 38.0° Rtot = 28°	βtot = 1.6	β(Distrib. Def) ≈
		βF1+F2 = 2.24 β(Distrib. Def) ≈ 4.4		

Table 3.4: Data extracted from Fig. 3.10 are tabulated here. Table documents the incremental rotation of the second fault generation in the dipole PPF mechanism. Here, only the second fault generation is considered, following on from the locking of the first fault generation (Fig. 3.7; **Table 3.1**). The data show that with increasing rotation (extension), lithostatic stress (σ1) is reduced, reactivation range widens and the value of each incremental fault rotation decreases to the point at which it is abandoned.

For these models I have only addressed the simple two dimensional case in order to illustrate the concept of polyphase faulting. However, it is possible that in nature that successive generations of faults may strike at some angle to the original fault generation. If this were to happen either for the monopole or dipole variant of the mechanism the preceding fault generation would likely be reactivated as a modified transfer system (Henza et al., 2009).

The simple models presented here assume that the crust is isotropic (unfaulted and unfractured) which in reality is not the case. As such, the form that polyphase faulting will take will be more complicated than the simple model described here because of crustal anisotropy. Instead the models presented here serve to demonstrate the theoretical basis for the polyphase faulting concept and the sorts of geometries that would be indicative of the mechanism.

3.3 Onshore Examples of Polyphase Faulting

There are several published onshore examples of extensional polyphase faulting. Many are from the western USA (Proffett, 1977; Chamberlin, 1982; Proffett & Dilles, 1984), but examples from the Eastern Betic Cordillera, SE Spain, where polyphase detachment faulting has been interpreted (Booth-Rea et al., 2002; Booth-Rea et al., 2004), are also discussed in this section. Here, some of the classic structural sections are revisited and shown to consist of some variation on the monopole PPF models discussed in **Section 3.2.** Simple palinspastic reconstructions of a selection of published structural sections (Proffett, 1977; Chamberlin, 1982; Proffett & Dilles, 1984) demonstrate how a lot of extensional strain can be accommodated by the PPF mechanism. For each of the sections (Figs. 3.12 – 3.15) β values are estimated for each intermediate step between unstretched and stretched – mainly for illustrative purposes only due to uncertainties in the dips at which each fault generation initiated, as such the final stretching value is the most robust.

The onshore examples are useful as their structural expression produces geometries very similar to those predicted by the conceptual models in **Section 3.2**, and to those that might be expected to stretch the crust to the point of embrittlement at MPRMs. The driving force behind the extension in these regions cannot be directly compared to that which drives extension at MPRMs, however, since the tectonic setting and rheological structure are very different. Fundamentally, despite large local amounts of extension, the onshore examples remain above sea level requiring very thick initial crust or significant lateral flow and/or magmatic addition to maintain crustal thickness (e.g. Buck, 1991).

3.3.1 Polyphase Faulting in the W. Basin & Range Provence

Proffett (1977) and Proffett and Dilles (1984) present a detailed geological map of the Yerington District, Nevada, as well as a number of structural cross-sections, based on fault geometries and relationships observed by of the work of Proffett (1977), showing multiple generations of cross-cutting faults extending the upper crust.

Figs 3.12 & 3.13 show reversed palinspastic restorations of the cross-sections presented by Proffett (1977) (Proffet & Dilles (1984) "Section D") and Proffett & Dilles (1984) "Section A", respectively. These restorations demonstrate the evolution of the structures in the published cross-sections. The Yerrington region is shown to have undergone very large amounts of extensional strain, c. 170% extension for Fig. 3.12, and c. 138% extension for Fig. 3.13.

The strain in both sections is accommodated by multiple, successive phases of normal faulting that have passively rotated earlier faulting phases to very low-angles (Proffett, 1977). For the purposes of the restorations it has been necessary to reconstruct the faults in multiple stages (due to the similarity of fault angles and the sequential nature of the faulting); as such the fault phases present in the restorations are more properly considered phases of movement rather than discrete fault generations. In general there appears to have been 3 – 4 separate fault generations (Fig. 3.13 & 3.12) that have accommodated the strain, with the majority of the extension being accommodated by Phase 2 & 3 (Fig. 3.12). It may be more appropriate to consider these phases (2 & 3) as one due to the similarity of fault orientations (see Fig. 3.12). Phase 1 (Fig. 3.13) should probably be most appropriately considered as Phase two in the regional extension since the first faulting phase responsible

for initial tilting of the fault block does not appear in the section and is likely some distance to the west (Fig 3.13).

The amount of extension calculated from the palinspastic restorations (Figs 3.12 & 3.13) is likely to be an underestimate, as the fault blocks have been treated rigidly with no internal deformation (c.f. Walsh et al., 1991) and layer parallel shear (Ferril et al., 1998) is not considered. Also uncertainties due to an incomplete stratigraphy contribute to the underestimations.

Figs 3.12 & 3.13 clearly show how the extensional system may have evolved, with faults propagating at initially high-angles, rotating (sometimes with dome evidence of flexural rotation and splay faulting in the shallower parts of the active faults (Fig. 3.12 – Phase 2), and agrees with the mechanism proposed by Proffett (1977) for the formation of low-angle normal faults, via the process of passive rotation by later fault generations.

It appears from the restorations that an initially quite simple tilted fault block system was dissected thoroughly by later fault generations as the original faults were abandoned. Reston & Pérez-Gussinyé (2007) proposed a similar mechanism for the formation of the hangingwall blocks above the S Detachment at the W. Galicia Margin. The dissection of the original fault block has produced very complex fault relationships, as can be seen in the final sections of Figs 3.12 & 3.13. In some cases, these fault relationships are further complicated due to the existence of early antithetic faults that have since been passively rotated and now have the appearance of reverse faults Fig. 3.12, Phase 5).

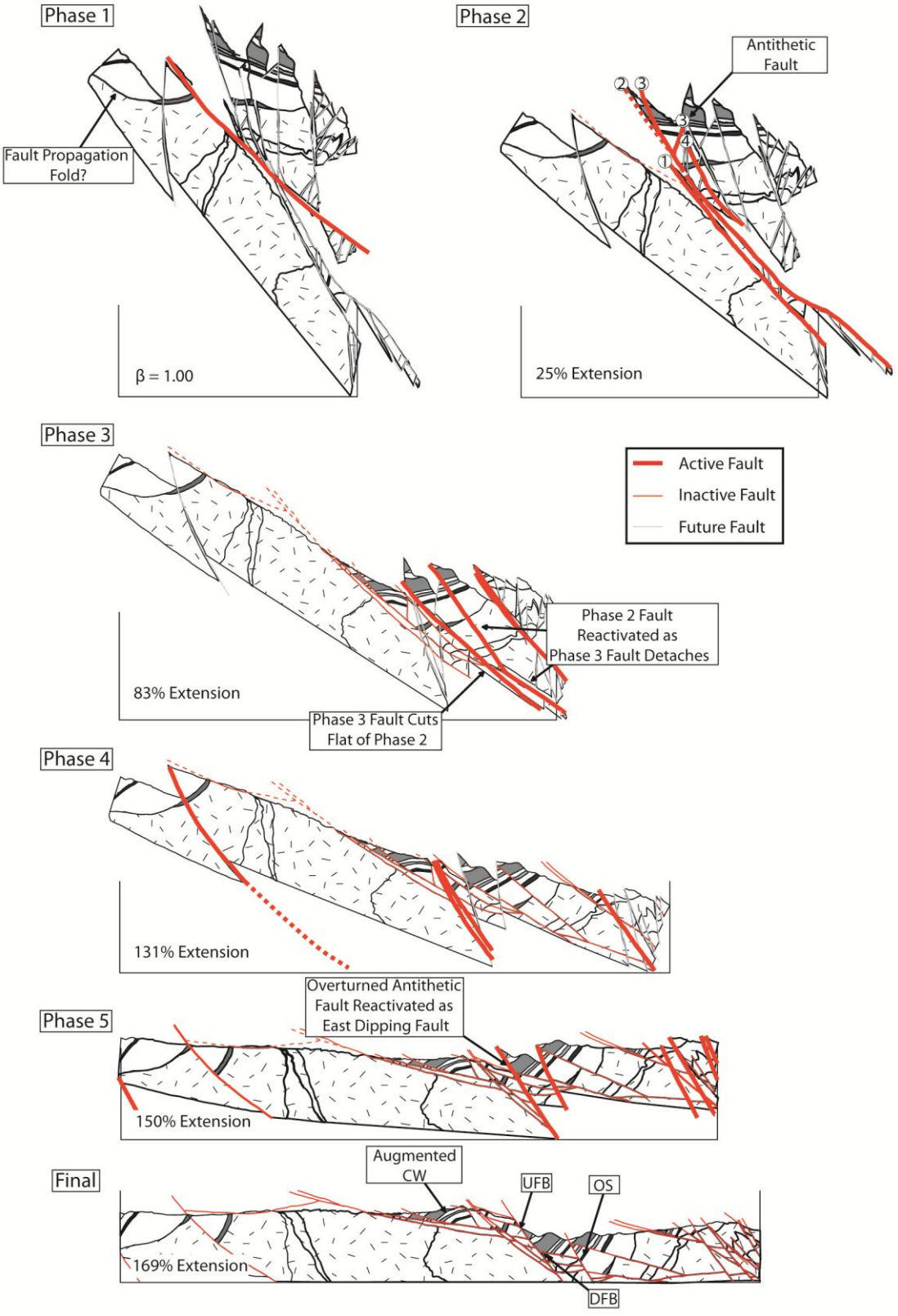
Phase 1
Fault Propagation Fold?
β = 1.00
Phase 2
Antithetic Fault
25% Extension
Phase 3
Active Fault
Inactive Fault
Future Fault
Phase 2 Fault Reactivated as Phase 3 Fault Detaches
83% Extension
Phase 3 Fault Cuts Flat of Phase 2
Phase 4
131% Extension
Overturned Antithetic Fault Reactivated as East Dipping Fault
Phase 5
150% Extension
Augmented CW
UFB
OS
Final
169% Extension
DFB

Fig. 3.12: Reversed palinspastic restoration of the classic cross-section presented by Proffet (1977) ("Section D" from Proffett & Dilles (1984)) showing the evolution of the structures in the published section. 169% extension has been achieved over (apparently) five separate fault generations of cross-cutting faults. The majority of the extension has been accommodated by fault Phases 2 & 3. Note the complex structure produced following the faulting, particularly the reactivation of a rotated antithetic fault formed in Phase 2, in Phase 5. A number of the PPF identifiers described in Fig. 3.6 are exhibited in the final stage of the restoration.

In fact, the potential antithetic fault (suggested from possible stratigraphic thickening towards it) associated with the earliest fault generation (Fig. 3.13, Phase 1) has, following passive rotation and the resulting change in polarity, become reactivated with normal sense of shear (Fig. 3.13, Phase 3). This early (potential) antithetic fault then appears to form one of the latest generation faults in the section and is seen to offset its original master fault. This interpretation is based on the restoration and assumes that the cross-section presented by Proffett & Dilles (1984) is accurate and correct. The fact that the reorientated and subsequently reactivated antithetic fault appears to propagate downwards is curious since in general terms tectonically controlled faults tend to propagate upwards rather than downward (John J. Walsh, pers. comm.). It is perhaps coincidence that a propagating fault met the (by the time of Phase 3) suitably orientated (originally antithetic) fault and caused reactivation same. To properly distinguish between whether the fault did indeed propagate downwards or upwards it is necessary to identify in which direction displacement appears to die out (i.e. if a fault propagates upwards then displacement should reduce up dip, and vice versa). In this cross-section it is not possible to identify the direction in which displacement dies out. Proffett (1977) states that many of the faults were likely slightly concave-up in geometry originally and that internal fault block deformation resulting from displacement on

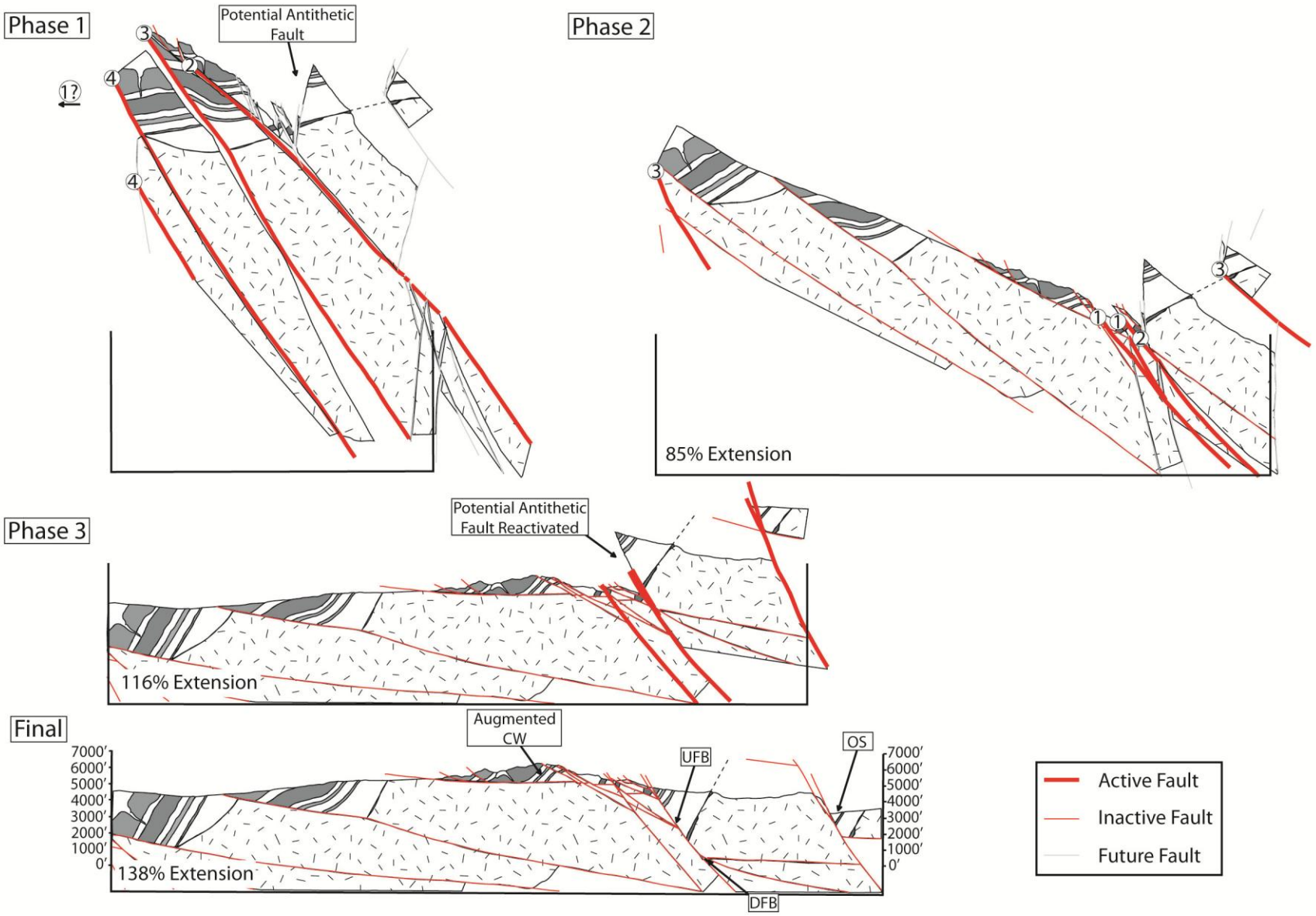
Phase 1
Potential Antithetic Fault
Phase 2
85% Extension
Phase 3
Potential Antithetic Fault Reactivated
116% Extension
Final
Augmented CW
UFB
OS
DFB
138% Extension
7000′
6000′
5000′
4000′
3000′
2000′
1000′
0′
Active Fault
Inactive Fault
Future Fault

Fig. 3.13: Reversed palinspastic restoration showing the evolution of "Section A" (Proffett & Dilles, 1984). The section is extended by 138 % over up to four fault generations. Restoration of the section is completed for the basement; however, restored displacement on the three fault phases present in the section does not restore the basement to horizontal. This is suggestive of another fault set west of the section tilting the fault block (Phase 1). Some faults in Phase 1 & 2 were active sequentially (numbered) while some were active simultaneously. Fault "3" in Phase 1 can be seen to be convex-up, suggesting that there may be some element of flexural rotation of the footwall during extension. The final section shows the published cross-section, and the geometries that have been produced following three cross-cutting fault sets. Some PPF identifiers (Fig. 3.6) are labelled.

the later fault generations has augmented the original faults resulting in more planar to convex-up geometries. This may be one of the reasons as to why there are large gaps in the unfaulted restorations (Figs 3.12 & 3.13).

The mode of extension here is slightly different to that in the Lemitar Mountains where it appears that a rolling-hinge style mechanism may have been at work with shallowly dipping faults becoming abandoned in favour of faults with steep dip.

3.3.2 Polyphase Faulting in the Rio Grande Rift

Additional examples of polyphase faulting that are observable come from the geological cross-sections constructed by Chamberlin (1982) from the Lemitar Mountains, New Mexico. Cross-sections presented by Chamberlin (1982) demonstrate complex extensional faulting relationships and although extensional strain is not as high as in the W. Basin and Range (Figs 3.12 & 3.13) it is still significant.

Figs. 3.14 & 3.15 show reversed palinspastic restorations of "Section A" and "Section D" as presented by Chamberlin (1982), and demonstrate the evolution of the structures. The sections have accommodated extensional strain of c. 83%, and c. 72%, respectively. Although these levels of strain are possible to achieve with only one generation of faulting

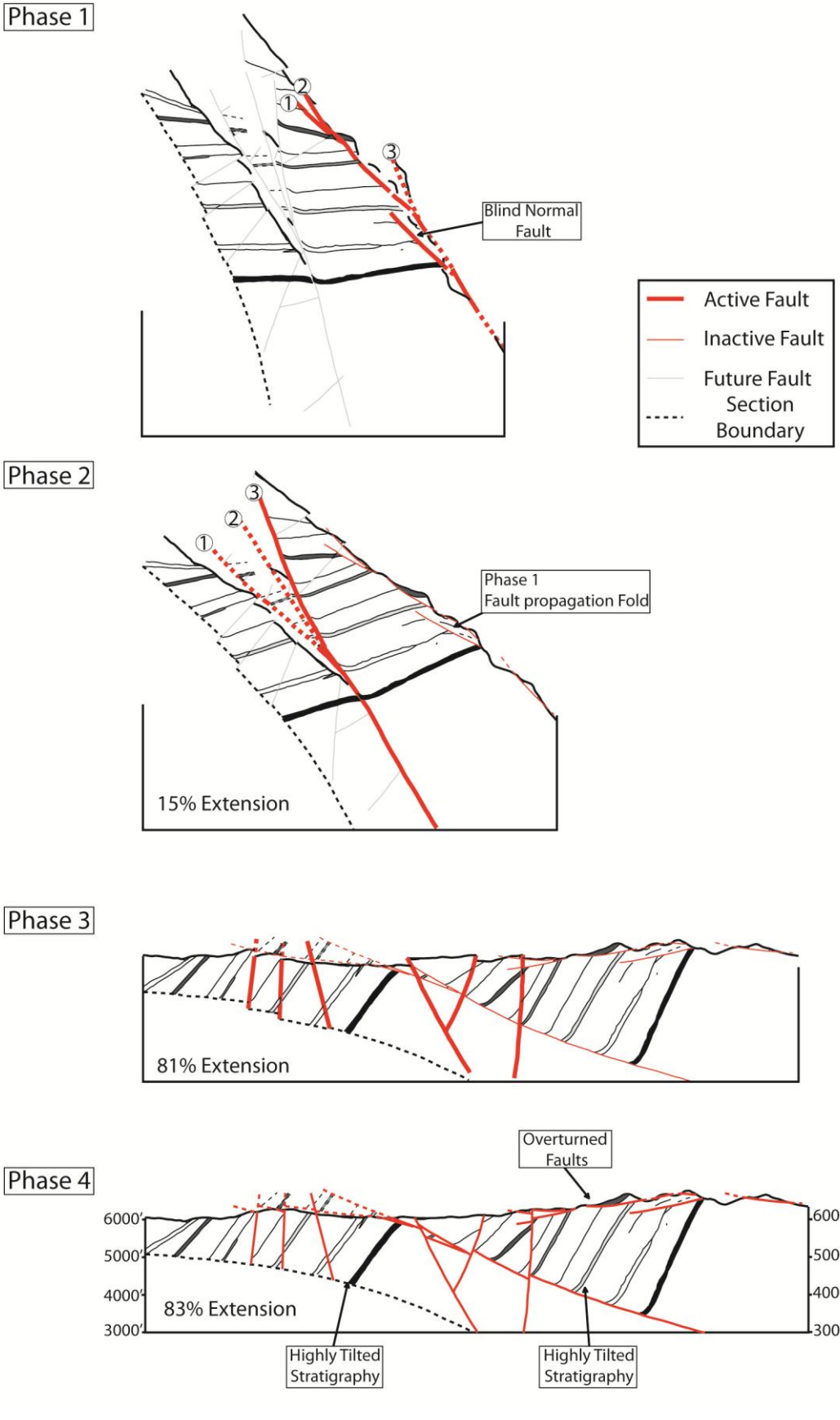
Phase 1
Blind Normal Fault
Active Fault
Inactive Fault
Future Fault
Section Boundary
Phase 2
Phase 1
Fault propagation Fold
15% Extension
Phase 3
81% Extension
Phase 4
Overturned Faults
6000′
5000′
4000′
3000′
83% Extension
Highly Tilted Stratigraphy
Highly Tilted Stratigraphy

Fig. 3.14: Reversed palinspastic restoration of Chamberlin (1982)'s "Section A". Evolution of the structures over three fault generations. Each fault phase is shown in the configuration where faults become active – extension estimates are the for the beginning of each phase (i.e. in Phase 2, before the faults move there is 15% stretching resulting from Phase 2 of faulting). Numbered faults show where fault system appears to be rolling-hinge-like, and the root zone is active throughout faulting phase and the shallower splays are active sequentially. The final section demonstrates some of the PPF identifiers shown in Fig. 3.6

(c.f. **Table 3.1/3.2**; Jackson & White, 1989), it has been accommodated in these examples (Figs 3.13 & 3.15) by 3 – 4 faulting phases.

The style of faulting for the Lemitar region appears to be slightly different to that in the Yerington region (Figs 3.12 & 3.13). This is especially evident in Fig. 3.14, where it appears that the early faults accumulated displacement in a similar way to a rolling-hinge system, accommodating c. 15% extension, where the root of the master fault deeper in the section has a number of splays faults closer to the surface. The uplifting footwall appears to have been undergoing (possible) flexural rotation (Fig. 3.14, Phase 1) with splay faults being active (and later abandoned) sequentially towards the hangingwall and rooting on a relatively steep master fault deeper in the section. It is likely that this fault phase is an original block bounding fault, and it might be expected that there is another fault of similar style and offset further to the west but is not sampled in the section. In contrast, there is not enough information in the restoration of Fig. 3.15 to suggest whether or not the first fault set acted as a rolling-hinge style but has only facilitated only c. 8% extension on apparently widely spaced fault sets tilting stratigraphy.

As was the case in Figs 3.12 & 3.13, the second faulting phase (Figs 3.14 & 3.15) appears to have been responsible for the majority of the stretching, $\beta \approx 1.66$ in Fig. 3.14, and c. $\beta \approx 1.50$ (or c. $\beta \approx 1.61$ if Phase 2 & 3 of the restoration are considered as one fault generation) in Fig.

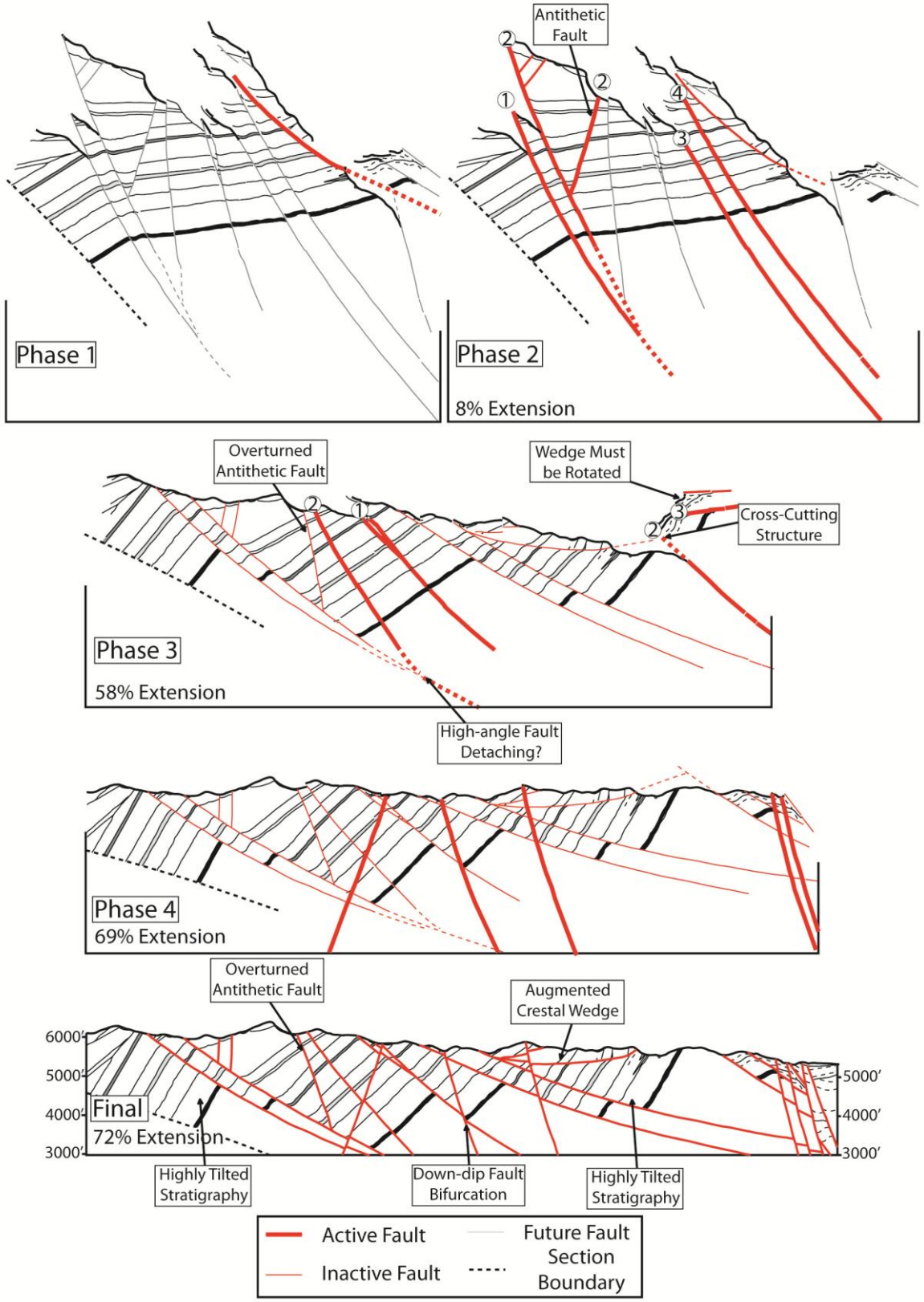

Fig. 3.15: Reversed palinspastic restoration of Chamberlin (1982)'s "Section D" showing the evolution of the structures in the published cross-section over four fault generations. Each phase of faulting is shown before they accumulate displacement and the resulting displacement can be seen when the succeeding fault phase

becomes active. Stretching values reflect stretching suffered by the section immediately before new fault activity. The majority of stretching has occurred during the second phase of faulting. The final section is further complicated by the presence of overturned antithetic (apparently reverse) faults. The final section demonstrates some of the PPF identifiers shown in Fig. 3.6.

3.15. The second fault generation of Fig. 3.14 appears to accommodate displacement in the rolling-hinge style also, and may have continued until the root zone reached a dip of c. 30°, with rotation of the second fault system apparently passively rotating the first generation faults (as was the case in Figs 3.12 & 3.13) faults and their associated structures for to the point where the first generation faults are sub-horizontal to overturned. (Fig. 3.14, Phase 2). In Fig. 3.15, Phase 1 faults were succeeded by a closely spaced fault set that dissected the original fault block and, as with the faults system in Fig. 3.14, it appears that these faults were sequentially active from west to east. It is not clear, however, if the Phase 2 faults were active as a rolling-hinge style system (as seems to be the case in Fig. 3.14), as they do not appear to converge at depth. It should be noted, however, that the Phase 2 & 3 faults were separated because presentation of the structural evolution clearer. It may be more appropriate to consider Phases 2 & 3 of Fig. 3.15 as the second fault generation. It is not clear whether westernmost active fault of Phase 3 cross-cuts the Phase 2 faults, which would require Phase 3 to be a separate fault generation, or soles onto them because the original section (Fig. 3.15, Final) does not contain sufficient information. In the reconstruction, the Phase 3 fault is shown to sole onto the Phase 2 fault (Fig. 3.15), as the Phase 2 fault is dipping at >30° and so could potentially remain active.

The final phase faults are all high angle and demonstrate very little, if any, rotational component (Figs 3.14 & 3.15 (Phases 3 & 4, respectively)). The final stage faults appear to

have contributed minimal stretching in to the final section. The late stage faults in Fig. 3.15 are of mixed polarity (Fig. 3.15, Phase 4), accommodate very little heave and are apparently irrotational (possibly due to their mixed polarity).

Although the latest faults do not contribute much extensional strain to the system, they do serve to complicate the section by obscuring vital information on equivalent seismic data (see **Chapter 4**) and by producing some of the geometries that were predicted by Fig. 3.6. These include; DFB & UFB structures, oversteepened stratigraphy (relative to the latest fault sets), and an augmented crestal wedge (Figs 3.14 & 3.15, Final).

The structural complexity Fig. 3.15 is complicated further by the presence of early antithetic faults which have been passively rotated throughout the stretching history of the section, leading to an apparent reverse offset of the stratigraphy along the now steeply dipping fault (similar to Figs 3.12 & 3.13). The rotated antithetic structures are active during Phase 2 (Fig. 3.15) and have been misinterpreted by Brady et al. (2000) as a single steeply inclined (east-dipping) normal fault soling out onto a lower-angle fault (from Phase 2) in an effort to apply their synchronous-slip model of extension developed for the South Virgin Mountains.

3.3.3 Polyphase Detachment Faulting in the Betic Cordillera, SE Spain

The eastern Betic Cordillera, SE Spain, has undergone major post-orogenic uplift and crustal thinning, potentially driven by delamination of the crustal root zone (Seber et al., 1996), or edge-delamination or subduction roll-back (Martínez-Martínez et al., 2006). Whatever the driving force of the crustal thinning may be, between 200 – 280 m/Ma of uplift has been recorded for the region (Braga et al., 2003). Major crustal thinning has been noted by Booth-Rea et al. (2002 & 2004) for the eastern Betic region, where a section originally c.

20km thick from thermobarometric studies (Booth-Rea et al., 2002; Booth-Rea et al., 2004) has been thinned over at least seven generations detachments faults to only c. 1 km (Fig. 3.16). The amount of crustal thinning (equivalent to $\beta \approx 20$) has resulted in the roughly 20 km section being condensed to about 1 km, where the lithological contacts are nearly always faulted contacts.

Although the region has not undergone PPF, as has happened in the previous examples, the Betic region has nevertheless experienced hyper-extension, and as such it is mentioned here. The cross-sections shown in Fig. 16 are also modelled seismically in **Chapter 4**, to demonstrate how when such extreme crustal stretching occurs it is impossible to identify on seismic data, in this case due to the lithological contacts being low-angle detachment faults.

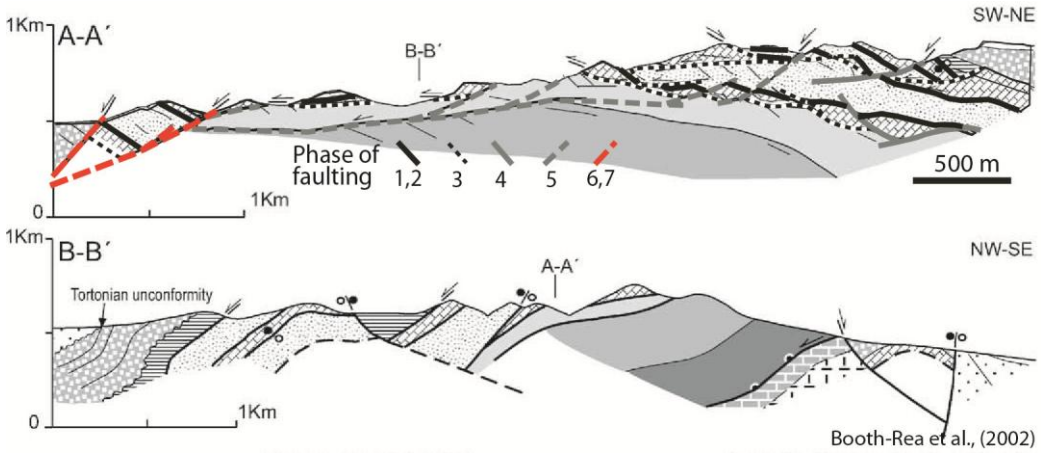

Fig. 3.16: Cross-sections taken from the Eastern Betics, SE Spain showing multiple generations of detachment faults, thinning the rock pile from c. 20km to 1km. Almost all lithological contacts are faulted contacts. Order of faulting for "A" is taken from Reston 2007, while the original cross-sections were presented by Booth-Rea et al., 2002, and Booth-Rea et al., 2004.

3.4 Discussion: Comparison between Model Results and Onshore Examples

From the published field sections (Chamberlin, 1982; Proffett, 1977; Proffett & Dilles, 1984) it is apparent that PPF does occur in nature, with later fault sets displacing earlier ones. The

sections presented are most similar to the mono-pole PPF mechanism described in Fig. 3.5a, with Fig. 3.12 being the closest to the monopole end-member in geometry.

There are, however, some discrepancies between the conceptual and mechanical models (described in **Section 3.2**), and the published sections (Figs. 3.12 – 3.15). The main discrepancy is the number of fault generations, and their associated extension is incompatible with the conceptual and mechanical models. In general, more faulting phases are required to achieve less stretching than might be expected from the same amount of fault generations in the models (**Section 3.2**). It is also possible that some extension may have occurred outside of the plane of section. Since rifting is a three dimensional process the section may not capture the full rotation of faulting.

One potential explanation for this could be that each fault phase is abandoned after a small amount of rotation and so more fault phases would be required to achieve the level of stretching the section has undergone. This could result from a loss of cohesion within the rock mass (real world crust contains fractures at all angles which, if orientated correctly to the principle stress directions, would be suited to failure) and so reduce the maximum rotation that a fault block can undergo before a new fault is forms (see **Section 3.2.6**). A similar effect could be produced by invoking pulsed extension where slight changes in the three-dimensional stress directions would cause faults to be abandoned earlier than expected for a progressively extending region as they are no longer favourably orientated in three dimensional space. Another potential reason for this may be that since the published sections exist in a region where the crust is thought to be extending in the style of a wide-rift (Buck, 1991), lower crustal flow towards the rift axis may have kept the lithostatic stress (σ_1)

relatively constant, so the faults were not able to rotate as far as they might have been able to if σ_1 were being progressively reduced concomitantly with extension (c.f. **Section 3.2.5**). However, from observations of fault intersection angles (**Table 3.5**) it does not always appear as if faults are undergoing minor rotations before being abandoned. Instead it appears that in some cases, unlike in the conceptual and mechanical models, fault rotation in the published sections (Figs 3.12 – 3.15) is not entirely related to extension, and that some other process may be responsible for at least some of the tilting observed (e.g. isostatic uplift (Brady et al., 2000)).

This notwithstanding, there is quite a good match between the predictions of the mechanical model (Figs 3.7 – 3.9) and Fig. 3.12. The fault intersection angles between Phases 1 & 2 of Fig. 3.12 are c. 24°, which is very similar to those produced for Phases 1 & 2 of the mechanical model, c. 21°. Phase 2 of Fig. 3.12 is more of an intermediate stage of extension and may be combined with Phase 3 (as discussed in **Section 3.3.1**), so that the fault intersection angles between Phases 3 & 4 of Fig. 3.12 are c. 34°. Again this is very similar to the fault intersection angles of Phases 2 & 3 of the mechanical model (**Table 3.5**).

The difference in stretching resulting from PPF extension in Fig. 3.12 compared with the Mechanical model is only c. 10%. Fig. 3.13 also appears to fit relatively well with the mechanical model, whereby the fault intersection angles are similar, but the amount of total extension is c. 40% less than would be expected if the model held true for the Fig. 3.13 example. It is possible that the faults in Fig. 3.13 may have undergone an element of flexural rotation (or isostatic uplift) at shallow levels in their hangingwalls, which would have served to increase the fault intersection angles between phases. Figs 3.14 & 3.15 do not conform

Section	Fault Phase	Intersection Angle	Stretching
C. Model	1 & 2	30°	β ≈ 1.7
	2 & 3	30°	β ≈ 3.0
M. Model	1 & 2	21°	β ≈ 1.4
	2 & 3	30°	β ≈ 2.8
Fig. 3.12	1 & 2	24°	
	2 & 3	9°	
	3 & 4	25°	β ≈ 2.7
Fig. 3.13	1 & 2	25°	
	2 & 3	24°	β ≈ 2.4
Fig. 3.14	1 & 2	20°	
	2 & 3	45 - 50°	β ≈ 1.8
Fig. 3.15	1 & 2	17°	
	2 & 3	19°	
	3 & 4	41 - 51°	β ≈ 1.7

Table 3.5: Observed intersection angles between fault generations for Conceptual Model (C. Model – Fig. 3.5a), Mechanical Model (M. Model – Figs. 3.7 – 3.9), and the published sections (**Section 3**). Stretching for each phase where it is most robust is also noted. Green shading indicates where the fault intersection angles are within what is predicted by the conceptual and mechanical models. Orange shading indicates where the intersection angles fall far outside what is predicted by the models.

well with either the conceptual or mechanical models for PPF (**Section 3.3.2**) as they have up to four separate phases (three if Phases 2 & 3 from Fig. 3.15 are combined as one – see **Section 3.3.2**) that only accommodate a maximum of β ≈ 1.83, almost the equivalent of what is possible with one phase of faulting in the conceptual model and what c. 40% more than one faulting phase in the mechanical model. Fault Phase 2 for Fig. 3.14 is presently at an angle of c. 20 – 30°, and its intersection angle with Phase 1 is c. 20°, and has probably rotated through 30 – 40°, which would account for a significant amount of stretching in the section. The smaller strain faults (totalling c. 18% extension) in this section could possibly be considered to contribute to distributed deformation within one major fault block (c.f. Walsh & Watterson, 1991). If this were the case, then Fig. 3.14 fits neatly between the strain predicted to result from one full fault rotation (in the mechanical model) of a rigid fault block and one where distributed strain (as shown in **Table 3.1 – 3.3)** is considered.

Where the models do not conform to the published sections, it may be possible to match the observations in these sections by changing the cohesive strength and frictional coefficient of the rock mass. Reducing the cohesive strength, for example, would have the effect of allowing less fault rotation before abandonment. Presented in this chapter are proof of concept models only, but these do in some cases appear to compare reasonably well to the published structures.

The fault restorations completed in **Section 3.3** considered the fault blocks to be rigid, and as such it is likely that the level of extension in all of the sections has been underestimated here. Significant layer-parallel stretching (Ferril et al., 1998) within the system coupled with fault propagation folding leading to pure-shear thinning of stratigraphy, as well as small offset faulting, all of which have very likely occurred would have the effect of increasing the amount of total extension, making the restoration estimations of extensions a possible underestimate of the total true extension. The dip of stratigraphy, in general, is not as high as might be expected from the models in **Section 3.2**. This is likely due to significant distributed deformation consisting of bedding parallel slip (Ferril et al., 1998) occurring within the system where as the stratigraphy is tilted to high-angle, bedding planes are orientated into the range of angles at which shear can occur. This would serve to reduce the degree of oversteepening of stratigraphy and would accommodate notable thinning of the crust.

Regardless of how well the published sections (Figs 3.12 – 3.15) conform with the models discussed in **Section 3.2,** the final stage of each section has examples of varying quality of the PPF identifiers presented in Fig. 3.4 (see individual figures for details).

It should be noted that field observations of the crust which has been stretched much past 100% ($\beta = 2$) are rare as under normal circumstances these regions will have subsided below sea-level (Jackson & White, 1989) as at MPRMs. Therefore, in order to study regions of extreme crustal stretching it is necessary to use geophysical methods, most commonly seismic imaging.

3.5 Conclusion

In the above chapter I have demonstrated how the polyphase faulting (PPF) model is capable of accommodating large amounts of extensional strain. From the examples presented it would appear that the monopole variant is favoured with dipole PPF either being less commonly developed, or more likely unrecognised, in nature.

The models presented in this chapter suggest that progressive extension of the crust over multiple fault generations may be capable of embrittling the crust and initiating mantle serpentinisation. This may occur over as little as two succeeding fault generations (that each rotate fully through 30°), provided strain rate is low and that lower crustal rheology is favourable. It is important to remember that the magnitude of the stretching predicted by the models presented in this chapter (both conceptual and mechanical) is based on the assumption that they are composed of rigid fault blocks. This assumption automatically has the effect of reducing the maximum amount of stretching that can be accommodated. Therefore, when distributed deformation is considered it is entirely possible that the number of fault phases required to embrittle the crust could be reduced.

Structural geometries related to PPF are known from the western United States, and some of the classic sections have been shown to accommodate up to 170% extension ($\beta \approx 2.70$ if applied to the whole crust) from palinspastic restorations, proving that the mechanism is capable of stretching the crust to high degrees.

It appears that the mechanical model of PPF presented here compares reasonably well with the observations made from the published onshore examples of PPF with regard to the geometric relationship between successive fault generations. The mechanical model could potentially be made to fit better and account for each feature of the onshore examples by changing the model's cohesive strength and/ or the frictional coefficient. This would have the effect of either increasing or decreasing the fault intersection angles.

While the onshore PPF examples demonstrate clearly the complexity of a PPF extensional system, they cannot be directly compared to the structures that may attenuate the continental crust to the point of rupture. This is because the driving mechanism for extension and the rheological make-up are not the same for the extending regions. Although the structures in the Basin & Range region have accommodated large amounts of extension, the region remains above sea-level. This may be suggestive of significant lower crustal flow towards the rift axis (similar to the situation described by Buck, 1991 for wide rift systems). Extension in the region appears to be concomitant with significant magmatism which may suggest that the lower crust is sufficiently hot to flow. MPRMs, in contrast, display very little, if any, evidence for syn-rift magmatism, due to low strain rates and crust-mantle temperature.

Identifying the more advanced stages of the PPF mechanism in nature is difficult due to the majority of regions where it might be expected being below sea-level. Regions of hyper-extended crust (>> 100%), such as MPRMs and highly extended margin basins, are usually beneath very deep water and are often sediment starved. As such, this environment favours mass wastage of uplifted fault blocks resulting in the loss of information, This could be especially problematic for the identification of monopole PPF structures. Misinterpretation of structures/ sediments at unintuitive attitudes (especially in the case of the monopole variant) is another possible reason as to why the mechanism is widely unrecognised. For the case of the dipole model, multiple fault generations would be subtly expressed and sediment compaction may alter the original sedimentary geometries, limiting interpretation of the oldest syn-faulting sediments. Due to processes like mass-wastage evidence of the earliest fault generations, in general, is most likely to survive in the hangingwall. However, commercial seismic surveys often do not have sufficient record time to image structures in the hanging walls clearly at the deepest and most stretched part of the basin/margin, and often their processing is optimised to image low-angle structures. This means that the probably steeply dipping sediments related to early PPF structures are likely to be invisible on commercial data.

The cross-cutting fault geometries discussed in this chapter are used in used in **Chapter 4** to investigate the seismic response to complex extensional structures. In **Chapter 4** the limits of seismic resolution coupled with complicated lateral and vertical velocity gradients resultant from the PPF mechanism are shown to make seismic imaging of PPF structures very difficult. In **Chapter 4** particular attention is given to the seismic expression of the PPF

identifiers described in this chapter, and how they might be recognised on seismic data in order to maximise the chances of the mechanisms interpretation at MPRMs.

CHAPTER 4

Synthetic Seismic Modelling: Exploring the seismic expression of structurally complex extensional systems

4.1 Introduction

Wide-angle seismic profiles from many Magma-Poor Rifted Margins (MPRMs) have shown that there is no major discrepancy in observed thinning across the margins between the upper and lower crust (Reston, 2007; Reston, 2009a). This observation implies that the paucity of seismically observed extensional structures is not evidence for depth-dependent mechanisms for crustal attenuation, as described by Davis & Kusznir (2004) and Kusznir & Karner (2007). Rather, it is more likely that at MPRMs the majority of extension is accommodated by seismically unrecognised/unresolved structures (Reston, 2007).

Tate et al. (1993) have suggested one possibility as to why crustal structure is difficult to resolve in the South Porcupine Basin is that the structural complexity that would be expected at high stretching factors would hinder seismic imaging of the crust. Successive generations of faults are expected to initiate when $\beta \geq 1.7 - 2.0$ (Jackson & White, 1987). As shown in **Chapter 2** the Porcupine basin has achieved $\beta >> 10$ at its centre (where localised mantle exhumation may have occurred as suggested by O'Reilly et al., 2006). Therefore, it is likely that multiple fault generations, combined with detachment tectonics, have been involved in the attenuation of the crust beneath the basin.

Here, synthetic seismograms generated from both published and unpublished structural cross-sections and conceptual models are presented. These sections have been modelled in order to characterise the seismic response to complex geometries predicted by the

polyphase faulting (PPF) model, and low angle normal faults/detachments (see **Section 4.3**). The associated pitfalls of how these seismic data could be misinterpreted are also discussed.

4.2 Seismic Modelling Method – Ray tracing

Reflections on multi-channel seismic data are generally taken to correspond to a discontinuity, or layer interface somewhere in the rock pile. Similarly, reflections observed on synthetic seismograms are assumed to correspond to a layer interface. Reflections are produced in seismic data where there is a contrast in acoustic impedance. The acoustic impedance, Z, of a rock medium is the product of its seismic velocity (P-wave in this case), v, and its density, ρ, and is given by the expression,

$$Z = \rho v$$

The amplitude, or brightness, of a given reflection depends on the reflection coefficient of the media, defined as,

$$\frac{Z_2 - Z_1}{Z_2 + Z_1}$$

where Z_1 is the acoustic impedance of the transmitting rock layer and Z_2 is the acoustic impedance of the receiving rock layer. The greater the difference in acoustic impedance between different media, the larger the amplitude of the reflection produced. If $Z_2 > Z_1$, an amplitude peak is produced, and when $Z_2 < Z_1$ an amplitude trough is produced.

So, in order to calculate if there will be reflection generated at a rock interface, it is necessary to know both the density and the seismic velocity of the medium. The seismic

velocity of a medium is dependent on its elastic properties (the bulk and shear modulii). However, when these properties are unknown, or unnecessary for the generation of synthetic data (as is the case here), the seismic velocities of a given rock can be estimated via other means.

A number of workers have identified empirical relationships between the seismic velocity for rocks and their density, most notably Nafe & Drake (1957) and Gardener et al., (1984). For the models described below in **Section 4.3**, I have estimated seismic velocities for a number of different lithologies based on their densities (given in Henderson & Henderson, 2009), and the P-wave velocity vs density curve defined by Nafe & Drake (1957) (Fig. 4.1). I have not used the P-velocities of Gardner et al. (1984) as they are best suited to sedimentary rocks only. S-wave velocities for the synthetic seismic models are calculated as a ratio of the P-wave velocity where the V_P/V_S ratio is equal to the square root of three (NORSAR 2D manual).

The ray tracing method provides a way to generate synthetic seismograms as it provides an approximate solution of the seismic wave equation through layered media (Norsar 2D Manual; Telford et al., 1991). The NORSAR2D software package is capable of performing two types of ray tracing, although for the successful generation of synthetic data both are required, kinematic ray tracing and dynamic ray tracing. Kinematic is based purely on the seismic velocities within a given model and yields two-way travel times to interfaces within the model (Norsar 2D manual). At each interface the rays obey Snell's Law of reflection and transmission. Snell's Law (Haliday et al., 2003) describes how, depending on the velocity contrast between two media, a ray transmitted from one layered media to another will be refracted, or reflected. Snell's Law is written as follows:

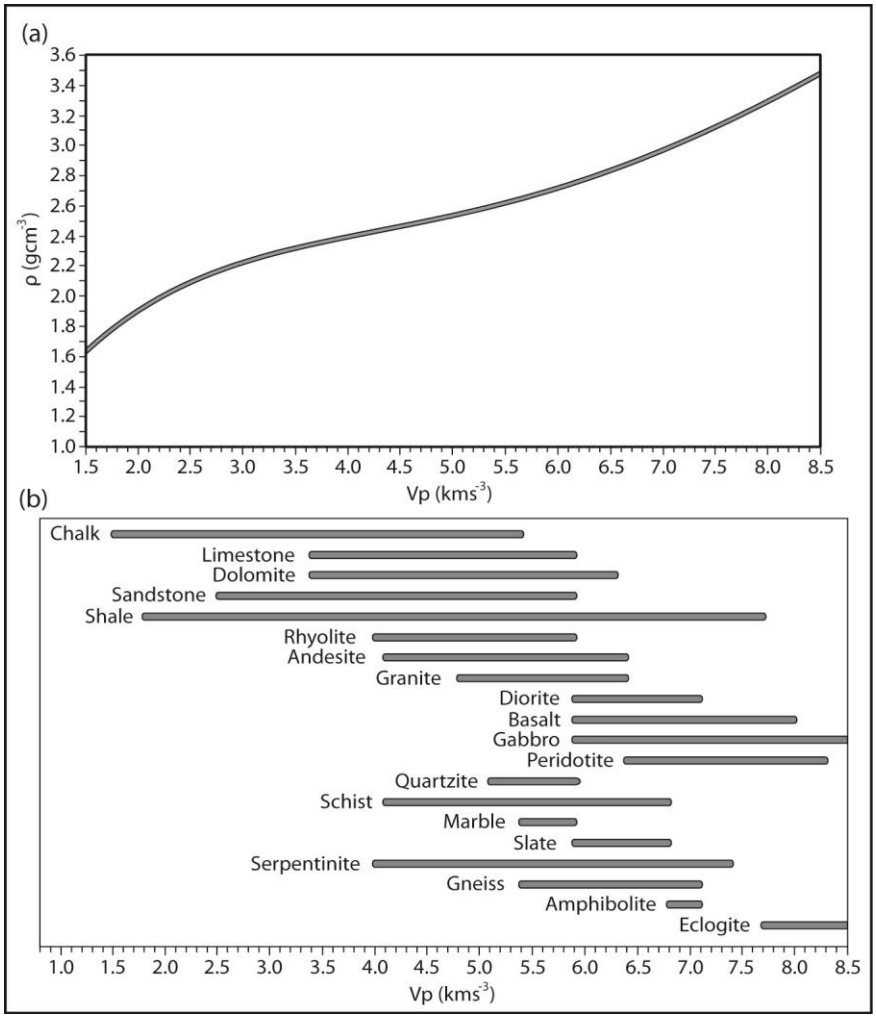

Fig. 4.1: (a), Relationship between Vp (P-wave velocity) and density as empirically defined by Nafe & Drake (1957). Vp for synthetic models described here has been defined using this relationship. (b), Vp ranges for a selection of sedimentary, igneous, and metamorphic rocks, for their range of densities, as reported by Henderson & Henderson (2009).

$$\frac{\sin i_1}{v_1} = \frac{\sin i_2}{v_2}$$

where i, is the angle between the ray and the normal to the refractive/reflective interface, and v is the seismic velocity of the medium, and the subscripts 1 and 2 represent different layers. For the case where a ray is transmitted from medium to another;

$v_2 > v_1$ leads to $i_2 > i_1$, or if, $v_2 < v_1$ leads to $i_2 < i_1$. Or, in the case of where a ray is reflected from an interface, $i_1 = i_2$.

However, kinematic ray tracing does not provide sufficient information to generate a synthetic seismogram as the rays carry only information on the two-way travel time (TWTT) to each interface within the model. In order to generate reflections and a synthetic seismogram, it is necessary to also perform dynamic ray tracing on the model. Dynamic ray tracing requires information about the density of the media through which the rays are passing (Norsar 2D manual), thus allowing calculation of the acoustic impedance between media and the amplitude coefficient (reflection coefficient) along the ray path. Dynamic ray tracing is also capable of calculating the geometrical spreading of the wave (if desired), and the wavefront curvature as the rays pass though the model (Norsar 2D manual). So, by performing kinematic and dynamic ray tracing it is possible to get enough information to calculate the acoustic impedance, as well as the reflection coefficient of an interface and so generate synthetic seismic data.

The synthetic seismograms presented in **Section 4.3** were generated by performing ray tracing on input models within the Image Ray Tracing module in the NORSAR2D package. The image ray tracer basically simulates a migrated 2D two-way travel time seismogram of a model built in depth space, creating a SEGY file (a file format that stores seismic data digitally on magnetic tapes, Barry et al, 1975) that can be read by a seismogram displayer. A forward modelling approach was adopted, whereby a geological model was built within the Model Builder module of the NORSAR 2D package and ray tracing was then performed on this input model. Forward modelling is a very useful practice which can significantly aid in

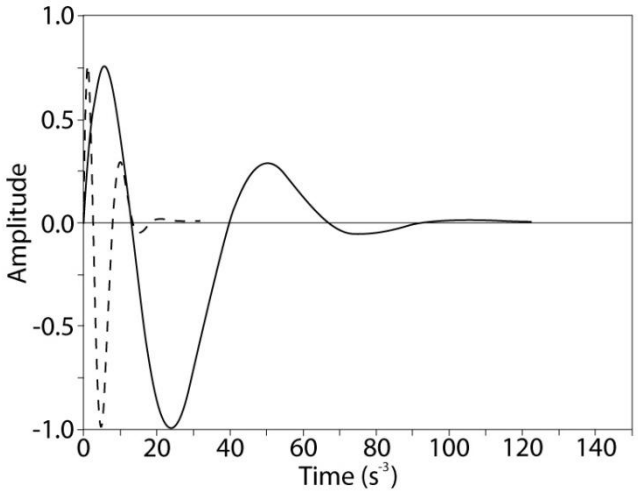

Fig. 4.2: Example of a Ricker minimum wavelet used for the generation of synthetic seismic data in this chapter. Solid wavelet has a frequency of 20Hz, and dashed wavelet has a frequency of 100Hz

elucidating the structure responsible for a given seismic reflection. Modelling is generally a highly iterative process and adjustments can easily be made. A model is created and expected seismic attributes are calculated from those of the model. It should always be borne in mind that forward modelling is a very powerful tool but by its nature it necessitates the making of certain assumptions during model construction, and the approximations which are made initially must be considered when taking conclusions from model outputs (Telford et al., 1990).

In this case, forward modelling of simplified geological models and structural cross-sections was conducted. Geological models consisting of discrete blocks were built in NORSAR 2D and seismic attributes assigned to each block (P & S wave velocities, and density). For each model, seismic traces were generated every 10 – 50m depending on the resolution the scale of the model would allow within the software. A Ricker minimum wavelet (Fig. 4.2) was

used to generate the seismic response from the input models. The sections were modelled for a dominant frequency of 20Hz.

4.3 Results – Synthetic Seismic Sections

The geological models presented here, both published and unpublished, have been digitised within the NORSAR2D package and have undergone ray tracing (as described in **Section 4.2**) within the Image Ray Tracer module of the software. The event file that is output from the ray tracing stage is then processed using the Seismogram Generator module to create a SEGY file that can then be displayed and further processed (if required) in the Seisee SEGY viewing software. Ultimately, a migrated TWTT 2D seismic section is created from the input depth model.

The synthetic seismograms are presented at high migration apertures relative to the thickness of the velocity models. This biases the data towards imaging steeply dipping events. On a real seismic section, most steeply dipping events would not be imaged. In some models, fault zones have been modelled as low-velocity zones (LVZs) in order to artificially ensure that intra-basement faults are imaged on the data. Fracturing within the basement, associated with the damage zones of a fault, can result in velocity and density reductions across the fault zone of 30 – 40% (Mooney & Ginzburg, 1986). In most cases, intra-basement fault reflections are uncommon, with fracture healing (Hölker et al., 2002) creating difficulties in producing sufficient acoustic impedance to cause a reflection across a fault zone as the basement appears seismically isotropic. Bearing this in mind, the models presented below should be considered as the absolute best case scenario with respect to structures that can be imaged by the seismic method.

Where fault zones generate intra-basement reflectors, it should be possible to use down-dip fault bifurcations (DFBs) to identify the PPF mechanism. However, when sufficient acoustic impedance is not generated by fault zones to produce reflections within the basement, other identifiers of the PPF mechanism may be possible to identify shallower in seismic sections. Crestal Wedges (CWs), up-dip fault bifurcations (UFBs) and oversteepened stratigraphy may be observed. For details on each of the PPF identifiers see **Section 3.2.4**. Many of the PPF identifiers rely on faults either generating intra-basement reflections or being identified from possible stratigraphic offset or imaged directly from velocity contrasts across fault zones, (see **Section 4.3.1**). The published (cross-sections shown in **Chapter 3**) and unpublished examples presented below contain combinations of each of the PPF identifiers described in **Chapter** 3.

The models of published onshore examples (**Section 3.3**) are relatively shallow – c. 2.5 km – and so in order to properly compare these structures with those that might be observed at MPRMs it is necessary to scale them up. Due to scale independence and the fractal nature of many geological structures (Walsh & Watterson, 1991; Lei & Kusunose, 1999; Peacock, 2003) this is a reasonable approach to take. Scaling is achieved during ray tracing stage of model generation by generating the original model for a dominant frequency of 20 Hz to simulate the seismic response to this model. Taking the original scale velocity model and re-conducting ray-tracing, this time for a dominant frequency of 100 Hz, simulates a section (and structures) five times larger than the original. The scale bars are adjusted on the output seismogram and it is the same as that which would have been generated by modelling a section five times as large, for a dominant frequency of 20Hz.

4.3.1 Conceptual Rifted Margin

The first model discussed is of a conceptual rifted margin, with a realistic thinning profile based on the Newfoundland Margin (NFM). The conceptual (and idealised) geological model (courtesy of Prof. Tim Reston - University of Birmingham) (Fig. 4.3) is described first as it contains many of the possible geometries that are predicted to result when the Polyphase Faulting (PPF) mechanism stretches and thins the crust. The model is constructed of multiple blocks of varying size with each block assigned one of ten lithotypes and its associated petrological properties (**Appendix B**). Four syn-rift phases/packages are present in the model, related to three separate fault sets that thin the crust. The fault blocks do not deform rigidly as they do in the simple rigid PPF models, with some of the dip decrease associated with progressive extension related to distributed deformation within the fault blocks flattening the fault. The fault blocks behave similarly to the "soft-domino" PPF mechanism mentioned in **Chapter 3**. Structural complexity increases dramatically oceanward along the margin as increased stretching factors ($\beta_{max} \leq 3.5$) are accommodated by up to three successive fault sets (LVZs are ≤ 5m wide) cross-cutting earlier generations (Fig. 4.3). A post-rift layer, a Moho transition zone -similar to that observed on wide-angle data from the Rockall Trough (Hauser et al., 1995; O' Reilly et al., 1995; O'Reilly et al., 1996), and a thin layer of serpentinised mantle (oceanward of km 105, Fig. 4.3, where the crust is embrittled) are also included in the velocity model.

Shot-receiver (S-R) points are placed at 50 m intervals across the margin due to limitations on the number of S-R points the NORSAR package allows within a single model for image ray tracing. The seismogram resolution is not compromised as the structures are large enough

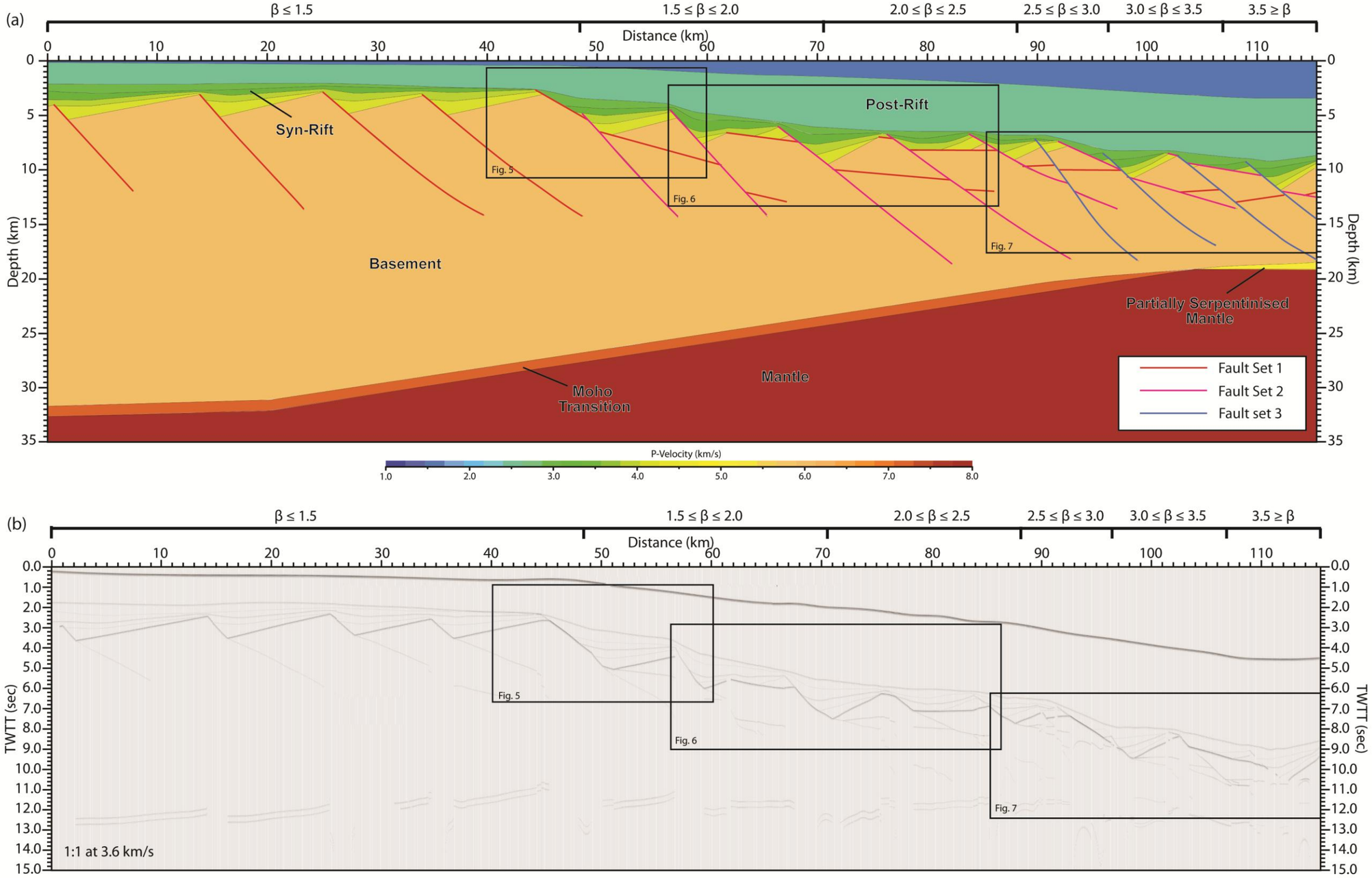
(a)
β ≤ 1.5
1.5 ≤ β ≤ 2.0
2.0 ≤ β ≤ 2.5
2.5 ≤ β ≤ 3.0
3.0 ≤ β ≤ 3.5
3.5 ≥ β
Distance (km)
Depth (km)
Syn-Rift
Post-Rift
Basement
Fig. 5
Fig. 6
Fig. 7
Partially Serpentinised Mantle
Mantle
Moho Transition
Fault Set 1
Fault Set 2
Fault set 3
P-Velocity (km/s)
(b)
TWTT (sec)
1:1 at 3.6 km/s

Fig. 4.3: (a) Velocity model of a conceptual rifted margin, with realistic oceanward taper. The model is colour coded according to the Vp in each lithology/unit. The margin has been stretched over three successive fault generations with stretching factors increasing towards the ocean concomitant with increasing structural complexity. Boxed areas are described in more detail Figs 4.5 – 4.7. (b) Synthetic seismogram resulting from ray-tracing of (a). Note that seismic reflections become more complex as stretching factors increase. This should highlight the difficulty in identifying these structures and why they may be unaccounted for in many estimations of crustal stretching at MPRMs. See Figs. 4.5 – 4.7 for more detail

to be well covered by S-R points. The synthetic seismic data resulting from ray tracing is shown in Fig. 4.3b.

4.3.1.1 First Fault Phase

In the low strain part of the model, km 0 – 44 (Fig. 4.3), fault plane reflections are clearly visible and can be seen to shallow within the basement (Fig. 4.3b). The model is biased towards producing and imaging fault plane reflections. This is accomplished by using a large migration aperture (to image steeply dipping structures) and introducing narrow LVZs to simulate faults within the basement (to ensure that fault planes produce a reflection). A shallowing effect is observed in Fig. 4.3b due to velocity pull-up resulting from the planar faults in Fig. 4.3a. This effect has been noted from synthetic seismic investigations of low-strain extensional systems (Withjack & Pollack, 1984, Fig.4.4). In Fig. 4.4 the curvature of the fault is a result of velocity pull-up effects. The velocity pull-up is occurs because there is a greater amount of relatively low velocity material overlying the fault plane within the shallower part of the hangingwall, and a greater thickness of relatively high velocity material overlying the deeper part of the fault plane downdip in the hangingwall. The effect of this set up is that the reflections from the shallower part of the fault return to the receivers slower relative to the reflections returning from the deeper section of the fault. This gives rise to a fault that is apparently listric, or concave-up. Velocity distortions can mask vital information, are very important to consider in high strain extensional systems.

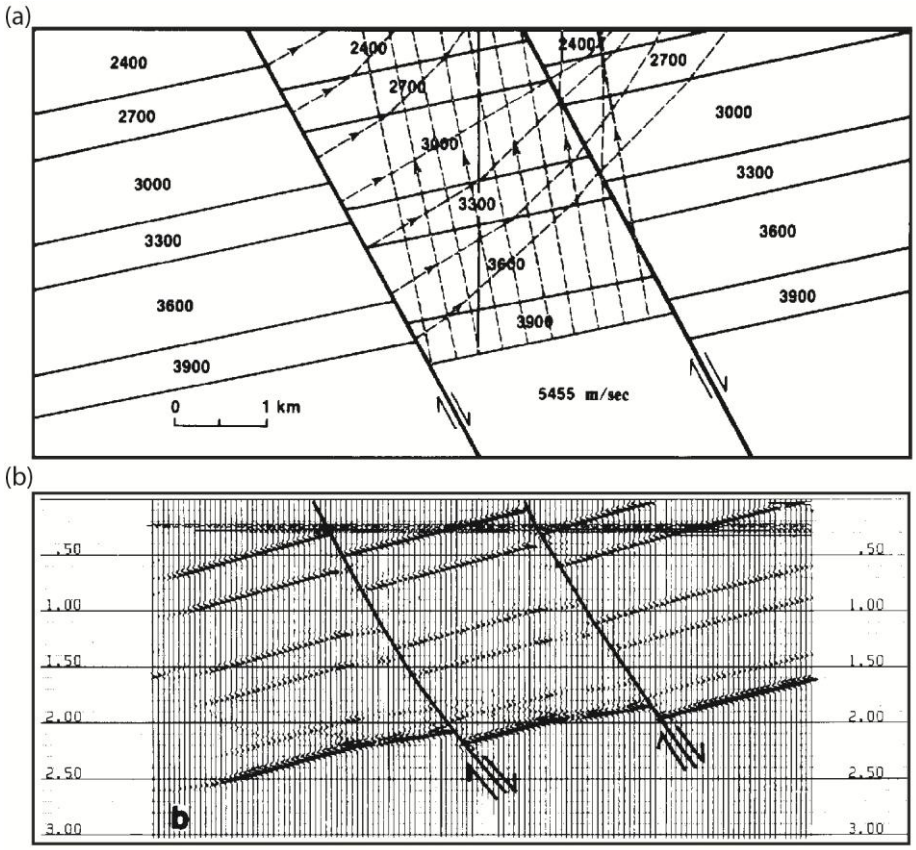

Fig. 4.4: Synthetic seismic model of a (low strain) normal fault system (Withjack & Pollock, 1984). (a) Velocity structure of the fault model, showing general increase in seismic velocity with depth. Note planar fault geometry. (b) Synthetic seismogram demonstrating how planar faults appear curved due to velocity distortions (pull-up). Faults generate discrete reflections independent of layer juxtapositions

4.3.1.2 Second Fault Phase (Low-Strain)

The first instance where stretching $\beta \rightarrow 2.0$ in the crust it is accommodated on a second, cross-cutting fault set. At km 40 – 60 (Fig.4.3 & Fig. 4.5) the simplest iteration of cross-cutting fault sets in the model is displayed and examples of both UFB and DFB are present (Fig. 4.5; **Table 1**). The intra-basement reflector patterns produced in this section of the model are in similar to and are in agreement with the simple synthetic models of Yarnold (1993). These identifiers are expected to be common where extension is accommodated by successive fault generations. Reflection amplitude varies within the data (Fig. 4.5(i)(a & b)) with the brightest reflection caused by the seabed (km 51 – 60, 1.0 – 1.5s TWT) (Figs 4.3b & 4.5(i)). The first generation fault produced a bright reflection where it juxtaposes sediment

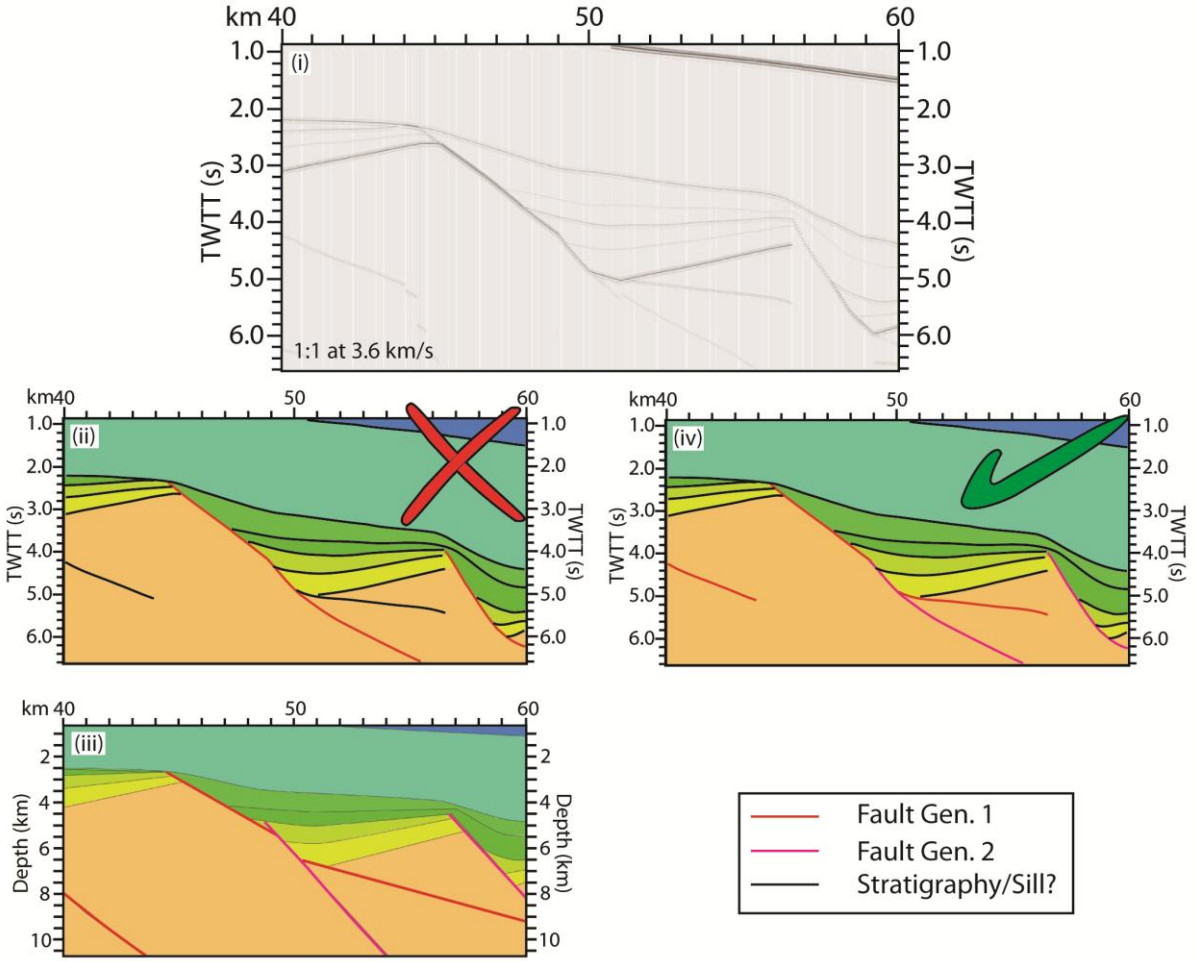

Fig. 4.5: Box out from Fig. 4.3, a simple two fault PPF structure. Crustal stretching is β ≈ 1.5 – 1.7. Refer to Fig. 4.3 for Vp scale. (i) Synthetic seismic section. No vertical exaggeration at 3.6km/s. PPF identifiers; a UFB and a DFB (produced by intra-basement reflections). Note changes in reflector amplitude are dependent on

the nature of the related interface in (iii) (e.g. lower amplitude of sediment-sediment interfaces relative to sediment-basement interfaces), and reduction in amplitude of steeply dipping structures dipping. (ii) Possible (incorrect) interpretation of (i), where the data is interpreted as a simple tilted fault block system. First generation fault is considered to be a sill or other intra-basement feature. (iii) Correctly interpreted PPF structure. The first generation fault is cut, and offset by a later high-angle fault. (iv) Input velocity model used to generate (i). Note how intra-basement reflections are affected by velocity pull up affecting fault geometries in the data. See **Table 4.1** for details on individual PPF identifiers.

against basement (Figs. 4.3b & 4.5(i)(a & b)). The amplitude of the fault reflection is greatly reduced above 2.6s TWT (Figs. 4.3b & 4.5(i)(a & b)) as it forms a sediment-sediment contact and the acoustic impedance is not as great. The top basement reflection (km 40 – 45, 3.1 – 2.7s TWT, and km 51 – 56.5, 5.1 – 4.5s TWT) is also particularly bright. However the steeply dipping reflector (km 49 – 50, 4.2 – 4.9s TWT) which relates to a sediment-basement contact is not as strong as the top basement reflections. This is probably due to the steeply dipping nature of the contact.

The synthetic data (Fig. 5(i)(a)) could potentially be interpreted as a single block bounding fault with a small hangingwall syncline present adjacent to the block bounding fault plane. In this interpretation, the hangingwall block appears to have some intra-basement reflectivity (Fig. 4.5(ii)). This is especially true for the case where fault zones do not generate sufficient acoustic impedance to produce a reflection (Fig. 4.5(i)(b)). However, comparing the synthetic data (Fig. 4.5(i)(a)) with the input model (Fig. 4.5(iii)), it is apparent that the interpretation in Fig. 4.5(ii) is incorrect, and the reflections in Fig. 4.5(i) can be interpreted according to the structures (Fig. 4.5 (iii)) that generated them, to produce the correct interpretation of the synthetic data (Fig. 4.5(iv)). Due to velocity distortions, the second generation fault appears to be slightly listric in the uninterpreted (Fig. 4.5(i)) and interpreted

data (Fig. 4.5(iv)). DFBs and UFBs are present in the data (**Table 4.1**) and can be used to suggest the presence of the PPF mechanism from the observation of the data. It should be noted that even if the modelled faults did not produce reflections, as in Fig. 4.5(i)(b) it would still be possible to identify the PPF mechanism (Fig. 4.5(v)) due to the presence of UFB in the data (**Table 4.1**), although knowledge of the total crustal thinning would probably be required to convincingly argue that the apparent kink at UFB is related to PPF and not just a splay fault resulting from flexural rotation of the footwall.

PPF Identifier	Velocity Model (km, km)	Seismogram (km, s TWT)	Comments
Crestal Wedges			None present
Up-dip Fault Bifurcation	49.0, 5.5	49, 4.2	
Down-dip Fault Bifurcation	50.0, 6.5	50.0, 4.8	Strongly distorted down-dip reflections

Table 4.1: Coordinates of where PPF identifiers and associated structures can be observed where present in the model (Compare with Fig. 4.5).

4.3.1.3 Second Fault Phase (High-Strain)

Where stretching reaches $\beta \rightarrow 2.5^{-}$ in the model a more complex iteration of the two fault PPF mechanism accommodates the strain (Fig. 4.6). The increase in structural complexity leads to further difficulties in correctly interpreting the data, not least due to increased complexity of the velocity gradient within the crust. At this point in the model, first

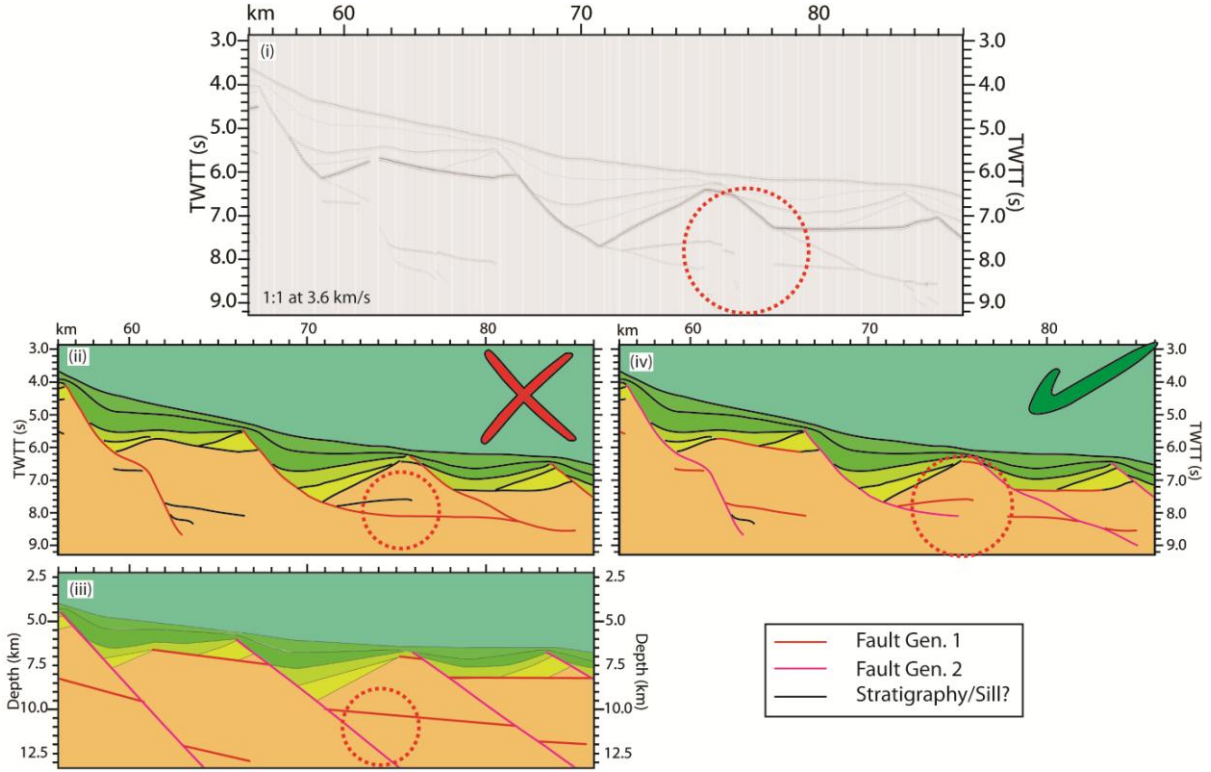

Fig. 4.6: Box out from Fig. 4.3 highlighting the difficulty in interpreting a more complex two fault PPF structure, where crustal stretching is c. $\beta \approx 1.7 - 2.5$, from its seismic response. Refer to Fig. 4.3 for Vp scale. (i) Synthetic seismic section, shown with no vertical exaggeration at 3.6km/s. PPF identifiers include examples of UFBs, DFBs (produced by intra-basement reflections), and crestal wedges (with internal reflections). Changes in reflector amplitude are dependent on the nature of the related interface in (iii). Note that brightest reflections are caused by passively rotated "top-basement" faults. (ii) Possible (incorrect) interpretation of (i), where the data is interpreted as a ramp-flat-ramp, and listric fault system. First generation faults are very low-angle and in some cases considered to be basement reflectivity. (iii) Input velocity model used to generate (i). (iv) Correctly interpreted PPF structure, demonstrates how each structure looks in two-way time. First generation faults appear sub-horizontal or overturned in some cases due to velocity distortion. Note that the correct interpretation is dissimilar to the input model (iii). Red circle shows area where misinterpretation of the data is most likely to occur due to velocity pull-up causing apparent linkage between separate fault generations. See **Table 4.2** for details on individual PPF identifiers.

generation faults have been passively rotated to very low/sub-horizontal angles, while the cross-cutting (second generation) faults are now moderately to shallowly dipping.

The brightest reflections in Fig. 4.6(i) are related to sub-horizontal first generation (top basement) faults. Top basement reflections are of reduced amplitude because they have been tilted to moderate to steep dips.

DBFs are well represented within the basement (Fig. 4.6(i); **Table 4.2**), preserved in the hangingwalls of the latest fault generation. Where developed, DFBs may be the most useful PPF indicator at MPRMs due so the relatively poor reservation potential of CWs, and many examples can be observed in Fig. 4.6(i & iv) (see **Table 4.2**).

A possible interpretation of the synthetic data (Fig. 4.6(i)) is shown in Fig. 4.6(ii), where a normal fault with ramp-flat-ramp geometry and associated roll-over anticline is present at km 56 – 63, and a listric fault system at km 65 – 84. This is a reasonable interpretation based on the reflector patterns in Fig. 4.6(i); however, a comparison between the synthetic seismic (Fig. 4.6(i)) and the input, depth model (Fig. 4.6(iii)) shows that the interpretation of the listric system (Fig. 6(ii)) is incorrect. The PPF interpretation (Fig. 4.6(iv)) of the data does not look anything like the input model due to complex lateral and vertical seismic velocities. It should be noted that because the fault zones on the synthetic data (Fig. 4.6i(a)) manifest with such unintuitive reflector geometries, they are unlikely to ever be interpreted correctly.

If the fault zones did not produce reflections as in (Fig. 4.6i(b)) DFBs will not be interpretable. However, the PPF mechanism may still be recognisable from observation of CWs and UFBs (**Table 4.2**). Incorrect interpretation if the data is still very likely. The correct, PPF,

interpretation of the data is presented in Fig. 4.6(v), based on prior knowledge of the input model (Fig. 4.6(iii)).

PPF Identifier	Velocity Mode (km, km)	Seismogram (km, s TWT)	Comments
Crestal Wedges	61.5, 5.5 - 67.0, 7.5	61.5, 5.6 - 67.0, 6.1	
	75.0, 6.25 - 76.0, 7.0	75.0, 6.2 - 76.0, 6.6	
	78.0, 7.0 - 86.0, 8.25	78.0, 6.6 - 86.0, 7.2	
Up-dip Fault Bifurcations	60.0, 9.5	61.0, 6.7	Distorted up-dip reflections.
	67.5, 7.5	67.0, 6.0	
	76.5, 7.0	76.5, 6.6	
	81.5, 11.0	81.5, 8.2	
	86.0, 8.0	85.0, 7.1	
Down-Dip Fault Bifurcations	62.5, 11.5	62.0, 7.7	Distorted down-dip reflections.
	71.0, 10.0	72.0, 7.8	Distorted down-dip reflections.
	83.0, 11.5	84.5, 8.5	

Table 4.2 Coordinates of where PPF identifiers and associated structures can be observed where present in the model (Compare with Fig. 4.6). Crestal wedges are shown top left and bottom right corners of a rectangle.

4.3.1.4 Third Fault Phase

As crustal attenuation approaches the point of total crustal embrittlement, faults penetrate down as far as the crust-mantle boundary (O'Reilly et al., 1996; Pérez-Gussinyé & Reston, 2001). In Fig. 4.7, crustal stretching is at its greatest value ($2.5 \leq \beta \leq 3.5$) and accommodated by three fault sets. Structural complexity has increased dramatically, particularly within the

basement. First generation faults are increasingly back-rotated (sub-horizontal), oceanward along the profile, and are cross-cut by the second and third generation faults.

Marked velocity distortions are apparent in the synthetic data (Fig. 4.7i(a)) especially relating to intra-basement reflectors resulting from complexities introduced by PPF. These velocity distortions lead to increased difficultly in correctly interpreting the data. The brightest reflections in Fig. 4.7(i) relate to second generation (top basement) faults that have been rotated to moderate dips, with true "top basement" reflections being of lower amplitude due to their relatively low impedance contrast. The seismic response (Fig. 4.7(i)(a)) to basement structures is quite complex and difficult to interpret. Obvious expressions features related to the PPF mechanism are not present within the data. One possible interpretation of the data (Fig. 4.7(i)(a)) is shown in Fig. 4.7(ii). Here, ramp-flat-ramp, and listric extensional structures are interpreted, and are a reasonable interpretation of the seismic data, although unlikely to be capable of accommodating the stretching observed at this section of the model. Comparison of Fig. 4.7(ii) with the input velocity model (Fig. 4.7(iii)) shows that the actual structure imaged is completely different and the interpretation is incorrect, and caused by a combination of velocity distortions within the data and the generation of reflections from all interfaces within the model.

DFB structures are abundant within the velocity model (Fig. 4.7(iii)) and where LVZs have been modelled, within the synthetic data (Fig. 4.7(i)(a)), involving all three fault generations. Bifurcation results from all fault generation permutations (Fig. 4.7; **Table 4.3**), but intersections between fault generation one and three tend to be almost orthogonal. In the instance where fault zones do not produce intra-basement seismic reflections (Fig. 4.7(i)(b)),

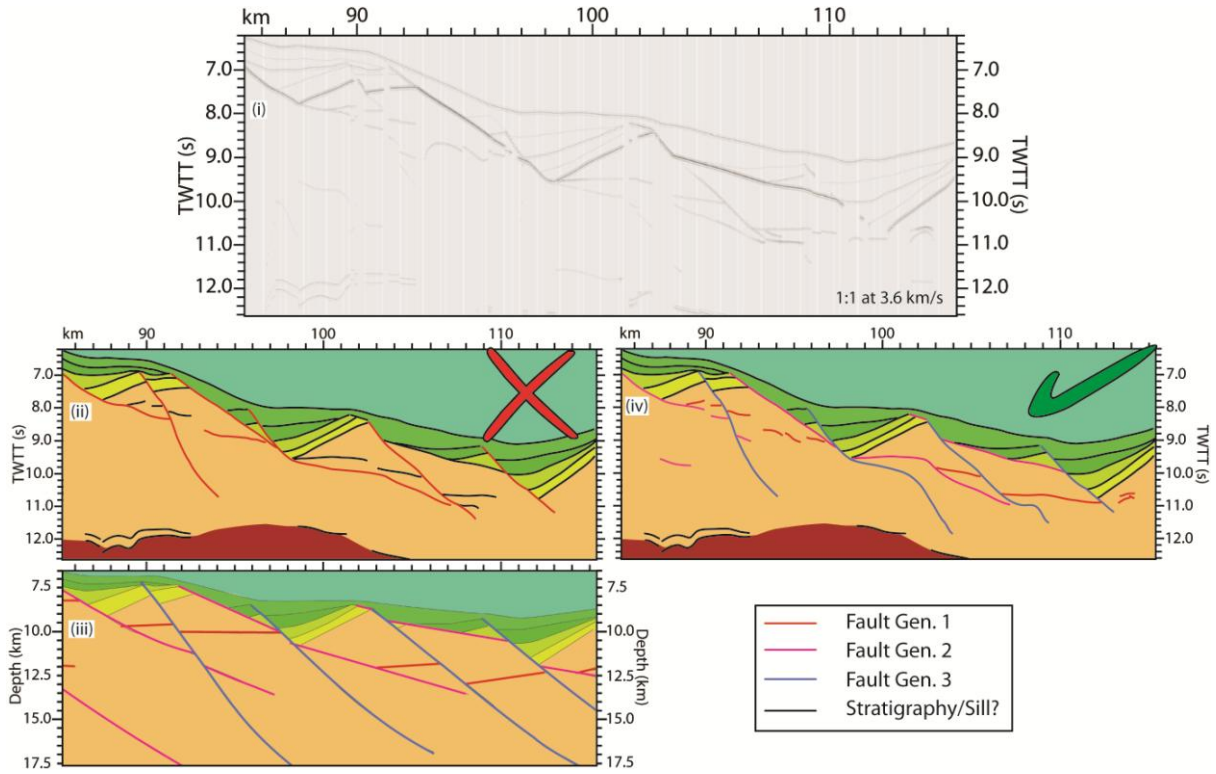

Fig. 4.7: Box out from Fig. 4.3 highlighting the difficulty in interpreting PPF systems involving three fault generations from its seismic response. Crustal stretching is c. $\beta \approx 2.5 - 3.5$. Refer to Fig. 3.3 for Vp scale. (i) Synthetic seismic section, shown with no vertical exaggeration at 3.6km/s. Velocity distortions significantly affect the imaging of PPF identifiers. Intra-basement reflections are highly discontinuous and distorted, and crestal wedges (with internal reflections). Changes in reflector amplitude are dependent on the nature of the related interface in (iii). Large-offset and passively rotated "top-basement" faults produce high-amplitude reflections. (ii) Possible interpretation of (i) where PPF is identified, but incorrectly (late faults cross-cut earlier listric extensional system). (iii) Input velocity model demonstrating complex structural geometry associated with three fault generations (i). (iv) Correct interpretation of (i) Note the severe distortion of sub-basement structures, and how the structures appear totally dissimilar to those in (iii) How likely are these reflections to be interpreted correctly even when the faults are all imaged as in (i)? Locations of individual PPF identifiers are described in **Table 4.3**.

DFBs are not observable and the structure of the synthetic data appears relatively uncomplicated. However, other features above top-basement may betray the presence of multiple fault generations.

Large CWs bounded by fault generations one and two are augmented by fault generation three are present in Fig. 4.7. Only one true crestal wedge (bounded by the second and third generation faults) is present at this part of the margin (Fig. 4.7; **Table 4.3**). Another, smaller fault bounded wedge is present in Fig. 4.7, but is not a CW, as it is not on the crest of its footwall block. Differentiating the mechanism of wedge formation between PPF or flexural rotation of the footwall block and a splay fault (forming a UFB) is extremely difficult. All types of fault-bounded wedge display UFBs, both in the velocity models (Fig. 4.7a) and the synthetic data (Fig. 4.7b). However, to convincingly differentiate the mechanisms of formation, it is necessary to identify DFBs in the hangingwall. as can be done in this example (Fig. 4.7). However, in regions of extremely attenuated crust fault bounded wedges may well be indicative of multiple fault generations.

Fig. 4.7 also demonstrates oversteepened stratigraphy that strongly suggests that extension occurred over multiple fault generations, with fault-stratum intersections (km 90.75, 8.5km/ km 90.75, 7.5s TWT; and km 112, 12.0km/ km 112, 10.8s TWT (Fig. 4.7(i, iii, iv)) to 90°. Taken together with the extreme crustal attenuation on this part of the margin suggests there has been more than one fault phase. This evidence can be used to identify the PPF mechanism even if there are not intra-basement fault zone reflections.

PPF Identifier	Velocity Model (km, km)	Seismogram (km, s TWT)	Comments
Crestal Wedge	105.0, 9.5 - 110.0, 10.0	105, 9.0 - 110, 10.0	
	101.5, 8.5 - 103.0, 9.0	101..5, 8.2 - 102.5, 8.4	
	94.5, 8.5 - 97.0, 10.0	94.5, 8.1 - 97.0, 9.0	Small fault bounded wedge. (CW - like)
	85.0, 7.5 - 97.0, 10.0	85.0, 6.8 - 97.0, 9.0	Large fault bounded wedge (CW-like)
Up-dip Fault Bifurcations	97.5, 10.0	97.0, 9.0	Intersection all fault gens.
	92.5, 11.25	91.5, 8.4	Intersection 2nd & 3rd gen.
	103.0, 8.75	02.5, 8.4	Intersection 2nd & 3rd gen.
	110.5, 10.5	110.5, 10.0	Intersection 2nd & 3rd gen.
	91.0, 9.5	91.5, 8.0	Intersection 1st & 3rd gen.
	106.5, 12.0	106.5, 10.0	Intersection 1st & 3rd gen.
	112.5, 12.25	112.5, 10.9	Intersection 1st & 3rd gen.
Down-Dip Fault Bifurcations	88.5, 9.5	89.0, 7.9	Intersection 1st & 2nd gen.
	103.0, 12.0	102.5, 9.8	Intersection 1st & 2nd gen.
	104.0, 12.25		Intersection 1st & 2nd gen Highly distorted
	114.5, 12.25		Intersection 1st & 2nd gen. Highly distorted
	93.5, 12.0		Intersection 2nd & 3rd gen Highly distorted
	98.0, 10.5	98.5, 9.6	Intersection 2nd & 3rd gen.
	103.5, 9.5	103.5, 9.0	Intersection 2nd & 3rd gen.
	112.0, 12.0		Intersection 2nd & 3rd gen Highly distorted
	92.0, 10.0	91.5, 8.2	Intersection 1st & 3rd gen.
	108.0, 13.0	107.0, 10.7	Intersection 1st & 3rd gen.

Table 4.3: Coordinates of where PPF identifiers and associated structures can be observed where present in the model (Compare with Fig. 4.7). Crestal wedges are shown top left and bottom right corners of a rectangle.

From comparison between the synthetic data (Fig. 4.7(i)) and the velocity model (Fig. 4.7(iii)) ,it is clear that much of the structure is affected by severe velocity distortions. Most of the PPF structures would almost certainly be misinterpreted, causing the mechanism to go unrecognised on seismic data. PPF structures will go unrecognised not simply because

they are not imaged on seismic data, but even when 100% of the faults produce reflections the reflection patterns are so complicated that they would never be interpreted correctly. Depth migration of the data may aid in the identification of the PPF mechanism at MPRMs, but this would require that the correct velocity model is chosen for the conversion, which can only be obtained from drilling and refraction seismic. However, the highly variable lateral velocity gradient will hinder correct and depth migration and still structural information will be lost. This will lead to estimations of extension in the highly extended parts of margins and hyper-extended basins to be severely underestimated

4.3.2 Yerrington District PPF, W. USA (Proffett, 1977)

A real world example of the polyphase faulting mechanism is shown in Figs 4.8 & 4.9. The model is based on structural cross-sections produced by Proffett (1977) for the Basin & Range region (USA). Proffett (1977) presented the first widely known example of PPF in the literature (**Section 3.3.1** for description). Palinspastic restoration of Proffett (1977)'s section (**3.3.1**), show the section has been extended by c. 230%, accommodated by at least three individual fault generations - although the latest, high-angle faults are not responsible for a very significant portion of the stretching (Proffett, 1977; Zoback et al., 1981). The oldest fault generation was passively rotated to sub-horizontal orientations, by extension on the succeeding fault generations via the PPF mechanism (Discussed in **Chapter 3**). The extension estimate based on the Proffett (1977) cross-section assumes rigid block rotation, and as such probably is an underestimate of the total extension. So, this modelled section may be considered a "rigid" domino PPF model, where there is very little internal block deformation.

The section presented by Proffett (1977) is modelled both without and with fault zones (LVZs) at different scales; Proffett (1977)'s original section dimensions (Figs 4.8a & 4.9a), and at five times the original section dimensions in order to create structures that are comparable in size to those that might be encountered in a rifted margin setting (Margin scale) (Figs 4.8b & 4.9b). The limit of seismic resolution for these models, for a dominant frequency of 20 Hz and an average velocity of 3 km/s, is c. 37.5 m. As such, it is expected that the margin scale sections will have greater resolution of structures than the original scale sections as they are much larger. The Proffett (1977) section demonstrates examples of crestal wedges (CW), up- and down-dip fault bifurcations (UFB & DFB), and oversteepened stratigraphy (OS). However, depending on the initial modelling conditions (scale, inclusion of discrete fault zones), not all identifiers will be imaged or interpretable on output seismograms (see Figs 4.8 & 4.9; **Table 4.4**).

PPF Identifier	Velocity Model (km, km) - (km, km)	Seismogram (km, s TWT - km, s TWT)	Comments
Crestal Wedge	9.2, 0.5 - 12.8, 1.2 (46.0, 2.5 - 64.0, 6.0)	9.2, 0.6 - 12.8, 1.15 (46, 3.0 - 64.0, 6.0)	
Up-Dip Fault Bifurcations			No obvious Expressions
Down-Dip Fault Bifurcation	13.0, 1.6 (65.0, 7.75)	13.0, 1.35 (64.75, 7.0)	
	13.7, 1.4 (68.5, 7.0)	13.7, 1.2 (68.25, 6.5)	

Table 4.4: Coordinates of where PPF identifiers and associated structures can be observed where present in the model (Compare with Fig. 4.8). Crestal wedges are shown top left and bottom right corners of a rectangle. Coordinate without parentheses relate to Fig. 4.8a, those within, relate to Fig. 4.8b.

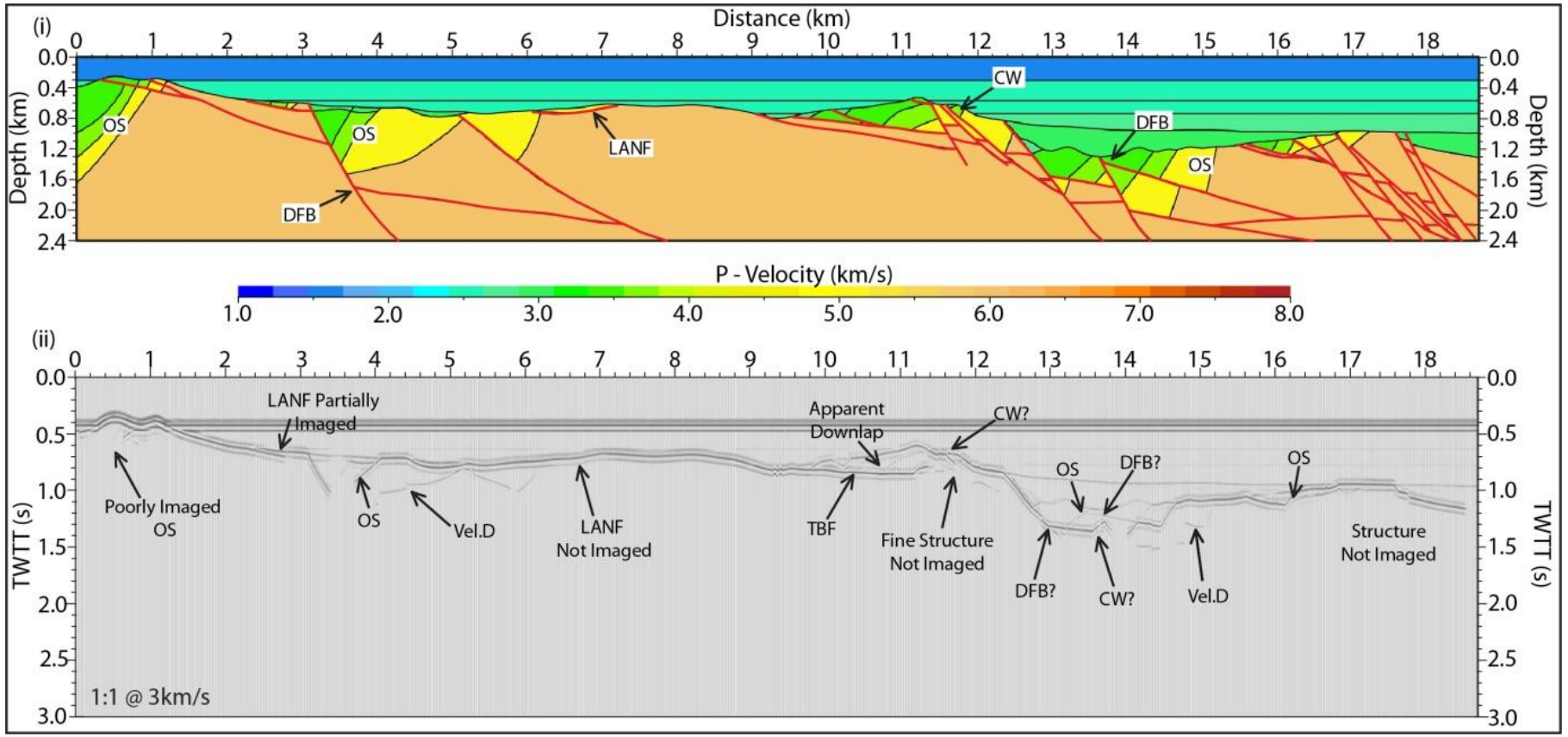

Fig. 4.8(a): (i) Velocity model derived from Proffett (1977), modelled original scale. Fault zones are not included in the velocity model. The section has undergone c. 230% extension over 2-3 fault generations. Older faults are rotated to shallower angles during progressive extension, and the earliest fault generation is now sub-horizontal. PPF identifiers present include; crestal wedge (CW), UFBs and DFBs (see **Table 4.4**). (ii) Seismic response to original scale model, shown at 1s = 1km at 3km/s. The PPF identifiers are well represented in the data (see Table 4). There is a strong possibility that these data may be misinterpreted however (see Fig. 4.10) Note that oversteepened stratigraphy at km 0 – 1 is not imaged due to proximity to model edge.

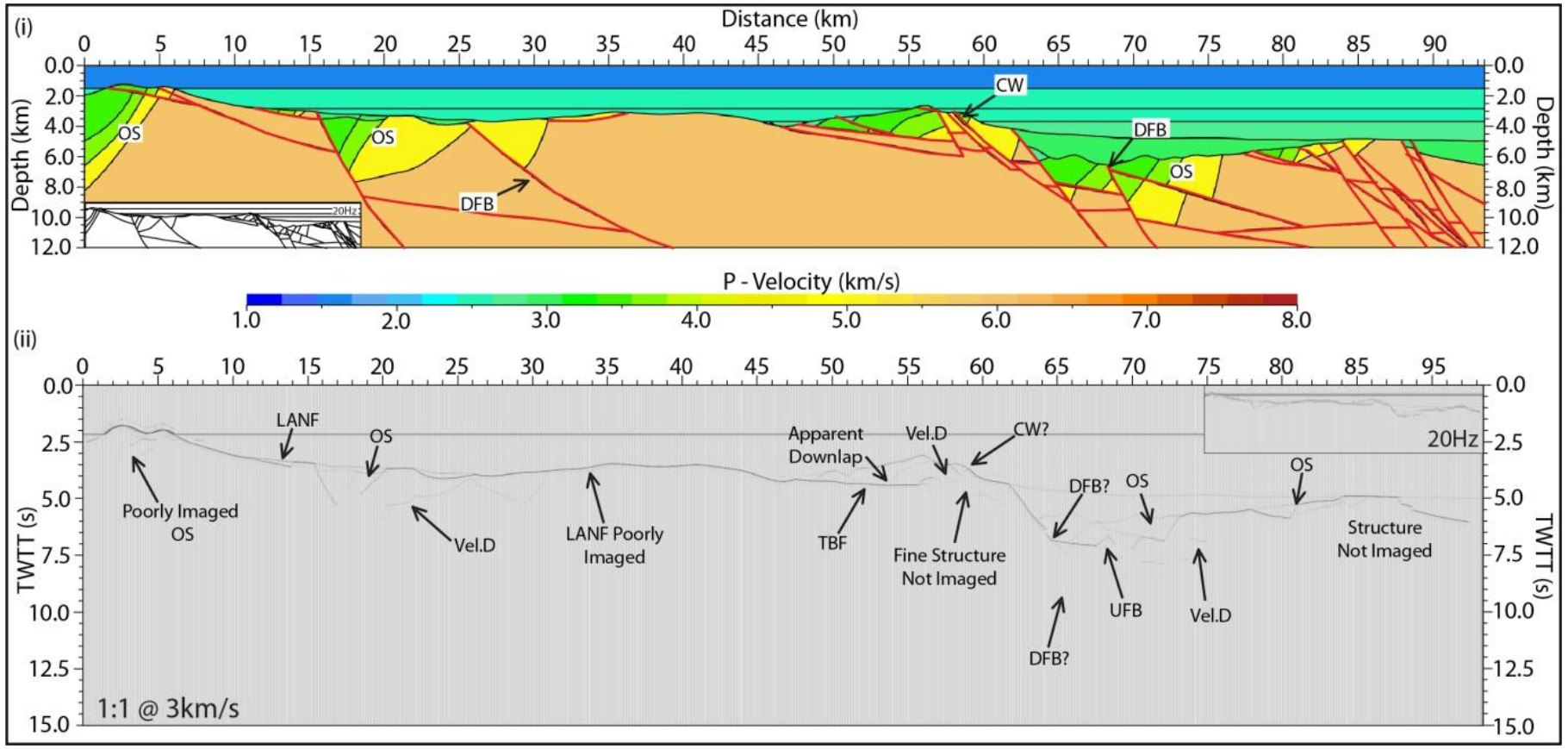

Fig. 4.8(b): (i) "Margin scale" version of (a). Modelled using a dominant frequency of 100Hz, simulating structures five times larger as though they were imaged with a frequency of 20Hz. (ii) Seismic response to "margin" scale model has no vertical exaggeration at 3km/s. Scale inset of (a) is shown for comparison. It is clear that PPF identifiers are more easily recognised at larger scale structures (a)(see **Table 4.4**). It is possible to identify reflections within the crestal wedge that were not observable in (a). Note. Oversteepened stratigraphy at km 0 – 5 is not imaged due to proximity to model edge.

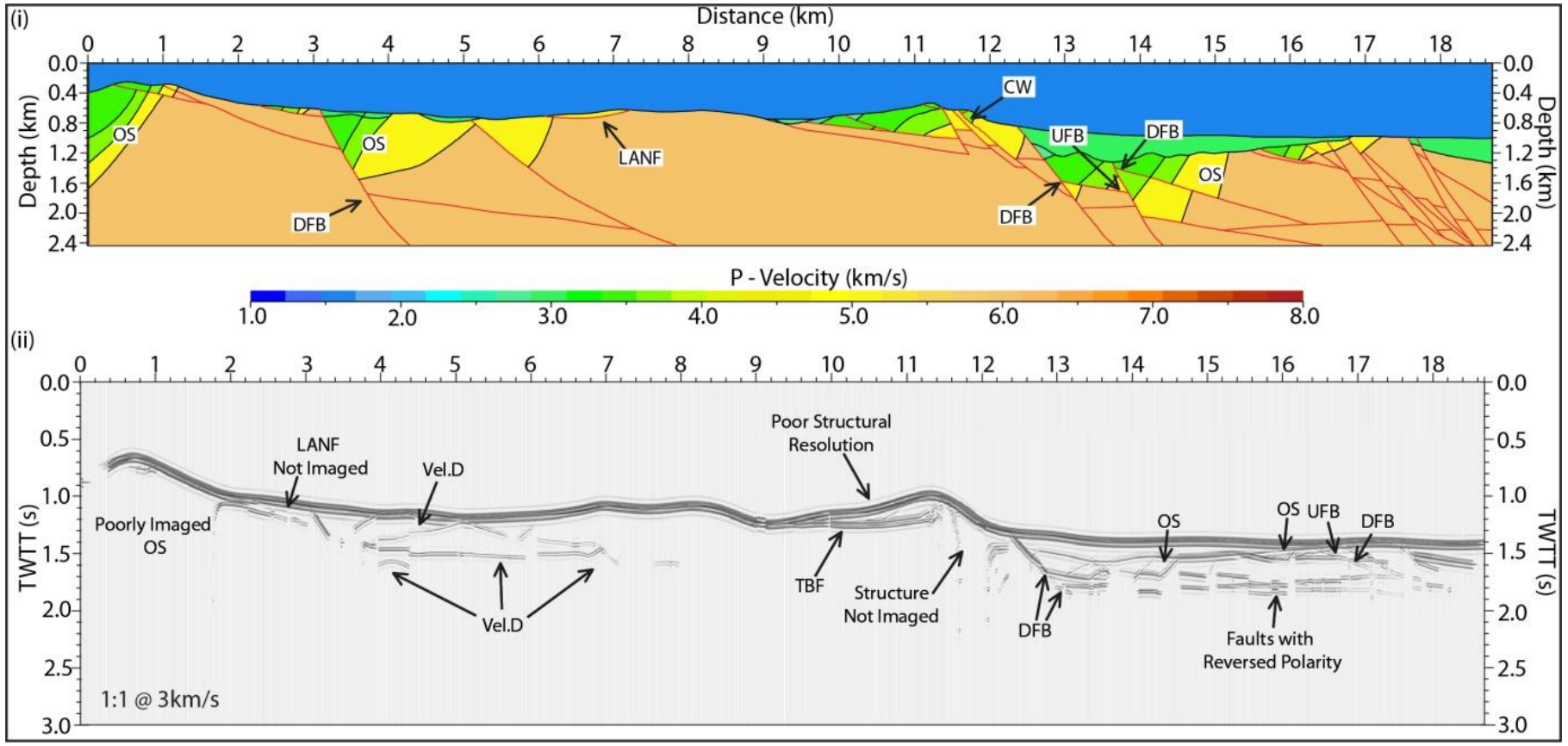

Fig. 4.9(a): (i) Velocity model based on the Proffett (1977) section. Similar section to Fig. 4.8a, but with low-velocity zones (LVZs) incorporated into the velocity model to simulate reflective faults. Post-rift sediments are not included in the velocity model due to limitations in number of model blocks allowed. (ii) The high amplitude seafloor reflection occurs because of the lack of post-rift sediments in the model. This has the effect of obscuring some of the structural information immediately below it. LVZs generate intra-basement reflections, and allow PPF identifiers such as DFBs to be better identified (see **Table 4.5**). Velocity pull up within the basement is quite severe and has a strong effect on intra-basement reflections, this is partially due to the shallow depth of section, and relatively high basement velocity compared with the sediment fill. This distortion can in some cases give the faults the appearance of possible stratigraphic layering, and must be considered during interpretation of the data.

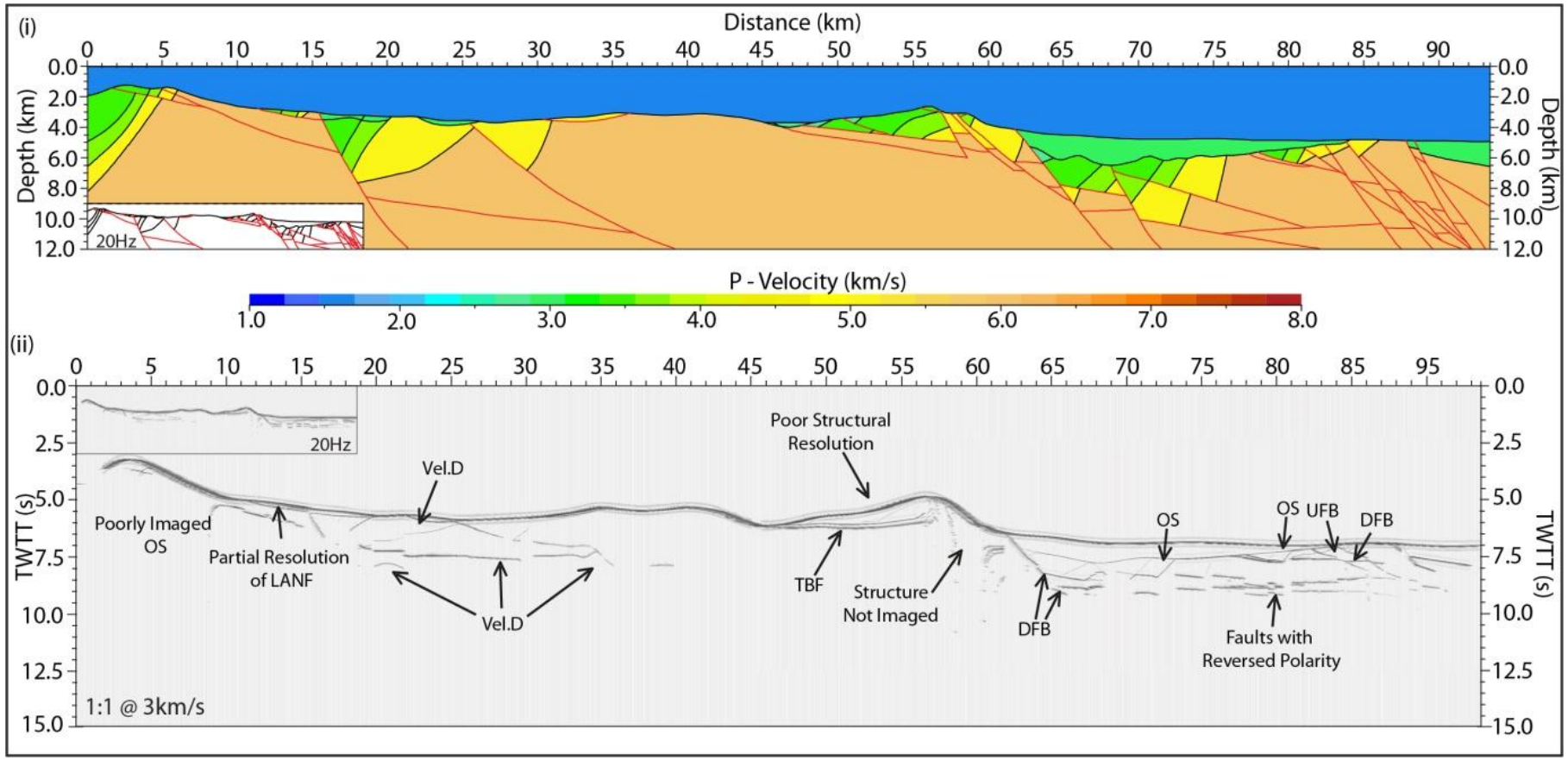

Fig. 4.9(b): (i) "Margin scale" velocity model, based on Fig. 4.9a, but modelled with a dominant frequency of 100Hz to simulate structures five times larger as if imaged with a dominant frequency of 20Hz. Fig. 4.9a is shown to scale in the inset for comparison. (ii) Very strong seafloor reflection due to lack of post-rift sediments. However, due to the larger scale of the structures here, it is possible to resolve some detail in the CW present at km 45 – 60 yield sub-horizontal reflections that give the appearance of stratigraphic layering. Careful attention must be paid to reflections that may be present between these sub-horizontal reflections that may relate to oversteepened stratigraphy and so suggest that the bright sub-horizontal reflection are fault plane reflections, aiding in the interpretation of PPF related structures (see **Table 4.5** for locations of PPF identifiers and structures).

The first model variant includes three layers of post-rift sediment (Fig. 4.8). The second includes discrete fault zones (≤ 5 m thick, low velocity zones; Fig. 4.9). Due to limitations within the modelling package, it was not possible to model Fig. 4.9 with post-rift sediment. The lack of post-rift sediments in Fig. 4.9 caused the "sea-bed" interface to generate very high amplitude reflections that reduce the amplitude of subsurface reflections (Fig. 4.9).

The structure of the velocity model (Figs 4.8 & 4.9) can be quantitatively split onto two separate sections. A relatively simple case for three fault sets interacting exists at km 0 – 9 (Fig. 4.8), where older fault structures are not obscured or overprinted by younger generations and dip at progressively shallower angles. The structure at km 9 – 18 (Fig. 4.8) of the section is far more complicated as many fault sets tend to nucleate, cross-cut, overprint, and offset one another. The structure here is further complicated by the presence of antithetic faults (see Figs 4.8 & 4.9) overturned via passive rotation during subsequent faulting and now appear as reverse faults (**Section 3.3.1**).

An example of a crestal wedge (CW) can be observed on the velocity models (Figs 4.8 & 4.9). Although complicated by splay faults, the seismic response to the structure is quite good (Figs 4.8a(ii)/b(ii) & 4.9a(ii)/b(ii)). Down-lapping reflector geometries between moderately to steeply dipping strata and the lower bounding fault surface, which forms a bright sediment-basement reflection, can be observed in Fig. 4.8a(ii)/b(ii). However, due to the high-amplitude seabed reflector, down-lapping reflectors are obscured and not easily identified within the CW (Fig. 4.9). The internal structure of the CW is better resolved on the larger scale model (Fig. 4.9b) and it is possible to identify the presence of a splay fault at km 51 – 52. Fig. 4.9(b) shows slight improvement over the structure than in Fig. 4.9(a) as some

downlapping reflector geometries are better resolved within the wedge. This increases the chances of the lower bounding fault surface being identified as such. The crestal wedge is highly complex over the ranges km 11 – 12.8 (Fig. 4.8a & 4.9a) and km 56 – 62 (Fig. 4.8b & 4.9b). The internal structure of the CW over this interval is fairly well resolved in Fig. 4.8, and moderately dipping reflectors (synthetic to the high-angle bounding fault) can be seen (Figs 4.8a & b), whereas the structure is unresolvable in Fig. 4.9, where no post-rift sediments are modelled. It should be noted that little additional information is gained from the larger model's seismic response (Figs 4.8b & 4.9b), relative to the smaller structural model's (Figs 4.8a & 4.9a).

Down-dip fault bifurcations (DFBs) are best observed where FZs have been modelled within the basement (Fig. 4.9) but in some cases they are observable from fault induced juxtapositions within the later faults' hanging walls (Fig. 4.8). DFBs are not easily identifiable in Fig. 4.8 since FZ are not modelled discretely as in Fig. 4.9. Some evidence for DFB development can be identified in at km 13, 1.35s TWT, and somewhat convincingly at km 13.7, 1.2s TWT (Fig. 4.8a). The larger structures in Fig. 4.8b demonstrate the development of DFB more clearly and it is observed at km 64.75, 7.0s TWT and km 68.25, 6.5s TWT. Where discrete FZ are modelled within the basement (Fig. 4.9), intra-basement reflections are generated and, as such, DFBs are common and readily identifiable. Velocity distortions are exacerbated beneath older, higher velocity material. This could be problematic when trying to interpret fault structures (where they generate reflections). This velocity distortion causes otherwise planar faults to appear strongly listric (Fig. 9a(ii)/b(ii)). The majority of the structures within the basement are moderate to shallowly dipping, and so effectively yield

sub-horizontal reflections, possibly giving them the appearance of stratigraphic layering. Despite these complications, many examples of DFB can be observed by comparison between the velocity model and the output synthetic data in Fig. 4.9. From km 16 (Figs 4.8a & 4.9a) and km 80 (Fig. 4.8b & 4.9b) onwards, it is especially difficult to identify DFBs. In the case of Fig. 4.8, where FZs are not modelled, DFB are not observable as the majority of the structure is intra-basement in nature. Even when FZs are modelled as in Fig. 4.9, the fault plane reflections being offset are sub-horizontal and appear similar to mild to moderately tilted sedimentary layering. These FZ reflections are likely only to be recognised as fault plane reflections if down-lapping reflections geometries can be identified. The geometry of the fault zone reflections are more easily identifiable in Fig. 9b because the structures are much larger than in Fig. 4.9a.

PPF Identifier	**Velocity Model (km, km) - (km, km)**	**Seismogram (km, s - km, s)**	**Comments**
Crestal Wedge	9.0, 0.5 - 12.8, 1.2 (46.0, 2.5 - 64.0, 6.0)	9.2, 0.6 - 12.8, 1.15 (46, 3.0 - 64.0, 6.0)	(UFBs & DFBs are present within CW, but are not resolved)
Up-Dip Fault Bifurcations	3.4, 1.15 (17.0, 5.5) 7.20, 2.20 (36.0, 11.0) 13.85, 1.7 (81, 10.5)	3.3, 1.30 (17. 0, 6.75) 6.95, 1.45 (34.4, 7.25) 13.8, 1.7 (80, 8.75)	
	16.2, 2.2 (84.0, 7.0)	16.1, 1.75 (84.0, 7.5)	Not true PPF structure. Site of fault splay.
	16.2, 1.0 - 18.2, 2.2 (81 - 92, 5.0 - 11.0)	16.2, 1.4 - 18.2, 1.8 (82 - 91.5, 7.0 - 9.0)	Nucleation of closely spaced faults
Down-Dip Fault Bifurcation	3.75, 1.75 (18.5, 8.5) 13.0, 1.6 (64.5, 7.75) 13.15, 1.90 (66.0, 9.5) 13.7, 1.4 (68.5, 7.0) 15.1, 2.2 (76.0, 11.0)	3.6, 1.5 (18.0, 7.5) 12.8, 1.65 (64.5, 8.25) 13.1, 1.8 (65.5, 9.0) 13.7, 1.65 (68.5, 8.25) 15.5, 1.8 (77.5, 9.0)	
	16.2, 1.0 - 18.2, 2.2 (81.0, 5.0 - 92, 11.0)	16.2, 1.4 - 18.2, 1.8 (82.0, 7.0 - 91.5, 9.0)	Nucleation of closely spaced faults

Table 4.5: Coordinates of where PPF identifiers and associated structures can be observed where present in the model (Compare with Fig. 4.8). Crestal wedges are shown top left and bottom right corners of a rectangle. Coordinates without parentheses relate to Fig. 4.9a, and those within, Fig. 4.9b.

Oversteepened stratigraphy is very common PPF identifier on the Proffett (1977) section. Stratigraphy in the region is very often steeply inclined, with tilts far in excess of what might be expected from the latest high-angle faults, due to block rotation on multiple fault generations. The block rotation introduces significant lateral variations in seismic velocity, and so effects on how structures beneath an individual fault block are imaged. Fault zone reflections are sometimes highly fragmented (Fig. 4.9a, km 13 – 17.2; Fig. 4.9b, km 66 – 86) caused by this induced lateral velocity gradients in the hangingwall of the latest fault sets in regions of high extensional strain. The orientation of the strata within the fault blocks lead to very high degrees of lateral velocity heterogeneity, and so potentially the production of complex reflection patterns beneath steeply dipping strata.

Two interpretations (a plausible, but incorrect interpretation and the correct interpretation) of the synthetic data from Fig. 4.8, where no intra-basement FZs are imaged, are shown in Fig. 4.10. The CW from Fig. 4.8a is interpreted as a contourite/drift deposit, while the rest of the section appears as a series of low-strain tilted fault blocks. This incorrect interpretation could account for the reflections present, if PPF identifiers are not recognised. Fig. 4.10(ii) demonstrates the most correct interpretation that can be made from the synthetic seismogram, and takes into consideration PPF identifiers. Recognition of OS within the section is crucial in identifying the mechanism on seismic data. However, this is problematic as steeply dipping reflections are not imaged particularly well on the data in all cases (Fig. 4.8a(ii) & b(ii)).

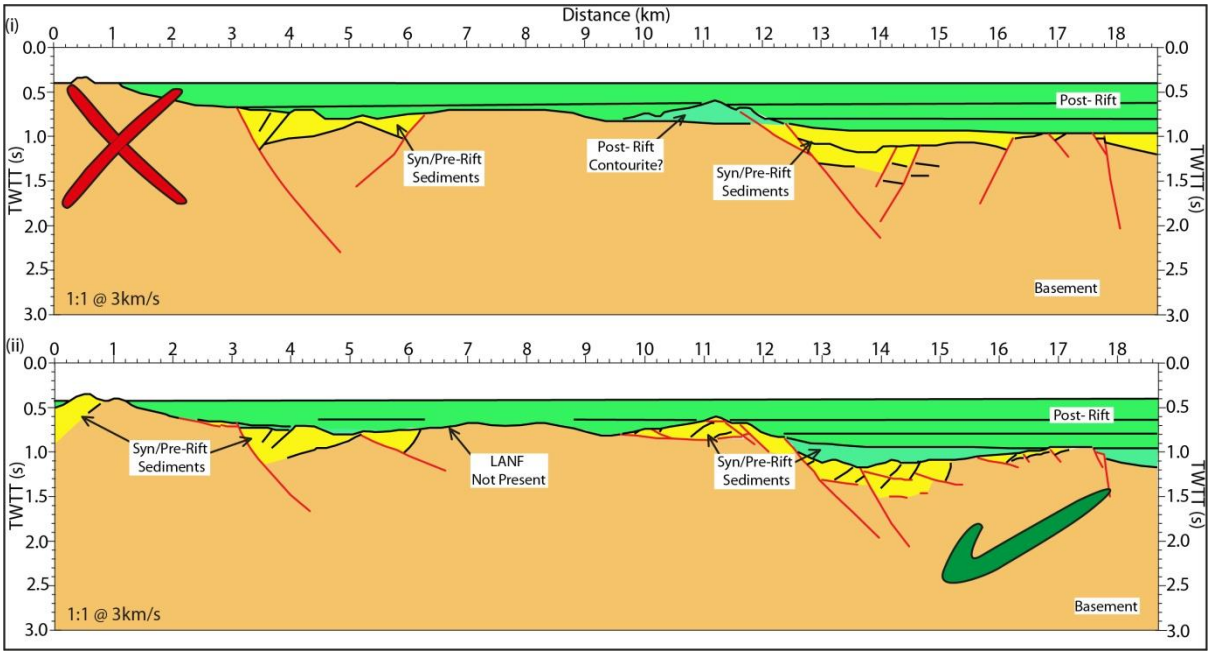

Fig. 4.10: (i) Potential (incorrect) interpretation of the synthetic data in Fig. 4.8. The data is interpreted as a low-strain extensional system where with only high-angle faults present. This is often the case at MPRMs where only the high-angle faults are recognised on seismic data. The result of which is to massively underestimate the amount of extension attributable to faults. (ii) The correct interpretation of the data in Fig. 4.8. Comparison of reflections with the input model drove this interpretation. This interpretation is more likely to be made if significant crustal thinning is known to be present, then combinations of PPF identifiers can be used to build the case for the PPF mechanism extending the crust.

4.3.3 Lemitar Mountains PPF, New Mexico (Chamberlin, 1982)

As observed in the previous sections, oversteepened stratigraphy can be a very useful identifier of the PPF mechanism for extension. Here, two sections originally presented by Chamberlin (1982) from the Lemitar Mountains, New Mexico, USA, are investigated. Although probably not true PPF (as in **Section 3.3.2)**, the stratigraphy has been strongly tilted due to displacement on now low-angle faults that likely operated as a rolling-hinge style system (Buck, 1988; **Section 3.3.2**).

Palinspastic restoration of Figs 4.11 & 4.12 show that the sections have been extended by c. 136% and 145% respectively (**Section 3.3.2**) with 3 - 4 fault phases. The majority of the extension was accommodated by the low-angle, large offset fault system (**Section 3.3.2**).

Some minor extension was later accommodated by the high-angle cross-cutting extensional system.

As in **Section 4.3.2**, some of the sections presented by Chamberlin (1982) are modelled at two scales; the original dimensions (Figs 4.11a & 4.12a), and at margin scale (Figs. 4.11b & 4.12b), five times larger than the original. The resulting seismograms are considered to have been modelled for a dominant frequency of 20 Hz and so the seismic resolution (if an average velocity of 4 km/s is considered) for Figs 4.11 & 4.12 is c. 50 m. The sections include post-rift sediments in order to maximise the resolution of the structures, but do not include modelled LVZs.

The PPF identifiers (discussed in previous sections) are present to varying degrees, but as the latest fault phase is not always synthetic to the preceding fault generations, it is not always possible to identify DFBs. The lack of modelled low-velocity zones coupled with relatively low amounts of displacement on the latest fault sets is not conducive to DFB imaging. Faults within the models are instead identified from observation of offset reflections. In some causes fault, planes are identified from the reflections caused by sediment-sediment, or sediment- basement juxtapositions. The post-erosional remains of CWs are present in the data, but unfortunately they are not well imaged on the synthetic data. These sections demonstrate how crestal wedges would likely manifest in regions of low sedimentation, and high erosion rates. The strongest evidence for PPF in these sections comes from the OS, relative to the latest fault sets. The steeply dipping strata, and their associated low-angle faults are well imaged in the data.

Section A from Chamberlin (1982) (Fig. 4.11) is described first. A severely eroded crestal wedge can be observed on the velocity models in the areas bounded by km 3.4, 0.40 km – km 5.0, 0.48 km (Fig. 4.11a); km 17.2, 2.0 km – km 25, 2.6 km (Fig. 4.11b), above an overturned fault. The velocity models demonstrate the composite nature of the wedge. The wedge consists of multiple low-angle faults that form a basal bounding surface. The low angle faults cut up through the wedge and form were probably the original edge bounding fault to the undisected fault block (Fig. 4.11a(i)&b(i)). Many of the smaller scale faults were likely splay faults rather than a series of successive fault generations.

The present day edge bounding fault is out of the plane, to the right of the section. The CW is not imaged well in Fig. 4.11a(ii) because erosion and mass-wastage has removed so much of the feature that it is on the limits of seismic resolution. The data do hint as to its presence however, and two closely spaced reflections can be seen at the base of the post-rift at km 3.5, 0.58s TWT – km 4.2, 0.50s TWT and km 4.36, 0.50s TWT – km 5.0, 0.57s TWT (Fig. 4.11a(ii)). Although it is not possible to resolve the internal structure of the crestal wedge, the dip of stratigraphy (km 2.56, 0.6s TWT – km 4.00, 0.95s TWT, Fig. 4.11a(ii) beneath these closely spaced reflections are consistent with the lowermost reflection being a low-angled (basal bounding) fault. The same structure on Fig. 4.11b (km 17.6, 2.85s TWT – km 22.6, 2.55s TWT) is more clearly resolved and reflections are observed between the two sub-horizontal reflections that down-lap onto the basal reflection (basal bounding fault). The down-lapping reflections are steeply dipping, and are of similar orientation to the steeply dipping reflections beneath the crestal wedge (km 12.7, 2.9s TWT – km 20.0, 4.6s TWT), suggesting that these reflections are also strongly tilted stratigraphy. From these

observations it can be convincingly argued that the feature is a CW. This is a good example of how the scale of a structure can determine whether it is recognised on seismic data or not.

DFBs are not common in Fig. 4.11a(ii)&b(ii) for reasons described above. The best examples of DFB can be seen at km 2.16, 0.76km (Fig. 11a); km 10.8, 3.8km (Fig. 4.11b). The DFB formed from the interaction between a late stage high-angle normal fault and one of the early, low-angled fault sets. This feature is expressed on the synthetic data as a strong kink at km 2.16, 0.75s TWT (Fig. 4.11a(ii)), and perhaps more clearly at km 10.8, 3.7s TWT (Fig. 4.11b(ii)). This high-angled fault clearly offsets the high amplitude (sediment-basement contact) low-angle fault associated with the steeply dipping sediments.

The low-angle normal faults tend to form synformal geometries on the synthetic data (Fig. 4.11a(ii) & b(ii). From comparison with the input model, it can be clearly seen that this is a velocity distortion caused by the strongly tilted stratigraphy. Generally seismic velocity increases with depth, so as deeper lithologies are exhumed by rotation within fault blocks they impose strong lateral variations in velocity gradient. This in turn causes reflections beneath the tilted stratigraphy to be distorted on seismic data. The effect is exacerbated beneath higher velocity material.

The strong velocity distortions that are imposed on the well-imaged low-angle normal faults could result in misinterpretation of parent structure. Bearing in mind that the synthetic seismic generation was biased towards imaging of steeply dipping structures, the best case imaging scenario, a potential interpretation of the data is shown in Fig. 4.11c(i).

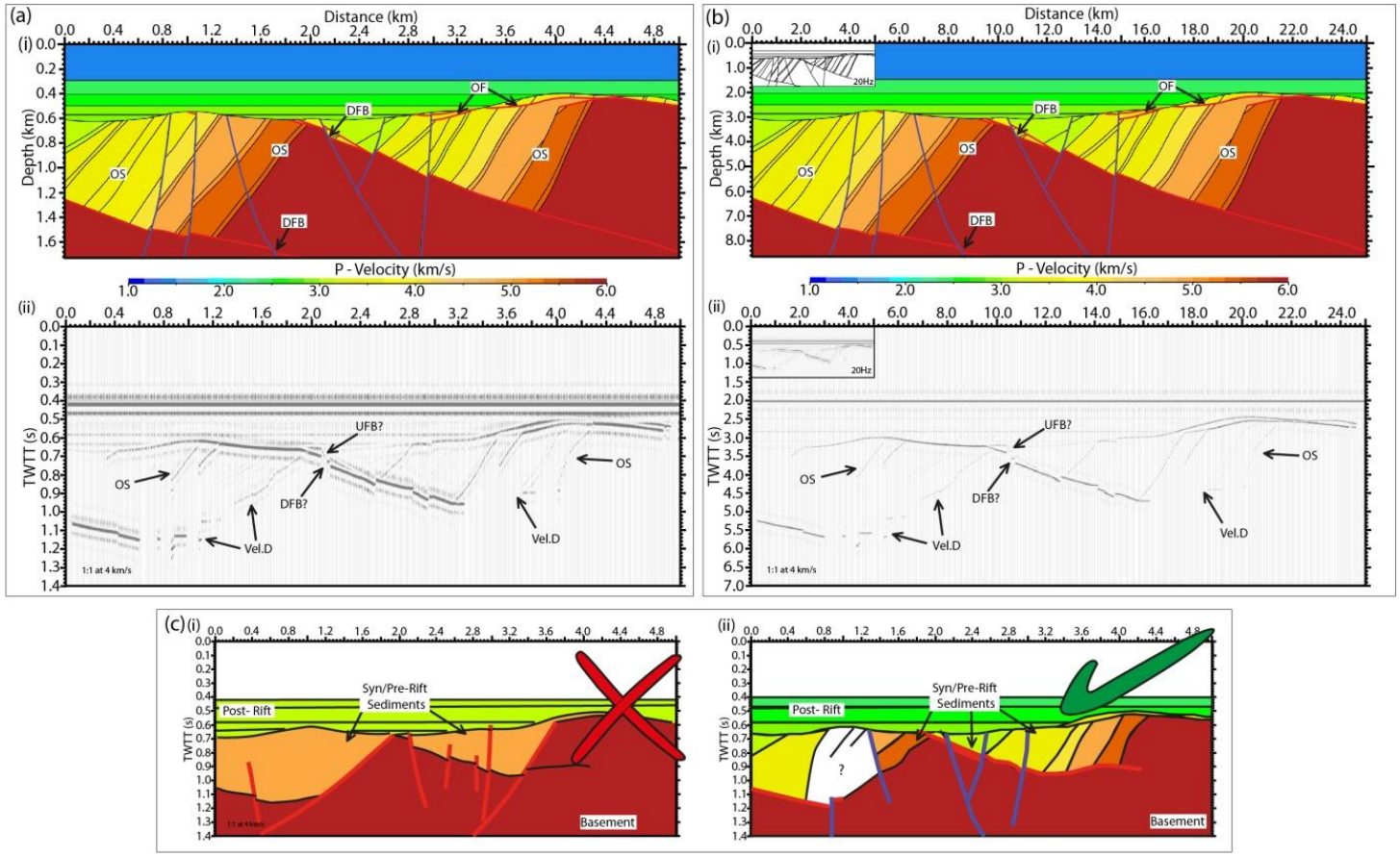

Fig. 4.11: Section A from Chamberlin (1982). Extended by c. 136% over 3-4 fault phases. Three major low-angle fault structures strongly tilt stratigraphy. Structure is complicated by a high-angle fault system that cross-cuts everything. PPF identifiers; an eroded crestal wedge (CW), and sporadic UFBs and DFBs are present (see **Table 4.6**). (a) (i) No LVZs are incorporated into the velocity model. (ii) Seismic response to (i). No vertical exaggeration at 3km/s. No intra-basement reflections present. High-amplitude sub-horizontal reflections at top-basement level relate to low-angles faults. PPF identifiers are present, see **Table 4.6**. The data suffer from strong velocity distortions and other imaging problems due to OS, and structures below seismic resolution. Note crestal wedge remnant km 3.4 – 4.8 is imaged as two very closely spaced reflectors, no observable internal structure. (b)(i) Margin scale version of (a)(i) modelled at for a dominant frequency of 100Hz

to simulate structures five times larger. (a)(i) is shown, to scale as an inset. (ii)Seismic response to "margin" scale model. No vertical exaggeration at 3km/s. Synthetic section from (a)(ii) is shown to scale. Note superior resolution of structures at larger scale. It is possible to observe some internal structure within the remnant wedge at km 17 – 24 at this larger scale. (c) Two possible interpretations of (a)(ii). (i) Incorrectly interpreted as a series of tilted fault blocks. This interpretation requires that the very steeply dipping structures are not imaged (they are only partially imaged here in the data because a 30km migration aperture). This interpretation would yield a major underestimation of extension. (ii) Correct interpretation based on comparison of reflections with their parent structures. Not all of the structures are fully imaged however. Note the distortion of the low-angle faults.

If a smaller migration aperture were used, and some random noise introduced to the data, the interpretation in Fig. 4.11c(i) would be quite a reasonable one, as the OS would be virtually impossible to identify due to its high-angle. Unfortunately, the interpretation of well-developed tilted fault blocks (Fig. 4.11c(i)) is not correct when the synthetic data is compared to the velocity model, and estimations of extension would be massively underestimated. The best interpretation that can be made of the data (Fig. 4.11c(ii)) assigns the reflections (where possible) to their parent structures within the velocity model (Fig. 11a(i)). Due to imaging problems associated with the oversteepened stratigraphy on the left of the velocity model (Fig. 4.11a(i)), the interpretation in Fig. 4.11c(ii) is not 100% correct. The interpretation is somewhat incomplete also, since faults were not modelled using discrete LVZs, and so do not generate reflections except where sediment-basement/sediment-sediment juxtapositions occur.

Section D from Chamberlin (1982) (Fig. 4.12) is extended to a greater degree than Section A (Fig. 4.11) over 3 – 4 fault generations. The structural expression of the stretching is not as obvious on the synthetic data (Figs. 4.12a(ii), b(ii)). The velocity model (Fig.4.12a(i), b(i)) appears to have a greater amount of high-angle faults than in Fig. 4.11 but, as described in **Section 3.3.2**, not all are from the latest fault generation.

PPF Identifier	Velocity Model (km, km) - (km, km)	Seismogram (km, s - km, s)	Comments
Crestal Wedge	6.2, 0.25 - 9.9, 0.5 (31.0, 1.25 - 49.5, 3.0)		2ng gen faults within CW. km 6.3 - 8.8, 0.4 - 0.65s TWT (km 44.0 - 52.5, 2.0 - 4.25s TWT)
Up-Dip Fault Bifurcation	2.50, 0.9 (12.5, 43.5)	2.5, 0.85 (12.4, 4.1)	Probable splay fault. No associated DFB
	(22.3, 2.2)	(22.2, 2.60)	Probable splay fault. No associated DFB
Down-Dip Fault Bifurcation	2.12, 0.64 (10.6, 3.40) 2.16, 0.76 (10.8, 3.8)	2.12, 0.70 (2.16, 0.76) 2.16, 0.76 (10.8, 3.65)	
Cross-cut faults	2.12, 0.64 (10.6, 3.40) 2.16, 0.76 (10.8, 3.8) 2.52, 0.88 (12.6, 4.4) 2.96, 1.08 (14.8, 5.3)	2.12, 0.70 (2.16, 0.76) 2.16, 0.76 (10.8, 3.65) 2.52, 0.83 (12.6, 4.05) 2.96, 0.93 (14.8, 4.5)	

Table 4.6: Coordinates of where PPF identifiers and associated structures can be observed where present in the model. Crestal wedges are shown top left and bottom right corners of a rectangle. Coordinates without parentheses relate to Fig. 4.11a, and those within, Fig. 4.11b.

The synthetic data appears complex due to the large lateral velocity gradients resulting from steeply dipping strata and an irregular topography present at the base of the post-rift (Fig.4.12a(i), b(i)). Since the section has been stretched over multiple fault generations it is possible several PPF identifiers are manifested on the synthetic data.

An erosional remnant of a crestal wedge is present on the velocity model (Fig. 4.12a(i), b(i), **Table 4.7**) but it is not very well imaged on the seismic data (Fig. 4.12a(ii), b(ii), **Table 4.7**), and is expressed in a similar fashion to the example in Fig. 4.11. The CW is expressed

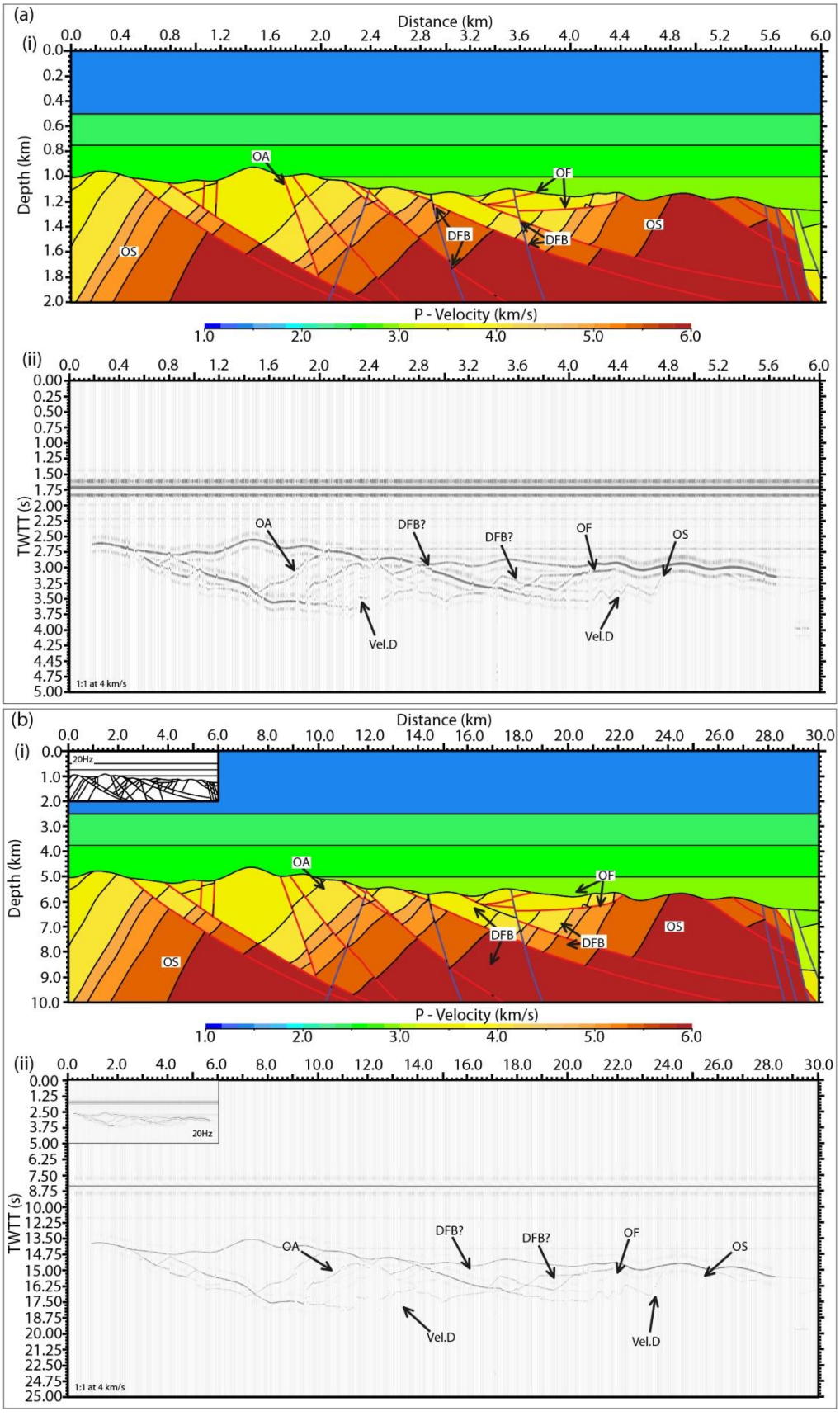
(a)
(i)
Distance (km)
Depth (km)
OA
OF
DFB
DFB
OS
OS
P - Velocity (km/s)
(ii)
TWTT (s)
OA
DFB?
DFB?
OF
OS
Vel.D
Vel.D
1:1 at 4 km/s
(b)
(i)
Distance (km)
20Hz
Depth (km)
OA
OF
DFB
DFB
OS
OS
P - Velocity (km/s)
(ii)
TWTT (s)
20Hz
OA
DFB?
DFB?
OF
OS
Vel.D
Vel.D
1:1 at 4 km/s

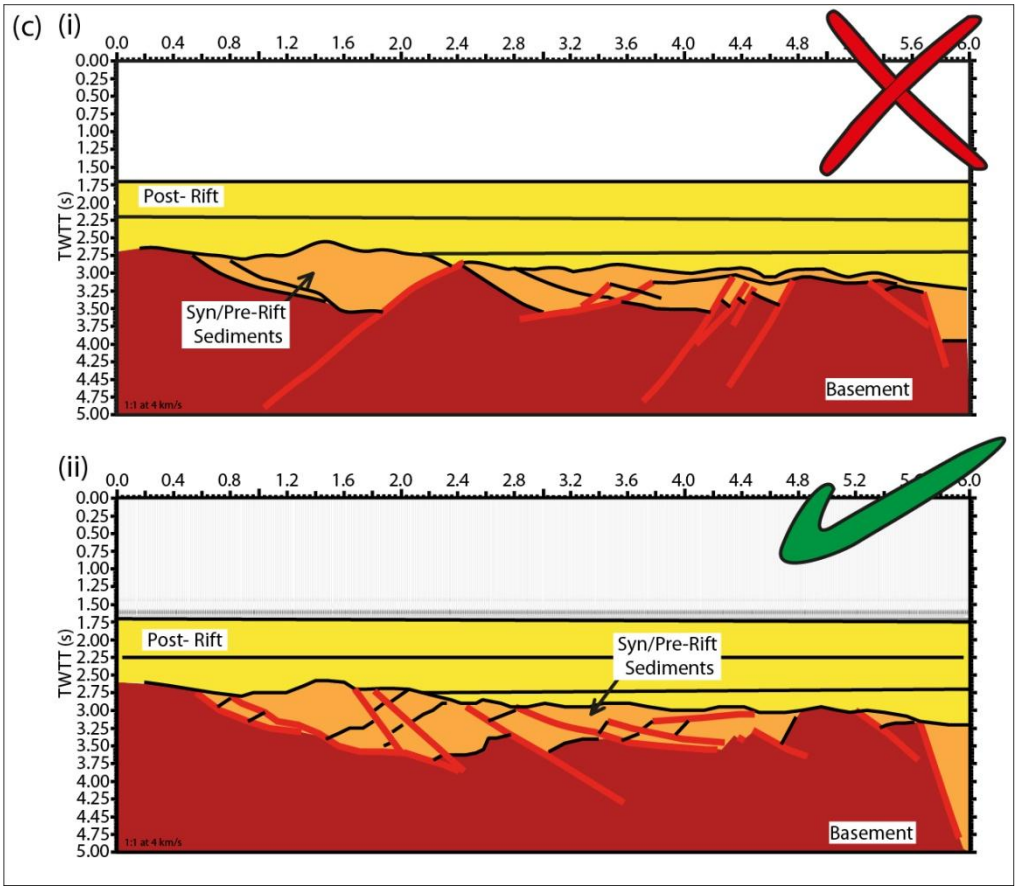

Fig. 4.12: Section D from Chamberlin (1982). Extended by c. 145% over 3-4 faulting phases. Two major low-angle, one moderately dipping, and numerous cross-cutting high-angle normal faults are present. Some of the high-angle faults are related to the low-angle structures (see text). PPF identifiers are present on the section (see **Table 4.7**). (a)(i) Velocity model with no LVZs incorporated. Imaged structure suffers from velocity distortions caused by OS and irregular topography. Despite this PPF identifiers can be observed (see **Table 4.7**). Note, that due to the scale of the structures some details are not resolvable. (b)(i) "Margin scale" section, modelled for a dominant frequency of 100Hz to simulate structures five times larger than (a). (a)(i) shown, to scale as an inset. (ii) Seismic response to "margin" scale model with no vertical exaggeration at 3km/s. Scale inset of a(i), shown for comparison. Larger structures are far better resolved, especially within the remnant crestal wedge (see **Table 4.7**). The deeper expression of the structure is affected by velocity distortions. (c) Two interpretation of (a)(ii). (i) Incorrectly interpreted as a series of tilted fault blocks based on the reflector patterns in the synthetic data (assuming that the oversteepened stratigraphy is not imaged). The bright reflections generated by the low-angle faults are interpreted as top basement. (ii) Correct interpretation, made from comparison between reflectors and their parent structures in a(i). Imaging and identification of oversteepened stratigraphy is key to properly correctly interpreting the data as being generated from a PPF system.

seismically as two closely spaced sub-horizontal reflections, where the uppermost reflection is related to the base of the post-rift succession and lower reflection is related to the basal

bounding fault of the crestal wedge. It is not possible to identify any structure with the CW in Fig. 4.12a(ii) because of the relatively small scale of the feature relative to the seismic resolution of the model. It is possible to identify apparently down-lapping reflections within the feature on Fig. 4.12b(ii), due to the relatively larger scale of the structure.

Although there are multiple late stage high-angle faults visible in the velocity models, most are not imaged on the synthetic data, due to their low offset and high-angle with respect to the interfaces they cross-cut (Fig. 4.12a(ii), b(ii), **Table 4.7**). The faults offsetting the low-angled structure at km 2.9, 1.2 km and km 3.04, 1.7 km (Fig. 4.12a(i)); km 14.6, 6.1 km and km 15.2, 8.5 km (Fig. 4.12b(i)) can be seen to offset a bright low-angled reflection at km 2.92, 1.22s TWT (Fig. 4.12a(ii)); km 14.5, 6.0s TWT (Fig. 4.12b(ii)). Velocity distortions mask the deep expression of the fault. A very clear example of a late-stage high-angle fault can be seen at km 5.8 – 5.92, 1.44 – 2.0 km (Fig. 4.12a(ii)); 29.0 – 29.6, 7.1 – 10.0km (Fig. 4.12b(ii)).

While the large-offset low-angle faults are evident in both the velocity models and seismograms, true PPF structures are only clearly seen in the velocity models and are not well imaged on the synthetic data because the low amount of displacement accrued by the late stage faults.

Fault bifurcations are not very common in the synthetic data partially because LVZs are not included in the velocity model, so no intra-basement reflections are present, and the latest fault generation is dipolar, so although cross-cutting relationships do exist and are observable from reflection offsets (Fig. 4.12, **Table 4.7**), fault bifurcations are not well developed. This notwithstanding, a UFB-DFB pair is present in the centre of the sections (Fig.

4.12), but is more visible on Fig. 4.12b(ii), than Fig. 4.12a(ii), due to the seismic resolution. This is one of the major basin forming faults of the region and has a large offset compared with the majority of the late stage faults. A change in reflection characteristics at km 28.2, 6.25s TWT from high amplitude reflections relating to high-velocity lithologies to the left of this point and generally steeply dipping reflections, to weaker reflections that are more characteristic of a low strain basin (shallow dipping to sub-horizontal) to the right (Fig. 4.12). The fault itself is not imaged due to the combined effect of the steep dip of the structure and the close proximity to the model edge.

By combining all of the evidence, including presence of (highly eroded) crestal wedges, small offsets of (bright) low-angle fault reflections, and strongly tilted stratigraphy, it is possible to infer the action of the PPF mechanism in extending the section. Fig. 4.12 is also a good example of how the scale of the structure is important to its likelihood of being identified.

These models are probably a good representation of structures that might be observed at a sediment starved MPRM, where evidence for the earliest fault sets may subtle or non-existent due to mass-wastage and erosion. Fig. 4.12c demonstrates two potential interpretation of the synthetic data in Fig. 4.12a(ii). The data is relatively ambiguous, bearing in mind that the oversteepened stratigraphy is only partially imaged due to the 30 km migration aperture applied during modelling, and could potentially be interpreted as a series of low-strain tilted fault blocks. If the data were interpreted as such, the amount of extension would be massively underestimated. However, by interpreting the reflections based on their parent structures a, mostly, correct interpretation of the data can be made.

Even though the structural geometries are well known, due to the velocity distortions and lack of structural reflectivity, the correct interpretation is incomplete.

PPF Identifier	Velocity Model (km, km) - (km, km)	Seismogram (km, s - km, s)	Comments
Crestal Wedge	3.40 - 4.44, 1.12 - 1.28 (16.6 - 22.2, 5.8 - 6.4)	3.8 - 44, 1.22 - 1.8 (19.0 - 22.22, 5.58 - 6.3)	CW expressed as closely spaced sub-horizontal reflections
Cross-cut faults	2.9, 1.2 - 3.04, 1.7 (14.6, 6.1 - 15.2, 8.5)	2.92, 1.22 (14.5, 6.0)	Lower fault intersection is not imaged
	3.6, 1.36 - 3.64, 1.52 (18.0, 6.7 - 8.3, 7.7)	3.6, 3.25 - 3.64, 3.45 (18.0, 16.2 - 19.0, 16.4)	
	5.8, 1.44 - 5.92, 2.0 (29.0, 7.1 - 29.6, 10.0)	5.8, 3.25 - 5.92, 4.0 (29.0, 16.2 - 29.1, 2-.9)	Fault plane location is approximate.

Table 4.7: Coordinates of where PPF identifiers and associated structures can be observed where present in the model. Crestal wedges are shown top left and bottom right corners of a rectangle. Coordinates without parentheses relate to Fig. 4.12a, and those within, Fig. 4.12b

4.3.4 Detachment systems, SE Spain (Booth-Rea et al., 2002)

The Betic Cordillera (SE Spain) is similar to the basin and range province in that it too has undergone extreme attenuation. The structural sections modelled here (Booth-Rea et al., 2002) represent thinning of a 20 km thickness of crust to only 1km (Booth Rea et al., 2004), equating to c. 95% thinning. This has been accommodated by multiple generations (up to nine, Reston, 2007) of detachment faults that form almost all of the lithological contacts observed on the section.

Two orthogonal sections (Booth-Rea et al., 2002) from Sierra de la Tercia, Murcia (SE Spain) demonstrate the structural complexity of the extensional system and the three-dimensional variation in structures. As before the sections are modelled at their true scale (Figs. 4.13a & 4.14a) and at an enlarged “margin” scale (Figs. 4.13b & 4.14b). A post-rift layer of sediment

is included in order to suppress velocity distortions and energy loss from the irregular topography of the sierra.

The lithologies modelled are not the lithologies that are present in the real geological sections (Booth-Rea et al., 2002; Booth-Rea et al., 2004), and instead the lithologies used are ones that might be expected in a rifted margin setting (**Appendix B**), and will provide sufficient acoustic impedance to generate reflections.

The structure of the Sierra de la Tercia is not well imaged on the synthetic data, especially in Figs. 4.13a. This is because the limit of seismic resolution at 20Hz and an average velocity of 4km/s is c. 50 m. May of the fault bounded blocks on the section are smaller than this limit, effectively making the structure sub-seismic. This combined with low-angle detachment faults forming almost all of the lithological contacts leads to the structures becoming irresolvable on the seismic data. The larger scale sections (Figs 4.13b & 4.14b) succeed in resolving individual reflectors quite well, but again the actual structures are very difficult to identify. A small number of late stage faults can be identified on the data (Figs. 4.13 a(ii) & b(ii)), but the vast majority of the other structures are just not resolvable, due to the scale and orientation of the sections. Velocity distortions complicate matters further.

The synthetic seismograms (Figs 4.13 a(ii) & b(ii) – 4.14 a(ii) & b(ii)) do little to aid in identification of the structures responsible for the extreme attenuation observed at the Sierra de la Tercia. The seismograms do demonstrate that when such extreme extension has occurred over multiple generations of detachment faults it is effectively impossible to resolve on seismic data. This in itself is an important observation as almost all of the

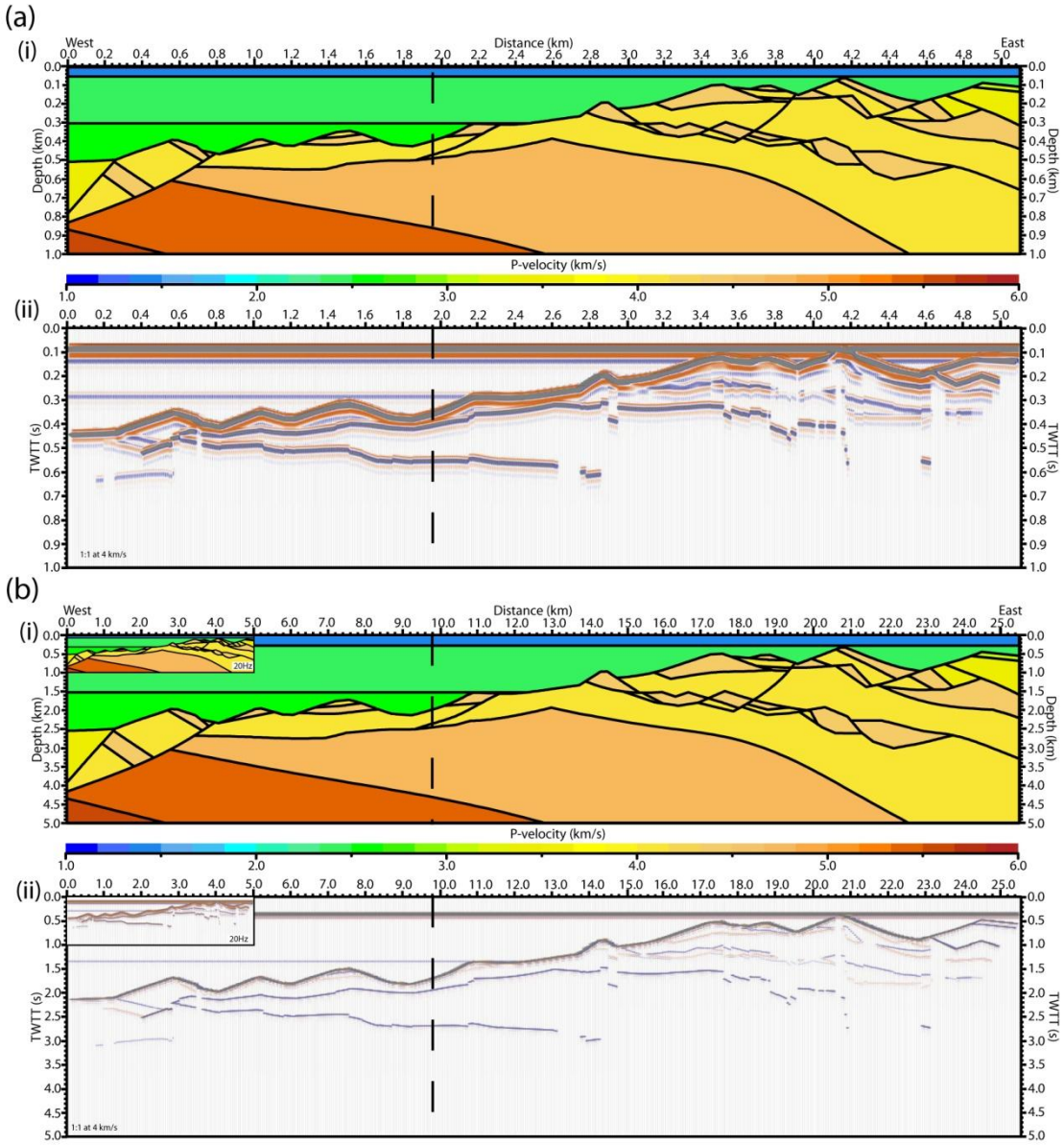

Fig. 4.13: E- W trending section based on Booth-Rea et al.,(2002 &2004). Up to nine detachment fault generations led to 95% thinning. Nearly all lithological boundaries are faulted contacts, with later high-angle faults detaching onto earlier generation faults. (a)(i) Velocity model includes a post-rift succession, and no LVZs are incorporated (since boundaries are faulted contacts). Dashed line is intersection with (Fig. 4.14). (ii) Seismic response to model. No vertical exaggeration at 4km/s. Note due to the limits of seismic resolution (c. 50m at 4km/s) many of the structures are too small to be imaged. Only two potential faults are imaged at km 0.4 – 0.7, 0.4 – 0.55s TWT, and km 4.6 – 4.8, 0.1 – 0.3sTWT and section does not appear faulted at all. It is practically impossible to observe the structures in this section. (b)(i) Margin scale velocity model (five times that of (a)). (ii) Seismic response to "margin" scale. No vertical exaggeration 4km/s. Scaled version of (a) is inserted for comparison. Larger structures are far better resolved than in (a). It is possible to observe some offset between reflectors. Complicated reflector patters can be seen in the data, particularly from km 14 onwards, and it may be possible to pick out a number of potential faults. Note, it would be impossible to interpret the true structure of in either (a) or (b), and so crustal extension would be grossly underestimated from seismic data if it were achieved via a mechanism involving multiple detachment faults.

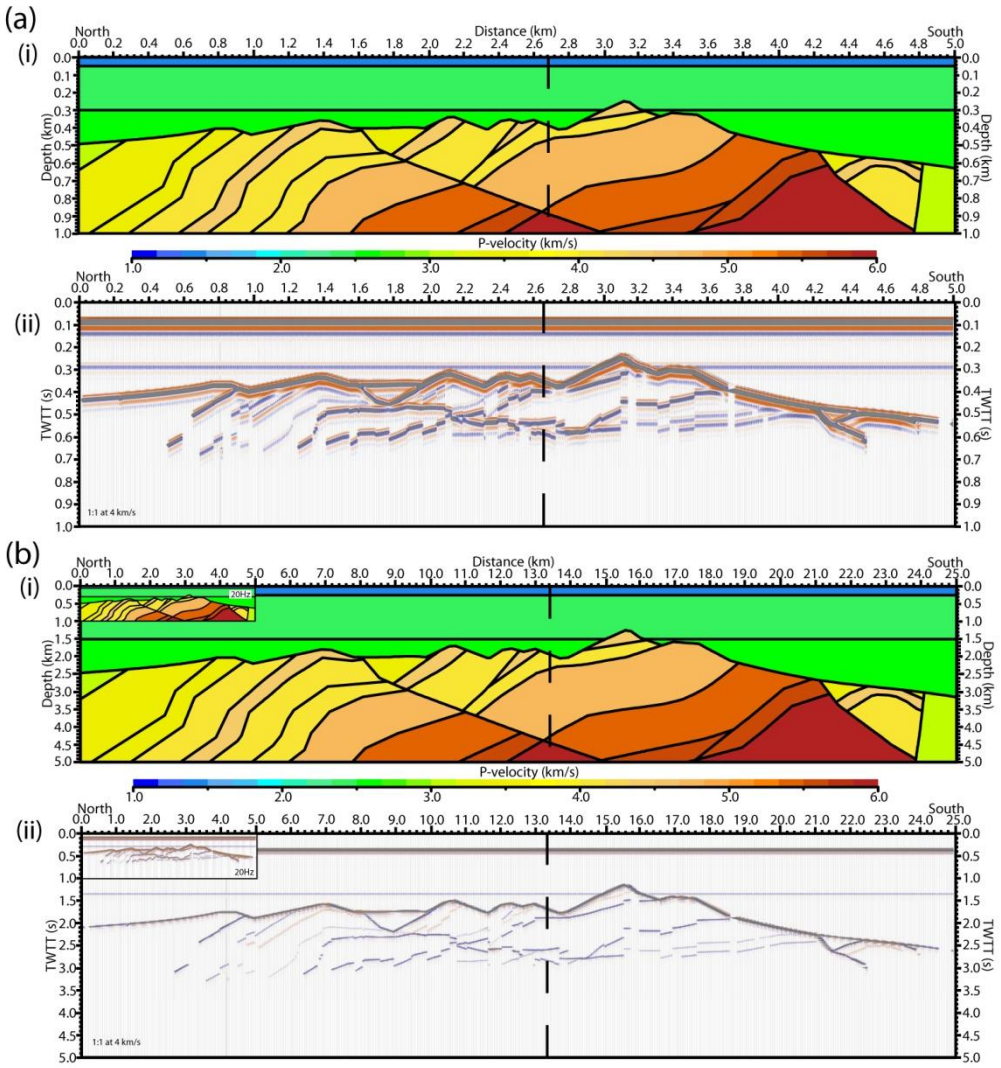

Fig. 4.14: (a)(i) N - S trending velocity model derived from structural cross-sections published by Booth-Rea et al., (2002). Dashed line is intersection with (Fig. 4.13). Velocity model appears simpler than in Fig 4.13, but thinning is still c. 95%. Detachment faults form the lithological boundaries. Two fault structures are apparent in this section. (ii) Seismic response (i), where there is no vertical exaggeration at 4km/s. The two obvious fault structures are well imaged, but are affected by topographically induced velocity distortions. It is impossible to interpret any of the detachment structures from the seismic data. (b)(i) "Margin scale" version of (a)(i) shown at five times the scale. (ii) Seismic response to "margin" scale model. No vertical exaggeration at 4km/s. Synthetic section from (ii) is shown to scale for comparison. Structural layering is well resolved, but due to the section orientation it is impossible to tell that the structure is more complicated, thus making it impossible to discern the amount of stretching in the crust.

extension will not be accounted for by summation of observed faults on seismic data where detachment systems are common.

4.4 Summary & Conclusion

The models presented in this chapter were generated so as to obtain the best possible seismic response from the PPF mechanism. Large migration apertures used during modelling predispose imaging of steeply dipping structures within the data, and in some of the models (Figs 4.5 – 4.7, & 4.9) the insertion of low-velocity zones (simulating fault zones) into the velocity models ensure intra-basement reflections are produced. No random noise, multiples, diffractions, or artefacts of any description are present in the models, and make certain that the best possible images of the PPF mechanism are generated.

The PPF sections modelled in this chapter are structurally very complex, and this complexity is reproduced within the synthetic data. The PPF mechanism produces strong vertical and lateral velocity gradients, especially at high strain, imposing strong velocity distortions within the data, resulting in the complex reflector patterns in the seismic data that in many cases do not echo their parent structure's geometry.

I have endeavoured to demonstrate how the PPF identifiers (describe in **Chapter 3**, and this chapter) are imaged on seismic data. The main result of this highlights how the PPF mechanism is best observed in regions of high extensional strain, but not in regions approaching hyper-extension, e.g. Fig. 4.7 (discussed further in **Chapter 5**). The structural expression of the PPF mechanism within hyper-extended crust is such that the structure's seismic expression is practically impossible to interpret correctly. The modelling suggests that to identify the mechanism in hyper-extended regions it is better to search for the

expression of PPF identifiers in relatively low strain zones ($\beta \rightarrow 2.5^{-}$). All of the major PPF identifiers (crestal wedges, fault bifurcations and oversteepened stratigraphy) can be developed within this strain interval.

However, there are problems (as demonstrated in the above section) with identifying the PPF mechanism on seismic data. The reflector patterns that are produced by the mechanism can result from any number of possible structures (this is demonstrated quite well in the alternate (incorrect) interpretations (Figs. 4.5(ii), 4.6(ii), 4.7(ii), 4.10, 4.11c, & 4.12c). To correctly interpret, or to at least identify, the presence of the PPF mechanism in reflections seismic data, it would be very useful to already have an idea of the degree to which the crust has been stretched. Knowledge of the degree of stretching as region has undergone should enable an interpreter to identify where the PPF mechanism may be expressed along a given seismic profile. Even having identified a potential (individual) candidate for a PPF structure on seismic data it is not possible definitively say that the PPF mechanism caused the extension. However, from observation of other potential PPF candidate structures on the data, in high-strain parts of the crust, it may be possible to suggest confidently that the PPF mechanism was in operation in a given region. Although, due to the effects of velocity distortions on the seismic data, it is unlikely that all of the structures will be interpreted correctly, even if they have been identified as structures related to the PPF mechanism (in detail they may still be incorrectly interpreted).

A potential way to alleviate the problem of incorrectly interpreted PPF structures (having been identified as such) would be to depth migrate the data. In order to properly depth migrate TWT reflection seismic data, the seismic velocities in the crust be very well

constrained by both well data in the shallow parts of the section and ideally with a coincident refraction seismic profile. Unfortunately these constraints are not always present, so the absolute geometries of the structures may not be described with absolute certainty.

One of the interesting things to note about the synthetic models presented in this chapter is that for all complexity of reflector patterns produced by the PPF mechanism, relatively simple structural interpretations appear possible from the data, and this may be one of the reasons as to why the PPF mechanism has gone unrecognised in hyper-extended regions. This has serious implications with respect to elucidating the amount of extension that is attributable to faulting in the upper (and brittle) crust on regions of hyper-extension. It is clear from the synthetic models that the latest generation faults are relatively easily interpreted even in the hyper-extended domains. Failure to recognise the earlier fault generations will result in considerable underestimation of the degree of crustal stretching that is attributable to faulting mechanisms, and so would lead to the apparent extension discrepancy at MPRMs and hyper-extended basins.

CHAPTER 5

Discussion

5.1 Overview

The polyphase faulting (PPF) mechanism has been shown to be mechanically feasible and capable of accommodating very large amounts of extensional strain (**Chapter 3**). The resulting structural geometries are highly complex, especially at higher strain, and the mechanism has been implicated in accommodating the highly stretched crust in the Basin & Range region, W. USA. However, examples of the PPF mechanism cited from MPRMs have been relatively rare, with the majority of interpretations coming from the well-studied W. Iberian Margin (Reston, 2005, Fig. 5.1). Even when PPF structures are known to exist, the PPF mechanism is difficult to identify on reflection seismic data, as was demonstrated in **Chapter 4. I**t may be that the specific identifiers of the mechanism have been overlooked at many MPRMs due to the complicated and unintuitive structural geometries produced, imaging problems associated with complex vertical and lateral velocity gradients, or the structures produce insufficient acoustic impedance in order to exhibit a noticeable reflection (particularly problematic for intra-basement faults). Here, the hyper-extended crust of the Porcupine Basin is investigated as to whether the synthetic seismic models generated **Chapter 4** aid in identifying PPF within the basin and help to account for the crustal stretching observed.

5.2 Likelihood of Identifying PPF on Industry Seismic Data

The synthetic models presented in **Chapter 4** assumed the absolute best case imaging scenario. Every fault, including intra-basement faults, was modelled as a low-velocity zone (LVZ) in order to guarantee that an acoustic impedance existed across the fault and that it

would produce a discrete reflection. Image ray tracing of the velocity models (**Chapter 4**) using very large migration apertures ensured that a simulated (perfect) time migration seismic profile, optimised for imaging steeply dipping structures, was generated. The resulting reflection seismic models demonstrated quite complex reflector geometries, which increased in their complexity as β-values increased. However, the increase in complexity was to the point that even when all fault planes generated reflections, regardless of their dip, the structure became impossible to interpret correctly (Fig. 4.7) unless prior knowledge of the input model were available

Intra-basement faults are potentially even more difficult to identify, partly due to the extremely low impedance contrast generated across a fault at these deeper levels, and partially because of fracture healing following faulting causing the rock mass to appear seismically isotropic (Hölker et al., 2002). However, even if basement lithologies have relatively uniform seismic velocities, density contrasts should be sufficient to generate reflections (Milkereit & Eaton, 1998; Reston 1988; Rutter et al., 1999). Faults tend to be thought of as discrete planar structures but in detail they are more complicated, composing of anastomosing, interconnected fractures dominated by cataclastic deformation in their core, with secondary fractures formed outside of the main fault zone distributing deformation either side of the main fault zone to the faults damage zone (Twiss & Moores, 2007). Depending on the relative size of the fault, these damage zones can be many times wider than the core of the fault zone (Twiss & Moores, 2007). Fracturing within the damage zone of a fault can result in velocity and density reductions across fault zones (Mooney &

Ginzburg, 1986) and is capable of producing 30 – 40% drops in velocity across a fault within the basement.

Larger faults are more likely to be seismically observable when large gouge zones are developed and may be observable to depths of c. 10 – 12km (Mooney & Ginzburg, 1986). Deeper within the basement it may even be possible to image the more ductile mylonite zones associated with the more shallow faults, providing there is relatively low levels of noise in the data (Fountain et al., 1984) and if the shear zones have drawn lithological contrasts into parallelism (Reston, 1988). As an example, the Outer Isles Thrust, also known as the Outer Hebrides thrust, is visible as a strong reflection from near the surface to depths in excess of 20 km (Lailey et al., 1989). So, the basement is unlikely to be seismically isotropic and intra-basement faults should be able to produce seismic reflections, although they would likely be very discontinuous because of rapidly changing velocity contrasts along the fault (Sheriff & Geldart, 1995), and depending on the degree of fracture healing and width of damage zones. In practice, fault planes rarely give rise to reflections on migrated data (partially due their associated diffractions visible on unmigrated data being removed during the migration process (Sheriff & Geldart, 1995) and are generally identified in the upper levels of seismic data from offset stratigraphy.

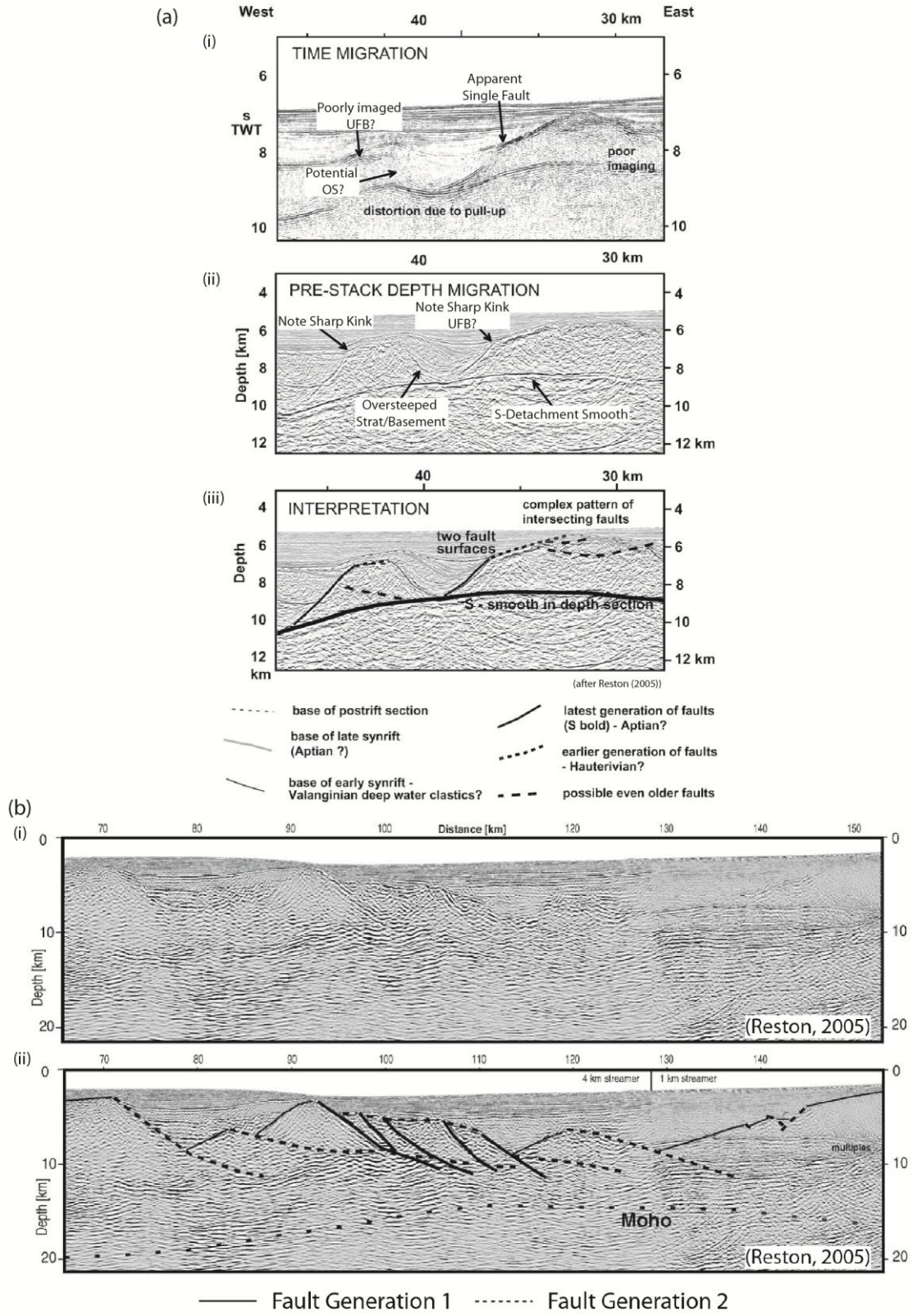

Fig. 5.1: Published examples of polyphase faulting. (a) Deep Galicia Margin. (i) Uninterpreted (but annotated) Seismic time section, where two faults appear as one due to velocity distortions. Not the undulating nature of

the-detachments. (ii) Uninterpreted (but annotated) PSDM seismic data provide superior structure closer to reality. The up-dip fault bifurcation (UFB) PPF identifier can be clearly identified on the data, the original apparently planar fault is seen to be two cross-cutting fault generations. (iii) Interpreted PSDM data detailing PPF structures. (b) (i) Uninterpreted PSDM data from the Galicia Interior Basin. (ii) Interpreted PSMD data detailing two phases of faulting

The synthetic models were also run to test the seismic response to the PPF mechanism where no fault plane reflections are generated within the basement, and no faults were modelled with associated low-velocity zones (LVZs). This resulted in no intra-basement reflectors being generated, and the only evidence of faulting comes from the shallower levels where offset in stratigraphy as well as juxtapositions of sediments against basement produced discrete fault plane reflections. As can be seen in **Chapter 4**, the PPF mechanism is even more difficult to recognise where faults are not expressed at deeper levels, since identifiers such as DBFs are most likely to be developed at intra-basement level. Where faults do not generate discrete reflections, recognition of PPF structures relies on identification of structures at relatively shallow level such as crestal wedges (CWs) and oversteepened stratigraphy (OS). In certain circumstances, however, it may be possible to identify down-dip fault bifurcations (DFBs) above basement level, as they may occur within the sedimentary fill (see Figs 4.11 & 4.12).

On industry-collected seismic data, faults will mostly likely have an expression somewhere between these end members, where faults are perfectly reflective or are unreflective. CWs and OS are both excellent identifiers of the PPF mechanism but there are of course problems associated with their identification on seismic data, including poor preservation potential of CWs and difficulties in imaging steeply dipping features.

Reflection seismic data collected by industry, such as the SPB97 survey, discussed in **Section 5.3**, in some cases is capable of recording discontinuous reflections from fault planes within the basement. Both time and depth migrations are presented, both with benefits and drawbacks. In time sections, and consequently the depth sections, steeply dipping features are not particularly well imaged (if at all). The SPB97 survey was processed using Kirchoff migration, and so unless a wide migration aperture was applied information on steeply dipping structures is lost during migration (Yilmaz, 1987). In general, seismic data collected by industry is not processed using large migration apertures, in order to reduce the chances of noise being migrated to the point where it appears as large migration smiles (Sheriff & Geldart, 1995).

Dip information that is lost relating to steeply dipping structures is unfavourable in terms of recognising PPF structures because, as described in **Chapter 3,** steeply dipping stratigraphy is predicted when $\beta \geq 2$. Smaller migration apertures used during migration of industry seismic data may reduce the possibility of these important PPF identifiers from being recognised.

5.3 Is the PPF Mechanism Present or Absent in the Porcupine Basin?

In order to investigate properly whether the PPF mechanism can be identified within the Porcupine Basin, it is best to compare features identified on the synthetic models (**Chapter 4**) with two-way travel time (TWTT) industry seismic data. Both time migration and depth migrations are investigated here, but the initial comparison is made in time because the synthetic models are displayed in time space and are free from bias in terms of the seismic

velocities chosen in order to generate the depth migrations. Depth migrations are very useful, however, since if suitable seismic velocities are chosen during migration the geometries and angular relationships within the data are closer to what they might be in reality. Angular relationships within the seismic data are particularly useful in terms of identifying the PPF mechanism.

A selection of seismic profiles from the Porcupine Basin (Fig. 5.2) is here separated into four separate stretching domains based on observed crustal stretching (from stretching analyses, **Chapter 2**). The segregation of the profiles into separate stretching domains is useful because each division (based on **Chapter 3**) should coincide with a change in structural style across the basin, if the PPF mechanism was in effect during rifting. It has been shown that the maximum stretching that can be accommodated by a single fault generation is $\beta \approx 1.7 – 2.0$ (Jackson & White, 1989). So, assuming that rifting occurs via the PPF mechanism, a second generation of normal faults is expected to exist where the crust has been stretched to $\beta \approx 2$. By the time the crust becomes fully embrittled at $3 \leq \beta \leq 5$ (Pérez-Gussinyé & Reston, 2001), additional faulting generations will be required. Indeed, conceptual and mechanical PPF models (**Chapter 3**) have shown that stretching of this magnitude can be accommodated by two or three individual fault generations. Consequently, the stretching domains are as follows: (I) $\beta < 2$, (II) $2 < \beta < 3$, (III) $3 < \beta < 5$, and (IV) $\beta > 5$ (Fig. 5.2).

The amount of stretching that can potentially be accommodated by the conceptual and mechanical PPF models in **Chapter 3** suggests that each domain number can be used as a proxy for the minimum amount of fault generations required to produce the observed crustal stretching. For this analysis it is assumed that the maximum stretching at which the

crust becomes fully embrittled is $\beta \approx 5$ (Peréz-Gussinyé & Reston, 2001), at which point (but potentially anywhere where $3 \leq \beta \leq 5$) any additional crustal stretching observed is likely to be accommodated via detachment faulting mechanisms following the initiation of mantle serpentinisation. As discussed in **Chapter 2**, in the centre of the Porcupine Basin, specifically beneath the Porcupine Arch, there is evidence of large scale mantle serpentinisation (O'Reilly et al., 2006). Reston et al. (2001) and Reston et al. (2004) have interpreted the high-amplitude reflection (Fig. 5.3) as a detachment system following the crust-mantle boundary, and have likened it to the S reflector present at the W. Iberian Margin, terming it the P-reflector and interpreting it as a serpentinite detachment system, similar to S. The P-reflector/detachment is seen only where $\beta \geq 3.5$ (Fig. 5.2). This suggests that once the crust beneath the Porcupine Basin became fully embrittled and mantle serpentinisation began, the extensional style changed from a possible pure shear (the PPF mechanism, thinning the crust to the point of embrittlement) to simple shear where the remaining crustal stretching occurred over a detachment system.

For the purposes of recognising the PPF mechanism within the Porcupine Basin, the domain boundary where $\beta = 2$ is very important. If the PPF mechanism was responsible for the crustal stretching observed in the Porcupine Basin, then where $\beta \geq 2$, it should not be possible for only one fault generation to have achieved this degree of stretching (see **Chapter 3**; Jackson & White, 1989), making this the ideal place to search for the identifiers of PPF as described in **Chapter 3**. Since $\beta \approx 2$ is the limit of what is achievable by only one fault generation, one might expect that if a succeeding fault generation had initiated, then the rotation it will have accumulated should be relatively low (with earlier structures passively

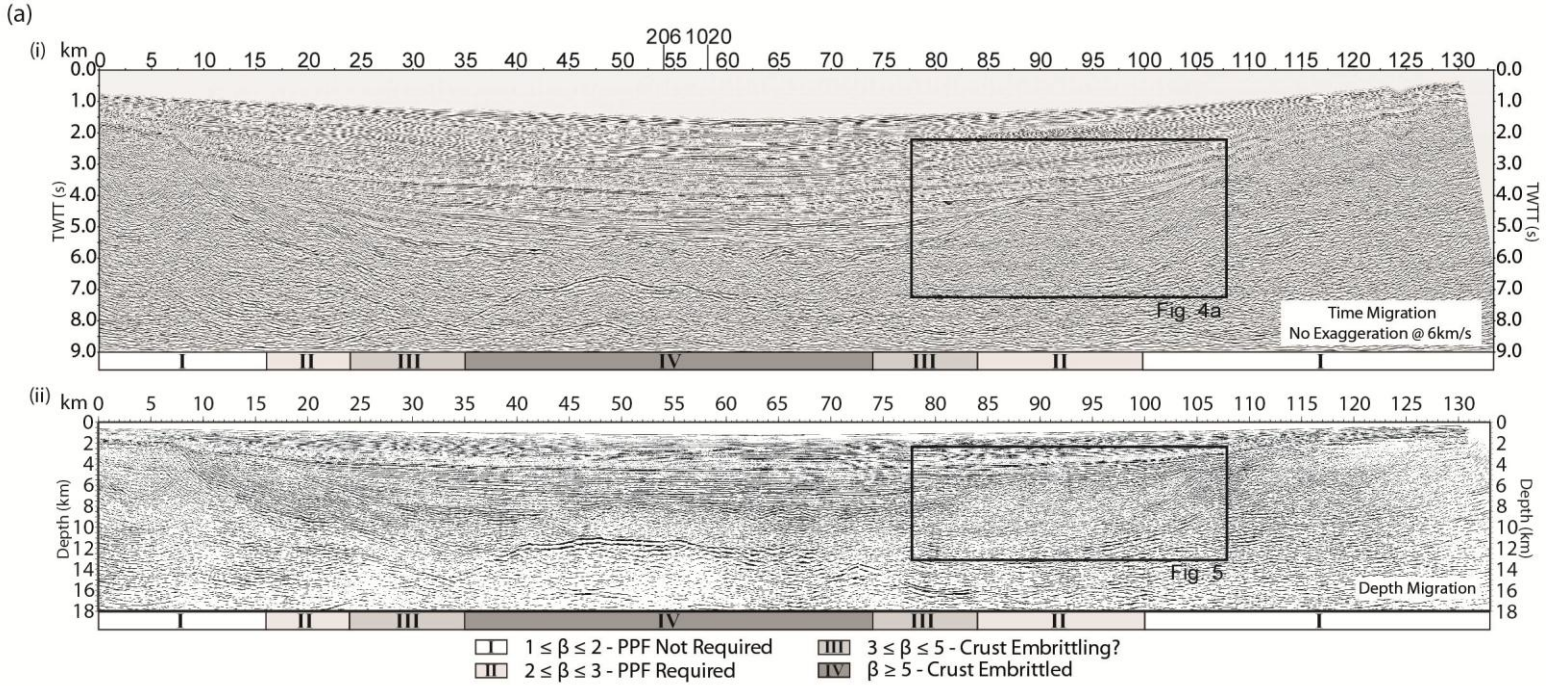
(a)
(i) km
206 1020
TWTT (s)
Fig. 4a
Time Migration
No Exaggeration @ 6km/s
(ii) km
Depth (km)
Fig. 5
Depth Migration
I
II
III
IV
1 ≤ β ≤ 2 - PPF Not Required
2 ≤ β ≤ 3 - PPF Required
3 ≤ β ≤ 5 - Crust Embrittling?
β ≥ 5 - Crust Embrittled

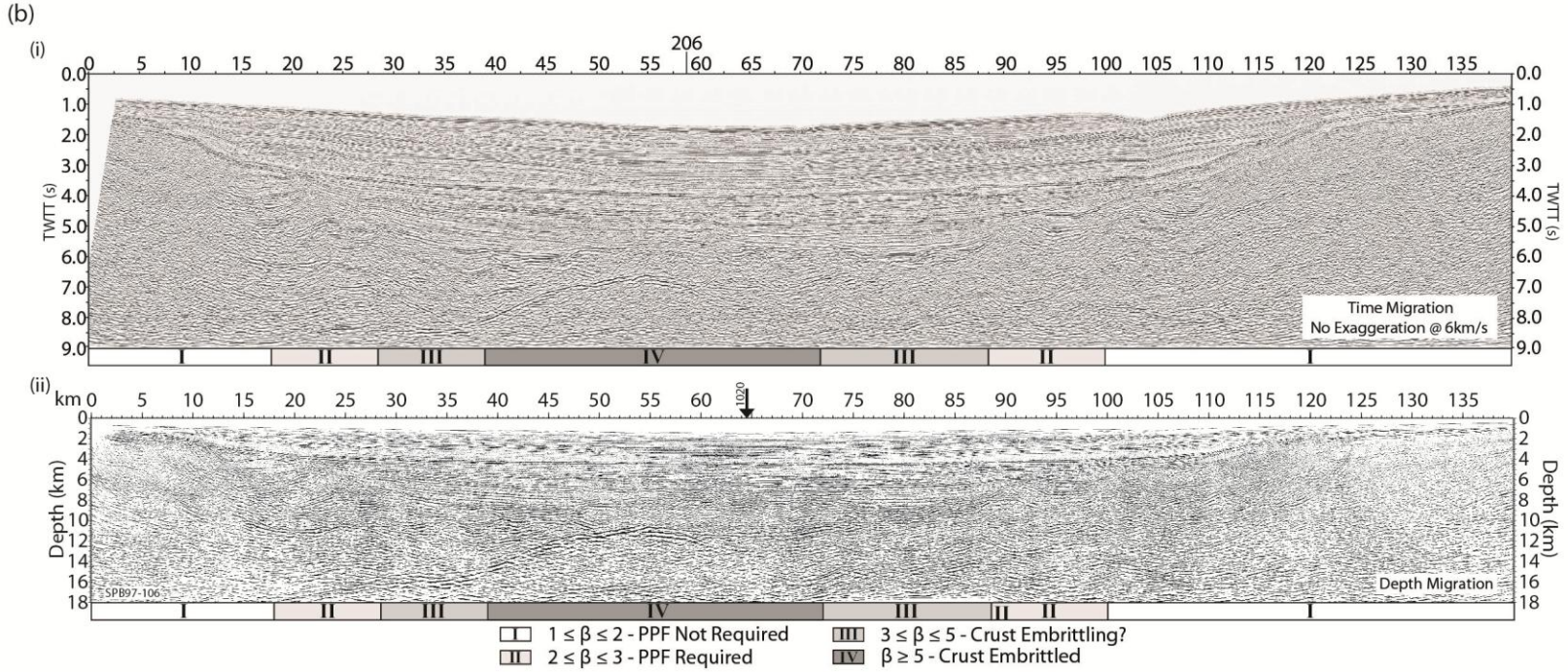
(b)
(i)
206
TWTT (s)
Time Migration
No Exaggeration @ 6km/s
(ii)
km
1020
Depth (km)
SPB97-106
Depth Migration
I
II
III
IV
1 ≤ β ≤ 2 - PPF Not Required
2 ≤ β ≤ 3 - PPF Required
3 ≤ β ≤ 5 - Crust Embrittling?
β ≥ 5 - Crust Embrittled

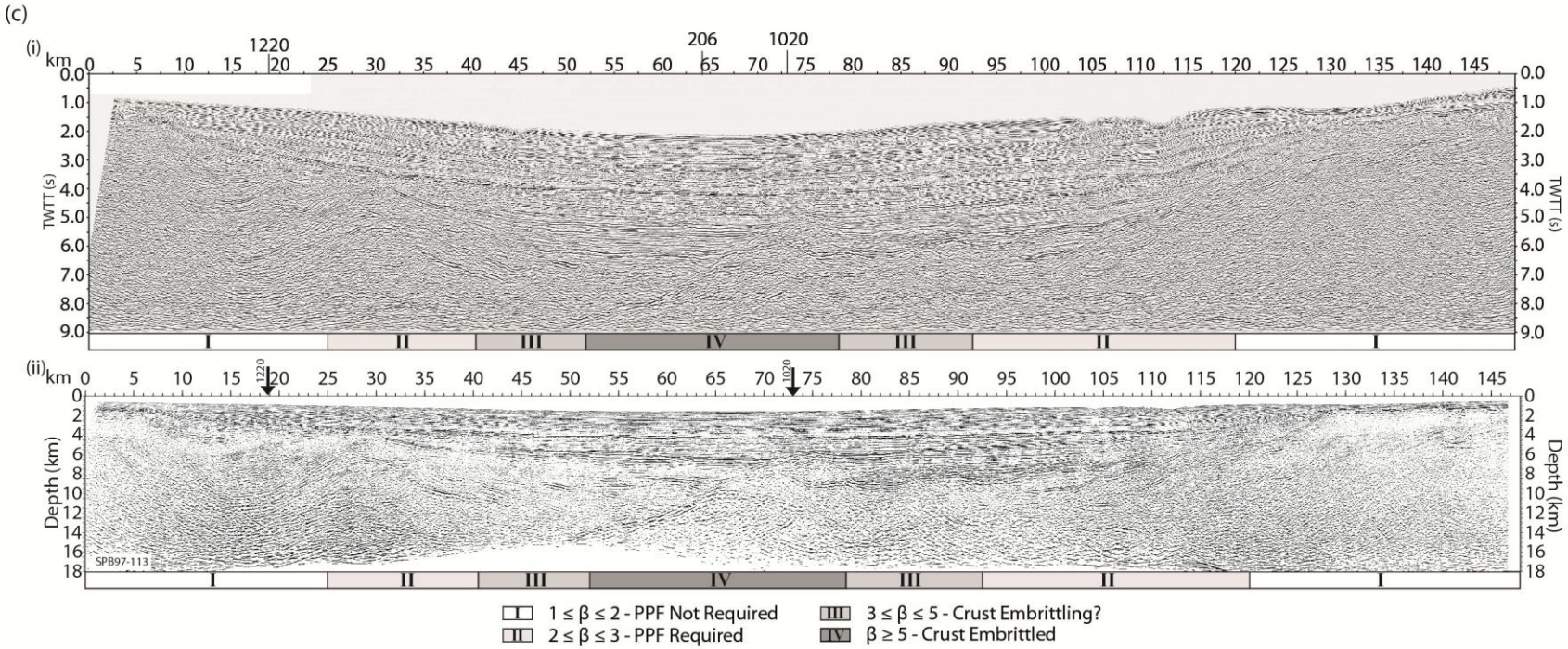
(c)
(i)
km
1220
206
1020
TWTT (s)
(ii)
Depth (km)
SPB97-113
I
II
III
IV
1 ≤ β ≤ 2 - PPF Not Required
2 ≤ β ≤ 3 - PPF Required
3 ≤ β ≤ 5 - Crust Embrittling?
β ≥ 5 - Crust Embrittled

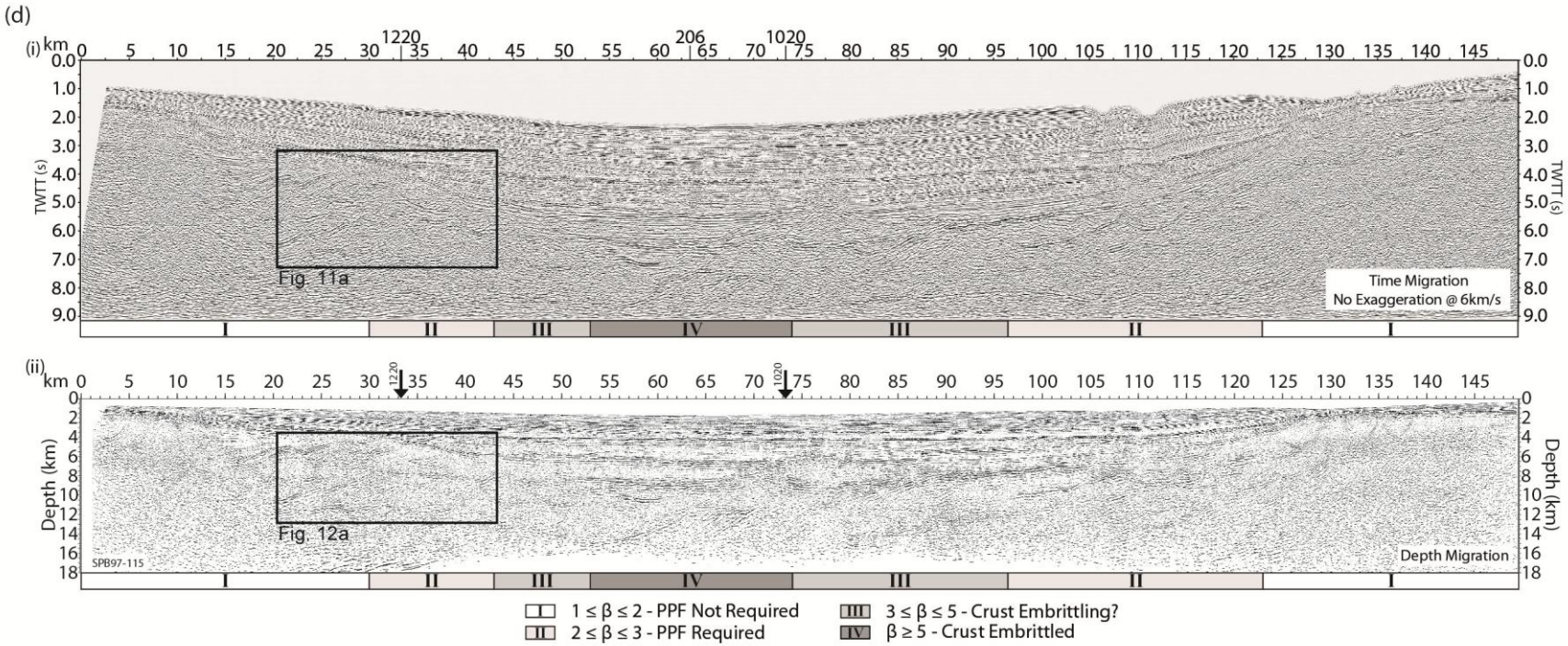
(d)
(i) km
1220
206
1020
TWTT (s)
Fig. 11a
Time Migration
No Exaggeration @ 6km/s
(ii) km
Depth (km)
Fig. 12a
SPB97-115
Depth Migration
I
II
III
IV
1 ≤ β ≤ 2 - PPF Not Required
2 ≤ β ≤ 3 - PPF Required
3 ≤ β ≤ 5 - Crust Embrittling?
β ≥ 5 - Crust Embrittled

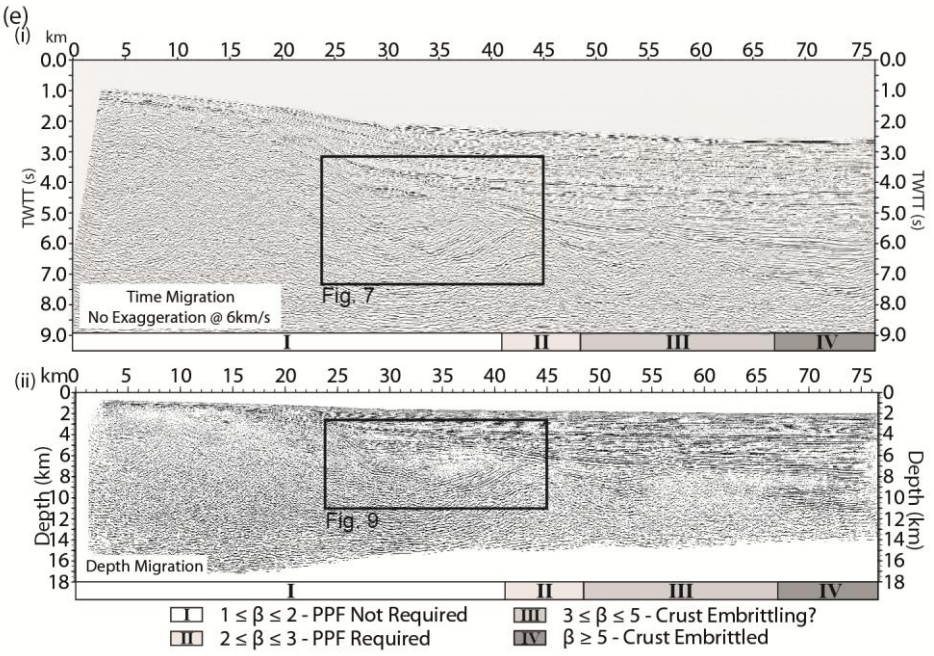

Fig. 5.2: Uninterpreted reflection data from the Porcupine Basin. (a) SPB97-103, (b) SPB97-106, (c) SPB97-113, (d) SPB97-115, (e) SPB97-121. For each sections (i) Time migration, with no vertical exaggeration at 6km/s, (ii) Depth migrated seismic data. Each line is split into discrete stretching domains, based on stretching factors derived in Chapter 2. Boxes refer to area on lines that are looked at in greater detail later. Each numbered stretching domain can be used as a proxy to determine the minimum number of fault generations that would be required to stretch the crust by the appropriate amount. Domain I, at least one fault generation, Domain II, at least two fault generations, etc.

rotated to the same degree). It is likely that the structural geometries should not be too complex making recognition of PPF identifiers an easier task because Crestal Wedges (CW)s, Up-dip Fault Bifurcations (UFB)s, Down-dip Fault Bifurcations (DFB)s, Oversteepened Stratigraphy (OS), and Oppositely Thickening Wedges (OTW)s, will not have been overly complicated by excessive tilting (and its associated imaging problems).

Examples of all the PPF identifiers, with the exception of OTWs have been identified in the Porcupine Basin. Generally the PPF identifiers are present in close proximity to the $\beta = 2$ domain boundary. Some of these examples are described **Sections 5.3.1 – 5.3.3**.

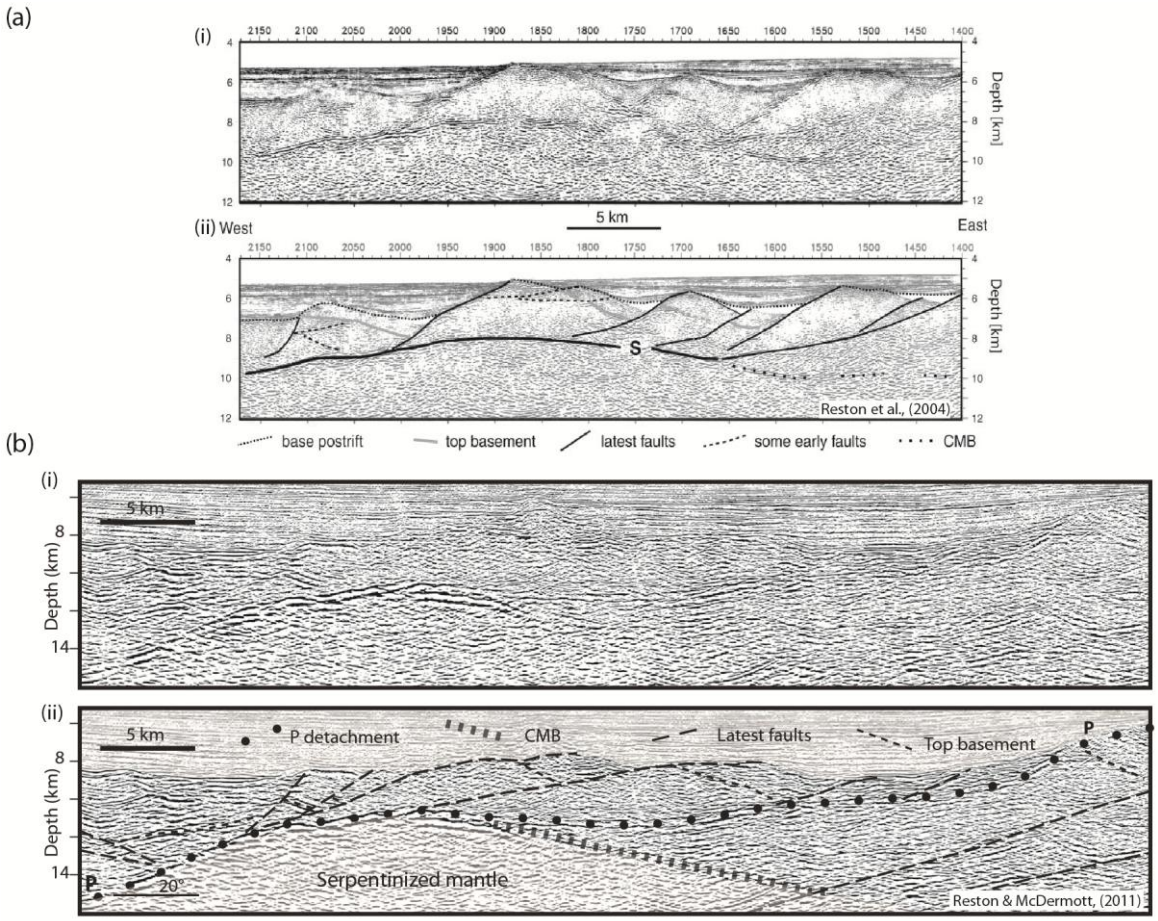

Fig. 5.3: (a) S-detachment on the W. Iberian Margin, (i) uninterpreted, and (ii) interpreted, PSDM data. (b) P-detachment in the Porcupine Basin, (i) uninterpreted, and (ii) interpreted PSDM data. Note the similarity of the reflector geometries, particularly in the west of sections (a) & (b). Faults are better imaged in (a) than in (b) due to it having thinner post-rift sediment cover

5.3.1 Oversteepened Stratigraphy

The eastern margin of SPB97 – 103 (Fig. 5.2a) displays an excellent example of oversteepened stratigraphy within stretching domain II and, as such, one might expect there to be at least two fault generations accommodating the crustal stretching here. One of the most useful characteristics of oversteepened stratigraphy with regard to its being an identifier of the PPF mechanism, is that the early fault generations do not need to be observed but instead can be implied from the observed stratigraphic dips.

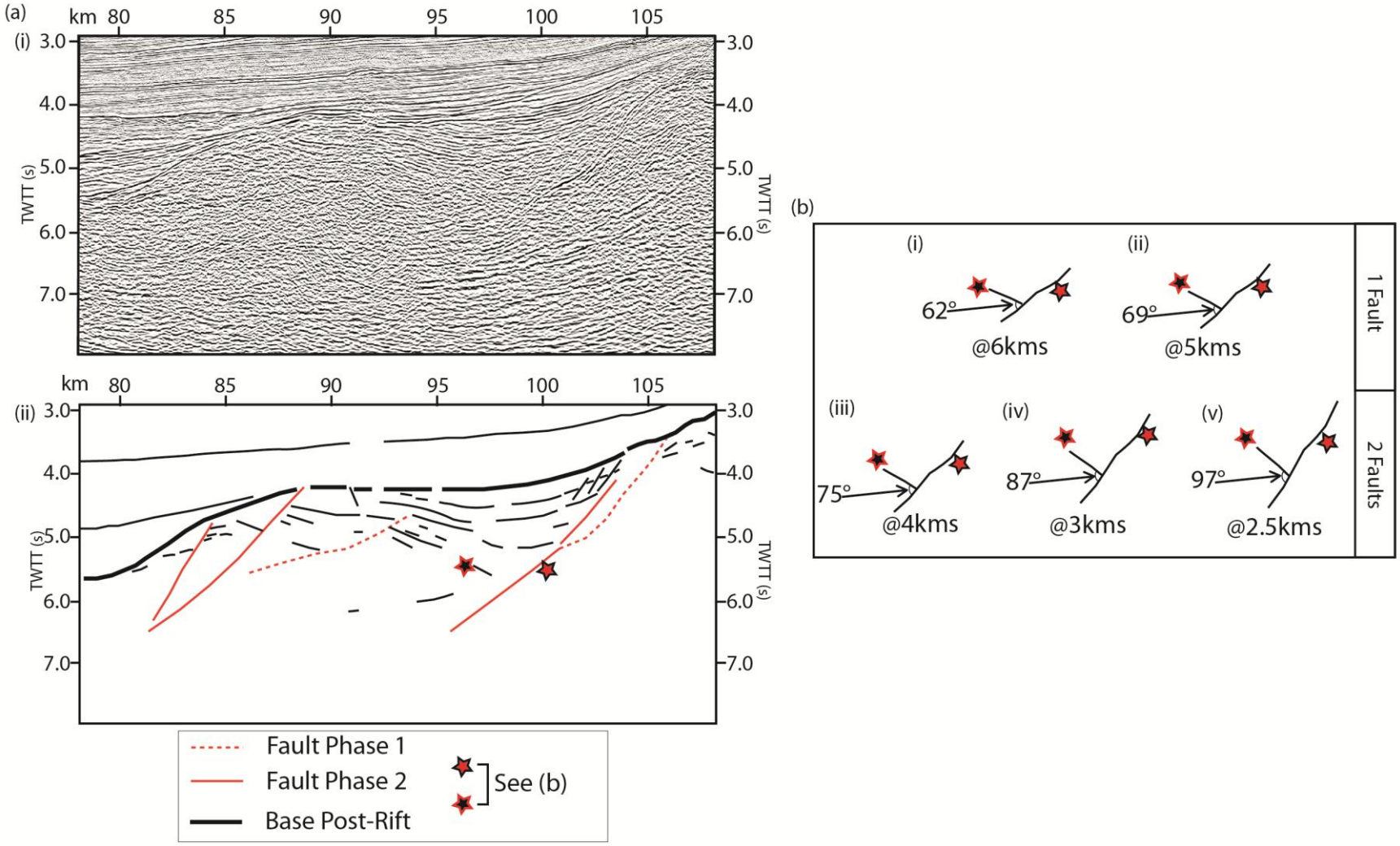
(a)
km 80 85 90 95 100 105
(i) 3.0
4.0
5.0
6.0
7.0
TWT (s)
(ii)
Fault Phase 1
Fault Phase 2
Base Post-Rift
See (b)
(b)
(i)
62°
@6kms
(ii)
69°
@5kms
1 Fault
(iii)
75°
@4kms
(iv)
87°
@3kms
(v)
97°
@2.5kms
2 Faults

Fig. 5.4: Zoom in of the Ruadan Ridge (see Fig. 5.2a for location), demonstrating oversteepened stratigraphy. (a) (i) Uninterpreted data. (ii) Line drawing of structure with two phases of faulting. (b) Pseudo-depth migration of features in the for possible seismic velocities (a)(i). (i – ii) For these seismic velocities it is possible that the geometries in (a)(ii) result from only one fault generations, but in (iii – v) where velocities are more probably more appropriate, the interpreted geometries are most likely caused by at least two generations of faulting.

Fig. 5.4a(i) is a blow up from the TWTT reflection seismic profile shown in Fig. 5.2a, and shows a large tilted fault block known as the Ruadan High (Naylor et al., 2002), which is notably shallower than the adjacent Porcupine Arch. The seismic data quality is such that syn-rift sediment packages, probably of Jurassic age (Naylor et al., 2002), are clearly imaged. There are also a number of faults that can be observed in the data, interpreted from observation of offset reflectors, as well as some potential fault plane reflections – especially in the footwall of the tilted fault block. The line drawing interpretation shows clearly the relationship between the sediments deeper within the fault block and the footwall bounding fault (Fig. 5.4a(ii)).

Fault-bedding intersection angles are detailed in Fig. 5.4(b) with the different coloured stars representing the corresponding features in the line drawing interpretation. As the section in TWTT, a pseudo-depth conversion is performed in to ascertain the most likely (true) intersection angle. For a seismic velocity of c. 3 – 4 km/s, the probable velocity of the sediments in question (O' Reilly et al., 2006), it is found that the fault-bedding intersection angle is c. 75 - 87°. A fault cut off at this angle requires that there must have been some pre-tilting of the stratigraphy prior to the initiation of displacement on the block bounding fault. This conclusion is based on the assumption that the sediments were originally deposited horizontally, and that there is no fault displacement in or out of the plane of section. However, if the dip of either the stratigraphy or the block bounding fault were considered to

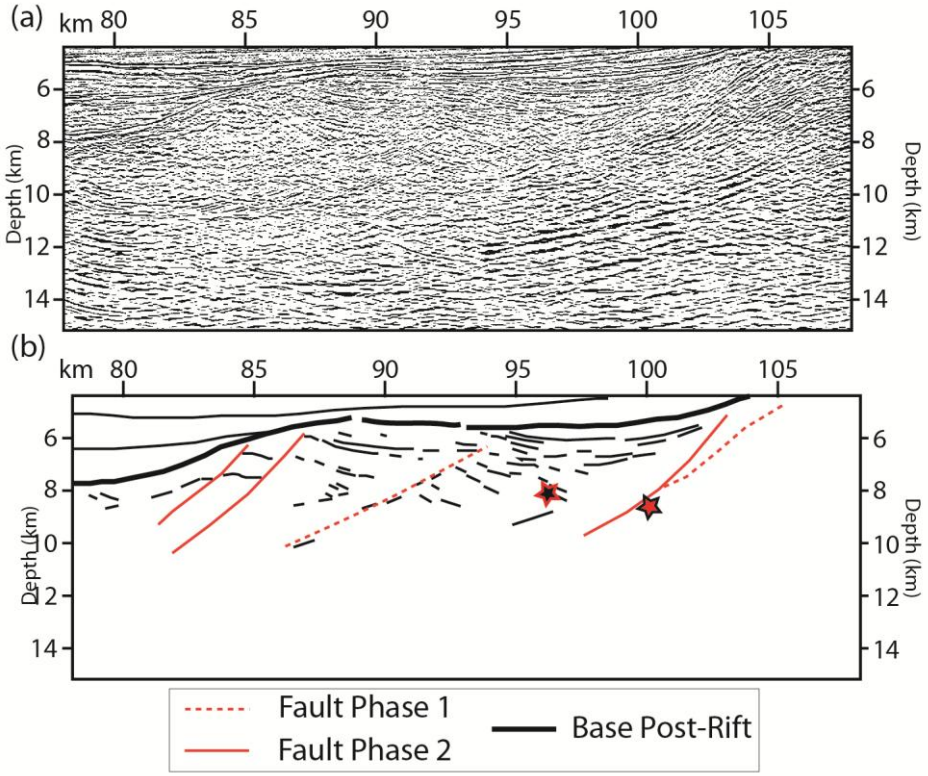

Fig. 5.5: Depth migration of Ruadan Ridge (see Fig. 5.2a for location). (a) Uninterpreted data, (b) line drawing interpretation showing two fault generations. Note the fault-bedding intersection is almost orthogonal, so oversteepened stratigraphy is present in the data

be an apparent dip, prior tilting of the stratigraphy would still be required to produce the observed fault-bedding relationship. This is because the actual dip of either the fault or the stratigraphy cannot be lower than what is observed on this section, and increasing the dip of one, or both of the interfaces will serve to increase the intersection angle. If the observed tilt were accomplished by the interpreted block bounding fault alone, then it would be necessary for the fault to have initiated with a sub-vertical dip, which is not mechanically feasible.

Fig. 5.5 shows a depth migrated version of the Ruadan High, which also clearly shows the high-angles between the stratigraphic dip and the block bounding fault. On the basinward side of the ridge some moderate-steeply dipping faults can be observed.

Although the faults that were responsible for the initial tilting of the stratigraphy appear to not be present, the observation of oversteepened stratigraphy, relative to the latest, seismically observable fault serves as good evidence that there must have been some pre-tilting of said stratigraphy, probably by a previous generation of extensional faults.

5.3.2 Down-Dip Fault Bifurcations

Down-dip fault bifurcations (DFB) are an excellent identifier of the PPF mechanism. However, their usefulness is limited by the fact that their recognition is dependent on the fault planes producing reflections, or at least being inferable from reflector offsets on seismic data. DFBs also tend to occur deeper on seismic profiles within the basement of the hangingwall blocks of the latest fault generations. These potential problems notwithstanding, when DFBs can be identified, they are a powerful indicator of the PPF mechanisms activity in an area.

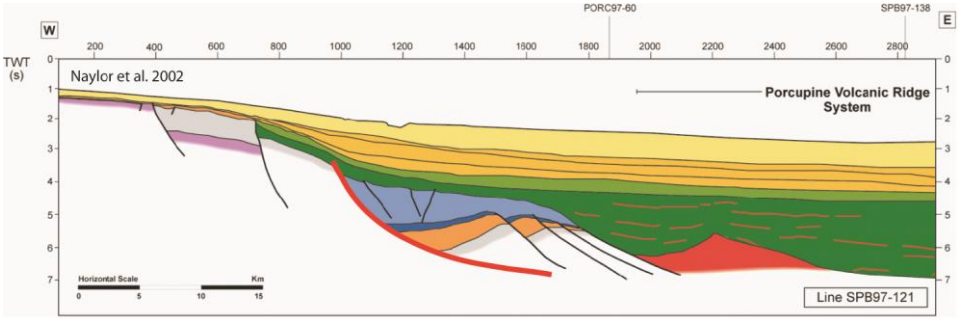

Fig. 5.6: Geoseismic interpretation of SPB97-121 (Fig. 5.2e). Note that the data was interpreted as a listric fault system.

SPB97 – 121 (Fig. 5.2e), located on the western margin of the Porcupine Basin demonstrates, probably, the best example of DFB within the entire basin. The structure in question is located slightly marginward of the $\beta = 2$ domain boundary, at $\beta \approx 1.6$ -1.7, the lower end of

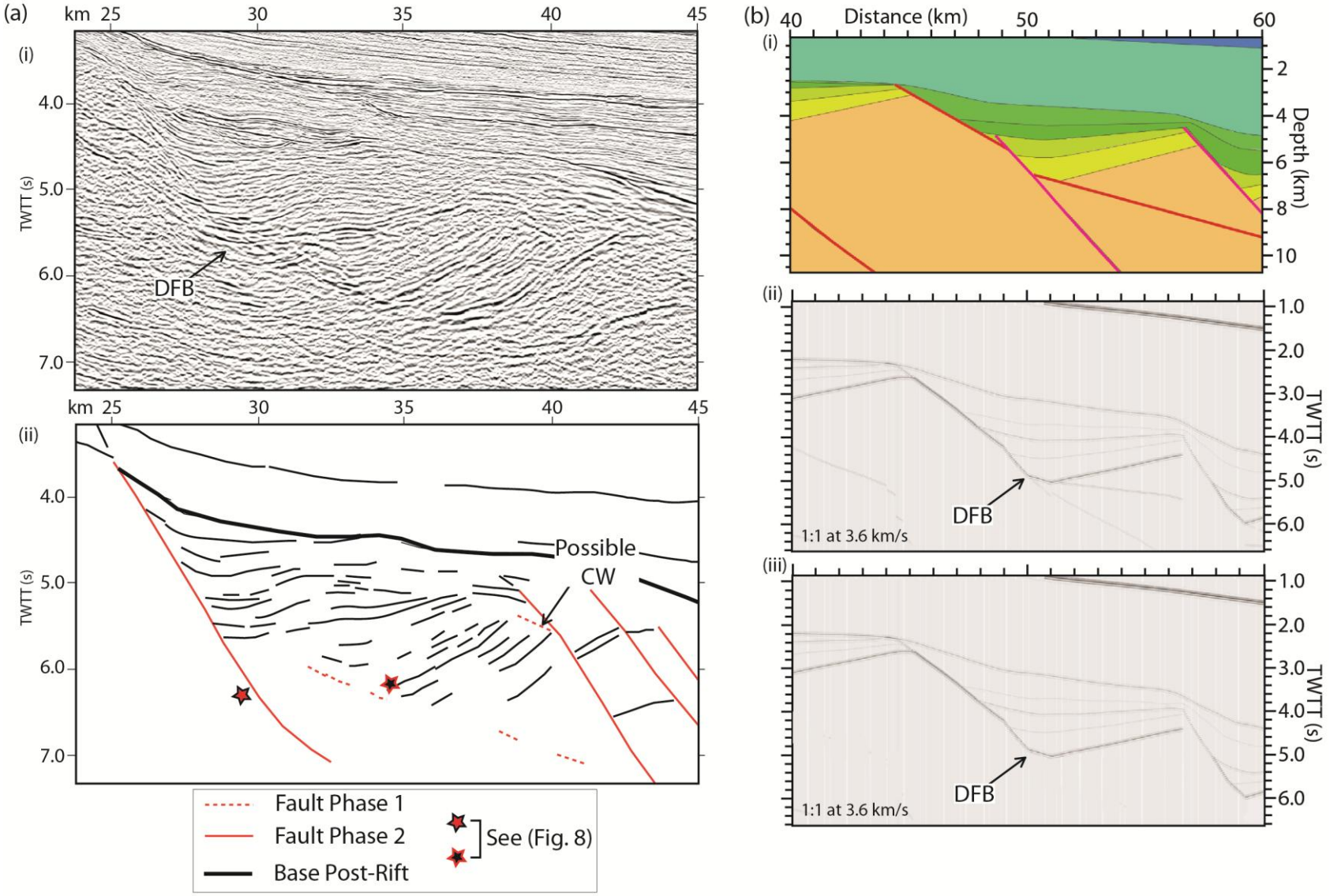
(a)
km 25
30
35
40
45
(i)
TWTT (s)
4.0
5.0
6.0
7.0
DFB
(ii)
Possible
CW
Fault Phase 1
Fault Phase 2
Base Post-Rift
See (Fig. 8)
(b)
Distance (km)
40
50
60
Depth (km)
2
4
6
8
10
(ii)
1:1 at 3.6 km/s
DFB
(iii)
1:1 at 3.6 km/s
DFB
1.0
2.0
3.0
4.0
5.0
6.0

Fig. 5.7: See Fig. 5.2e for location. (a)(i) Uninterpreted seismic data, (ii) line drawing interpretation with two cross-cutting fault generations. Down-dip fault bifurcations, oversteepened stratigraphy, and a possible crestal wedge are present. (b) Synthetic seismic model showing two cross-cutting fault generations. (i) Velocity model, (ii) synthetic seismic with fault zone reflectivity, (iii) no intra-basement reflections. Note expression of DFB, and the relationship of basement reflections relative to the latest faults forming OS.

the maximum achievable stretching possible to accommodate with only one fault generation. The structure has previously been interpreted as a listric fault system (Fig. 5.6, Naylor et al., 2002) but the results from the synthetic models (Figs 4.5 & 4.6) require that caution is exercised when apparently listric structures are observed at high stretching values. This is especially true of TWTT reflection seismic profiles.

Fig. 5.7a(i) shows a zoomed in view of the apparent listric fault system and a line drawing interpretation (Fig. 5.7a(ii)), as well as a synthetic seismogram (Fig. 5.7b) that have very similar reinterpreted here as two discrete fault generations where the earlier fault has been rotated to low angle and abandoned, and is then cross-cut and passively rotated by the – latest, high-angle fault generation. In this example, the first generation fault produces discontinuous (but bright due to sediment-basement juxtaposition) reflections that are seen to clearly truncate early stratigraphy (Fig. 5.7a). The later, high-angle fault produces some well-developed bright reflections higher in the section, again due to sediment-basement/sediment-early sediment juxtapositions. The deeper expression of the fault is not as well imaged but there are some weaker discontinuous reflections that are seen to dip in a similar, if not a slightly lower angle than the fault reflections in the upper part of the section. The apparent reduction in dip is likely due to velocity pull up beneath the hangingwall. If the first fault generation was not well imaged, it would still be possible to interpret at least two phases of faulting here due to the observed oversteepened stratigraphy.

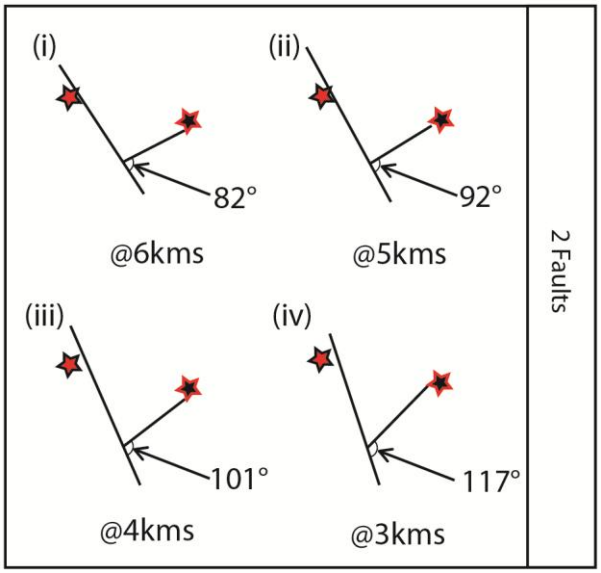

Fig. 5.8: Psuedo-depth migration of relationship between fault (latest generation)- basement intersection. Note that for all potentially realistic seismic velocities the intersection angle is too high for the basement tilt to have been caused by only one fault generation. Even if DFBs were not interpretable in Fig. 7, the presence of OS in the data strongly suggests extension over at least two fault generations.

Fig. 5.8 demonstrates that when the dip of the early sediments is compared to the dip of the latest faults for the time migrated data, the intersection angle is too large to be caused by only one fault set, assuming sediments were deposited horizontally, and the intersection angle between the high-angle fault and the early sediments is even greater than that observed for SBP97-103. It would not be possible for only one fault generation to accommodate the tilting for any reasonable seismic velocities (as shown in each of the pseudo-depth converted panels).

The cross-cutting nature of the faults is very well developed in the depth-migrated version of the data (Fig. 5.9), and both the low-angled first generation fault and the upper section of the high-angled late generation fault are very well imaged. The high-angle fault's deeper

expression does not appear to shallow as it does in the depth section, suggesting that the shallowing was indeed a velocity effect.

A very similar structure to the apparent listric fault described from SPB97-121 (Fig. 5.7), can be observed on the Goban Spur Margin. Fig. 5.10 shows a segment of ION-GXT's IR1-1080 PSDM line. An apparently listric fault sits in the same part of the stretching domain as the comparative structure on the western margin of the Porcupine Basin. The zoom-in of the structure (Fig. 5.10b) shows very well imaged sediments within the half graben and, upon closer inspection, some very well imaged low-angle faults, as demonstrated in the line drawing interpretation (Fig. 5.10b(ii)). The structure shown in Fig. 5.10 is very similar to Figs 4.5 & 4.6, and can be interpreted as being formed by at least two discrete generations of normal faults.

It can also be seen that the oldest sediments within the hangingwall are clearly oversteepened with respect to the latest high-angle fault, again suggesting that, even if the early generation faults were not imaged, as they are in this and the previous example, there may have been an earlier generation of fault that pre-tilted the stratigraphy before the initiation of the latest fault generation, thus proving the usefulness and predictive strength of oversteepened stratigraphy as a PPF identifier.

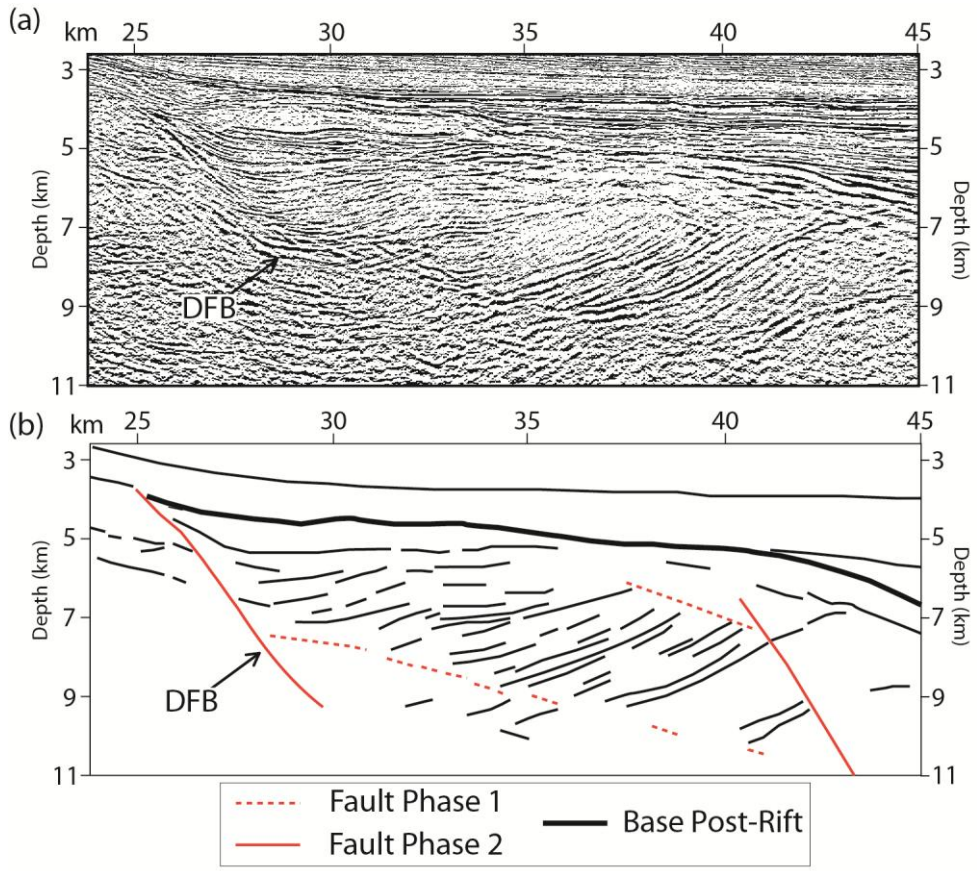

Fig. 5.9: Depth migrated seismic data, taken from Fig. 5.2e(ii). (a) Uninterpreted data, and (interpreted data. Note how clearly the two cross-cutting fault generations can be identified in the depth section, compared to the time section (Fig. 7). Also note that the structure is clearly not listric and that the fault curvature was very likely due to velocity distortion. The DFB indentifier appears as a very strong kink in the uninterpreted data. Also note almost continuous first generation fault reflection.

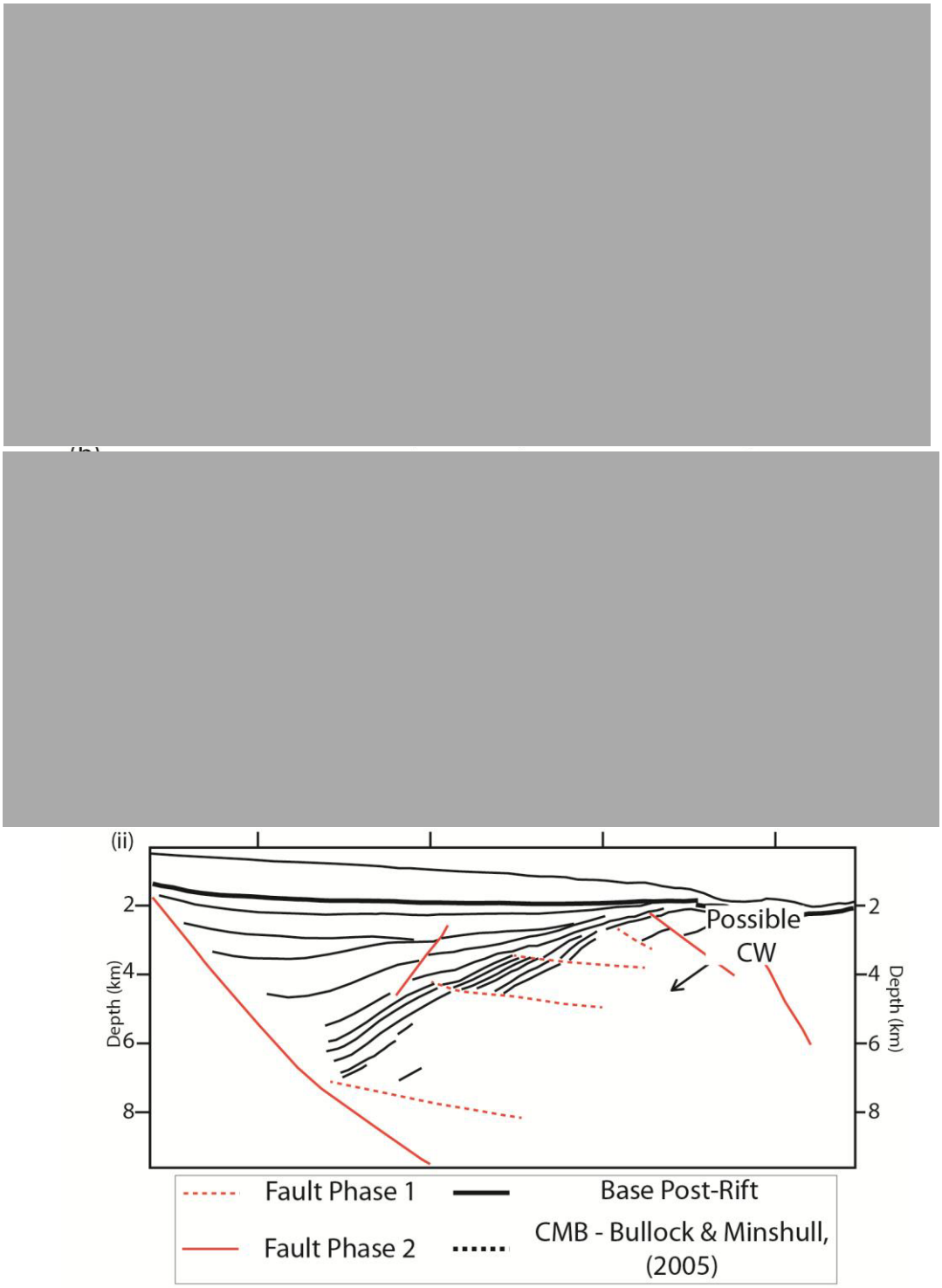

Fig. 5.10: Segment of ION-GXT's IR1-1080 PSDM line from the Goban Spur Margin. (a) Uninterpreted data, with refraction Moho applied. Stretching domains are also assigned. (b) (i) Blow up of half graben structure (Uninterpreted), (ii)Line drawing interpretation of (i) clearly demonstrating two discrete fault generations, forming DFB structures within the half graben. Also note the clearly oversteepened stratigraphy, relative to the latest fault generation.

5.3.3 Crestal Wedges and Up-Dip Fault Bifurcations

Crestal wedges (CWs) and up-dip fault bifurcations (UFBs) are excellent PPF identifiers, that produce cross-cutting fault relationships (described more fully in **Chapter 3**) on seismic data which can be very apparent on seismic data. Their presence high in the syn-rift section or on footwall crests of large fault blocks means that, unlike is the case for DFBs, their associated faults are likely to be expressed seismically and can generally be identified from stratigraphic offsets, or sediment-basement juxtapositions. However, there are issues regarding the preservation potential of these structures. If CWs are not buried relatively quickly, they are susceptible to mass-wastage and erosional process, which would result in the loss of the information they carry.

Examples of CWs and UFBs can be seen atop footwall crests of two large fault blocks seen within stretching domain II (SPB97 – 115; Fig. 5.2d), on the western margin of the Porcupine Basin (Fig. 5.11a). From the blow-up of the time section (Fig. 5.11a), relatively bright reflections dipping at low- moderate angles basinward are observed on the crests of the fault blocks. The sediments immediately above these bright reflections are moderately to steeply dipping marginward, and appear to downlap onto the bright reflections. In Fig. 5.11a(ii) I have interpreted these bright reflections as first generation faults that have been actively rotated (while they were accumulating displacement) and then passively rotated (by later faulting) to their present attitudes, with their high amplitudes resulting from a large impedance contrast produced from sediment-basement juxtapositions; a very similar structure is modelled in Fig. 5.11b. Although it could be argued that these high amplitude reflections may be the seismic expression of igneous intrusions such as sills, it is worth

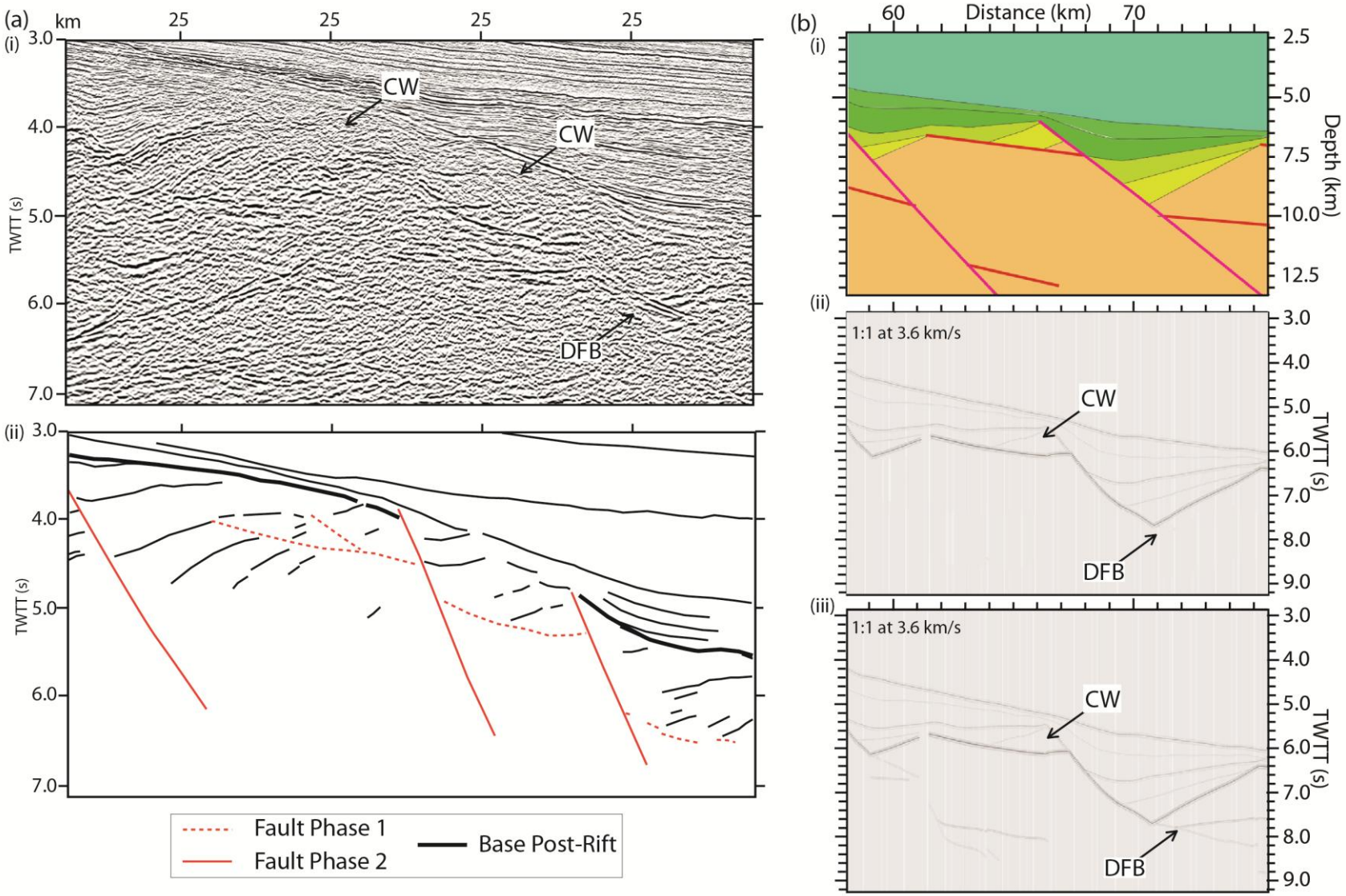
(a)
km
25
25
25
25
(i)
3.0
4.0
5.0
6.0
7.0
TWTT (s)
CW
CW
DFB
(ii)
3.0
4.0
5.0
6.0
7.0
TWTT (s)
Fault Phase 1
Fault Phase 2
Base Post-Rift
(b)
60
Distance (km)
70
(i)
2.5
5.0
7.5
10.0
12.5
Depth (km)
(ii)
1:1 at 3.6 km/s
CW
DFB
3.0
4.0
5.0
6.0
7.0
8.0
9.0
TWTT (s)
(iii)
1:1 at 3.6 km/s
CW
DFB
3.0
4.0
5.0
6.0
7.0
8.0
9.0
TWTT (s)

Fig. 5.11: (a) Blow up of Fig. 2d. (i) Unintepreted data, (ii) line drawing interpretation, highlighting two cross-cutting fault generations forming crestal wedge structures. Note oversteepened stratigraphy relative to the latest fault generation. (b) Synthetic seismic model showing the seismic expression of a well-developed crestal wedge. (i) Input velocity model, (ii) synthetic seismogram, with no intra-basement reflections, (iii) synthetic seismogram showing well developed DFB structures within the basement. Note that the synthetic model (b), compares very well with the data in (a).

noting that such intrusions tend to exploit the path of least resistance - pre-existing faults, or bedding planes, etc. - (Thomson & Schofield, 2008; Schofield et al., 2012; Magee et al., 2012). Even if the high amplitude reflections were related to sills within the section, they are very likely "painting" low-angled faults. There are actually two examples of crestal wedges in this section which can be seen in the two adjacent fault blocks. These examples are displaced from one another by the latest fault generation which, as is generally the case, is clearly imaged on the seismic data and offsets the low-angle faults and their associated sediments, and juxtaposes the latest syn-rift sediments against the crestal wedges. The basinward CW is particularly well imaged and internal structure is visible in Fig. 5.12(a).

The intersection between the latest, high-angle, faults and the early, low-angle faults forms the up-dip fault bifurcations. UFBs are ubiquitous where CWs are developed, but can be developed elsewhere (as is seen in **Chapter 4**). SPB97-121 (**Section 5.3.2**) also shows an example of an UFB, visible on both the time and depth migrations.

Oversteepened stratigraphy can also be observed in this part of the basin between the early sediments and the latest block bounding faults. Although not shown in Fig. 5.11, it can be seen that the early sediments would form large intersection angles with the latest faults, so even if there were no evidence for the presence of crestal wedges or up-dip fault

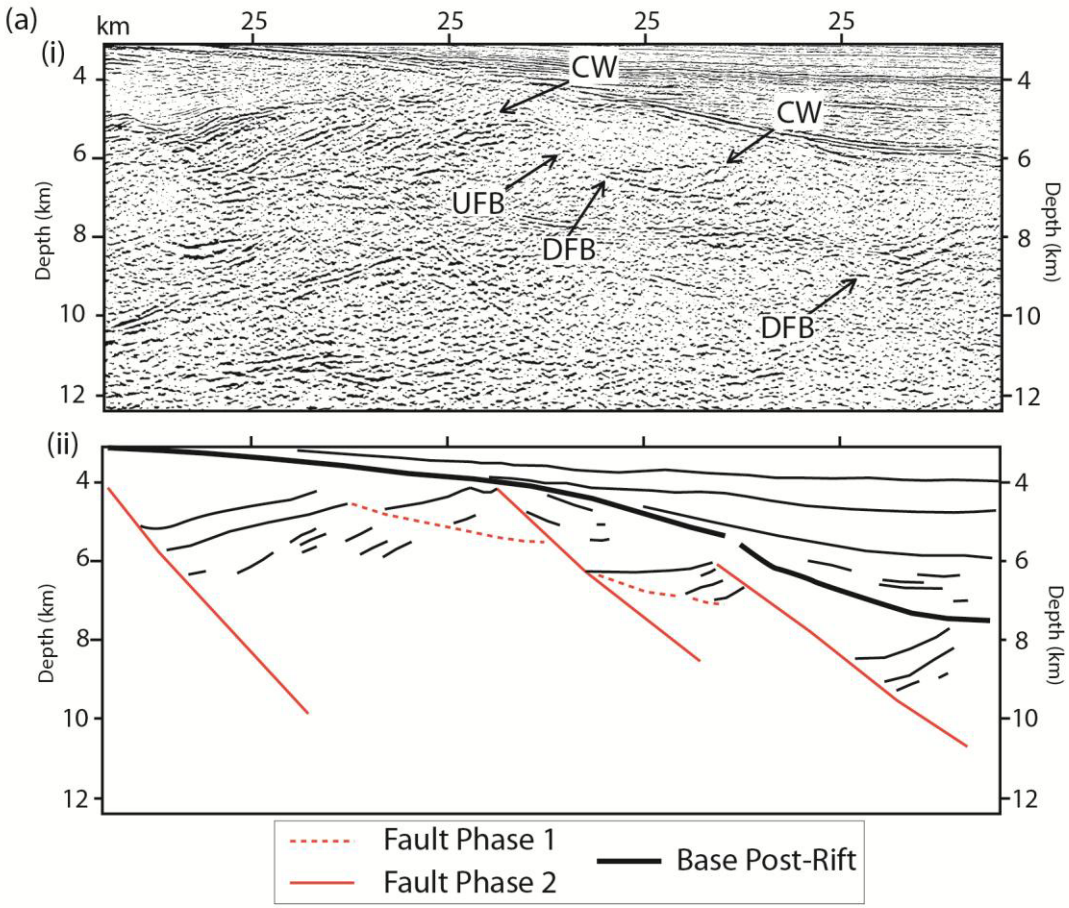
(a)
km
25
25
25
25
(i)
CW
CW
UFB
DFB
DFB
Depth (km)
4
6
8
10
12
(ii)
Fault Phase 1
Fault Phase 2
Base Post-Rift

(b)

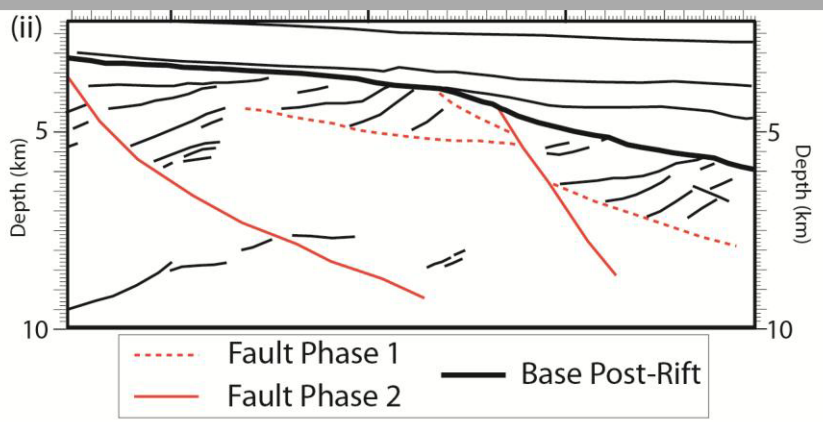
(ii)
Depth (km)
5
10
Fault Phase 1
Fault Phase 2
Base Post-Rift

Fig. 5.12: Crestal wedges in PSDM seismic data from the Porcupine Basin. (a) Blow up of Fig. 5.2d(ii), (i) uninterpreted data, (ii) line drawing interpretation demonstrating the geometry of the crestal wedges in the data. (b) Segment of ION-GXT's IR1-1200 line, showing an along strike view of (a). (i) Uninterpreted data, (ii) line drawing interpretation showing the geometry and internal structure of the crestal wedge.

bifurcations in this section, it would be possible to suggest the presence of the PPF mechanism from the existence of oversteepened stratigraphy alone.

This structure from SPB97-115 is also observed on one of the ION-GXT's PSDM lines, IR1-1220. A blow-up of the area of interest is shown in Fig. 5.12b (Line location**, see 2.1**). The upper CW is very well imaged on this data sediments within the wedge can clearly be seen to "downlap" onto the (bright) low-angled basal fault of the CW. The latest generation fault offset is also very clearly imaged on this section, resulting in good resolution of the UFBs present. Fig. 5.12b also shows quite well the sense of displacement on the low-angled fault.

5.4 Implications of the PPF Mechanism

As described in **Section 5.2** the indicators of PPF are really only observable between Domains I & II. This is not surprising when the results of the seismic modelling in **Chapter 4** (specifically Figs. 5.6 & 5.7) are considered. At higher stretching factors it becomes practically impossible to interpret correctly the structures responsible for the stretching, and the resulting reflector patterns are generally very incoherent and quite chaotic (see Fig. 5.2, paying particular attention to stretching domains III & IV). While depth migrations of the time sections increase the chances of observing hints of the PPF mechanism at lower extensional strains on the basin margins, they do not appear to enhance the interpretability of the mechanism at very high extensional strains. In Domains III & IV the seismic velocity

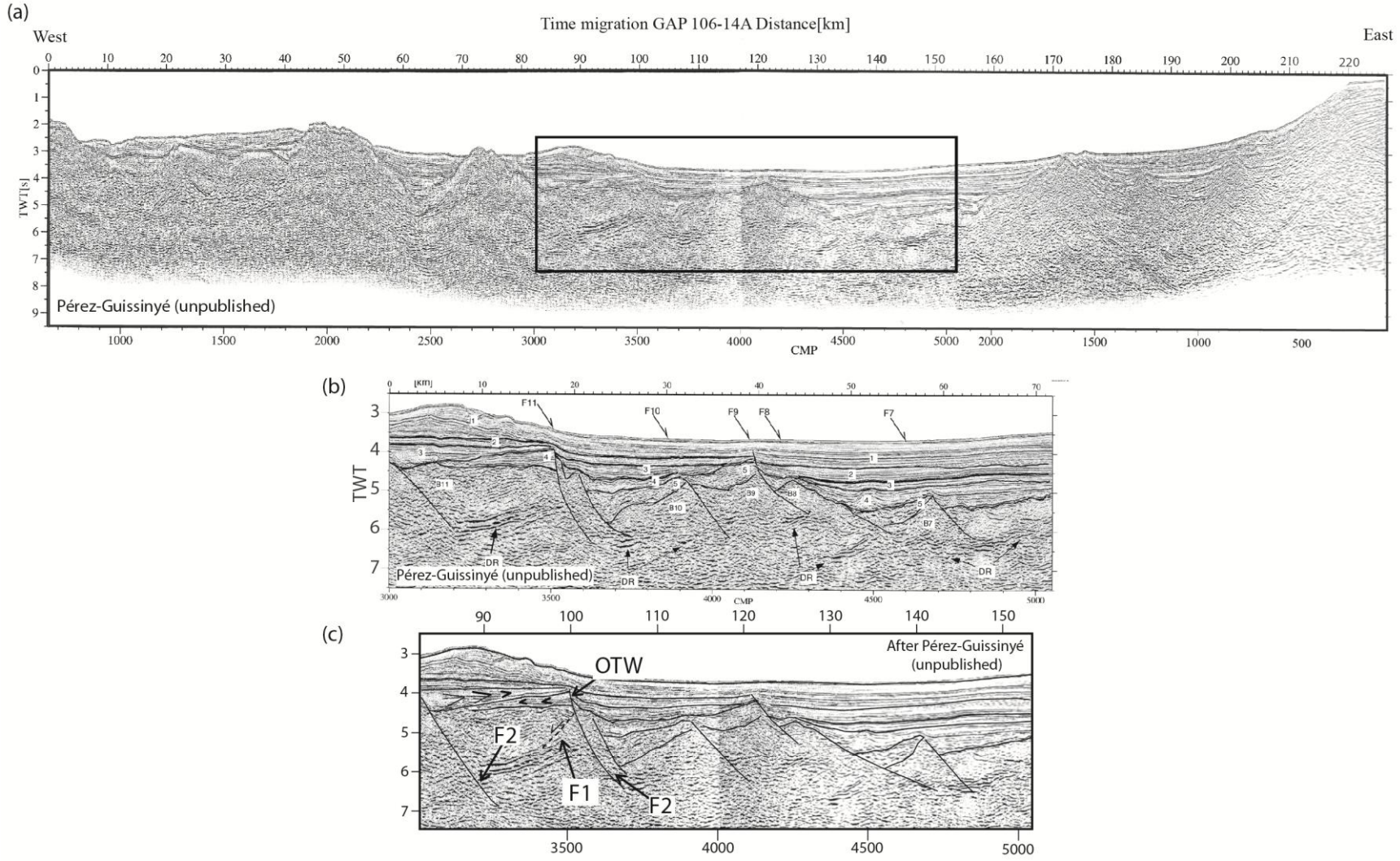
(a)
Time migration GAP 106-14A Distance[km]
West
East
TWT[s]
Pérez-Guissinyé (unpublished)
CMP
(b)
TWT
F11
F10
F9
F8
F7
DR
Pérez-Guissinyé (unpublished)
CMP
(c)
OTW
F2
F1
F2
After Pérez-Guissinyé
(unpublished)

Fig. 5.13: Time section across the Galicia Interior basin. (b) original Pérez-Gussinyé interpretation, (c) reinterpreted data showing evidence for dipole PPF within the basin. Note oppositely thickening wedges (OTW) west of km 110, and relatively low-angle of the first fault generation (F1), compared with the second fault generation (F2).

profile probably varies strongly both vertically and laterally, and so (unless the velocity structure of the crust was already known) depth migration of the time data in these domains is unlikely to provide significant improvement in structural imaging over the time migrations in this part of the basin, since a depth migration is only as good as its velocity model. Reston et al. (2001 & 2004) note that faults above the P-detachment system are very poorly imaged, relative to the S-detachment system in the W. Iberian Margin. This may be in part due to the great thickness of post-rift sedimentary rocks in the centre of the Porcupine Basin causing high levels of seismic energy attenuation, when compared to the sediment starved W. Iberian Margin. This effect can also be seen by comparing Figs 5.4a, 5.7a & 5.10, where FBs and OS are far better imaged from the relatively sediment starved Goban Spur Margin, than those observed from the Porcupine Basin.

While many examples characteristic of the monopole PPF variant have been convincingly recognised within the Porcupine Basin (and also the Goban Spur Margin) within Domains I (high end) and II in **5.2**, convincing examples of the dipole PPF variant have not been identified within the basin, and it may be simply that it had not developed during rifting. The dipole PPF variant does appear to exist in other basins and rifted margins (e.g. Tommasso et al., 2008; **Chapter 3**). The GIB exhibits evidence for polarity changes and oppositely thickening wedges (OTW) resulting from progressive stretching (Pérez-Gussinyé (2000), unpublished thesis , Fig. 5.13) but the significance in terms of the PPF mechanism has not been previously noted.

5.5 Compatibility of PPF with Other Extensional Models

A number of other structural explanations for the extension discrepancy have recently been advanced and it is worthwhile discussing these briefly in the light of the results presented in this thesis and the demonstrable importance of PPF.

The stretching domains presented for the Porcupine Basin in Fig. 5.2, may correlate with the extensional phases described by Lavier & Manatschal, (2006). In this comparison the extensional stages described by Lavier & Manatschal, 2006 (stretching, thinning, and exhumation), stretching phase faults might be expected to be confined to stretching domain I, thinning phase faults potentially being present between domain II & III, and exhumation phase structures within domains III & IV. Stretching phase faults are responsible for the initial stretching of the crust, thinning stage faults generally are described as large-offset, sometimes convex-up detachment style systems that thin the mid-crust preferentially and lead to crustal embrittlement, and exhumation stage faults are where the crust has already been embrittled and mantle exhumation occurs along convex-up detachment style systems (Lavier & Manatschal, 2006). On the surface, this comparison appears reasonable as relatively low strain faults are found within Domain I, as would be expected from the stretching phase, and serpentinite detachment "exhumation" faults are present within Domain III & IV. However, faults relating to the thinning phase of Lavier & Manatschal (2006) should be present within Domains I & II since they are considered to thin the crust to the point of embrittlement (Manatschal et al., 2004; Lavier & Manatschal, 2006). However, structures matching the description of these thinning faults do not appear to be observable within the appropriate stretching domains in the Porcupine Basin. Within stretching

Domains II & III there are, however, hints that structures relating to the monopole PPF mechanism are present, and it could be the PPF mechanism has overprinted examples of the these thinning faults within the basin, if they existed at all, making them extremely difficult to interpret.

Domains II & III correspond to the steepest stretching gradients observed within the Porcupine Basin (**Chapter 2**) and may represent the area where crustal necking preceding total crustal embrittlement occurred leading to the onset of partial mantle serpentinisation. With this in mind, it is reasonably to suggest that Domains II & III would be equivalent to the thinning phase described by Lavier & Manatschal, (2006).

While thinning phase faults (Lavier & Manatschal, 2006) have not been recognised within the Porcupine Basin, that is not to say that they are not present, either there or anywhere else. Péron-Pinvidic & Manatschal (2009) suggested the existence of thinning stage faults within the Galicia Interior Basin, where Reston (2005) has presented some of the first seismically observable PPF structures consisting of two discrete cross-cutting fault generations. Restoration of the latest fault generation in the GIB (Reston, 2005) reveals that first generation of observable faults likely accommodated the majority of the extension within the GIB. These large offset faults may be equivalent to the thinning faults that are required by the Péron-Pinvidic & Manatschal (2009) model in the GIB. It may be that if the resolution of the seismic data were such that all of the faults were interpretable within the Porcupine Basin, similar large offset faults may be identified following palinspastic reconstruction of the latest generation faults. Manatschal et al. (2007) have noted that thinning stage faults would be extremely difficult to identify on seismic data collected from

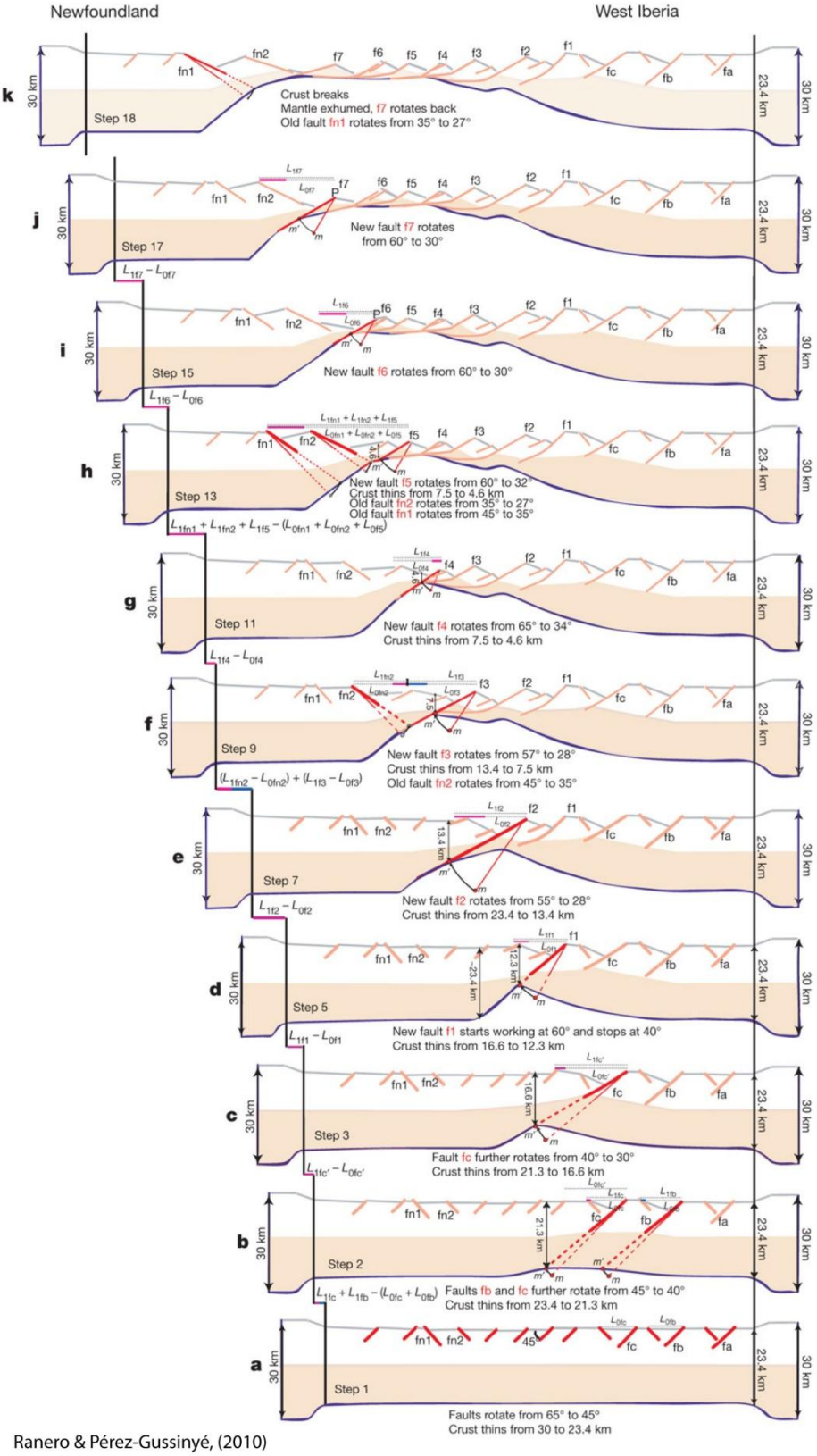

Ranero & Pérez-Gussinyé, (2010)

Fig. 5.14: The Ranero & Pérez-Gussinyé, (2010) sequential faulting model of crustal stretching. Note that pre-

thinning of β≈1.3, is required before sequential faulting initiates. Also note that each fault is active only once, and that only one fault is active at a given time.

MPRMs and are apparently not imaged, conceding that later deformation may mask the thinning structures.

It appears possible that the polyphase rifting model (Lavier & Manatschal, 2006) works well with the PPF mechanism of extension, a possibility which may present good evidence within the GIB. This is not surprising, considering that the initial and final stages are very similar in both models. Both models also lead to embrittlement of the entire crust with lower crustal rheology evolving during progressive thinning as extension is gradually focused into a narrow zone where eventually serpentinite detachment systems take over extension.

Ranero and Perez-Gussinye (2010) proposed that the extension discrepancy can be addressed if faulting occurs sequentially (Fig. 5.14) rather than simultaneously, with later faults cutting crust that has been pre-thinned by the earlier faults. The initial thinning (similar to the stretching phase of Lavier & Manatschal, 2006) thins the crust from 30 km to 23.4 km (β ≈ 1.3, which should produce well developed tilted fault blocks) over a widely distributed area before sequential faulting initiates in stage four of their model (Fig. 5.14). In their model, only one fault is active at a given time, rotating to lower angles as it stretches and thins the crust until the point at which it locks up and is abandoned. New faults become active sequentially toward the basin centre and site of eventual break-up.

Ranero & Pérez-Gussinyé (2010) state that the model is capable of producing the structural geometries and basement thinning observed at the Iberia-Newfoundland, with fault blocks becoming smaller towards the site of eventual break up, concomitant with thinning brittle

layer thickness. However, as shown in Fig. 5.15, the Ranero & Pérez-Gussinyé, (2010) model, overestimates the crustal thickness, and does not match that which is observed directly from depth migrated seismic data (Reston, pers. comm.).

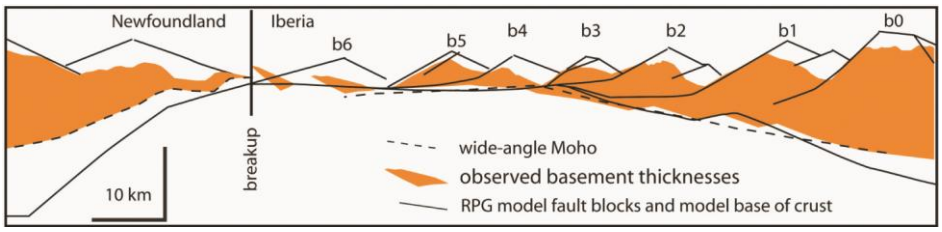

Fig. 5.15: From McDermott & Reston, 2012. Comparison between basement thinning and reduction in fault block size predicted by the sequential faulting mechanism, and that which is observed. Note that the predicted thinning does not match the observed basement thinning at all.

Ranero & Pérez-Gussinyé (2010) also specifically state that the observed stretching on the margins occurs without the requirement for a PPF mechanism but, as is shown in Fig. 5.16, one (and probably more) of their "single" fault generations exhibits clear evidence of a UFB, and potentially a top-basement fault. Evidence of severely oversteepened stratigraphy (the "smoking gun") can also clearly be seen east of km 90 (Fig. 5.16), where the stratigraphic-fault intersection is close to 90°. Among the potential attractions of the sequential faulting model is that it does not require faults to operate outside of typical Andersonian limits. However, the same is also true of the PPF mechanism, demonstrated by the mechanical models for fault rotation in **Chapter 3**, and in no instances is it necessary for a fault to be active below c. 30°. However, once total crustal embrittlement has been achieved, faults may remain active to very low angles (outside the range of typical Andersonian mechanics) due to the extremely low coefficient of friction associated with serpentine. Therefore, the PPF mechanism operates within the ranges that would be considered typically Andersonian. Any low-angle structures present in the section may be via passive rotation of older, now

inactive fault sets, by younger, high-angle fault sets as described in **Chapter 3.** Fig. 5.17 shows a reconstruction of the sequential faulting model from stage 18 – stage 4 (Ranero & Pérez-Gussinyé, 2010). The key thing to note about this is that the extension accommodated in the intervening stages can actually be calculated by summation of the fault heaves as measured in stage 18. This suggests that the order of faulting is not important and that sequential nature of faulting is not strictly necessary. Reston et al. (2007) have demonstrated, using the geometry of syn-tectonic sediment wedges, that multiple faults were active simultaneously during the development of the S-detachment system on the W. Iberian Margin, and were likely active to angles as low as 12 – 15°. This is at odds with the sequential faulting model, as Ranero & Pérez-Gussinyé (2010) state that no faults were active below c. 28° in their model, and that only one fault was active at any given time. Syn-tectonic sedimentation in the presence of low-angle detachment systems has been shown to be somewhat unconventional, in that sediments need not thicken toward the active fault but instead may appear parallel layered (Péron-Pinvidic et al., 2007), similar to what might be expected for post-rift sediments. The implication here is that a low-angle fault system may be active to extremely low angles, and not be readily interpreted as such from study of their associated syn-tectonic sediments.

Furthermore, as is highlighted in Fig. 5.17, in order for the sequential faulting mechanism to work, significant DDS is required, and this can be seen in the thickening that is observed beneath the rift margins in stage 18. So, it can be shown that the model of sequential faulting presented by Ranero & Pérez-Gussinyé (2010) cannot solve the extension

discrepancy unless PPF is incorporated, and without invoking DDS, which has been shown in **Chapter 1** to be unlikely to occur on the WIM.

While the Manatschal-style and the Ranero & Pérez-Gussinyé (2010) models provide potential explanations for the structural evolution of MPRMs, they generally display variations of the PPF mechanism. However, it has been shown that both of these rifting styles, especially the Ranero & Pérez-Gussinyé (2010), actually require that the PPF mechanism be incorporated in order to better account for features in the seismic data, and explain some of their observations and predictions (but they do not state this).

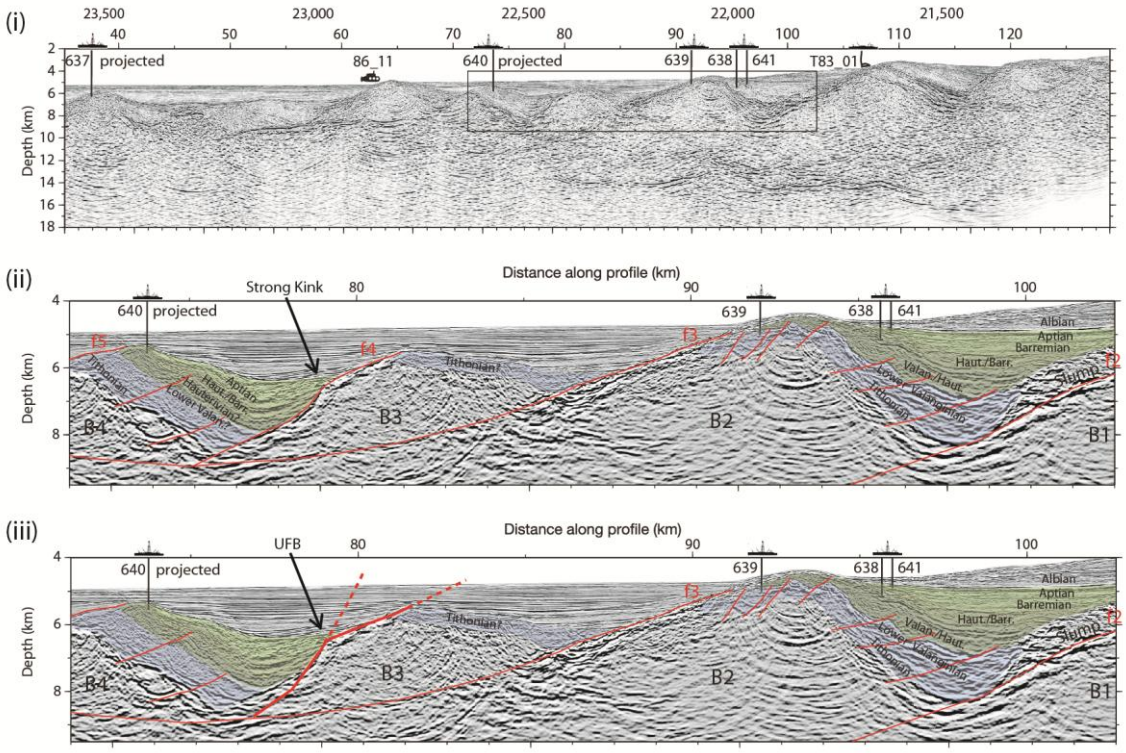

Fig. 5.16: Seismic data taken from Ranero & Pérez-Gussinyé (2010). (a) Uniterpreted data. (b) Ranero & Pérez-Gussinyé's interpretation, of sequential faulting, with fault blocks younging westwards. Note the strong kink on F4. (b) Reinterpretation of F4, as a PPF structure. This is a clear example of an up-dip fault bifurcation (UFB), so the geometry of B3 has been affected by at least two fault generations. Also note the highly oversteepened stratigraphy on B2, relative to F2 (almost orthogonal).

(a)

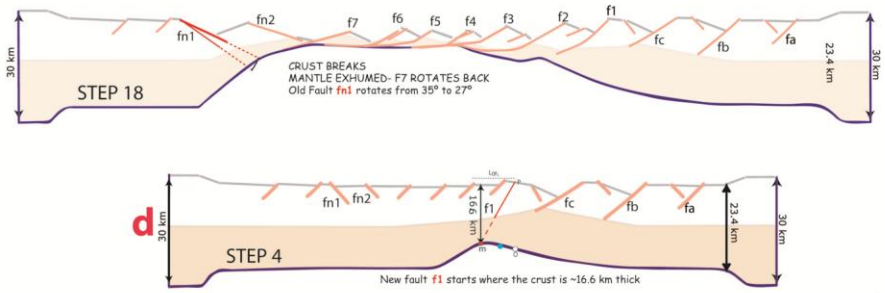

Ranero & Pérez-Gussinyé (2010)

(b)

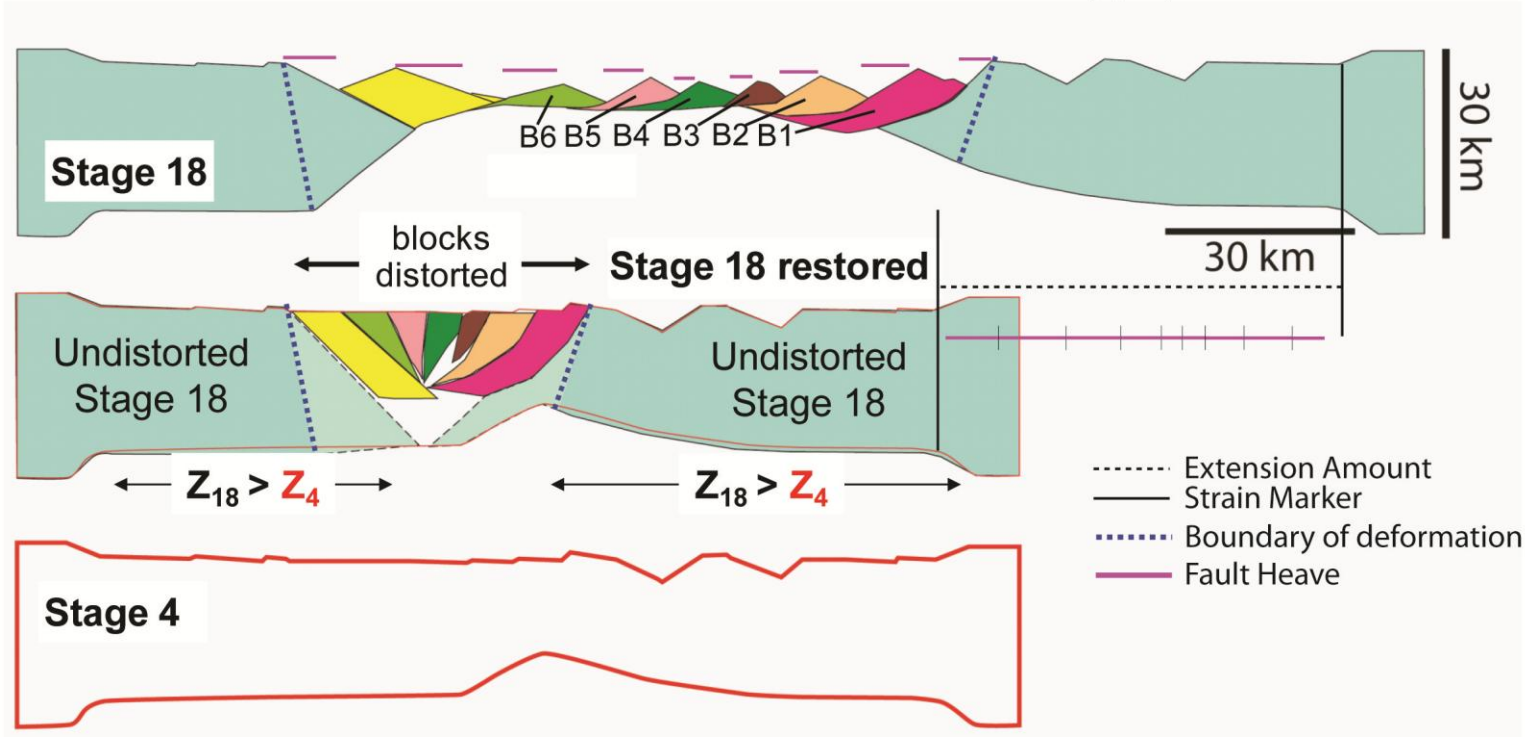

Fig. 5.17: after McDermott & Reston, 2012. (a) Stage 18 and Stage 4 (where sequential faulting initiates) of the sequential faulting model (Ranero & Pérez-Gussinyé, 2010). (b) Restoration of stage 18 of the sequential faulting model to stage 4. For the restoration, blocks from stage 18 are fit inside the stage 4 outline of stage 4 with no gaps at the surface. It is found that there is empty space present in the centre of the basin, equivalent in area to blocks B1, 2 & 3. This area is balanced by thickening the margins of stage 18 (which can be seen to be thicker than the outline of stage 4). Landward directed DDS is required to make the model area balance, thickening the base of the margins. Note that the total fault heaves from stage 18, equal the total amount of stretching since stage 4. This suggests that sequential faulting is not necessary, and the order of faulting is unimportant, and fault movements could even be simultaneous. Therefore, the model does not sequential faulting is not necessary and the faults could have moved in any order, or even simultaneously. See text for more detailed discussion.

Throughout this thesis, I have shown that polyphase faulting is both mechanically feasible and, moreover, capable of accommodating the levels of extensional strain that are observed at MPRMs. I have shown that the identifiers of the PPF mechanism clearly exist on the margins of the Porcupine Basin, and suggest that there have been at least two generations of faulting prior to the initiation of serpentinite detachment tectonics over the P-detachment system. Similar PPF identifies have also been identified on a number of published seismic sections (as discussed in this chapter), and as discussed in **Chapter 3** PPF is observable onshore in the western United States, as such the PPF mechanism is my preferred stretching model to explain hyper-extension of the continental crust.

From the ideas presented in this thesis, it is possible to suggest a simple model of hyper-extension where two to three fault generations would be sufficient to (**Chapter 3**) thin the crust to the point of embrittlement and initiate mantle serpentinisation, purely by structural means without requiring significant DDT. For the case of the Porcupine Basin, at least two generations of cross-cutting faults have been observed, this together with the presence of the P-detachment system support the case for the PPF model leading to hyper-extended rifting. Further stretching to c. 3km thickness is accommodated by the P-detachment system.

5.6 Summary

From investigation of the different stretching domains within the Porcupine Basin, it has been found that evidence for the existence of the PPF mechanism for hyper-extension can be observed. Examples of all the main PPF identifiers discussed in **Chapter 3** have been shown to be present on the margins of the Porcupine Basin. The most robust of these, and the most likely to be recognisable appears to be oversteepened stratigraphy relative to the latest generation of faults. Oversteepened stratigraphy, does not rely on complex structure to be imaged by reflection seismic data, only that the sediments are imaged (although they will only be imaged to a finite inclination (due to the use of limited migration apertures, and processing bias towards low-angle reflections on industry data), so it is a very useful tool to aid in the recognition of hyper-extension accomplished by multiple generations of extensional faults within a basin, or rifted margin.

The fact that the evidence for PPF is best seen in the relatively low strain domains is compatible with the results of seismic modelling in **Chapter 4** where high degrees of stretching, requiring large rotations on a second or third generation fault, produce highly complex structural geometries that are practically impossible to interpret on reflection seismic data. **Chapter 3** has demonstrated that the PPF mechanism is capable of accommodating very large amounts of extensional strain on relatively few fault generations, effectively leading to total crustal embrittlement in as few as two fault generations, at which point mantle serpentinisation is considered to initiated concomitantly with further crustal stretching over detachment systems. The existence of the P-detachment system (which effectively hyper-extends the crust to the cusp of rupture in the region of the Porcupine Arch)

within the appropriate stretching domains, suggests a potential model for the observed stretching in the basin.

Pure-shear crustal stretching over at least two generations of extensional faults, where extension focused toward the basin centre, thinned the crust to the point of total embrittlement. Following embrittlement fluids were able to penetrate the mantle and begin the process of mantle serpentinisation, and further extension, now strongly influenced by the frictional coefficient of serpentine (**Chapter 3**), occurred over a serpentinite detachment system – P-detachment. Extension in the basin continued, almost to the point of crustal separation, but the regional focus of extension then likely shifted westward to the adjacent Rockall Basin.

Where crustal thickness is observed to be extremely thin on refraction seismic data and gravity models, it is worth looking for the identifiers of the PPF mechanism within stretching Domain II of the particular basin, as it is a powerful and viable mechanism for hyper-extending the crust. Unfortunately due to the complex geometries resultant from the mechanism it is highly unlikely to be interpretable in the deeper more highly stretched parts of a basin, or margin.

If the crust is known to be hyper-extended (from refraction or gravity studies), observation of PPF identifiers on the relatively low-strain sections of margins, may make it reasonable to assume that PPF structures may exist deeper in the more highly-strained parts of the margin/basin. Synthetic seismic modelling has shown that the mechanism would very likely be impossible to interpret correctly. So, by building up a case using as much evidence for

the PPF mechanism that can be identified on a margin/basin, it may be possible to account for some, if not all of the apparent extension discrepancy at Magma-Poor Rifted Margins, and hyper-extended margin basins.

CHAPTER 6

Summary and Conclusion

Throughout the course of this thesis, I have attempted to demonstrate the polyphase faulting (PPF) model can (at least partially) solve the extension discrepancy that is commonly associated with magma-poor rifted margins (MPRMs) and other hyper-extended regions of continental crust. I have demonstrated that the mechanism is capable of accommodating the required amounts of extension to account for the "missing" extension at MPRMs, while remaining hidden, or difficult to see on reflection seismic data.

Both the monopole and dipole variants of the PPF mechanism have been shown to be mechanically feasible, and capable of accommodating the required extension. Rotation of normal fault systems from an initially high-angle to lower angles is a fundamental requirement for the PPF mechanism, and the effect of progressive crustal thinning via rotating fault systems has been shown to be of great importance (from the mechanical models presented in **Chapter 3**). It appears that the magnitude of the lithostatic stress imposed on an extensional system controls the maximum degree through which an extensional fault can rotate. The models show that as the crust is thinned and the lithostatic stress is reduced, the maximum rotation a fault can undergo increases to c. 30°, rotating from 60 - 30°. Although this number has been suggested previously by many workers, this is the first time that the evolution of the ambient stress field with regard to *progressive* crustal thinning has been shown to directly affect the amount of rotation a fault is capable of achieving before it becomes mechanically unfeasible to continue extension along it. The effect of total crustal embrittlement and the development of faults that may remain active

to low-angle were also investigated mechanically. The effect of serpentinisation has been shown to be of great importance to the development of late stage low-angle fault systems. The simple models presented here demonstrate that total crustal embrittlement can be achieved over a minimum of two discrete fault generations, and that further crustal extension will likely be accommodated by serpentinite detachment systems.

Simple conceptual models which demonstrate the complex structural styles that are expected to develop as a PPF system evolves to accommodate greater amounts of extensional strain are also presented (**Chapter 3**). From these conceptual models, structural geometries that are characteristic of the polyphase faulting mechanism (PPF identifiers) have been highlighted for both end members of the PPF mechanism; monopole and dipole (see-saw). For the monopole PPF mechanism these identifiers include oversteepened stratigraphy, fault bifurcations (up-dip, and down-dip), and crestal wedges. The dipole PPF mechanism displays oppositely thickening sediment wedges and top-basement faults. Published examples of areas that have been extended via the PPF mechanism from the onshore western United States have been palinspastically restored, and it is demonstrated that the mechanism is capable of accommodating very large amounts of extension. The onshore examples are found to compare very well with the predictions made by the mechanical models, so strengthening the case for the PPF model capability to hyper-extend the continental crust.

Analysis of 2D PSDM reflection seismic from the region of the Porcupine Arch (Main Porcupine Basin, west of Ireland), has shown that the basin can and should be reclassified as a magma-poor aulacogen (MPA) where the conjugate margins, normally separated by

thousands of kilometres of oceanic crust, can be imaged in a single seismic profile. The Porcupine Basin therefore provides an excellent place to study the evolution and structures associated with magma-poor margins immediately prior to crustal rupture and mantle exhumation. The hyper-extended nature of the crust can clearly be seen on reflection seismic data in the centre of the basin, where the crust has been thinned to only 2 – 3 km (β ≈ 10 – 15). Refraction seismic and gravity modelling confirm the presence of a serpentinite undercrust, and comparison between the Porcupine Arch and the W. Iberian margin strongly suggests the presence of a serpentinite detachment system at the centre of the basin. These features, combined with the extremely low-volumes of syn-rift magmatism, allow the reclassification of the basin as a magma-poor aulacogen. As the crust is hyper-extended in the Porcupine Basin, it forms an excellent area to investigate whether the PPF mechanism can be observed, and accommodate any of the high strain known to have been suffered by the basin.

In order to test whether the PPF mechanism occurred during the hyper-extension of the crust at the Porcupine Basin, a number of synthetic seismic sections were generated and presented in **Chapter 4** using both published examples of PPF (from the western United States) and also conceptual models of rifted margins. The purpose of the synthetic model was to investigate the seismic expression of the PPF mechanism and to observe the manifestation of PPF identifiers on seismic data, as well as to test how well PPF structures would be imaged at very high strain levels. It was found that for very high strain levels (β ≥ 3), the PPF structures are effectively impossible to interpret correctly, and that they can only be identified with any confidence at relatively low strain levels. The best imaged and most

interpretable structures were in the regions where the second generation faults had only just become active and had not rotated to a significant degree.

From comparison between the synthetic models and reflection seismic data from the Porcupine Basin and adjacent Goban Spur Margin, it was possible to identify evidence for the action of the PPF mechanism. Examples of downdip fault bifurcations, crestal wedges and oversteepened stratigraphy were all present within the appropriate stretching domains (**Chapter 5**). As was predicted by the synthetic models, strong evidence for the presence of the PPF mechanism in the more highly extended regions of the data was impossible to identify. As the PPF mechanism has been identified on the relatively low-strain margins of the basin, it is reasonable to assume that extension in the higher strain sections of the basins, too, was accommodated by the PPF mechanism, but as was demonstrated quite clearly by the synthetic models, these structures would be highly unlikely to be interpretable on seismic data.

It is reasonable to say that, from the evidence presented, the stretching observed within the Porcupine Basin likely is, accommodated via the PPF mechanism. Two discrete fault generations have been shown to exist on the margins of the basin and in the centre of the basin the detailed structure of the hyperextended crust is not resolved, probably because it is simply too complex and too disrupted. Taken together with the presence of a probable serpentinite detachment system in the centre of the basin, it is possible to tentatively suggest that the crust was stretched to the point of total embrittlement, over two to three fault generations (where the high strain forms of the second generation faults, or potential third generation faults are not visible on the data). Following total crustal embrittlement,

strain was strongly focused in the centre of the basin above the region of serpentinising mantle, and the remainder of the stretching accommodated by the P-detachment system.

In this way, hyper-extension of the crust and mantle serpentinisation of the crust can be achieved via faulting, without the need to invoke depth-dependent mechanisms.

References

Abers, G., A. 2001. Evidence for seismogenic normal faults at shallow dips in continental rifts. In: Wilson, R.C.L., Whitmarsh, R.B., Taylor, B. & Froitzheim, N. 2001. Non-volcanic rifting of continental margins: A comparison from land and sea. Geological society , London. Special publications, 187, 305-318.

Agnon, A. and Reches, Z., 1995. Frictional Rheology - Hardening by Rotation of Active Normal Faults. *Tectonophysics,* **247**(1-4),.

Allen, P., A., and Allen, J., R., 2005. Basin Analysis: Principles and Applications 2nd Edition. *Blackwell Publishing*.

Anderson, E. M., 1951. *The Dynamics of Faulting.* Oliver and Boyd, Ltd.,London.

Axen, G.J., 1992. Pore Pressure, Stress Increase, and Fault Weakening in Low-Angle Normal Faulting. *Journal of Geophysical Research-Solid Earth,* **97**(B6),.

Axen, G.J. and Bartley, J.M., 1997. Field tests of rolling hinges: Existence, mechanical types, and implications for extensional tectonics. *Journal of Geophysical Research-Solid Earth,* **102**(B9),.

Axen, G.J., 2007. Research Focus: Significance of large-displacement, low-angle normal faults. *Geology,* **35**(3),.

Barry, K.M.; Cavers, D.A.; Kneale, C.W. (1975). Recommended standards for digital tape formats. *Geophysics*, **40**, no. 2, pp. 344 – 352.

Barton, A., J. and White, R., S. 1995. The Edoras Bank margin; continental break-up in the presence of a mantle plume. *Journal of the Geological Society, London*, **152**, pp. 971 – 974.

Barton, A., J., and White, R., S. 1997. Crustal structure of Edoras Bank continental margin and mantle thermal anomalies beneath the North Atlantic. *Journal of Geophysical Research.* **102**, no. B2, pp. 3109- 3129.

Baxter, K., Buddin, T., Corcoran, D. & Smith. S.2001. Structural modelling of the south Porcupine

Basin, offshore Ireland: implications for the timing, magnitude and style of crustal extension. *In:* SHANNON, P.M., HAUGHTON, P.D.W. & CORCORAN, D.V. (eds) *The Petroleum Exploration of Ireland's Offshore Basins.* Geological Society. London, Special Publications, **188**. 275-290.

Berger, M. & Roberts, A.M. 1999. The Zeta Structure: a footwall degradation complex formed by gravity sliding on the western margin of the Tampen Spur, Northern North Sea. In: Fleet, A.J. & Boldy, S.A.R. (eds) Petroleum Geology of Northwest Europe: Proceedings of the 5th Conference. 107-116.

Boillot, G., Feraud, G., Recq, M. and Girardeau, J., 1989. Undercrusting by Serpentinite Beneath Rifted Margins. *Nature,* **341**(6242),.

Boothe-Rea, G., Azanon, J. and Garcia-Duenas, V., 2004. Extensional tectonics in the northeastern Betics (SE Spain): case study of extension in a multilayered upper crust with contrasting rheologies. *Journal of Structural Geology,* **26**(11), pp. 2039-2058.

Booth-Rea, G., Garcia-Duenas, V. and Azanon, J., 2002. Extensional attenuation of the Malaguide and Alpujarride thrust sheets in a segment of the Alboran basin folded during the Tortonian (Lorca area, Eastern Betics). *Comptes Rendus Geoscience,* **334**(8), pp. 557-563.

Bown, J.W. and White, R.S., 1995. Effect of Finite Extension Rate on Melt Generation at Rifted Continental Margins. *Journal of Geophysical Research-Solid Earth,* **100**(B9),.

Brady, R., Wernicke, B. and Fryxell, J., 2000. Kinematic evolution of a large-offset continental normal fault system, South Virgin Mountains, Nevada. *Geological Society of America Bulletin,* **112**(9),.

Braga, J.C., Martin, J.M. and Quesada, C., 2003. Patterns and average rates of late Neogene-Recent uplift of the Betic Cordillera, SE Spain. *Geomorphology,* **50**(1-3), pp. PII S0169-555X(02)00205-2.

Buck, W., R. 1988. Flexural rotation of normal faults. Tectonics. Vol. 7. No. 5. pp. 959-973.

Buck, W., 1991. Modes of Continental Lithospheric Extension. *Journal of Geophysical Research-Solid Earth,* **96**(B12), pp. 20161-20178.

Buck, WR, and Lavier, L., 2001. A tale of two kinds of normal fault: the importance of strain weakening in fault development. In WILSON, R.C.L., WHiTMARSH, R.B., TAYLOR, B. & FRO1TZHEIM, N. (eds.). *Non-Volcanic Rifting of Continental Margins: A Comparison of Evidence from Land and Sea.* Geological Society, London, Special Publications, **187**, 289-303

Bullock, A.D. & Minshull, T.A., 2005. From continental extension to seafloor spreading: crustal structure of the Goban Spur rifted margin, southwest of the UK, *Geophys. J. Int.,* **163,** 527–546.

Byrlee, J. 1978. Friction of Rocks. Pure Appl. Geophys., 116; 615-626

Calves, G., Torvela, T., Huuse, M. and Dinkelman, M.G., 2012. New evidence for the origin of the Porcupine Median Volcanic Ridge: Early Cretaceous volcanism in the Porcupine Basin, Atlantic margin of Ireland. *Geochemistry Geophysics Geosystems,* **13**, pp. Q06001.

Chamberlin, R., M. 1982.Geologic map, cross section, and map units of the Lemitar Mountains, Socorro County, New Mexico. *New Mexico Bureau of Geology and Mineral Resources* Open File Report 169

Chian, D., Reid, I., D., and Jackson, H., R. 2001. Crustal structure beneath Orphan Basin and implications for nonvolcanic rifting. *Journal of Geophysical Research*.**106**. pp 10,923 – 10,940.

Coleman, R.G., 1971. Petrologic and Geophysical Nature of Serpentinites. *Geological Society of America Bulletin,* **82**(4),.

Collettini, C. and Sibson, R.H., 2001. Normal faults, normal friction? *Geology,* **29**(10),

Conroy, J., J., and Brock, A., 1989. Gravity and magnetic studies of crustal structure across the Porcupine Basin west of Ireland. *Earth & Planetary Space Research Letters*. **93**. Pp. 371 – 376

Davis, M. and Kusznir, N., 2004. *Depth-dependent lithospheric stretching at rifted continental margins.*

deMartin, B.J., Sohn, R.A., Canales, J.P. and Humphris, S.E., 2007. Kinematics and geometry of active detachment faulting beneath the Trans-Atlantic Geotraverse (TAG) hydrothermal field on the Mid-Atlantic Ridge. *Geology,* **35**(8),.

Driscoll, N. and Karner, G., 1998. Lower crustal extension across the Northern Carnarvon basin, Australia: Evidence for an eastward dipping detachment. *Journal of Geophysical Research-Solid Earth,* **103**(B3), pp. 4975-4991.

Ferrill, D.A., Morriss, A.P., Jones, S.M. and Stamatakos, J.A., 1998. Extensional layer-parallel shear and normal faulting. *Journal of Structural Geology,* **20**(4),.

Forsyth, D., W. 1992. Finite extension and low-angle normal faulting. *Geology*, vol. **20**, p. 27-30

Fountain, D.M., Hurich, C.A. and Smithson, S.B., 1984. Seismic Reflectivity of Mylonite Zones in the Crust. *Geology,* **12**(4),.

Gans, P.B., Miller, E.L., McCarthy, J. and Ouldcott, M.L., 1985. Tertiary Extensional Faulting and Evolving Ductile-Brittle Transition Zones in the Northern Snake Range and Vicinity - New Insights from Seismic Data. *Geology,* **13**(3),.

Gardner, G., H., F., Gardner, L., W., and Gregory, A., R., 1984. Formation velocity and density – The diagnostic basics for stratigraphic traps. *GEOPHYSICS*, VOL. **39**, NO. 6. pp.770 - 780

Gradstein, F., Ogg, J., Schmitz, M., and Ogg, G., 2012. The geologic time scale 2012. Elsevier, ISBN: 9780444594259

Hauser, F., O'Reilly, B.M., Jacob, A.W.B., Shannon, P.M., Makris, J. and Vogt, U., 1995. The Crustal Structure of the Rockall Trough - Differential Stretching without Underplating. *Journal of Geophysical Research-Solid Earth,* **100**(B3),.

Hauser, F. & O'Reilly, B.M. 2010. Deep seismic refraction modeling in the South Porcupine Basin, offshore Ireland. Irish Petroleum Infrastructure Programme Report.

Healy D and Kusznir, N., 2001. Early kinematic history of the Goban Spur rifted margin derived from a new model of continental breakup and sea-floor spreading initiation. In: KARNER, G. D.,MANATSCHAL, G.&PINHEIRO, L.M. (eds) 2007. *Imaging, Mapping and Modelling Continental Lithosphere Extension and Breakup*. Geological Society, London, Special Publications, 282, 199–215

Henderson, P., and Henderson, G., M., 2009. The Cambridge Handbook of Earth Science Data. Cambridge University Press, ISBN:9780521693172

Halliday, D., Resnick, R., Walker, J., 2000. Fundementals of Physiics, 6th edition. *John Wiley & Sons Inc.*ISBN-10: 0471320005

Henza, A.A., Withjack, M.O., Schlische, R.W. 2009. Normal-fault development during two phases of non-coaxial extension: An experimental study, *Journal of Structural Geology*, doi: 10.1016/j.jsg.2009.07.007

Hölker, A., B., Holliger, K., Manatschal, G., & Anselmetti, F. 2002. Seismic reflectivity of detachment faults of the Iberian and Tethyan distal continental margins based on geological and petrophysical data. *Tectonophysics*. **350**, 127-156

Hopper, J. and Buck, W., 1998. Styles of extensional decoupling. *Geology,* **26**(8), pp. 699-702.

Huismans, R. and Beaumont, C., 2002. Asymmetric lithospheric extension: The role of frictional plastic strain softening inferred from numerical experiments. *Geology,* **30**(3), pp. 211-214.

Huismans, R., and Beaumont, C. 2011. Depth-dependent extension, two-stage breakup and cratonic underplating at rifted margins. *Nature.* **473**, pp. 74 - 78

Jackson, J. and White, N., 1989. Normal Faulting in the Upper Continental-Crust - Observations from Regions of Active Extension. *Journal of Structural Geology,* **11**(1-2), pp. 15-36.

Johnson, R., A., & Loy, K., L. 1992. Seismic reflection evidence for seismogenic low-angle faulting in southeastern Arizona. Geology, 20; 597- 600

Johnson, H., Ritchie, J.D., Gatliff, R.W., Williamson, J.P., Cavill, J. & Bulat, J. 2001. Aspects of the structure of the Porcupine and Porcupine Seabight basins as revealed from gravity modelling of regional seismic transects. In: Shannon, P.M., Haughton, P.D.W. & Corcoran, D.V. (eds) *The Petroleum Exploration of Ireland's Offshore Basins*. Geological Society, London, Special Publications, **188**, 265-274

Jones, S., M., White, N., and Lovell, B. 2001. Cenozoic and Cretaceous transient uplift in the Porcupine Basin and its relationship to a mantle plume. In: Shannon, P., M., Haughton, P., D., W, Corcoran, D., V. (eds), The petroleum exploration of Ireland's offshore basins. *Geological Society of London, Special Publications,* **188,** pp. 354 – 360.

Keen, C., E., and Dehler, S., A. 1993. Stretching and subsidence: Rifting of conjugate margins in the North Atlantic Region. *Tectonics.* **12**. no. 5. pp. 1209 – 1229.

Kimbell, G.S., Ritchie, J.D. and Henderson, A.F., 2010. Three-dimensional gravity and magnetic modelling of the Irish sector of the NE Atlantic margin. *Tectonophysics,* **486**(1-4),.

Krawczyk, CM, Reston, TJ, Beslier, M-O and Boillot, G, 1996. Evidence for Detachment Tectonics on the Iberia Abyssal Plain margin. In: Whitmarsh, R, Sawyer, D and Klaus, A. eds: *ODP Leg 149 Scientific Results Volume*, 603-615

Kusznir, N. J., Hunsdale, R., Roberts, A.M. & iSIMM Team. 2005. Norwegian margin depth-dependent stretching. In: Doré , A., G., & Vinning, B., A., (eds). Petroleum Geology: North-West Europe and Global Perspectives—Proceedings of the 6th Petroleum Geology Conference, 767–783

Kusznir, N. & Karner, G. 2007. Continental lithospheric thinning and breakup in response to upwelling divergent mantleflow: application to the Woodlark, Newfoundland and Iberia margins. *In:* Karner, G.D., Manatschal, G. & Pinheiro, L.M. (eds) *Imaging, Mapping and Modelling Continental Lithosphere Extension and Breakup*. Geological Society, London, Special Publications, **282**, 389–419.

Lailey, M., Stein, A.M. and Reston, T.J., 1989. The Outer Hebrides Fault - a Major Proterozoic Structure in Nw Britain. *Journal of the Geological Society,* **146**.

Lavier, L.L., Buck, W.R. and Poliakov, A.N.B., 1999. Self-consistent rolling-hinge model for the evolution of large-offset low-angle normal faults. *Geology,* **27**(12),.

Lavier, L. and Manatschal, G., 2006. A mechanism to thin the continental lithosphere at magma-poor margins. *Nature,* **440**(7082), pp. 324-328.

Lei, X.L. and Kusunose, K., 1999. Fractal structure and characteristic scale in the distributions of earthquake epicentres, active faults and rivers in Japan. *Geophysical Journal International,* **139**(3),.

LePichon, X. and Sibuet, J., 1981. Passive Margins - a Model of Formation. *Journal of Geophysical Research,* **86**(NB5), pp. 3708-3720.

Leythaeuser, T., Reston, T. and Minshull, T., 2005. Waveform inversion of the S reflector west of Spain: Fine structure of a detachment fault. *Geophysical Research Letters,* **32**(22), pp. L22304.

Lister, G., Etheridge, M. and Symonds, P., 1986. Detachment Faulting and the Evolution of Passive Continental Margins. *Geology,* **14**(3), pp. 246-250.

Louden, K and Chian, D, 1999. The deep structure of non-volcanic rifted continental margins. *Phil. Trans. R. Soc. Lond.* A (1999) **357**, 767-805

Lowe, C. & Jacob, A.B., 1989. A north-south seismic profile across the Caledonian Suture zone in Ireland, *Tectonophysics,* **168,** 297–318.

Lundin, E.R. and Dore, A.G., 2011. Hyperextension, serpentinization, and weakening: A new paradigm for rifted margin compressional deformation. *Geology,* **39**(4),.

Magee, C., Stevenson, C., O'Driscoll, B., Schofield, N., McDermott, K., 2012. An alternative emplacement model for the classic Ardnamurchan cone sheet swarm, NW Scotland, involving lateral magma supply via regional dykes. *Journal of Structural Geology*, **43**, pp. 73-91

Makris, J. et al. 1988. Continental crust under the southern Porcupine Seabight, west of Ireland. Earth and Planetary Science Letters, 89, 387–397.

ManatschalL, G., Froitzeim, N., Rubenach, M. & Turrin, B. D. 2001. The role of detachment faulting in the formation of an ocean-continent transition: insights from the Iberian Abyssal Plain. In: WILSON, R. C. L.,WHITMARSH, R. B., TAYLOR, B.&FROITZHEIM, N. (eds) Non-volcanic Rifting of Continental Margins: A Comparison of Evidence From Land and Sea. Geological Society, London, Special Publications, 187, 405–428

Manatschal, G., 2004. New models for evolution of magma-poor rifted margins based on a review of data and concepts from West Iberia and the Alps. *International Journal of Earth Sciences,* **93**(3), pp. 432-466.

Manatschal, G., Muntener, O., Lavier, L., Minshull, T., Peron-Pinvidic, G., 2007. Observations from the Alpine Tethys and Iberia–Newfoundland margins pertinent to the interpretation of continental breakup. In: KARNER, G. D., MANATSCHAL, G. & PINHEIRO, L. M. (eds) *Imaging, Mapping and Modelling Continental Lithosphere Extension and Breakup*. Geological Society, London, Special Publications, 282, 291–324

Marrett, R. and Allmendinger, R., 1992. Amount of Extension on Small Faults - an Example from the Viking Graben. *Geology,* **20**(1), pp. 47-50.

Martinez-Martinez, J.M., Booth-Rea, G., Azanon, J.M. and Torcal, F., 2006. Active transfer fault zone linking a segmented extensional system (Betics, southern Spain): Insight into heterogeneous extension driven by edge delamination. *Tectonophysics,* **422**, pp.. 1 – 4

McDermott, K., and Reston, T. 2012. Explaining the extension discrepancy at rifted margions: seismic modelling and seismic recognition of polyphase faulting. *Deep-water Continental Margins (Conference Abstract).* Burlington House, London.

McKenzie, D., 1978. Some Remarks on Development of Sedimentary Basins. *Earth and Planetary Science Letters,* **40**(1), pp. 25-32.

McLeod, A.E. & Underhill, J.R. 1999. Processes and products of footwall degradation, northern Brent Field, Northern North Sea. In: Fleet, A.J. & Boldy, S.A.R. (eds) Petroleum Geology of Northwest Europe: Proceedings of the 5th Conference. 421-431.

Milkereit, B. and Eaton, D., 1998. Imaging and interpreting the shallow crystalline crust. *Tectonophysics,* **286**(1-4),.

Miller, E.L., Gans, P.B. and Garing, J., 1983. The Snake Range Decollement - an Exhumed Mid-Tertiary Ductile-Brittle Transition. *Tectonics,* **2**(3),.

Mooney, W.D. and Ginzburg, A., 1986. Seismic Measurements of the Internal Properties of Fault Zones. *Pure and Applied Geophysics,* **124**(1-2),.

Morewood, N., Mackenzie, G., Shannon, P., O'Reilly, B., Readman, P. & Makris, J., 2005. The crustal structure and regional development of the Irish Atlantic margin. In: Doré, A. & Vining, B.,(eds.) *Petroleum Geology of North West Europe and Global Perspectives: Proceedings of the Sixth Petroleum Geology Conference,* pp. 1023–1033

Nafe, J., E., and Drake, C., L., 1957. Variation with depth in shallow and deep water marine seiments of porosity, density and the velocity of compressional and shear waves. *Geophysics*. **22**. 3. Pp 523 - 552

Naylor, D., Shannon, P.M. & Murphy, N. 2002. Porcupine–Goban region—a standard structural nomenclature system. Petroleum Affairs Division, SpecialPublication, 1/02

O' Reilly, B., M., Hauser, F., Jacob, A., W., B., Shannon, P., M., Makri, J., & Vogt, U. 1995. The Erris and eastern Rockall Troughs: Structural and sedimentological development. In: Croker, P., F., & Shannon, P., M. (eds) The Petroleum Geology of Irelands Offshore Basins, Geological Society Special Publications, no. **93**. pp 413-422

O'Reilly, B.M., Hauser, F., Jacob, A.W.B. & Shannon, P.M. 1996. The lithosphere below the Rockall Trough: wide-angle seismic evidence for extensive serpentinization. *Tectonophysics,* 255, 1–23.

O'Reilly, B.M., Hauser, F., Ravaut, C., Shannon, P.M. and Readman, P.W., 2006. Crustal thinning, mantle exhumation and serpentinization in the Porcupine Basin, offshore Ireland: evidence from wide-angle seismic data. *Journal of the Geological Society,* **163**.

O' Reilly, B., M., Hauser, F., and Readman, P., W., 2009. The fine-scale structure of upper continental lithosphere from seismic waveform methods: insights into Phanerozoic crustal formation processes. *Geophys. J. Int.* doi: 10.1111/j.1365-246X.2009.04420.x

O'Sullivan J., M., Jones, S., M., and Hardy, R., J., 2010. Comparative analysis of the Porcupine Median Volcanic Ridge with modern day Pacific Ocean seamounts – further evidence of an amagmatic Mesozoic basin history for the South Porcupine Basin, offshore Ireland. 2nd Central and North Atlantic Conjugate Margins Conference, Volume V – p. 216 – 219, ISBN: 978-989-96923-1-2

Parsons, T. and Thompson, G.A., 1993. Does Magmatism Influence Low-Angle Normal Faulting. *Geology,* **21**(3),.

Peacock, D.C.P., 2003. Scaling of transfer zones in the British Isles. *Journal of Structural Geology,* **25**(10),.

Pérez-Gussinyé, M., 2000. Continental Rifting and Break-up at the West Iberia Margin: An Integrated Geophysical Study. *Unpublished Thesis*

Pérez-Gussinyé, M., Ranero, C., Reston, T. and Sawyer, D., 2003. Mechanisms of extension at nonvolcanic margins: Evidence from the Galicia interior basin, west of Iberia. *Journal of Geophysical Research-Solid Earth,* **108**(B5), pp. 2245.

Pérez-Gussinyé, M. and Reston, T., 2001. Rheological evolution during extension at nonvolcanic rifted margins: Onset of serpentinization and development of detachments leading to continental breakup. *Journal of Geophysical Research-Solid Earth,* **106**(B3), pp. 3961-3975.

Péron-Pinvidic, G., Manatschal, G., Minshull, T., A., & Sawyer, D., S. 2007. Tectonosedimentary evolution of the deep Iberia-Newfoundland margins: Evidence for a complex breakup history. Tectonics, Vol. 26. TC2011

Péron-Pinvidic, G. and Manatschal, G., 2009. The final rifting evolution at deep magma-poor passive margins from Iberia-Newfoundland: a new point of view. *International Journal of Earth Sciences,* **98**(7), pp. 1581-1597.

PICKUP, S., WHITMARSH, R., FOWLER, C. and RESTON, T., 1996. Insight into the nature of the ocean-continent transition off West Iberia from a deep multichannel seismic reflection profile. *Geology,* **24**(12), pp. 1079-&.

Praeg,D., Stoker, M.S., Shannon, P.,Ceramicola, S., Hjelstuen,B.O., Laberg,J.S. & Mathiesen, M., 2005. Episodic Cenozoic tectonism and the development of the NW European 'passive' continental margin, *Mar. Petrol. Geol.,* **22**(9-10), 1007–1030.

Proffett, J., 1977. Cenozoic Geology of Yerington District, Nevada, and Implications for Nature and Origin of Basin and Range Faulting. *Geological Society of America Bulletin,* **88**(2), pp. 247-266.

Proffett jnr., J., M., and Dilles, J., H. 1984. Geologic map of the Yerington District, Nevada. *Nevada Bureau of mines and geology* .Map 77

Quinlan, G., Walsh, J., Skogseid, J., Sassi, W., Cloetingh, S., Lobkovsky, L., Bois, C., Stel, H. and Banda, E., 1993. Relationship between Deeper Lithospheric Processes and Near-Surface Tectonics of Sedimentary Basins. *Tectonophysics,* **226**(1-4), pp. 217-225.

Ranero, C., R., & Reston, T., J. 1999. Detachment faulting at ocean core complexes. Geology. v. **27**; p. 983-986

Ranero, C.R. and Perez-Gussinye, M., 2010. Sequential faulting explains the asymmetry and extension discrepancy of conjugate margins. *Nature,* **468**(7321), pp. 294-U180.

Readman, P.W., O'Reilly, B.M., Shannon. P.M. & Naylor, D. 2005. The deep structure of the Porcupine Basin, offshore Ireland, from gravity and magnetic studies. In: Dore. A.G. & Vining. B.A. (eds) Petroleum Geology: NorthWest Europe and Global Perspectives. Proceedings of the 6th Petroleum Geology Conference. Geological Society. London, 1047-1056

Renard, F., J. P. Gratier, and B. Jamtveit (2000), Kinetics of crack-sealing, intergranular pressure solution, and compaction around active faults, *J. Struct. Geol*., **22**(10), pp. 1395– 1407.

Reston, T.J., 1987. Spatial Interference, Reflection Character and the Structure of the Lower Crust Under Extension - Results from 2-D Seismic Modeling. *Annales Geophysicae Series B-Terrestrial and Planetary Physics,* **5**(4),.

Reston, T.J., 1988. Evidence for Shear Zones in the Lower Crust Offshore Britain. *Tectonics,* **7**(5),.

Reston, T.J., 2009. The structure, evolution and symmetry of the magma-poor rifted margins of the North and Central Atlantic: A synthesis. *Tectonophysics,* **468**(1-4), pp. 6-27.

Reston, T.J., Gaw, V., Pennell, J., Klaeschen, D., Stubenrauch, A. and Walker, I., 2004. Extreme crustal thinning in the south Porcupine Basin and the nature of the Porcupine Median High: implications for the formation of non-volcanic rifted margins. *Journal of the Geological Society,* **161**.

Reston, T.J., Leythaeuser, T., Booth-Rea, G., Sawyer, D., Klaeschen, D. and Long, C., 2007. Movement along a low-angle normal fault: The S reflector west of Spain. *Geochemistry Geophysics Geosystems,* **8**, pp. Q06002.

Reston, T.J., Pennell, J., Stubenrauch, A., Walker, I. and Perez-Gussinye, M., 2001. Detachment faulting, mantle serpentinization, and serpentinite-mud volcanism beneath the Porcupine Basin, southwest of Ireland. *Geology,* **29**(7),.

Reston, T.J. and PEREZ-GUSSINYE, M., 2007. Lithospheric extension from rifting to continental breakup at magma-poor margins: rheology, serpentinisation and symmetry. *International Journal of Earth Sciences,* **96**(6),.

Reston, T.J. and RANERO, C.R., 2011. The 3-D geometry of detachment faulting at mid-ocean ridges. *Geochemistry Geophysics Geosystems,* **12**, pp. Q0AG05.

Reston, T., 2007. Extension discrepancy at North Atlantic nonvolcanic rifted margins: Depth-dependent stretching or unrecognized faulting? *Geology,* **35**(4), pp. 367-370.

Reston, T.J., 2009. The extension discrepancy and syn-rift subsidence deficit at rifted margins. *Petroleum Geoscience,* **15**(3), pp. 217-237.

Reston, T.J. and McDermott, K.G., 2011. Successive detachment faults and mantle unroofing at magma-poor rifted margins. *Geology,* **39**(11), pp. 1071 - 1074

Reston, T., 2005. Polyphase faulting during the development of the west Galicia rifted margin. *Earth and Planetary Science Letters,* **237**(3-4), pp. 561-576.

Reston, T., Ruoff, O., McBride, J., Ranero, C. and White, R., 1996. Detachment and steep normal faulting in Atlantic oceanic crust west of Africa. *Geology,* **24**(9), pp. 811-814.

Rietbrock, A., Tiberi, C., Scherbaum, F. & Lyoncaen, H. 1996. Seismic slip on a low-angle normal fault in the Gulf of Corinth: evidence from high-resolution cluster analysis of microearthquakes. *Geophysical Research Letters,* 23, 1817-1820.

Rutter, E., H., Khazaneehdari, J., Brodie, K., H., Blundell, D., J., & Waltham, D., A. 1999. Synthetic seismic reflection profile through the Ivrea zone-Serie dei Laghi continental crustal section, northwestern Italy. Geology. v. 27; no.1; p. 79-82

Schofield, N., Brown D.J., Magee C., Stevenson CT., (2012) Sill morphology and comparison of brittle and non-brittle emplacement mechanisms, Geological Society of London, *Journal of the Geological Society of London*, **169**, pp127-141

Seber, D., Barazangi, M., Ibenbrahim, A. and Demnati, A., 1996. Geophysical evidence for lithospheric delamination beneath the Alboran Sea and Rif-Betic mountains. *Nature,* **379**(6568),.

Shannon, P.M., Moore, J.G., Jacob, A.W.B. & Makris, J. 1993. Cretaceous and Tertiary basin development west of Ireland. In: Parker, J.R. (ed.) Petroleum Geology of Northwest Europe: Proceedings of the 4th Conference. Geological Society, London, 1057–1066

Sibson, R.H., 2000. Fluid involvement in normal faulting. *Journal of Geodynamics,* **29**(3-5),.

Shannon, P., Jacob, A.B., O'Reilly, B., Hauser, F., Readman, P. & Makris,J., 1999. Structural setting, geological development and basin modelling in the Rockall Trough, in *Petroleum Geology of North West Europe:Proceedings of the Fifth Conference,* Vol. 5, pp. 421–431, eds Fleet, A. &Boldy, S., Geological Society.

Sheriff, R., E., and Geldart, L., P., 1995. Exploration Seismology, 2nd ed. Cambridge University Press. ISBN:0-521-46286-4

Sibuet, J., 1992. New Constraints on the Formation of the Nonvolcanic Continental Galicia-Flemish Cap Conjugate Margins. *Journal of the Geological Society,* **149**, pp. 829-840.

Smith, D.K., Cann, J.R. and Escartin, J., 2006. Widespread active detachment faulting and core complex formation near 13 degrees N on the Mid-Atlantic Ridge. *Nature,* **442**(7101),.

Tate, M., P. 1992. The Clare Lineament: a relic transform fault west of Ireland. In: Parnell, J. (ed.) Basins of the Atlantic Seaboard: Petroleum Geology, Sedimentology and Basin Evolution. Geological Socienty Special Publication, **62**, pp. 375 – 384

Tate, M.P. 1993. Structural framework and tectono-stratigraphic evolution of the Porcupine Seabight Basin, offshore western Ireland. *Marine and Petroleum Geology*, 10, 95–123.

Tate, M.P., White, N. & Conroy, J.-J. 1993. Lithospheric extension and magmatism in the Porcupine Basin West of Ireland. *Journal of Geophysical Research*, 98, 13905–13923

Tate, M.P. & Dobson, M.R. 1988. Syn- and post-rift igneous activity in the Porcupine Seabight Basin and adjacent continental margin W of Ireland. In: Morton, A.C. & Parson, L.M. (eds) *Early Tertiary Volcanism and the Opening of the NE Atlantic*. *Geological Society, London, Special Publications*, **39**, 309–334

Telford, W., M., Geldart, L., P., and Sheriff, R., E., 1990. Applied Geophysics, 2nd Edition. *Cambridge University Press*. ISBN 0 521. 32693 1, f65.00

Tenthorey, E., Cox, S.F. and Todd, H.F., 2003. Evolution of strength recovery and permeability during fluid-rock reaction in experimental fault zones. *Earth and Planetary Science Letters,* **206**(1-2), pp. PII S0012-821X(02)01082-8.

Tenthorey, E. and Cox, S.F., 2006. Cohesive strengthening of fault zones during the interseismic period: An experimental study. *Journal of Geophysical Research-Solid Earth,* **111**(B9), pp. B09202.

Thomson, K., Schofield, N., 2008, Lithological and structural controls on the emplacement and morphology of sills in sedimentary basins, Structure and Emplacement of High-Level Magmatic Systems, *Geol. Soc. London, Special Publication*, **302**, p. 31-44.

Tomasso, M., Underhill, J.R., Hodginson, R.A. & Young, M.J. 2008. Structural styles and depositional architecture in the Triassic of the Ninian and Alwyn North fields: Implications for basin development and prospectivity in the Northern North Sea. *Marine and Petroleum Geology*, **25**, 588–605

Townend, J. and Zoback, M.D., 2000. How faulting keeps the crust strong. *Geology,* **28**(5),.

Tucholke, B.E., Behn, M.D., Buck, W.R. and Lin, J., 2008. Role of melt supply in oceanic detachment faulting and formation of megamullions. *Geology,* **36**(6),.

Twiss, R., J., and Moores, E., M., 2007. Structural geology, 2nd edition. *Freeman, W., H., & Co.*. ISBN-10: 0716749513

Van Den Berg, R., Daly, J.S. & Salisbury,M.H., 2005. Seismic velocities of granulite—facies xenoliths from central Ireland: implications for lower crustal composition and anisotropy, *Tectonophysics,* **407,** 81–99.

Vogt., U. Makris, J., O'Reilly, B., M., Hauser, F., Readman, P., W., Jacob, A., W., B. and Shannon, P., M. 1998. The Hatton Basin and continental margin: Crustal structure from wide-angle seismic and gravity data. *Journal of Geophysical Research*. **103**, no. B6, pp. 12,545 – 12,566.

Walsh, J., J., & Watterson, J. 1991. Geometric and kinematic coherence and scale effects in normal fault systems. In: Roberts, A., M., Yielding, G., & Freeman, B. (eds). The geometry of normal faults. Geological Society Special Publications, 56, pp 193-203

Walsh, J., J. & Watterson, J. 1992. Populations of faults and fault displacements and their effects on estimates of fault related regional extension. Journal of Structural Geology. Vol. 14, No. 14, pp. 701-712

Walsh, J., Watterson, J. and Yielding, G., 1991. The Importance of Small-Scale Faulting in Regional Extension. *Nature,* **351**(6325), pp. 391-393.

Welford, J.K., Shannon, P.M., O'Reilly, B.M., and Hall, J., 2010. Lithospheric density variations and Moho structure of the Irish Atlantic continental margin from constrained 3-D gravity inversion, Geophysical Journal International, **183**, pp. 79-95.

Welford, J.K., Shannon, P.M., O'Reilly, B.M., and Hall, J., 2012. Comparison of lithosphere structure across the Orphan Basin/Flemish Cap and Irish Atlantic conjugate continental margins from constrained 3-D gravity inversions. Journal of the Geological Society of London, **169**, 4, pp. 405-420

Wernicke, B., 1985. Uniform-Sense Normal Simple Shear of the Continental Lithosphere. *Canadian Journal of Earth Sciences,* **22**(1), pp. 108-125.

White, N. and McKenzie, D., 1988. Formation of the Steers Head Geometry of Sedimentary Basins by Differential Stretching of the Crust and Mantle. *Geology,* **16**(3), pp. 250-253.

White, N., Jackson, J. and McKenzie, D., 1986. The Relationship between the Geometry of Normal Faults and that of the Sedimentary Layers in their Hanging Walls. *Journal of Structural Geology,* **8**(8), pp. 897-909.

White, N., Tate, M., and Conroy, J., J., 1992. Lithospheric stretching in the Porcupine Basin, west of Ireland. In: Parnell, J. (ed.) Basins of the Atlantic Seaboard: Petroleum Geology, Sedimentology and Basin Evolution. *Geological Society Special Publication*, **62**, pp. 327 – 349.

Whitmarsh, R., Manatschal, G. and Minshull, T., 2001. Evolution of magma-poor continental margins from rifting to seafloor spreading. *Nature,* **413**(6852), pp. 150-154.

Withjack, M.O. and Pollock, D.J.D., 1984. Synthetic Seismic-Reflection Profiles of Rift-Related Structures. *Aapg Bulletin-American Association of Petroleum Geologists,* **68**(9),.

Wood, R. and Barton, P., 1983. Crustal Thinning and Subsidence in the North-Sea. *Nature,* **302**(5904), pp. 134-136.

Yarnold, J.C., Johnson, R.A. and Sorenson, L.S., 1993. Identification of Multiple Generations of Crosscutting Domino-Style Faults - Insights from Seismic Modeling. *Tectonics,* **12**(1), pp. 159 - 168

Yilmaz, Özdoğan (1999). Seismic data processing (9. print. ed.). Tulsa, Okla.: Soc. of Exploration Geophysicists. ISBN 0-931830-40-0.

Ziegler, P., 1983. Crustal Thinning and Subsidence in the North-Sea. *Nature,* **304**(5926), pp. 561-561.

Zoback, M. L., Anderson, R. E., and Thompson, G. A., 1981, Cainozoic evolution of the state of stress and style of tectonism of the Basin and Range province of the western United States: *Royal Society of London, Philosophical Transactions* (A), v. **300**, pp. 407-434.

Zoback, M.D. and Townend, J., 2001. Implications of hydrostatic pore pressures and high crustal strength for the deformation of intraplate lithosphere. *Tectonophysics,* **336**(1-4).

Appendix A

Tabulated data for crustal stretching analysis (Chapter 2)

SPB97 - 103

Distance (km)	Shot Point	CMB (m)	Base Post-Rift (m)	Crustal Thickness (m)	Stretching β	Thinning 1 - 1 / β
0	0	26700	2000	24700	1.21	0.18
5	400	24700	2300	22400	1.34	0.25
10	800	22750	3200	19550	1.53	0.35
15	1200	20300	4400	15900	1.89	0.47
20	1600	18200	5250	12950	2.32	0.57
25	2000	16900	7350	9550	3.14	0.68
30	2400	15500	8300	7200	4.17	0.76
35	2800	14700	8400	6300	4.76	0.79
40	3200	12100	8600	3500	8.57	0.88
45	3600	11400	8400	3000	10.00	0.90
50	4000	11350	7700	3650	8.22	0.88
55	4400	11400	7750	3650	8.22	0.88
60	4800	12450	8250	4200	7.14	0.86
65	5200	12750	8050	4700	6.38	0.84
70	5600	13600	8350	5250	5.71	0.83
75	6000	14700	8350	6350	4.72	0.79
80	6400	16200	7750	8450	3.55	0.72
85	6800	16450	6100	10350	2.90	0.66
90	7200	17450	5450	12000	2.50	0.60
95	7600	19100	5850	13250	2.26	0.56
100	8000	21000	6000	15000	2.00	0.50
105	8400	22400	4600	17800	1.69	0.41
110	8800	23900	3300	20600	1.46	0.31
115	9200	25300	2850	22450	1.34	0.25
120	9600	25950	2550	23400	1.28	0.22
125	10000	26650	1750	24900	1.20	0.17
130	10400	27500	1100	26400	1.14	0.12

Measurement s used to construct attenuation plots Chapter 2, Fig. 2.4(ii). Measurements were taken every 5km along profile. CMB – Crust-mantle boundary.

IR1-1240

Distance (km)	Shot Point	CMB (m)	Base Post-Rift (m)	Crustal Thickness (m)	Stretching β	Thinning 1 - 1 / β
0	0	30000		30000	1.00	0.00
5	400	30000		30000	1.00	0.00
10	800	30000	900	29100	1.03	0.03
15	1200	30000	1000	29000	1.03	0.03
20	1600	29100	1300	27800	1.08	0.07
25	2000	27750	1500	26250	1.14	0.13
30	2400	26400	1900	24500	1.22	0.18
35	2800	24000	3150	20850	1.44	0.31
40	3200	20900	4150	16750	1.79	0.44
45	3600	19150	5000	14150	2.12	0.53
50	4000	17300	6600	10700	2.80	0.64
55	4400	15200	7950	7250	4.14	0.76
60	4800	14000	7900	6100	4.92	0.80
65	5200	11350	8050	3300	9.09	0.89
70	5600	10650	7850	2800	10.71	0.91
75	6000	9750	7600	2150	13.95	0.93
80	6400	11000	7200	3800	7.89	0.87
85	6800	12000	7250	4750	6.32	0.84
90	7200	12550	8650	3900	7.69	0.87
95	7600	13500	7750	5750	5.22	0.81
100	8000	15000	7700	7300	4.11	0.76
105	8400	14800	7550	7250	4.14	0.76
110	8800	15800	6250	9550	3.14	0.68
115	9200	17500	5600	11900	2.52	0.60
120	9600	19400	5450	13950	2.15	0.54
125	10000	18800	5250	13550	2.21	0.55
130	10400	18600	4400	14200	2.11	0.53
135	10800	19600	3050	16550	1.81	0.45
140	11200	21100	2150	18950	1.58	0.37
145	11600	22300	2100	20200	1.49	0.33
150	12000	22650	1700	20950	1.43	0.30
155	12400	23200	1350	21850	1.37	0.27
160	12800	24200	750	23450	1.28	0.22
165	13200	25500	700	24800	1.21	0.17
170	13600	26400	650	25750	1.17	0.14
175	14000	26900	500	26400	1.14	0.12
180	14400	27100	400	26700	1.12	0.11

Measurement s used to construct attenuation plots Chapter 2, Fig. 2.4(ii). Measurements were taken every 5km along profile. CMB – Crust-mantle boundary.

SPB97-106

Distance (km)	Shot Point	CMB (m)	Base Post-Rift (m)	Crustal Thickness (m)	Stretching β	Thinning 1 - 1 / β
0	0					
5	400					
10	800					
15	1200					
20	1600	17700	4000	13700	2.19	0.54
25	2000	17000	5400	11600	2.59	0.61
30	2400	16350	7100	9250	3.24	0.69
35	2800	15800	8450	7350	4.08	0.76
40	3200	14400	8650	5750	5.22	0.81
45	3600	12150	8900	3250	9.23	0.89
50	4000	11450	8400	3050	9.84	0.90
55	4400	11150	8300	2850	10.53	0.91
60	4800	11650	7900	3750	8.00	0.88
65	5200	11800	8200	3600	8.33	0.88
70	5600	13600	8000	5600	5.36	0.81
75	6000	15000	8400	6600	4.55	0.78
80	6400	16000	8550	7450	4.03	0.75
85	6800	16750	8100	8650	3.47	0.71
90	7200	18000	6800	11200	2.68	0.63
95	7600					
100	8000					
105	8400					
110	8800					
115	9200					
120	9600					
125	10000					
130	10400					
135	10800					
140	11200					

Measurement s used to construct attenuation plots Chapter 2, Fig. 2.4(iii). Measurements were taken every 5km along profile. CMB – Crust-mantle boundary.

SPB97-113

Distance (km)	Shot Point	CMB (m)	Base Post-Rift (m)	Crustal Thickness (m)	Stretching β	Thinning 1 - 1 / β
0	0					
5	400					
10	800					
15	1200					
20	1600					
25	2000					
30	2400					
35	2800					
40	3200	17500	7800	9700	3.09	0.68
45	3600	16550	8600	7950	3.77	0.74
50	4000	15500	8950	6550	4.58	0.78
55	4400	14050	9000	5050	5.94	0.83
60	4800	13200	8800	4400	6.82	0.85
65	5200	12450	8950	3500	8.57	0.88
70	5600	13000	7650	5350	5.61	0.82
75	6000	14350	9300	5050	5.94	0.83
80	6400	15550	9150	6400	4.69	0.79
85	6800	16550	8150	8400	3.57	0.72
90	7200	17300	7700	9600	3.13	0.68
95	7600	18000	7500	10500	2.86	0.65
100	8000					
105	8400					
110	8800					
115	9200					
120	9600					
125	10000					
130	10400					
135	10800					
140	11200					
145	11600					

Measurement s used to construct attenuation plots Chapter 2, Fig. 2.4(iv). Measurements were taken every 5km along profile. CMB – Crust-mantle boundary.

SPB97-115

Distance (km)	Shot Point	CMB (m)	Base Post-Rift (m)	Crustal Thickness (m)	Stretching β	Thinning 1 - 1 / β
0	0					
5	400					
10	800					
15	1200					
20	1600					
25	2000					
30	2400					
35	2800					
40	3200	18450	6650	11800	2.54	0.61
45	3600	16850	7850	9000	3.33	0.70
50	4000	16300	9200	7100	4.23	0.76
55	4400	15100	9700	5400	5.56	0.82
60	4800	13550	9200	4350	6.90	0.86
65	5200	12900	9300	3600	8.33	0.88
70	5600	13100	8550	4550	6.59	0.85
75	6000	15600	9150	6450	4.65	0.79
80	6400	16050	8950	7100	4.23	0.76
85	6800	16050	8700	7350	4.08	0.76
90	7200	16750	8150	8600	3.49	0.71
95	7600	17100	7600	9500	3.16	0.68
100	8000	17700	7150	10550	2.84	0.65
105	8400					
110	8800					
115	9200					
120	9600					
125	10000					
130	10400					
135	10800					
140	11200					
145	11600					

Measurement s used to construct attenuation plots Chapter 2, Fig. 2.4(v). Measurements were taken every 5km along profile. CMB – Crust-mantle boundary.

Distance (km)	Shot Point	CMB (m)	IR1-1200/1220 Base Post-Rift (m)	Crustal Thickness (m)	Stretching β	Thinning 1 - 1 / β
0	0	27000	1100	25900	1.16	0.14
5	400	27000	1250	25750	1.17	0.14
10	800	26700	1500	25200	1.19	0.16
15	1200	25600	1700	23900	1.26	0.20
20	1600	24700	2600	22100	1.36	0.26
25	2000	24000	3350	20650	1.45	0.31
30	2400	23400	3400	20000	1.50	0.33
35	2800	22750	3450	19300	1.55	0.36
40	3200	22200	3500	18700	1.60	0.38
45	3600	21000	3700	17300	1.73	0.42
50	4000	19350	4500	14850	2.02	0.51
55	4400	17800	4900	12900	2.33	0.57
60	4800	15800	5850	9950	3.02	0.67
65	5200	14800	7000	7800	3.85	0.74
70	5600	15300	7600	7700	3.90	0.74
75	6000	14700	7850	6850	4.38	0.77
80	6400	15750	8000	7750	3.87	0.74
85	6800	16000	8500	7500	4.00	0.75
90	7200	16100	7850	8250	3.64	0.73
95	7600	16500	8500	8000	3.75	0.73
100	8000	16900	8700	8200	3.66	0.73
105	8400	17200	7700	9500	3.16	0.68
110	8800	16900	7650	9250	3.24	0.69
115	9200	16500	7500	9000	3.33	0.70
120	9600	16600	7100	9500	3.16	0.68
125	10000	16800	6800	10000	3.00	0.67
130	10400	17700	6400	11300	2.65	0.62
135	10800	19000	5400	13600	2.21	0.55
140	11200	21200	5100	16100	1.86	0.46
145	11600	23300	3200	20100	1.49	0.33
150	12000	25050	1800	23250	1.29	0.23
155	12400	25850	1400	24450	1.23	0.19
160	12800	26100	1200	24900	1.20	0.17
165	13200	26200	1000	25200	1.19	0.16
170	13600	26200	900	25300	1.19	0.16
175	14000	26200	900	25300	1.19	0.16
180	14400	26100	900	25200	1.19	0.16
185	14800	26000	700	25300	1.19	0.16

Measurement s used to construct attenuation plots Chapter 2, Fig. 2.4(vi). Measurements were taken every 5km along profile. CMB – Crust-mantle boundary.

Distance (km)	Shot Point	CMB (m)	IR1-1020 Base Post-Rift (m)	Crustal Thickness (m)	Stretching β	Thinning 1 - 1 / β
105		18000	8150	9850	3.05	0.67
110		16700	7800	8900	3.37	0.70
115		15200	7900	7300	4.11	0.76
120		13500	7850	5650	5.31	0.81
125		12100	7850	4250	7.06	0.86
130		11000	7700	3300	9.09	0.89
135		11050	7750	3300	9.09	0.89
140		11200	8000	3200	9.38	0.89
145		11100	7750	3350	8.96	0.89
150		11400	8250	3150	9.52	0.90
155		11850	8150	3700	8.11	0.88
160		13200	8000	5200	5.77	0.83
165		15100	8250	6850	4.38	0.77
170		15850	8500	7350	4.08	0.76
175		16750	8400	8350	3.59	0.72
180		17800	8700	9100	3.30	0.70
185		17200	9000	8200	3.66	0.73
190		16950	9000	7950	3.77	0.74
195		17250	8700	8550	3.51	0.72
200		16750	9000	7750	3.87	0.74
205		16150	9250	6900	4.35	0.77

Measurement s used to construct attenuation plots Chapter 2, Fig. 2.4(vii). Measurements were taken every 5km along profile. CMB – Crust-mantle boundary.

Appendix B

P-wave velocities and densities of lithological units used for generation of synthetic seismograms (Chapter 4)

Figs. 4.3 & 4.5 – 4.7 - Synthetic Margin

Unit	ρ (gcm^{-3})	Vp (kms^{-1})
Water	1.00	1.50
Post-Rift	2.12	2.60
Syn-Rift 1	2.41	4.10
Syn-Rift 2	2.36	3.80
Syn-Rift 3	2.28	3.30
Syn-Rift 4	2.25	3.10
Basement	2.70	6.00
Moho Transition	2.97	7.00
Serpentinite	2.86	6.50
Mantle	3.29	8.00
Fault - Rock	2.42	4.20

Figs. 4.8 & 4.9 - Proffett, 1977

Unit	ρ (gcm^{-3})	Vp (kms^{-1})
Water	1.00	1.50
Post-Rift 1	2.10	2.50
Post-Rift 2	2.11	2.60
Post-Rift 3	2.14	2.70
Q (M.cmt Sst & Shl)	2.18	2.80
Ta (M.cmt Sst & Shl)	2.23	3.05
T9 (M.cmt Sst & Shl)	2.29	3.35
T6 (W.cmt Sst & Shl)	2.35	3.70
T2 (Conglomerate)	2.55	5.10
Basement (Gneiss)	3.70	5.90
Fault - Rock	2.28	3.30

Figs. 4.11 & 4.12 - Chamberlin, 1982

Unit	ρ (gcm^{-3})	Vp (kms^{-1})
Water	1.00	1.50
Post-Rift 1	2.09	2.50
Post-Rift 2	2.12	2.60
Post-Rift 3	2.18	2.80
M-P.cmt Sst & Shl	2.20	2.90
M-P.cmt Sst & Shl	2.25	3.00
W-M.cmt Sst & Shl	2.30	3.40
W-M.cmt Sst & Shl	2.35	3.50
W.cmt Sst	2.41	4.10
Lst & Shl	2.60	4.90
Qtz.Arn. & Shl	2.55	5.10
Qtz.Arn. & Shl	2.60	5.35
Gneiss	2.70	5.90

Figs. 4.13 & 4.14 – Booth-Rea et al., 2002/2004

Unit	ρ (gcm^{-3})	Vp (kms^{-1})
Water	1.00	1.50
Post-Rift 1	2.09	2.50
Post-Rift 2	2.12	2.60
Post-Rift 3	2.18	2.80
Post-Rift 4	2.20	2.90
M.cmt Sst	2.22	3.00
M.cmt Sst	2.30	3.40
Shl & Graywacke	2.30	3.40
Qtz.Arn. & Shl	2.40	4.10
Qtz.Arn.	2.45	4.40

Schist	2.60	5.40
Gneiss	2.70	5.90
High Density Gneiss	2.80	6.40